Optimization of Aqueous Electric Double-Layer Capacitors

WILLIAMS, RHYS,EDWARD

Optimization of Aqueous Electric Double Layer Capacitors

Rhys Williams

PhD Thesis

Department of Physics

Durham University

United Kingdom

1st October 2024

Optimization of Aqueous Electric Double Layer Capacitors

Rhys Williams

Abstract

This thesis examines three approaches to optimize the performance of aqueous electric double layer capacitors (EDLCs). First, a number of approaches to determining the maximum working voltage (MWV) of aqueous EDLCs are tested. A reliable method for MWV determination is proposed: three-electrode cyclic voltammetry, complemented by galvanostatic charge/discharge cycles, resulting in a MWV of 1.2 V for a standard activated carbon EDLC with an aqueous 6 M KOH electrolyte.

Next, the use of shear-exfoliated few-layer graphene (FLG) as a conductive additive for activated carbon (AC) electrodes is explored. A novel 'vacuum infiltration' approach to incorporating the FLG is shown to increase the specific capacitance (C_{sp}) by $\approx$ 50 %, reaching 142.3$\pm$0.1 F g^{-1} in 6 M KOH, without compromising equivalent series resistance (ESR) or stability compared with conventional carbon black additives.

Finally the impact of surfactants, particularly Triton X-100, on EDLCs with an aqueous 6 M KOH electrolyte, is examined. Triton X-100 reduces the ESR but also lowers C_{sp} by over 10 %. Soaking the AC electrodes in Triton X-100 increases the MWV to 1.4 V but substantially reduces C_{sp}. When the AC was annealed prior to soaking in Triton, the MWV was increased further to 1.6 V, indicating that electrode surface chemistry can significantly alter the effect of surfactants. Unfortunately, the enhanced MWV again came at the cost of a reduced C_{sp}, to the extent that the specific energy is lowered relative to untreated AC operating at 1.2 V.

This research demonstrates that while significant gains in specific energy from increases to the MWV are difficult to realise, there is still scope to improve specific capacitance by developing new electrode materials.

Outcomes

Publications:

- Work presented in Chapter 5 has been published as: R.E. Williams, S. Sukumaran, Q. Abbas, M.R.C. Hunt, "Few-layer graphene as an 'active' conductive additive for flexible aqueous supercapacitor electrodes", Carbon **218**, 118744 (2024).
- Chapters 4 and 6 are being prepared for publication.

Conference Presentations:

- R.E. Williams, S. Sukumaran, Q. Abbas, M.R.C. Hunt, "Few-Layer Graphene As an Electrode, Electrode Additive and an Interfacial Layer in Aqueous Supercapacitors" (Oral presentation), 242nd ECS Meeting, Atlanta, United States (2022).
- R.E. Williams, M.R.C. Hunt, "Using Shear Exfoliated Few-Layer Graphene as a Conductive Additive in Supercapacitor Devices" (Poster presentation), DEI Symposium, Durham, United Kingdom (2022).

Contents

List of Tables

List of Figures

Nomenclature

AA anodic alumina 64

AC activated carbon i

ACN acetonitrile 22

BET Brunauer-Emmett-Teller theory 37

BJH Barrett-Joyner-Halender theory 39

BMIM BF_4 1-butyl-3-methylimidazolium tetrafluoroborate 28

BSE backscattered electron 30

CA chronoamperometry 55

CB carbon black 17

CE counter electrode 43

CMC critical micellar concentration 141

CNT carbon nanotube 17

CPE constant phase element 52

CTR charge transfer resistance 53

CV cyclic voltammetry 45

CVD chemical vapour deposition 21

DMSO dimethyl sulfoxide 144

EDL electric double layer 7

EDLC electric double layer capacitor i

EDR equivalent distributed resistance 54

EDX energy dispersive X-ray spectroscopy ix

EMIM BF_4 1-ethyl-3-methylimidazolium tetrafluoroborate 28

EIS electrochemical impedance spectroscopy 51

ESR equivalent series resistance 6

EV electric vehicle 2

FLG few-layer graphene i

GCD galvanostatic charging/discharging 48

GO graphene oxide 22

GQD graphene quantum dot 114

HER hydrogen evolution reaction 13

hFLG highly centrifuged few-layer graphene 117

IHP inner helmholtz plane 9

IL ionic liquid 27

LiTFSI lithium bis(trifluoromethanesulfonyl)imide 144

LSV linear sweep voltammetry 45

mFLG moderately centrifuged few-layer graphene 117

MWCNT multi walled carbon nanotube 21

MWV maximum working voltage i

NMP n-methyl-2-pyrrolidone 24

OCP open circuit potential 68

OER oxygen evolution reaction 13

OHP outer helmholtz plane 9

PC propylene carbonate 27

PEG polyethylene glycol 144

SRP standard reduction potential 13

SSA specific surface area 17

SWCNT single walled carbon nanotube ix

TEABF$_4$ tetraethylammonium tetrafluoroborate 21

uFLG uncentrifuged few-layer graphene 117

UHP ultra high purity 59

VGCF vapour grown carbon fibres 112

WE working electrode 43

WiSE water-in-salt electrolyte 143

Copyright

Acknowledgements

I would like to first acknowledge my supervisor, Dr Michael Hunt, not only for his patience, support and guidance throughout my studies, but also for his more practical contributions of making the few-layer graphene suspensions used in chapter 5 and of obtaining and analysing the Raman data presented there.

I would next like to acknowledge the contribution Dr Qaisar Abbas, who obtained and analysed the BET data presented in chapter 5.

I would thirdly like to acknowledge the technical support staff in the physics department who aided in designing and building equipment vital to this research, most notably the electrochemical test cells and the USB potentiostats.

On a more personal note, I would like to acknowledge all of my friends, not just in Durham, but across the world, for all the countless ways they have helped me over the years. Thank-you to Izzy Daltry for doing so much to support me throughout this process. Special thanks to Dr Oliver Rigby for his company at lunchtimes and unerring friendship these past five years. Special not-thanks to him for shooting me in the eye with a Nerf gun. It was very painful.

I would like also at this point to make a special mention of my friend John Jose, who is never far from my thoughts, and I would like to dedicate this thesis to his memory.

Lastly, but far from least, I would like to thank my family, especially my parents, for all of their love and support, without which I could never have achieved this. And I would like to make a further dedication to my whole family, and a special dedication to my nieces.

Chapter 1

Introduction

1.1 Energy storage

New and improved energy storage technologies are urgently needed. At present most energy is supplied by the burning of fossil fuels, however this leads to CO_2 emissions linked to climate change [1]. As a result most, if not all, future energy supplies will need to come from carbon-zero sources such as renewables (wind, solar, tidal, geothermal, hydro, etc.) and nuclear.

Unfortunately, it will not be straightforward to make this transition: electricity demand is to a large extent uncontrollable and fluctuates throughout the day. This is not a problem for fossil fuel generators, as the energy they generate can be added or removed from the grid at will to match demand, but this is not the case for carbon-zero sources: many renewables are intermittent, and peaks in demand do not nescessarily coincide with peaks in availability; while the output of nuclear generators is not easily varied, supplying a constant output. This leads to surplus energy being wasted at times, while at other times generation may be inadequate. This mismatch is illustrated by the 'Duck Curve' shown in Figure 1.1 [2]. This shows the energy supply and demand for California on 10/10/2023. Renewable energy (mainly solar in this context) peaks in the middle of the day, supplying

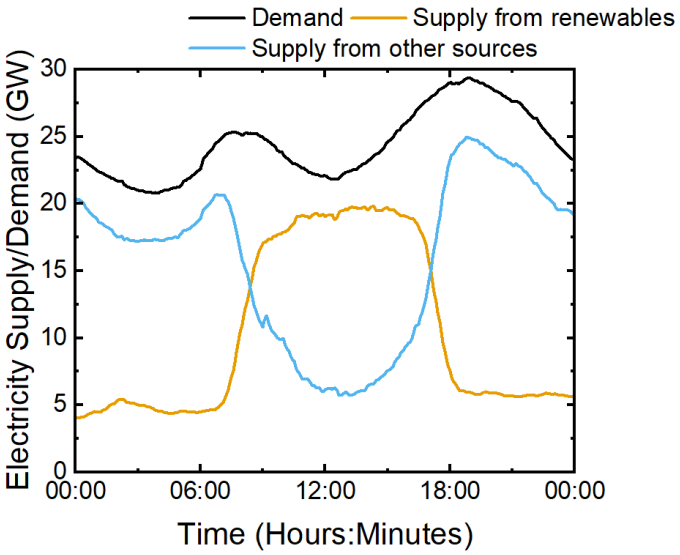

Figure 1.1: 'Duck Curve' showing energy supply and demand for California on 10/10/2023. Total demand is shown in black, supply from renewable resources (wind, solar, biomass, geothermal) is shown in orange, and supply from other sources is shown in blue. Data obtained from CAISO [2].

most electricity, however supply falls rapidly in the late afternoon, just as energy demand picks up, leading to a steep increase in supply from non-renewable sources (largely natural gas in this energy grid). Energy storage is therefore critical to enable the integration of carbon-zero electricity into the grid. These energy storage systems must be high capacity, high efficiency, low cost and responsive.

After power (electricity and heat), and industry, transport is the third largest contributor to global CO_2 emissions contributing 7.98 Gt of global emissions in 2022 [3]. The decarbonisation of transport is leading to growth in the number of electric vehicles (EVs) worldwide which, while they themselves require energy storage, also feed into increased electricity demand. Energy storage for EVs needs to be compact and lightweight, supply high power for acceleration, and possess high energy density to allow for good range. Long lifetimes and short charging times are also very desirable.

In the UK at present the main form of grid energy storage is pumped hydro

[4]. There is however relatively little capacity in comparison with total energy demand, it has lower round trip energy efficiencies (around 70-80%) than desirable, and extremely low energy density (≈1 Wh L^{-1}) [4]. In addition to this, pumped hydro is often impractical, and can have significant impacts on the environment and communities, requiring the construction of large reservoirs.

In contrast, lithium-ion batteries and supercapacitors are capable of energy efficiencies of over 90 % [5, 6], have much higher energy densities (up to 500 Wh L^{-1} in the case of Li-ion batteries [7]), and are highly portable making them well suited to the applications described above, and for use in portable electronics.

Despite these advantages, batteries and supercapacitors do have drawbacks. For example, batteries often contain toxic metals such as cadmium, nickel and lead, and both batteries and supercapacitors often contain flammable, carcinogenic, and toxic organic solvents, making them a challenge to safely dispose of [8, 9]. In addition to this, there are significant environmental or human costs to their production, for example there are concerns about child labour in the mining of cobalt used in Li-ion batteries [10]. Therefore, as new materials are researched to improve the performance of these energy storage devices, care must be taken to ensure that they are truly sustainable.

1.2 Batteries and Supercapacitors

Batteries such as lithium-ion cells store electricity chemically via redox reactions (Faradaic charge storage). In contrast supercapacitors may store charge physically via electric double layer capacitance, these are referred to as electric double layer capacitors (EDLCs); Faradaically, referred to as pseudocapacitors; or a

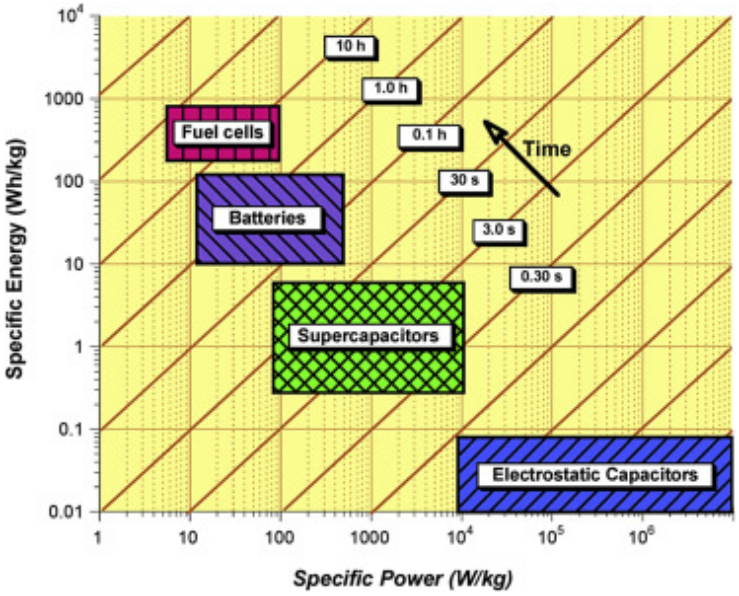

Figure 1.2: Ragone plot, showing specific energy and power as well as discharge times for fuel cells, batteries, electrostatic capacitors and supercapacitors [12].

combination of both (hybrid capacitors).

The Ragone plot (Figure 1.2) illustrates the key differences in performance between supercapacitors and batteries: supercapacitors have a higher power density (up to 10 kW kg^{-1}, or about 1000x that of a typical battery [11]); while batteries have an energy density on the order of 100 times greater than that of supercapacitors [11].

Table 1.1 compares the properties of supercapacitors and batteries further. Some key advantages of supercapacitors are: the electrode materials undergo less expansion/contraction during charging/discharging leading to much higher cycle lifetimes ($>10^5$ cycles in EDLCs) [11, 12]; although supercapacitors self-discharge more rapidly than rechargable batteries they have a much longer shelf life [13]; and supercapacitors can be used at low temperatures (experimental devices have demonstrated energy storage capabilities at temperatures as low as -100 °C) where batteries cannot function due to the slowing of redox reactions with decreasing temperature [14].

Characteristic	Li-ion Batteries	Supercapacitors
Specific Energy (Wh kg^{-1})	100-200	0.05-30
Specific Power (W kg^{-1})	150-315	500-5,000
Energy Efficiency (%)	<95	85-98
Lifetime (cycles)	800-3000	500,000
Charge/Discharge time	Hours	Seconds/Minutes

Table 1.1: Table comparing performance characteristics of Li-ion batteries and supercapacitors (Data taken from [12]).

Supercapacitors can be used in hybrid storage systems with batteries to provide higher power output, and decouple energy and power [11]. Such hybrid systems have better energy and power density than either component alone [12, 15]. These hybrid systems may, for example, be used in EVs where supercapacitors could deliver high power for acceleration and recover energy lost during braking, while batteries provide high electrical energy output for travelling greater distances at constant speeds [15].

1.3 Charge Storage in Supercapacitors

Capacitance, C, is defined as

$$C = \frac{Q}{V}, \tag{1.1}$$

where Q is the stored charge due to an applied potential difference V. For the case of a simple capacitor consisting of two parallel plates separated by an dielectric medium, this can be expressed in terms of the electrode surface area, A, the relative permittivity of the separating medium, ε, and the electrode separation, d:

$$C = \frac{\varepsilon A}{d}. \tag{1.2}$$

When characterizing a device, C is often reported as the Specific Capacitance (C_{sp}), which is defined as the capacitance per unit weight of electrode material.

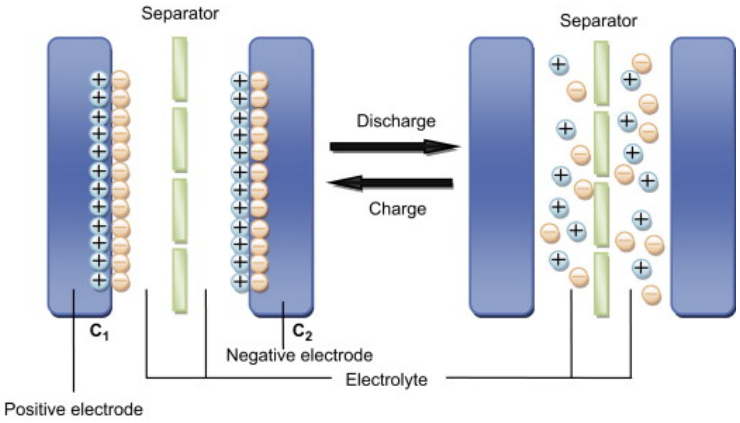

Figure 1.3: Diagram of charged and discharged states of a capacitor, showing how the double layers form two capacitors, C_1 and C_2, in series [16].

The energy stored, E, by a capacitor when charged to a voltage V, is given by

$$E = \frac{1}{2}CV^2. \tag{1.3}$$

An EDLC will also have an equivalent series resistance (ESR) associated with it, which limits the power output. The power output by the supercapacitor when connected to a circuit is determined by the load resistance, R_L, of the circuit, and is maximised when R_L is equal to the ESR. The maximum power output P_{max} is then given by

$$P_{max} = \frac{1}{4}\frac{V^2}{R}, \tag{1.4}$$

where R is the ESR of the cell.

1.3.1 The Electric Double Layer

At its most basic level, a supercapacitor is comprised of two electrodes immersed in an electrolyte, which store charge when oppositely polarised. As described in equation 1.2, the capacitance depends on electrode surface area, and so the electrodes are usually made from highly porous materials in order to maximise this. The electrolyte generally consists of a solvent containing dissolved ions, although there are alternatives such as solid electrolytes and ionic liquids.

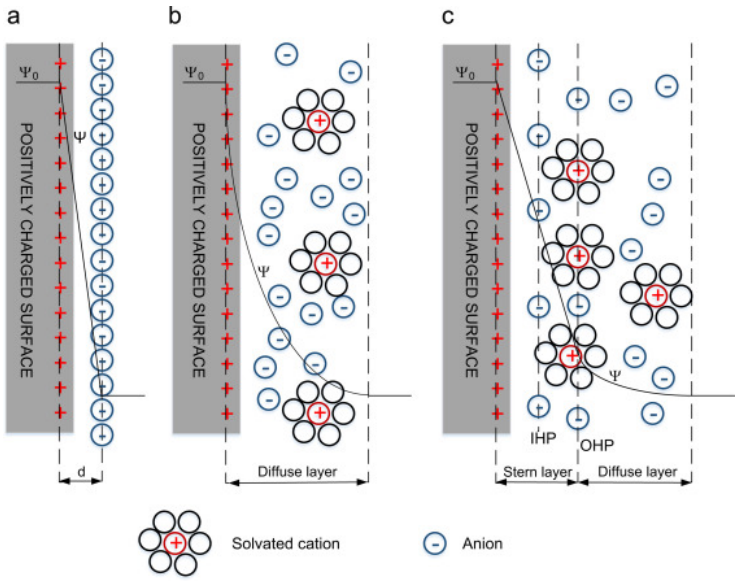

Figure 1.4: Three models of double layer capacitance; a), Helmholtz; b), Gouy-Chapman; c), Stern [11].

In an EDLC, charge is stored electrostatically by the formation of an electric double layer (EDL) at the electrode-electrolyte interface. In the bulk of an electrolyte, solvent molecules and dissolved ions move randomly due to Brownian motion, but in the vicinity of the interface between the electrolyte and a charged electrode the solvent molecules and dissolved ions organise themselves in such a way as to balance the charge of the electrode [17, 18]. The charged solvated ions in the electrolyte are attracted towards the surface of the electrode with opposite charge and into the pores of the electrode material, forming the EDL. This creates two capacitors connected in series by the electrolyte (Figure 1.3) [16]. There are three main models which are used to describe the structure of the electric double layer, which are illustrated in Figure 1.4, and described below.

1.3.1.1 Helmoltz model

The Helmholtz model is the simplest description of the organisation of the EDL, in which the charge in the electrode is neutralized by ions of opposite charge forming an ordered layer at a distance, d, from the electrode surface [11, 19]. This results

in a capacitance independent of potential, which unfortunately does not reflect the real behaviour of EDLCs [15, 20]. Instead, C varies with V, being approximately linear at low potentials, but plateauing at higher potentials [21, 22].

1.3.1.2 Gouy-Chapman or diffuse model

The Gouy-Chapman (or diffuse) model extends the simple description provided by the Helmholtz model by replacing the well-ordered array of ions at the electrode/electrolyte interface with a diffuse layer, reflecting effects such as thermally-driven disorder. In the diffuse model, rather than the ions forming a single layer at a fixed distance from the electrode surface, their concentration instead follows a Boltzmann distribution, forming a so-called 'diffuse layer' [11, 17, 19, 23]. This model leads to the non-linear capacitance observed in real experiments [20], however the model assumes the ions to be point charges which allows them to approach too closely to the electrode surface, resulting in an overestimation of capacitance [15].

1.3.1.3 Stern modification or diffuse double layer

The Stern model combines elements of the Helmholtz and Gouy-Chapman models, having some ions forming a Helmholtz layer with well-defined electrode-ion separation, while the remainder form a diffuse layer. This model also accounts for the finite size of ions, assuming their distance of closest approach to the surface to be δ, the diameter of the ion, overcoming the issue of the Gouy-Chapman model overestimating capacitance [11, 18, 19]. The total double layer capacitance, C_{dl} is then given by: $\frac{1}{C_{\mathrm{dl}}} = \frac{1}{C_{\mathrm{H}}} + \frac{1}{C_{\mathrm{diff}}}$, where C_{H} is the capacitance of the Helmholtz layer, and C_{diff} the capacitance of the diffuse layer [20, 23, 24]. The Grahame model extends this picture still further, suggesting that some ions will

lose their solvation shell and specifically adsorb on the electrode surface, forming the inner helmholtz plane (IHP), while others remain in solution forming the outer helmholtz plane (OHP) [17, 23]. This results in the term d in equation 1.1 being as small as the diameter of a desolvated ion, which – alongside the high surface area of electrode materials – accounts for the high capacitance of EDLCs relative to conventional capacitors [23].

In real EDLCs, however, the models above all fall short, and Equation 1.2 itself is limited as capacitance does not depend linearly on the surface area of the nanoporous materials, such as activated carbon, from which supercapacitor electrodes are often made (see 1.6.2.1) [25]. This is due to those pores; ion storage in nanoporous materials is highly complex and poorly understood as ion mobility is significantly influenced by pore size. If pores are too small they become inaccessible, with the size at which this happens varying depending on electrolyte [11]. Pores with characteristic linear dimensions (or 'size') below 0.5 nm are inaccessible to solvated ions in aqueous electrolytes [26], while due to the larger size of organic solvent molecules, pores below 1 nm are inaccessible in organic electrolytes [27]. Conversely, pores that are too large have been observed to reduce specific capacitance, with there being an optimal pore size (measured as 0.8 to 1 nm for H_2SO_4 [28]) at which double layer capacitance is maximised [28, 29].

1.3.2 Pseudocapacitors

Pseudocapacitors store charge via Faradaic reactions in which the charge transferred is voltage dependent according to equation 1.1, i.e. capacitor-like behaviour. This stands in contrast to battery, in which charge and discharge occur at particular electrode potentials, and therefore the relationship between charge stored and cell voltage is more complicated. Pseudocapacitors can achieve specific capacitances 10-100 times greater than EDLCs, but in common with

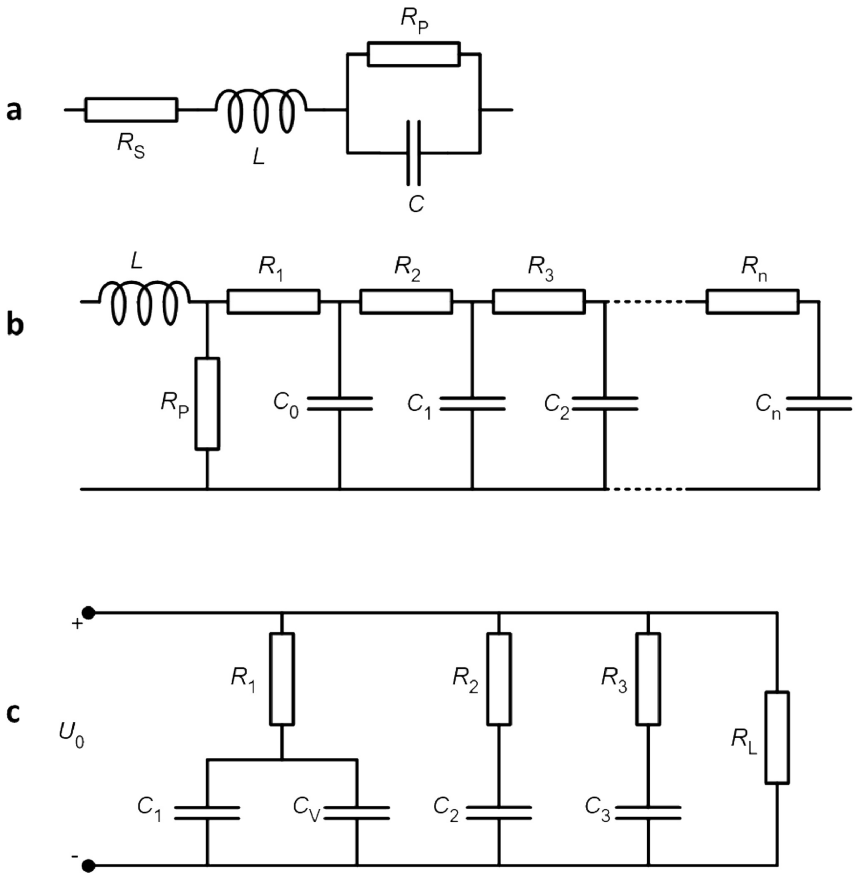

Figure 1.5: Three equivalent circuit models for supercapacitors. a) Simplified Randles circuit, b) transmission line model, c) Zubieta-Bonert model. Reproduced from reference [32].

batteries suffer from inferior cyclability and a reduced power density [11, 30]. Pseudocapacitive materials include metal oxides such as ruthenium or bismuth, or conducting polymers [11, 30, 31], however even EDLCs may have ≈ 5 % of their capacitance contributed from pseudocapacitance, as is described in section 1.6.2.1.

1.4 Equivalent Circuit Models

The discussion of a supercapacitor in the previous section assumes it to basically behave as a resistor and capacitor in series. Although this is useful for extracting basic parameters such as capacitance and ESR, it is inadequate to properly

represent the real behaviour of a device. Across the literature, a number of more complex equivalent circuits have been used to attempt to more accurately model the behaviour of a supercapacitor. A selection of these are summarised below.

1.4.1 Simplified Randles Circuit

The most basic variation on the RC circuit is the simplified Randles circuit, shown in Figure 1.5 (a). This circuit adds an inductance L in series with the resistance R_{s}, and a resistance R_{p} in parallel with the capacitance. This parallel resistance accounts for the leakage current due to a range of processes from short circuits to redox reactions, and is ideally much larger than R_{s}, allowing it to be neglected at short timescales. L, meanwhile, accounts for the inductance of the cell as well as that of the wires and connectors [32].

1.4.2 Transmission Line Circuit

The transmission line circuit is shown in Figure 1.5 (b) and consists of an infinite series of parallel RC elements. This circuit can be used to model the formation of the EDL in a semi-infinite pore. The impedance response is found to be identical to that of a Warburg element (W), which is used to model semi-infinite diffusion [33]. This is described in greater detail in Chapter 2, section 2.2.4.

1.4.3 Zubieta-Bonert Model

Figure 1.5 (c) shows the Zubieta-Bonert model of a supercapacitor. This consists of four parallel branches. The first is of a resistance R_1 in series with fixed capacitor C_1, which is itself in parallel with a variable capacitor C_V. Here the capacitance is dependent on voltage according to $C_V = C_0 + V \times C_u$. This

branch has a time constant of around 1 s, and models the immediate charging and discharging of the device [21, 32, 34].

The next two branches each consist of a resistor and capacitor in series. The first has a time constant of a few minutes and models charge redistribution, while the second has a longer time constant on the order of hours and represents self-discharge [21, 32, 34]. The latter branch partially covers the function of R_p in the simplified Randles circuit, however a final parallel resistance may be included to model other sources of leakage current.

1.5 Basic Electrochemical definitions and equations

As mentioned above, a supercapacitor contains two oppositely polarised electrodes in an electrolyte. While this polarisation leads to the formation of an EDL, which in an EDLC is responsible for charge storage, it can also allow the transfer of charge carriers between the electrode and electrolyte via redox reactions [17, 18]. In batteries and pseudocapacitors, these redox reactions allow for charge storage [11, 20, 23], however in both of these devices and in EDLCs they can also lead to the corrosion of the electrode, the decomposition of the electrolyte and ultimately the failure of the device [35]. This makes it important to understand such reactions even when focusing on EDLCs. This section will introduce some of the terminology and equations used to describe redox reactions.

Electrode materials can be characterised as polarisable or non-polarisable. For a non-polarisable electrode charge transfer happens readily, with a large current flowing in response to any change in potential; in contrast, an ideally polarisable electrode would undergo an infinite change in potential without any current flow at all [17, 18]. An ideal supercapacitor electrode would be inifinitely polarisable,

whereas non-polarisable electrodes are useful as reference electrodes as described in chapter 2.

Any redox reaction in an electrochemical cell can be broken up into two half reactions; one involving the reduction of a species at the cathode, the other involving the oxidation of a species at the anode [18]. In the case of the electrolysis of water, the overall reaction of $2H_2O(aq) \rightarrow 2H_2(g) + O_2(g)$ is split into the two half reactions of the reduction of H^+ at the cathode and the oxidation of H_2O at the anode, which are given below in the form of the hydrogen evolution reaction (HER) and oxygen evolution reaction (OER) in acidic environments [17]:

$$H^+(aq) + e^- \rightarrow \frac{1}{2}H_2(g) \tag{1.5}$$

$$2H_2O(aq) \rightarrow O_2(g) + 4H^+(aq) + 4e^-. \tag{1.6}$$

While in alkaline environments they are instead:

$$H_2O(aq) + e^- \rightarrow \frac{1}{2}H_2(g) + OH^-(aq) \tag{1.7}$$

$$4OH^-(aq) \rightarrow O_2(g) + 2H_2O(aq) + 4e^-. \tag{1.8}$$

Each half-reaction has a standard reduction potential (SRP) associated with it which is defined relative to the standard hydrogen reduction potential in acidic media, hence the HER in acid has an SRP of 0.00 V [18], whilst the OER in acid has an SRP of 1.23 V. In alkaline environments, the HER and OER potentials are instead -0.828 V and 0.401 V, respectively. The overall cell potential, E_{cell} is given by $E_{\text{cathode}} - E_{\text{anode}}$, which in the case of the reactions above comes to -1.23 V in both acidic and alkaline media. As this is negative, it indicates that the reaction

cannot occur spontaneously, and instead requires an external voltage to drive it [17].

The standard reduction potential itself describes the reaction under standard conditions, which are: chemical activity = 1, temperature = 298 K, and pressure = 1 atm. For a pure solid or liquid the chemical activity is 1, for a gas it is proportional to the partial pressure, and for a species in solution it is proportional to concentration (although only at low concentrations). Standard conditions will rarely be encountered in a real experiment, and the reduction potential, E, is instead given by the Nernst equation [17]:

$$E = E^0 - \frac{RT}{nF} \ln Q, \tag{1.9}$$

where E^0 is the SRP of the half-reaction, R is the molar gas constant, T is the temperature in Kelvin, n is the number of electrons transferred in the half reaction, F is the Faraday constant, and Q is the reaction quotient. This latter variable is a measure of the relative quantities of reactants and products present at a given point in time, here Q is given by the ratio of the chemical activity of the reduced species to that of the oxidized species.

The pH of an electrolyte is given by $\mathrm{pH} = -\log a_{\mathrm{H}^+}$, where a_{H^+} is the activity of H^+ in the solution. This means that the stable region of water, and therefore that of an aqueous electrolyte will shift with pH. At room temperature the hydrogen reduction potential in Volts is given by [17]:

$$E = -\frac{RT}{nF} \cdot \mathrm{pH} = -0.059 \cdot \mathrm{pH}, \tag{1.10}$$

while the water reduction reaction would have a potential of

$$E = 1.23 - \frac{RT}{nF} \cdot \mathrm{pH} = 1.23 - 0.059 \cdot \mathrm{pH}. \tag{1.11}$$

This shows why the reduction potentials of the HER and OER are different for acidic and alkaline media.

At the potential given by the Nernst equation, the system should be in equilibrium, with reduction and oxidation currents at the electrode surface balancing one another out. In order to measure a given reaction current it is necessary to apply an *overpotential*, η, inputting extra energy into the system to overcome an activation barrier. The largest contributor to the activation barrier (and, hence, overpotential) is generally the electrode material – for example, glassy carbon has a much higher overpotential for hydrogen reduction than a catalytically active material such as platinum [17, 36].

The overpotential is linked to the observed current density j, by the Tafel equation:

$$\eta = a + b \log j, \tag{1.12}$$

provided the only limitation is the rate of heterogeneous electron transfer, as opposed to diffusion for example. Each half reaction can proceed as a cathodic or anodic reaction, and the Tafel constants a and b may not be the same for both. The Butler-Volmer equation develops the Tafel equation further, to account for the fact that cathodic and anodic reactions can occur simultaneously at the same electrode, and to account for the influence of mass-transfer [17, 37]:

$$j = j_0 \frac{C_{\mathrm{O}}(0,t)}{C^*_{\mathrm{O}}} \exp \frac{(1-\alpha)F\eta}{RT} - j_0 \frac{C_{\mathrm{R}}(0,t)}{C^*_{\mathrm{R}}} \exp \frac{-\alpha F\eta}{RT}, \tag{1.13}$$

where j_0 is the exchange current density (the current density at zero overpotential), $C_{\mathrm{O}}(0,t)$ the time dependent concentration of the oxidised species at the electrode surface, C^*_{O} the concentration of the oxidised species in the bulk electrolyte, $C_{\mathrm{R}}(0,t)$ the time dependent concentration of the reduced species at the electrode surface, C^*_{R} the concentration of the reduced species in the bulk electrolyte, and α is the

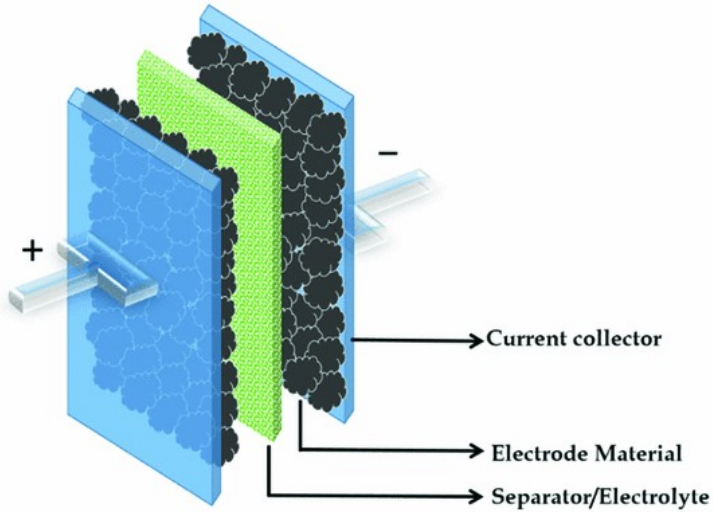

Figure 1.6: Diagram illustrating the components of a supercapacitor [38].

electron transfer coefficient. Neglecting mass-transfer, this simplifies further to [17, 37]:

$$j = j_0 \exp \frac{(1-\alpha)F\eta}{RT} - j_0 \exp \frac{-\alpha F\eta}{RT}. \tag{1.14}$$

At high overpotentials, this simplified form of the Butler-Volmer equation will simplify to the Tafel equation [17].

1.6 EDLC Materials

1.6.1 Device Structure

At the simplest level of conception, a supercapacitor can be considered as comprised of two electrodes with an electrolyte-soaked separator between them, as shown in Figure 1.6. Here, the electrolyte which facilitates ion transport, while an ion-permeable separator prevents electrical contact and shorting, however alternative architectures can feature a solid electrolyte which avoids the need for a separator all together. As charge storage in supercapacitors is a surface

phenomenon, these electrodes are made highly porous in order to maximise capacitance. The electrodes may be identical, in the case of a symmetric capacitor, or, in the case of an asymmetric device, different materials, or even different masses of the same material may be used at each electrode in order to optimise their performance. The electrodes are often attached to current collectors, made of highly conductive materials such as metal or graphite foils, which facilitate charge transport.

This section will introduce some of the most important carbon electrode materials: AC, carbon nanotubes (CNTs), and graphene; before moving onto the main types of electrolyte: aqueous, organic, ionic-liquid, and solid electrolytes.

1.6.2 Electrode Materials

Carbon-based materials are widely used in EDLCs electrodes. Carbon is a highly versatile element: forms exist having varying degrees of dimensionality including CNTs, graphene, fullerenes, and AC. Between them, these materials have a range of beneficial properties, which include: high conductivity, corrosion resistance, thermal stability, and low cost (compared to other electrode materials such as metal oxides) [12, 39], not to mention safety and low toxicity.

1.6.2.1 Activated Carbon

AC is the most widely used electrode material, owing to its high specific surface area (SSA) (up to 3000 $m^2\ g^{-1}$ [11, 40]), and low cost per unit of energy stored (only 2-3 US\$ $(Wh)^{-1}$ [41]) [11, 42]. As AC has a relatively high resistivity (40 mΩ cm [43]), it is conventionally mixed with a conductive additive such as carbon black (CB) (explored further in chapter 5), and a polymer such as PTFE

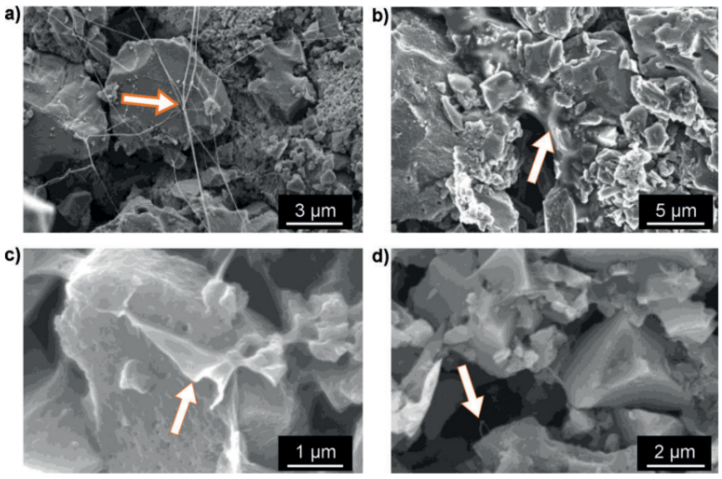

Figure 1.7: Activated carbon electrodes with different binders. a) PTFE, b) PVAc/polyisoprene blend, c) PVA, d) PVA crosslinked using borate salts. White arrows indicate the binder. [8].

or polyvinylidene fluoride (PVDF) is used to bind the material together (Figure 1.7). This results either in a slurry which can be used to coat current collectors, or in free-standing electrodes. Electrodes made in this way can achieve gravimetric specific capacitances (C_{sp}) of 100-120 F g^{-1} when used with organic electrolytes, or up to 300 F g^{-1} in aqueous electrolytes [44–46].

AC is produced from carbonaceous materials, such as fossil fuels or biomass, via a two-step process. The first stage, carbonisation, involves heating the precursor material under an inert atmosphere, leading to the removal of most elements other than carbon [42, 47]. The second step, activation, develops a network of pores and results in an increase of SSA. Activation can be characterised as physical or chemical; physical activation takes place at 400-1200 °C under an oxidizing atmosphere (eg. CO_2, H_2O); while chemical activation takes place at lower temperatures (< 700 °C) in the presence of oxidising agents such as H_2SO_4, KOH or ZnCl [12, 39]. These two approaches each have their own distinct advantages and disadvantages; physical activation is much safer, avoiding the use of dangerous oxidising agents; while chemical activation is faster and leads to higher SSAs [48].

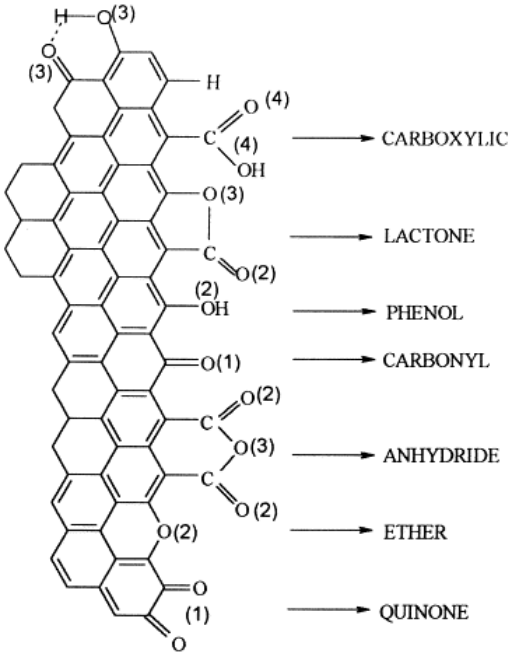

Figure 1.8: Oxygen-containing surface functional groups on carbon. Reproduced from [49].

As mentioned above, the SSA can reach 3000 m^2 g^{-1}, but is usually in the range of 1000-2000 m^2 g^{-1} [11, 40]. Such high surface areas are highly desirable in EDLC electrodes as they maximise the electrode-electrolyte interface and hence the electric double layer which can lead to high values of gravimetric specific capacitance. SSA, pore size and pore size distribution can be controlled by altering activation temperature, time, and the usage of chemical activation agents [11, 40]. Pores can be characterised through their diameter as micropores ($<$ 2 nm), mesopores (2-50 nm); or macropores ($>$50 nm). The pore size distribution of AC materials is often large and difficult to optimize, and the full SSA of electrode materials is never fully utilized; due in part to some pores being too small to be accessed by the electrolyte (as mentioned in 1.3); and, in the case of aqueous electrolytes, due in part to the limited wettability of the AC (described further in chapter 6) [25, 40].

The oxidising treatments used in activation can also lead to the development of oxygen-containing surface functional groups (SFGs) on the carbon. SFGs

are specific groups of atoms found on the surface of materials, and which affect the properties of those materials in specific ways. Examples of some of the oxygen-containing SFGs commonly found on AC are illustrated in Figure 1.8. Some, such as carbonyls, are electrochemically inactive, while others, such as quinone, provide redox activity and therefore contribute to pseudocapacitance [47]. Indeed, an AC device characterised as an EDLC can have ≈5 % of its capacitance arising from the pseudocapacitive contributions of SFGs [23]. In an aqueous device these SFGs can provide further benefit, as by lowering the surface charge of the material they reduce its hydrophobicity and allow a more complete wetting of pores [47, 50–54]. Conversely, in a device utilising an organic electrolyte they can adversely affect reliability, contributing to self-discharge, and they can decompose at high voltages, thus limiting the MWV of the device [41, 47, 55]. The impact of these SFGs on the performance of aqueous EDLCs will be explored in greater detail in chapters 4 and 6.

AC derived from polymeric precursors are the most common electrode materials thanks to high surface area, low resistance, good polarizability, inertness and low cost, however, AC can also be derived from plant materials [11, 12]. There has been significant work done in this latter area, including production of AC derived from cotton [56], rice husk [57], bamboo [58], wood [59], peanut shells [60] and Tamarind seed [61]. These materials have been found to exhibit high SSA and electrodes derived from them have high C_{sp}. For example, bamboo derived AC was produced with an SSA of 3000 $m^2\ g^{-1}$, and electrodes made with this material exhibited a measured C_{sp} of over 300 F g^{-1} when used in conjunction with an aqueous KOH electrolyte [58]. Of these materials, rice husks and peanut shells may be of particular interest as sustainable feedstocks: these are abundant waste products, for example, an estimated 140 million tonnes of rice husk are produced annually [57].

1.6.2.2 Carbon Nanotubes

CNTs can be considered as seamless tubes of sp^2 bonded carbon, often capped with fullerene hemispheres. CNTs can be classified as as SWCNTs, consisting of a single nanotube; or multi walled carbon nanotubes (MWCNTs), consisting of multiple concentric nanotubes. SWCNTs are of most interest as electrode materials, owing to their high SSA (2240 m^2 g^{-1} [41]), and low resistivity (as low as 3.8×10^{-5} Ω cm [62]), while the low density of defects on their surface lends them an oxidation resistance, allowing them to be used at MWVs as high as 4.0 V in an organic electrolyte (1 M tetraethylammonium tetrafluoroborate ($TEABF_4$)/propylene carbonate) [41, 63], significantly higher than the $\approx 2.5\ V$ working voltage more typical of organic electrolytes [11, 12, 64]. These properties can enable high energy and power densities [65]: SWCNTs have been demonstrated to achieve energy densities of up to 94 Wh kg^{-1} [63], compared with only 20 Wh kg^{-1} for AC electrodes [41].

CNTs can be produced by arc discharge, laser ablation, or chemical vapour deposition (CVD) [41, 66]. These first two techniques require the vaporisation of solid carbon precursors at temperatures of $\approx 4000 - 6000$ °C [66, 67], while CVD takes place at lower temperatures ($500 - 1000$°C) and involves metal catalysts being used to decompose a hydrocarbon gas (for example methane) and acting as 'seeds' for the growth of the CNTs [41, 66]. It has been demonstrated CNTs can be grown on conductive aluminiuim or graphite foil substrates which could then be used as a binder-free electrode in EDLCs with the substrate acting as a current collector (Figure 1.9) [68, 69].

Unfortunately, CNTs are relatively expensive comapared to other electrode materials: the cost per Wh of SWCNTs can be as high as 8300 US$ $(Wh)^{-1}$, over 1,000× that of AC [41]. CNTs can however be used as an additive to AC electrodes

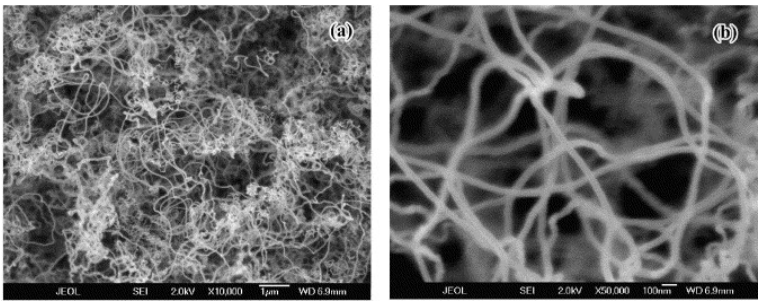

Figure 1.9: a) Low magnification, and b) high magnification SEM images of SWCNTs grown on a graphite foil substrate [69].

to reduce resistance and increase capacitance; as little as 0.15% MWCNTs by weight in AC was shown to increase C_{sp} from 50 to 135 F g^{-1}, when tested in a 1.5 M $TEABF_4$/acetonitrile (ACN) [70]. A more significant issue with CNTs is safety: studies have suggested that CNTs can behave similarly to asbestos, leading to health problems if inhaled [71, 72] and making them unsuitable as a sustainable material.

1.6.2.3 Graphene

Graphene is a 2D carbon structure composed of monolayers of sp^2 bonded carbon arranged in a hexagonal crystal lattice [73]. It has many promising properties including high surface area (2620 m^2 g^{-1}), low resistivity (2×10^{-4} Ω cm), good flexibility, and chemical and thermal stability [73]. It can be produced through a variety of methods including high shear exfoliation [74], mechanical exfoliation, and epitaxial growth by CVD [73, 75].

rGO is a closely related material and is produced by the oxidation of graphite and the exfoliation of the resultant graphite oxide to form graphene oxide (GO) sheets as illustrated in Figure 1.10. This is followed by reduction of the GO to form rGO flakes. This process has high yields [76, 77], and these rGO nanoflakes have been used on many occasions in supercapacitors as an electrode material without

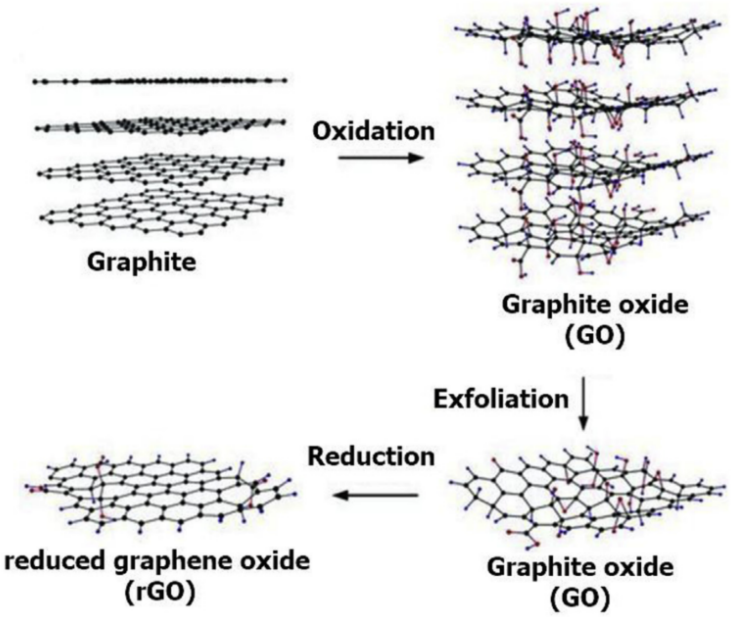

Figure 1.10: Diagram showing the production of rGO nanoflakes [91].

a binder [78–80], as a conductive additive [81], or as a binder material [82] in AC electrodes.

Generally, this reduction stage requires the use of toxic and potentially flammable materials such as isocyanate [83], hydrazine [84], hydroquinone [85] or $NaBH_4$ [86], making it unsuitable as a green material. However, a number of safer and more eco-friendly approaches to the reduction of GO have been demonstrated using $FeOH_2$ [87], urea [88], or by microwave irradiation [89]. In spite of these 'greener' approaches to reduction, the preparation of GO in the first place still relies on strong oxidising agents such as H_2SO_4 and potassium permanganate [90], rendering it inherently hazardous.

In terms of performance as an EDLC electrode material, although graphene has a high theoretical areal capacitance of 21 μF cm^{-2} , corresponding to a C_{sp} of 550 F g^{-1} [11, 92], in practise this so far proved impossible to realise due to the tendency of the graphene platelets to restack under the influence of van der Waals

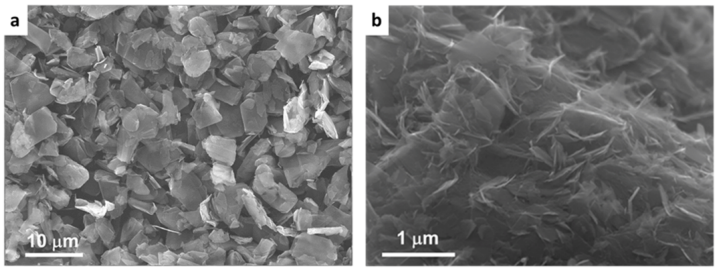

Figure 1.11: a) Graphite flakes, b) shear exfoliated few-layer graphene nanosheets [96]

forces [11, 73], reducing available surface area. This limitation means that only specific capacitances as high as 35 F g^{-1} in 1 M aqueous H_2SO_4 can be acheived [93]. In contrast, the highly disordered structure of rGO reduces this restacking, allowing capacitances of up to 279 F g^{-1} in 6 M KOH [94].

Liquid phase high shear exfoliation is a method for the production of graphene, in which shear forces are used to tear graphite flakes (Figure 1.11 (a)) into FLG platelets (Figure 1.11 (b)) [74], achievable with equipment as simple as a kitchen blender. By selecting a solvent with an appropriate surface energy, or by modifying the surface energy of water using a surfactant, the recombination of platelets is prevented. Although initial demonstrations utilised the hazardous [95] organic solvent n-methyl-2-pyrrolidone (NMP) [74, 96], even natural cellulose [97, 98], or household detergents such as Fairy Liquid [99, 100] can be used to prevent the recombination of the graphene, making this a safe and low cost way to produce high quality, defect free graphene [101].

FLG flakes produced by shear exfoliation have been used in supercapacitor electrodes on several occasions [96, 102, 103]. Although their use as a standalone electrode material is limited, due to the aforementioned tendency of graphene platelets to restack, a C_{sp} of 679 F g^{-1} was demonstrated for a composite electrode of FLG and pseudocapacitive MnO_2 [103] in 1 M aqueous Na_2SO_4. Chapter 4 will explore their utilisation as a conductive additive used in conjunction with AC.

As graphene can be made by such a wide variety of methods, which themselves deliver a wide variety of results estimating the cost per Wh of graphene EDLCs is difficult. Graphene itself has a broad range of costs from US$ $160 - 10,000$ kg^{-1}, which together with the variable performance means that the cost per Wh may vary from < 10 US$ (Wh)$^{-1}$ (comparable to AC), to > 1000 US$ (Wh)$^{-1}$.

1.6.3 Electrolyte

The electrolyte facilitates movement of ions between anode and cathode during charging/discharging. The diffusion of electrolyte ions into the pores of the electrode material has significant impact on cell performance, and in the case of aqueous electrolytes, so does the wettability of the electrode [104], and its breakdown potential is often the factor which limits the MWV of the cell [105]. An ideal electrolyte would have a wide potential window, low resistivity, low viscosity, be non-flammable, and have high electrochemical stability as well as being sustainable, have low-toxicity and be low cost [11]. The ion concentration of the electrolyte must also be sufficiently high as not to limit performance via the 'electrolyte starvation' effect. This is where the ESR of the cell significantly increases when fully charged, limiting deliverable power, due to a significant fraction of the conducting ions in the electrolyte being adsorbed in the double layer [106].

While most commercial devices use organic electrolytes for high energy and power densities [12], these can pose significant dangers, for instance ACN is metabolised into cyanide, leading to cyanide poisoning [8, 9]. Although safer, common aqueous electrolytes are not necessarily harmless, with both KOH and H_2SO_4 being highly corrosive, and sulfate and chloride compounds giving off dangerous gases during

decomposition [8]. Due to these drawbacks, a range of alternative, safer aqueous electrolytes have been investigated. For example, sodium acetate (CH_3COONa) has a small anion diameter (0.15 nm desolvated and 0.71 nm solvated) which should fit the pores of AC. A 1.0 M solution of sodium acetate has been shown to achieve a C_{sp} of 99 F g^{-1} on AC electrodes, in comparison to 81 F g^{-1} for Na_2SO_4 in the same cell [8].

Other approaches to overcoming the issues with organic and aqueous electrolytes include the use of ionic liquids and solid gel-polymer electrolytes, however, as detailed below, each of these has its own shortfalls which currently makes their use impractical. Because of this, trying to expand the MWV of aqueous electrolytes is a major field of research, which is detailed further in Chapter 6.

1.6.3.1 Organic Electrolytes

Use of organic solvents as the basis of electrolytes allows MWV of up 2.5 to 2.7 V ordinarily [11, 12, 64], and (as described above) up to 4 V on defect free materials such as CNTs [41, 63, 107], which in turn leads to an increase in energy density, according to equation 1.3. These materials have much lower melting points than water, allowing use at well below freezing point, for example ACN-based devices can operate well down to −40 °C, and, by modifying the ACN with the addition of 1,3-dioxolane, a C_{sp} of 164 F g^{-1} was obtained for AC electrodes at −100 °C [14]. One of the main drawbacks for these materials however is their volatility, flammability, and toxicity leading to safety concerns [8]. In addition to this, compared to aqueous electrolytes, their viscosity is higher (2.5 cP for propylene carbonate) [108], their conductivity lower (only 0.06 S cm^{-1} in the case of 1 M $TEABF_4$/ACN) [11, 108, 109], and their cost is higher [11, 31]. Beyond this, the requirement that the water content of these electrolytes be kept low, in or-

der to limit self-discharge, adds considerable complexity to their handling [11, 108].

Commonly used organic electrolytes include ACN, ethylene carbonate, diethyl carbonate, propylene carbonate (PC), and dimethyl carbonate [54, 110–112]. Of these electrolytes currently in use, reduced toxicity, high flash point, and wide temperature range have made PC a popular option [11].

1.6.3.2 Aqueous Electrolytes

Common aqueous electrolytes include solutions of KOH, H_2SO_4, and Na_2SO_4 [8]. Their MWV is around 1.23 V [12, 113], which is lower than for organic or ionic electrolytes [12, 114] and so limits energy and power storage, moreover there are safety concerns around highly corrosive KOH and H_2SO_4.

Aqueous electrolytes are, however, not without their advantages; they possess good conductivity (0.8 S cm^{-1} for 1 M H_2SO_4) [108], low viscosity ($\approx$ 1 cP) [115], low cost and are relatively safe when compared to organic electrolytes; hence they enjoy wide use. They are easy to handle as they do not require processing in moisture free environments; and their small ion size can penetrate smaller pores increasing available surface area and improving capacitance [11]. Other aqueous electrolytes which have been investigated include Li_2SO_4, NaCl, KCl, and LiCl [12, 116, 117]. Of these neutral electrolytes, the Li_2SO_4 is of particular interest having been reported to have better stability and a larger operating potential (1.6 V) than acidic or alkaline electrolytes.

1.6.3.3 Ionic Liquids

Ionic liquids (ILs) are room temperature molten salts. They have the highest

operating voltages of all electrolytes: they can ordinarily operate at over 3 V, with up to 5 V having been reported [12, 118]. The two most common electrolytes are those based on pyrrolidinium and imidazolium salts. Pyrrolidinium has the higher operating voltage, while imidazolium possesses a lower viscosity and higher conductivity [119]. ILs are stable over a wider temperature range than organic or aqueous electrolytes and are less volatile and less combustible so are considered to be 'green' solvents [11, 12, 120]. There are however several disadvantages associated with them: as with organic electrolytes, ILs need to be handled in a vacuum or under inert conditions [12, 121]; they have lower conductivity, and higher viscosities than even organic electrolytes (25 mS cm^{-1} and 41 cP, respectively, for 1-ethyl-3-methylimidazolium tetrafluoroborate (EMIM BF_4)) [11, 108]; and their cost is prohibitive [11, 120]. At temperatures below ambient, the viscosity and conductivity of the electrolyte can worsen further leading to reduced performance [12, 122].

1.6.3.4 Gel-polymer Electrolytes

An alternative approach to overcoming the shortcomings of organic and aqueous electrolytes is the use of gel-polymers. Supercapacitors using gel-polymer electrolytes are more reliable, safer, and have long shelf lives thanks to low internal corrosion and reduced risk of leakage compared with liquid electrolytes [123, 124]. A gel-polymer electrolyte consists of a liquid electrolyte (a salt dissolved in water, an organic solvent or an ionic liquid) suspended in a polymeric network, having some of the properties of a solid, but with the diffusive properties of a liquid [123].

Examples include: aqueous gels made by mixing aqueous LiCl and PVA [125, 126] or poly(propylsulfonate dimethylammonium propylmethacrylamide) (PPDP) [126]; and an IL-based gel-polymer made from 1-butyl-3-methylimidazolium tetrafluoroborate (BMIM BF_4) in a blend of PVA and PVDF [123]. Gel polymer

electrolytes, however, suffer from even lower conductivities than ILs (≈2 mS cm^{-1} in the case of the IL-based gel-polymer described above) [108], high interfacial resistances between the electrode and the electrolyte, and the ions can struggle to penetrate nanopores, reducing capacitance [12, 108, 124].

1.7 Summary

This literature review provides important background for the work presented in later chapters. First, the context of the work was supplied, before introducing definitions of supercapacitors, the equations governing their behaviour, and some of the key differences, advantages, and disadvantages of supercapacitors compared to the dominant electrochemical energy storage technology of lithium ion batteries. Next, background in electrochemistry was provided in order to help understand the electrochemical reactions leading to the degradation of supercapacitors, which are explored in the experimental chapters of the thesis. Finally the materials used in supercapacitors are introduced, most notably the activated carbon and graphene used as electrode materials in this work, and the aqueous electrolytes used throughout this thesis.

Chapter 2

Methodology

2.1 Materials Characterisation

2.1.1 Scanning Electron Microscopy

Scanning electron microscopy (SEM) is used for imaging samples with a resolution of the order of nanometres. In SEM, a narrow, convergent beam of electrons is scanned over a sample in a raster pattern. The incident electrons interact elastically and inelastically with the sample to produce a range of signals, including secondary electrons (SEs), backscattered electrons (BSEs), and X-rays, which can be used for imaging, or to obtain compositional data on the sample. The imaging resolution is ultimately limited by the area from which signals are emitted, which is linked both to beam diameter and the interaction of the electron beam with the sample [127, 128].

The primary signals used for imaging samples are SEs. These are defined as having low energies of <50 eV, and are produced from inelastic scattering of electrons, causing emission of loosely bound atomic electrons (Figure 2.1 (a)) [129]. They are categorised by their four sources: SE1 arise from the interaction of the primary electron beam with the sample; SE2 are caused by the interaction of high-energy BSEs with the sample; SE3 and SE4 are generated by the interaction of primary

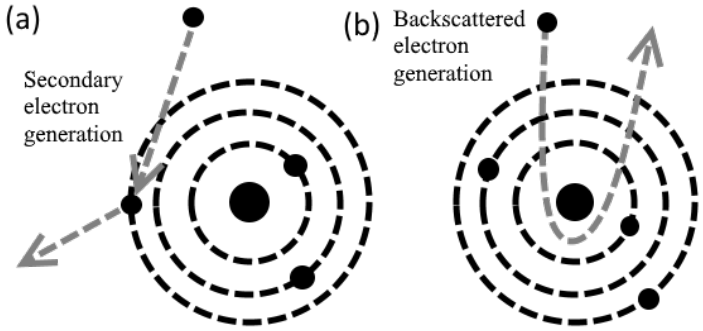

Figure 2.1: Schematic illustration of the emission mechanism of a) secondary electrons, and b) backscattered electrons.

electrons and BSEs with the SEM components. As only SE1 are emitted from the locality of primary electron beam incidence, only they are useful for imaging, with SE2-4 instead serving as sources of noise which limit image resolution [130].

SEs provide information on the topography of samples through two mechanisms. The first is detector-shadowing, where topographical features block the detection of secondary electrons. As the detector cannot lie in the path of the beam, and is instead positioned to one side, illustrated in figure 2.2, this results in 'shadows' on the image.

Topographical information is also provided by the variation of emission probability with angle of incidence, illustrated in Figure 2.3. The interaction volume of the primary electrons with the sample is roughly teardrop shaped. Owing to their low energy, the mean free path of the SEs in the sample is very small, and only those SEs generated near to the top of the interaction volume are able to escape, resulting in a weak signal. However, surfaces with normals which lie further away from the orientation of the electron beam can cut through this interaction volume, resulting in a larger emission volume and a greater current of electrons emitted [127].

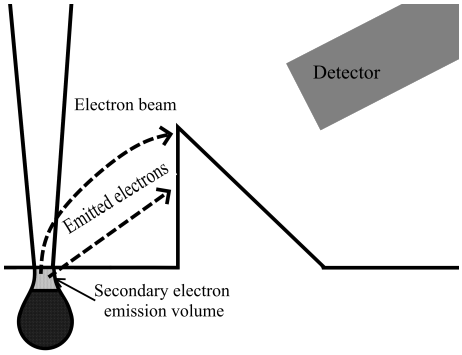

Figure 2.2: Illustration of secondary electron detector-shadowing effect.

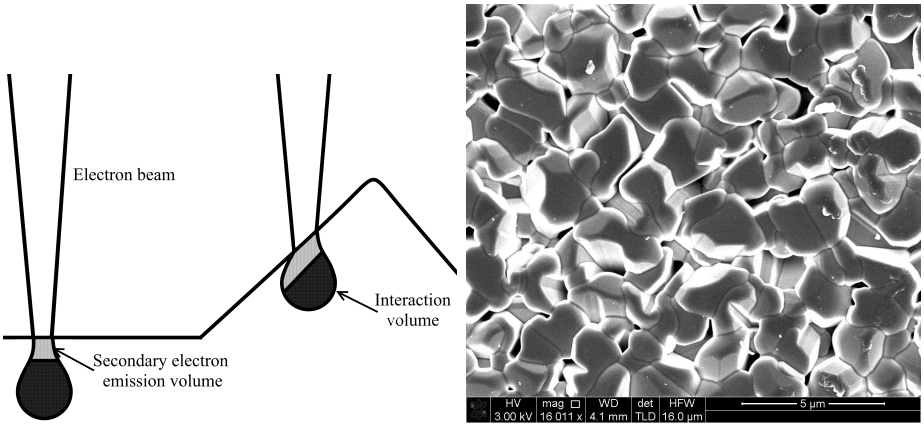

Figure 2.3: Left: Illustration of how the secondary electron emission volume varies with topography. Right: secondary electron image of an antimony selenide solar cell, showing how secondary electron emission is greater from the sides of the grains, causing them to appear bright in the image [131].

BSEs are incident beam electrons which have undergone quasi-elastic scattering, retaining over 40 % of their initial energy, but changing direction by large angles and being reemitted from the sample (Figure 2.1 (b)). They have higher energies than secondary electrons and can therefore be emitted from deeper within the sample [127]. The probability that a beam electron will be backscattered increases with atomic number, Z, according to the following equation [129]:

$$P = -0.0254 + 0.016Z - 1.86 \times 10^{-4}Z^2 + 8.3 \times 10^{-7}Z^3. \tag{2.1}$$

As heavier elements backscatter electrons more strongly than lighter elements, this means that BSEs can be used for imaging with chemical contrast. This is

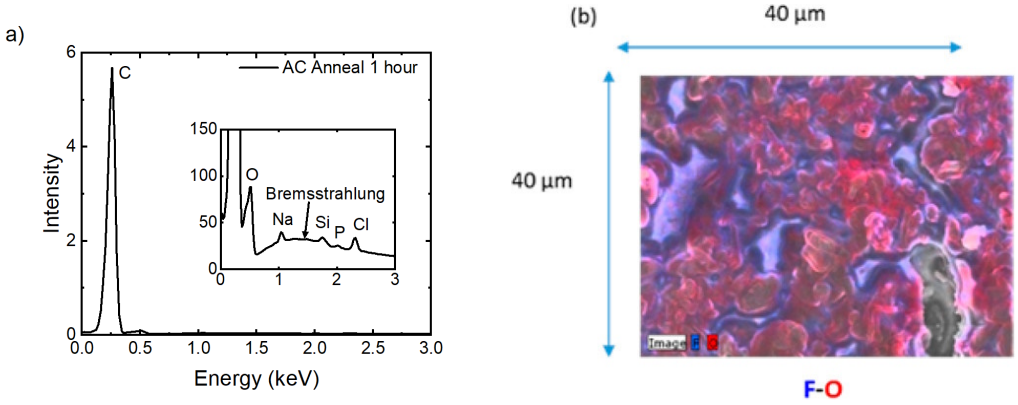

Figure 2.4: Examples of EDX data. a) EDX spectrum for activated carbon annealed at 1000 °C under N_2 for 1 hour. The C, O, Na, Si and S $K\alpha$ peaks are labelled, alongside the bremsstrahlung spectrum. b) SEM-EDX mapping, showing the distribution of fluorine (blue), and oxygen (red) on a lithium electrode treated in a 1 M PEG500-LiTFSI electrolyte [133].

of particular use in samples which have areas of differing composition, but are relatively flat with little topographical contrast [132].

2.1.2 Energy-Dispersive X-ray spectroscopy

During SEM imaging X-rays are produced by two mechanisms: The first is when electrons in the incident beam interact inelastically with inner shell (core) electrons, causing them to be excited to higher energy levels or ejected from the atom. When outer shell (valence) electrons relax to fill the newly vacant energy levels the excess energy is emitted in the form of an X-ray photon. As the energy levels of atomic electrons are determined by the size of the nucleus, they are characteristic of particular elements, and therefore the energies of the X-rays emitted will be characteristic of the sample material. This technique can be used to determine the composition of a sample and is used in this work to determine the presence of surface oxygen on activated carbon.

For light elements such as carbon there are only two energy levels, and as such only one transition is possible and only one wavelength of characteristic X-rays

are emitted. For heavier elements having more shells, transitions between any two are possible, and as such a whole family of characteristic X-rays are emitted. These characteristic X-rays are labelled according to the transition that led to their emission, for example X-rays emitted from electrons relaxing into the K shell are labelled K X-rays. If they dropped down to the K shell from the L shell they are referred to as $K\alpha$, and if they relaxed from the M shell they are labelled $K\beta$ and so on [129, 132].

X-rays can also be emitted by electrons as they change momentum during elastic scattering interactions with the atomic nucleus and with tightly bound core electrons. This second form of emission is known as bremsstrahlung or braking radiation. As these scattering events can remove any quantity of energy, up to the total energy of the electron, these X-rays exhibit a continuous range of energies rather than the discrete energies typical of the characteristic X-rays [129, 132].

In EDX, the emitted X-rays are detected and their energy measured to produce a spectrum, as shown in Figure 2.4(a). The first kind of X-rays, the characteristic X-rays, form sharp peaks in the spectrum, which can be used to identify (and with appropriate calibration, quantify) the elements present in a sample, while the bremsstrahlung X-rays form a continuous background. EDX can be used in conjuction with SEM to produce spatially-resolved elemental maps of the sample surface, an example of which is shown in Figure 2.4(b) [133–135].

2.1.3 Nitrogen Adsorption/Desorption

Nitrogen adsorption/desorption isotherms are widely employed for the determination of the surface area, pore size, and pore size distribution of solid materials, parameters which are particularly important in evaluating and understanding

the performance of the hierarchically porous materials which are typically used in supercapacitors. Whenever a solid is exposed to a gas, some quantity of that gas will inevitably adsorb on the surface of the solid. An adsorption/desorption isotherm plots the total quantity of gas adsorbed against the pressure of the system, commonly given as the relative pressure, $\frac{p}{p_0}$, where p is the gas pressure, and p_0 is its saturation pressure [136, 137].

Measurements are carried out at 77 K (the boiling point of nitrogen at 1 atm) in a quartz cell by the following procedure. First, a calibration cycle is carried out while the cell is empty; the cell is first evacuated and then the pressure is recorded against the volume of N_2 added, up to the saturation pressure at which the N_2 liquefies (1 atm at 77 K). The sample is then added to the cell and degassed, before the cell is evacuated and the adsorption and desorption isotherms recorded. Adsorption/desorption isotherms may by measured by two common approaches. The first involves introducing nitrogen gas into the system in discrete quantities, and waiting for the system to reach equilibrium, and the second involves introducing the nitrogen gas slowly to maintain a constant equilibrium. The total volume of gas adsorbed on the sample is then determined from the difference in pressure between the calibration cycle and the actual measurement cycle for a given quantity of gas added [137].

Isotherms can be divided into six types based upon their shape (as illustrated in figure 2.5) [137]. Type I isotherms correspond to materials with a high degree of microporosity: at low pressures gas is readily adsorbed into micropores, leading to a rapid increase in gas adsorbed, followed by a plateau at higher pressures after the pores have been filled. Non-porous or macroporous materials are characterised by type II isotherms. Point B on figure 2.5 II indicates the point at which the test material is covered by a monolayer of adsorbed molecules, and at which multilayer coverage begins. Type III isotherms arise where the interactions between the

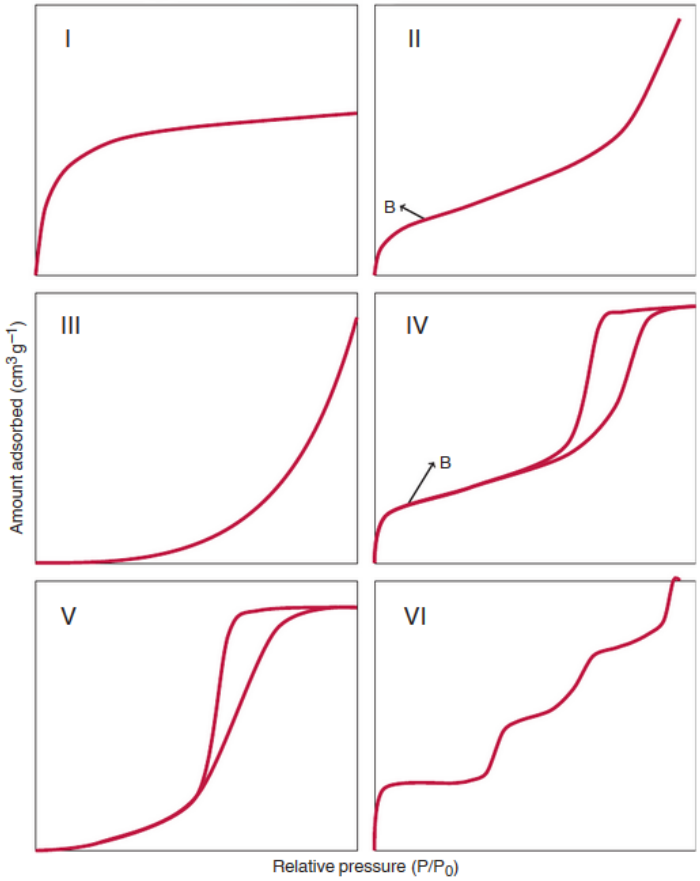

Figure 2.5: The six types of nitrogen adsorption/desorption isotherms, interpretations of which are given in the text. Point B, where present, indicates the transition from monolayer to multilayer coverage [137].

adsorbate and the test material are as weak or weaker than adsorbate/adsorbate interations, leading to little adsorbed gas at low pressures; here gas molecules are readily adsorbed on top of previously adsorbed gas molecules and Brunauer-Emmett-Teller (BET) theory cannot be applied to calculate SSA [137, 138].

The hysteresis loops in type IV and V isotherms are caused by capillary condensation in mesopores. As with type I isotherms, the rapid increase in adsorbed gas at low pressures observed in type IV isotherms indicates the presence of micropores alongside mesopores. Meanwhile, the low pressure behaviour of type V isotherms is similar to that seen in type III isotherms, again preventing the calculation of SSA. The final type of isotherm, type VI, corresponds to the stepwise formation

of adsorbate layers on uniform, non-porous surfaces. [137].

2.1.3.1 BET

Brunauer-Emmett-Teller theory (BET) theory is used for calculating specific surface area from adsorption/desorption isotherms [139] and is based on a simplified model of physiosorption. The key assumptions made by the BET theory are that: the adsorbent material consists of an array of equivalent sites upon which gas molecules may randomly be adsorbed; the probability of a site being occupied is independent of whether or not adjacent sites are occupied; there are no lateral interactions between adsorbed molecules; the adsorbed molecules can act as adsorption sites for further molecules; and all layers of adsorbed material above the first behave as a liquid [139, 140]. Using these assumptions it is possible to derive an equation relating p, p_0, with v (the total volume of adsorbed gas) and v_m (the monolayer adsorbed gas volume), known as the BET equation [139]:

$$\frac{p}{v(p_0 - p)} = \frac{1}{v_\mathrm{m} c} + \frac{c-1}{v_\mathrm{m} c}\frac{p}{p_0}, \tag{2.2}$$

where c is a constant referred to as the BET constant, which describes the differences in strength of the adsorption interaction between the first layer of adsorbed molecules and the second and higher layers [137]:

$$c = e^{\frac{E_1 - E_\mathrm{L}}{RT}}, \tag{2.3}$$

where E_1 is the heat of adsorption of the first layer, and E_L is the latent heat of condensation of the gas. Equation 2.2 can be fitted to the isotherm data, allowing v_m and c to be determined. From v_m the specific area of the material (SSA) can be derived using the average cross-sectional area of the adsorbed gas molecules (a)

[137, 139, 140] via the following relationship:

$$\mathrm{SSA} = \frac{v_\mathrm{m} N a}{V m}, \tag{2.4}$$

where N is Avogadro's number, V the molar volume of the adsorbate, and m the sample mass.

Although BET theory is very frequently used in the determination of specific surface area of porous materials, it should nonetheless be borne in mind that it is limited in accuracy; only a small section of the nitrogen adsorption isotherm follows the linear relationship defined by equation 2.2. In the case of a graphitised carbon adsorbent, the linear region usually only extends as up to relative pressures of ≈ 0.1. Further difficulties arise for porous materials, as there are limits to how many layers adsorbate may be adsorbed on the internal walls of a pore of finite radius [140].

2.1.3.2 Pore size analysis

A classical approach to calculating pore size distribution (PSD) makes use of the Kelvin equation, which describes capillary condensation. This is the process in which gas condenses in pores at pressures below p_0. The relative pressure at which this occurs in a pore of radius r_K is given by:

$$\log \frac{p}{p_0} = \frac{-2\sigma V}{RT r_\mathrm{K}} \cos\theta, \tag{2.5}$$

where σ is the surface tension of liquid nitrogen, V is the molar volume of liquid nitrogen, R the ideal gas constant, and θ the contact angle of the liquid with the pore wall. Generally θ is assumed to be zero, simplifying the equation slightly [138]. From this equation it can be seen that the gas will condense in the smallest pores at the lowest pressures, giving rise to the type I isotherm for microporous

materials. In the case of N_2 adsorption, at a relative pressure of 0.99, pores of up to $r_K = 95$ nm are filled, meaning that these are the largest pores measured by this approach. The total volume of adsorbed gas at $\frac{p}{p_0} = 0.99$ is the total volume of pores up to $r_K = 95$ nm [138].

Using the Kelvin equation neglects that capillary condensation is a secondary process, taking place on top of monolayer or multilayer adsorption of material. The Barrett-Joyner-Halender theory (BJH) approach takes this into account, giving the pore radius as $r_p = r_K + t$, where t is the thickness of the adsorbed layer. The pore-size distribution is determined using the desorption branch of the isotherm, assuming that each decrease in pressure results in both the emptying of condensed gas from the largest filled pores, and also a reduction in thickness of the adsorbed layer. Using this model, the radius of a pore filled at a given relative pressure can be calculated, and from the desorption isotherm, the volume of adsorbed gas can be related to pore radius, allowing for the PSD to be derived [137, 141].

2.1.4 Raman Spectroscopy

Raman Spectroscopy is a technique which utilises the inelastic scattering of light by matter (Raman scattering), to provide information on the vibrational modes of solids and molecules. Although Raman scattering can only be correctly described by using quantum theory, some insight into the process may nonetheless be obtained from a classical description: when light interacts with a molecule or solid it can induce a dipole moment (associated with which is a time/frequency dependent polarisability) which will oscillate and emit light.

The polarisability of a sample possessing time-dependent variation with a characteristic frequency Ω (e.g., associated with a molecular vibration or a phonon in a

solid) can be expressed as:

$$\alpha = \alpha_0 + \Delta\alpha \cos(\Omega t), \tag{2.6}$$

where t is time, α is the polarisability, α_0 its value in the absence of the characteristic vibration, and $\Delta\alpha$ the amplitude of the variation of polarisabilty induced by the vibration. If an electromagnetic field (such as that associated with a photon incident upon the sample) having amplitude $\mathbf{E}$ and angular frequency ω, $\mathbf{E}\cos(\omega t)$ is applied to the sample, then a (local) dipole moment is induced,

$$\begin{aligned} \mathbf{p} &= (\alpha_0 + \Delta\alpha \cos(\Omega t))\mathbf{E}\cos(\omega t) \\ &= \alpha_0 \mathbf{E}\cos(\omega t) + \frac{\Delta\alpha}{2}\mathbf{E}(\cos(\omega - \Omega)t + \cos(\omega + \Omega)t). \end{aligned} \tag{2.7}$$

This time-varying dipole moment re-emits light at three possible frequencies. The first term, associated with light emitted at the same frequency as the incident beam is due to *Rayleigh scattering* which is elastic. However the two components at lower and higher frequency are associated with the inelastic scattering of the incident photon resulting in the emission or absorption of a quantum of vibrational energy. The process by which photons are scattered with lower frequency/energy loss is known as Stokes scattering, and that by which the photons have increased frequency/energy gain is known as anti-Stokes scattering [142].

In a quantum picture of conventional Raman scattering, a photon having the incorrect energy to excite electronic transitions can interact with matter by exciting a material into an extremely short-lived higher energy *virtual state*. The material can be considered as emitting another photon as it de-excites. There are three outcomes to this: it can either return to its original state (Rayleigh scattering), de-excite into a higher energy state than the original state (Stokes scattering) or de-excite into a lower energy state (anti-Stokes scattering). The probability of Raman scattering by this process is of the order of 10^{-7}, with the result that most photons are Rayleigh scattered. However, if the incident photon energy matches

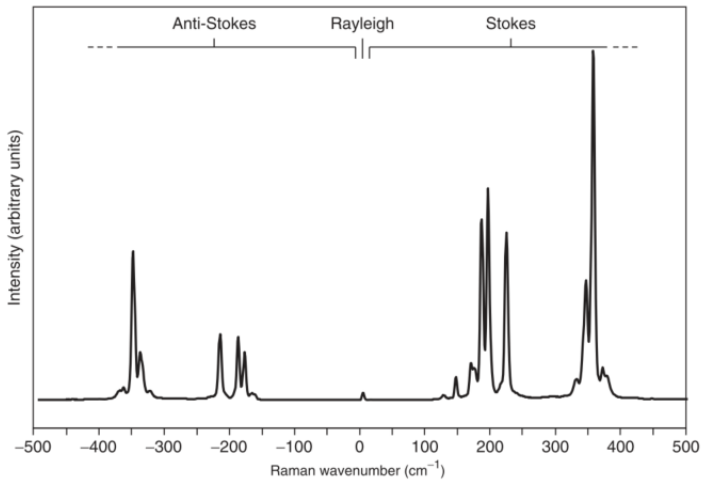

Figure 2.6: Example Raman spectrum of As_4S_4, showing the anti-Stokes region, Rayleigh line, and Stokes region. The intensity of the Rayleigh line has been reduced using a holographic filter [144].

with an electronic transition of the sample, the excited state is significantly longer-lived with the result that the probability of Raman scattering is enhanced. This process is known as resonant Raman scattering and it can be important in the spectroscopy of nano-carbons such as graphene and carbon nanotubes, in particular in enhancing the signal from small volumes of material (enabling, for example, Raman spectroscopy of individual carbon nanotubes) [143].

The energy of a vibrationally excited state is quantised according to the equation,

$$E_v = h\nu(v + 1/2). \tag{2.8}$$

Where E_v is the vibrational energy of a particular mode, h is Planck's constant, ν is the frequency of the vibration, and v is the vibrational quantum number. At room temperature, most atoms are in the the vibrational ground state, meaning that the Stokes scattering is more intense than the anti-Stokes. This effect becomes even more pronounced for higher energy vibrations, so studying the Stokes peaks is usually preferred [142].

In Raman spectroscopy, monochromatic light (usually from a laser) is focused on a sample, and the energy of the scattered light is measured. Due to Raman

scattering, light with a range of wavenumbers is emitted, which is recorded as a spectrum. A Raman spectrum obtained from the mineral As_4S_4 is shown in Figure 2.6 as an example. The Rayleigh scattered light has a much higher intensity than the Raman scattered light, so to obtain a Raman spectrum it is necessary to filter out the former which can be achieved by an optical element such as a holographic notch filter. Raman scattering gives rise to discrete peaks in the spectrum of the scattered light, corresponding to the Raman active vibrational modes for that molecule/solid, as well as higher energy peaks corresponding to combinations of vibrational modes and overtones (multiple excitations of a single mode). As the energies of the different vibrational modes and their relative intensities are unique to different materials, the Raman spectrum can provide a 'fingerprint' which can be used to identify the material being analysed [142]. This technique allows for more than just the identification of specific molecules and compounds: in the case of few-layer graphene, for example, Raman spectroscopy can give information on the nature and quantity of defects, and even on the number of layers in few-layer graphene (FLG) platelets [145].

2.2 Electrochemical Characterisation

2.2.1 Test Fixture Configuration

Electrochemical characterisation of energy storage materials can be done in either a two- or three-electrode test cell. Schematics illustrating these two distinct setups are shown in Figure 2.7. A two-electrode system (Figure 2.7 (a)) closely resembles the structure of a 'real-world' supercapacitor, as shown in Figure 1.6, where two electrodes are sandwiched together with a separator, soaked in a suitable electrolyte, between them. Here, the voltage applied/measured is referred to as the *cell voltage*, and reflects the potential difference between the two-electrodes.

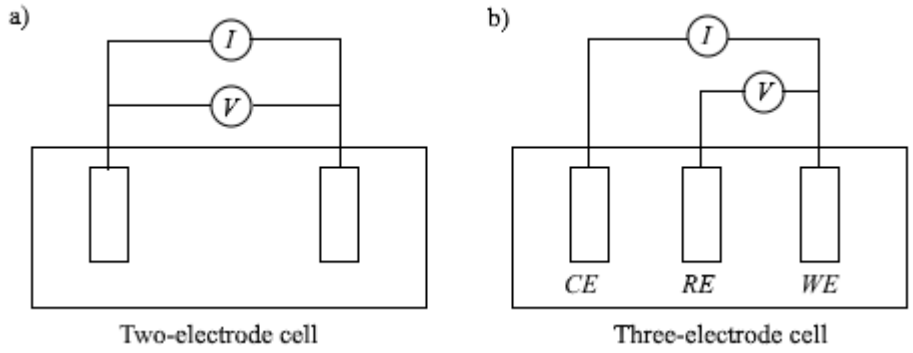

Figure 2.7: Schematic diagram of a) a two-electrode electrochemical cell, and b) a three-electrode electrochemical cell showing the Working Electrode (WE), Reference Electrode (RE), and Counter Electrode (CE).

A three-electrode cell features a working electrode (WE), counter electrode (CE), and reference electrode (RE). These may all be immersed directly in the electrolyte and spatially separated by the geometry of the test fixture, or alternatively may be sandwiched together with separators to prevent electrical contact between them. Only the working electrode contains the active material – a system with a known reduction potential is used as the reference electrode and the voltage/potential measured is that of the working electrode relative to this, which should be explicitly stated, while the counter-electrode balances the current at the working electrode, allowing the RE to maintain a constant potential [17, 18]. In this approach, the performance of the positive and negative electrodes can be examined individually in a three-electrode system, Faradaic processes can be more easily observed and their reduction potentials measured.

There are a number of key performance parameters which can be extracted from electrochemical analysis, which will be discussed in detail below. Among them, perhaps the most important in characterising the effectiveness of a supercapacitor electrode is the gravimetric specific capacitance, C_{sp}, which is the capacitance per unit mass of electrode material for a single electrode. For a three electrode cell this is simply given by

$$C_{\mathrm{sp}} = \frac{C}{m},$$

where C is the measured capacitance of the working electrode and m is its mass, as the behaviour measured is that of the single working electrode. However, for a symmetric two electrode test cell (i.e., one in which both electrodes are identical), C_{sp} is given by [146],

$$C_{\mathrm{sp}} = \frac{4C}{M}, \tag{2.9}$$

where C is the measured capacitance and M is the *total* mass of both electrodes. The factor of 4 arises as the capacitance of a single electrode is twice that of the whole device (since each electrode/electrolyte ion combination forms a separate capacitor and the pair are connected in series), and the mass of a single electrode is half that of the total mass.

Attention must also be paid to the thickness and mass loading of electrodes: extremely thin or lightweight electrodes can lead to an overstatement of C_{sp} [146]. Likewise, extremely low voltage scan rates and long charge/discharge times can lead to an overstatement of C_{sp} [146]. These effects are due to the ESR and electrolyte permeability; thicker electrodes will have greater ESRs, and it will be more difficult for ions in the electrolyte to permeate throughout the full thickness of the electrode, causing losses in capacitance which are particularly acute at high scan rates. Further care must be taken when comparing results from the literature, as some papers may only take into account the mass of the active material and do not include any binder, support or additives which may be present in their determination of C_{sp}, while other papers consider the total electrode mass, which is arguably of more relevance for evaluating the potential 'real world' applicability of the electrode materials [146].

2.2.2 Linear Sweep Voltammetry and Cyclic Voltammetry

In linear sweep voltammetry (LSV) and cyclic voltammetry (CV) a potentiostat is used to vary the potential across a test cell between an upper and lower limit at a constant predefined rate, while the resulting current flow is measured [147]. In the case of LSV, a single sweep is performed between the two limits, while for CV at the very least a single complete cycle from an upper limit to a lower limit and back again is recorded (or alternatively starting from a intermediate potential and returning to that). Several CV cycles may be performed in order to either 'precondition' the cell or measure its performance as a function of electrochemical cycling [18].

In both CV and LSV experiments, the presence of peaks in the resultant plot of current against potential (a voltammogram) can indicate Faradaic processes — i.e. processes in which a current flows as a result of redox reactions. The voltammogram resulting from CV can provide further information, with the area enclosed being used to determine the capacitance, energy and power output of a supercapacitor cell, while the shape of the curve may give clues about the internal cell resistance and the presence of pseudocapacitive or electric double layer behaviour.

For an ideal capacitor, according to Equation 1.1, the measured current should be constant at a constant voltage scan rate, resulting in a rectangular voltammogram. Total capacitance is then easily calculated as

$$C = \frac{|i|}{dV/dt}, \tag{2.10}$$

where $|i|$ is the absolute value of the current across the test cell, and dV/dt is magnitude of the voltage scan rate.

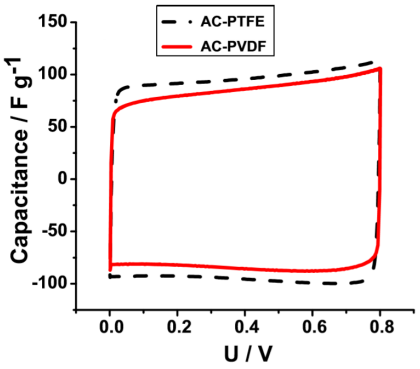

Figure 2.8: Example cyclic voltammograms, cycling at 2 mV s^{-1} between 0 and 0.8 V, of AC supercapacitors in 1 M $NaNO_3$ electrolyte, with PTFE and PVDF binders [148].

Example voltammograms obtained from AC electrodes with PTFE and PVDF binders are shown in Figure 2.8. It can be seen that in reality, the capacitor does not yield a voltammogram with the form of perfect rectangle with a constant absolute value of current. Due to this behaviour, the capacitance, C, is often calculated by integrating the area under the discharge curve [8]:

$$C = \int_{v_{\max}}^{V_0} idV \frac{1}{(v_{\max} - V_0)s}, \tag{2.11}$$

where $v_{\max}$ and V_0 are the maximum and minimum voltages in the voltammogram, respectively, m the total mass of electrode material, and s the scan rate. The specific energy of a single electrode can be found from C_{sp} using equation 1.3. The power P produced/consumed by the electrode during a single discharging/charging sweep as a function of time is given by,

$$P(t) = i(t)\frac{dV}{dt}t, \tag{2.12}$$

with the average power input/output thus being found from the area under the discharge curve by,

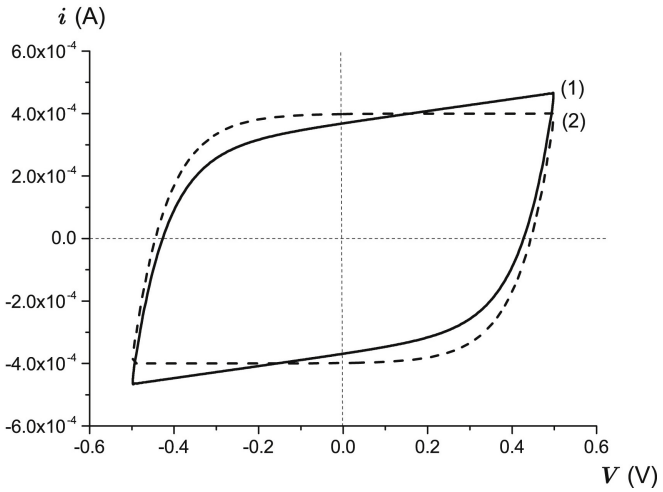

Figure 2.9: Simulated voltammograms for a simplified Randles circuit, reproduced from reference [149]. In the case of curve (1), $R_{\mathrm{p}} = 5 \times 10^3\ \Omega$, while for curve (2) $R_{\mathrm{p}} \to \infty$.

$$P_{\mathrm{av}} = \int_{v_{\mathrm{max}}}^{V_0} iV dV \frac{1}{v_{\mathrm{max}} - V_0}. \tag{2.13}$$

As mentioned above, in common with LSV, the presence of peaks and similar features can indicate the presence of Faradaic behaviour, particularly in a three-electrode cell. However, the shape of the voltammogram can also be used to indicate the presence of series and parallel resistances associated with a device. Figure 2.9 shows simulated CV curves for a simplified Randles circuit [149] (as shown in Figure 1.5 (a)). In curve (1) the parallel resistance is finite, while in curve (2) it is infinite. It can be seen that for curve (2), while i becomes constant towards the end of the sweep, the rectangular curve predicted for a simple capacitor becomes a parallelogram with rounded corners. These rounded corners, present on both plots, are indicative of a non-zero series resistance. When the parallel resistance is finite, as in curve (1), this has the effect of adding a linear function. This prevents i from reaching a constant value, and in a two-electrode device will result in the area under the discharge curve being smaller than that under the charging curve, which indicates that capacitance, energy and power

will also be reduced during discharging due to current leaking across the parallel resistance, reducing device efficiency. In the most extreme cases, where the ESR is very high, or the parallel resistance is very low, these distinct effects become much harder to distinguish, as the resistor-like behaviour will dominate and the voltammogram will tend towards a linear function [149].

2.2.3 Galvanostatic Cycling

Galvanostatic charging/discharging (GCD) is an alternative method, complementary to CV, for characterising the electrochemical performance of supercapacitor cells. In this technique a constant current is applied to the test cell using a galvanostat to charge a cell, and then an opposite (and usually equal) current is applied to discharge the cell. The cell potential is measured as the cell is charged to an upper potential limit, and then discharged to a lower potential limit [11, 150, 151].

For a capacitor in series with a resistance R_{s}, the variation of voltage as a function of time $V(t)$, when a constant current is applied is given by [151, 152],

$$V(t) = V_0 + \Delta I R_{\mathrm{s}} + I_{\mathrm{cc}} \frac{t}{C}, \tag{2.14}$$

where V_0 is the initial voltage before application of the current, ΔI the change in current when switching to charging/discharging, I_{cc} the applied current, and C the capacitance of the cell. ΔI will usually be equal to $2I_{\mathrm{cc}}$.

A simulated plot of V against t resulting from a GCD measurement over a single charge/discharge cycle is shown in Figure 2.10. The voltage profile over the cycle is roughly triangular, with a vertical discontinuity (the Ohmic drop) at the point of

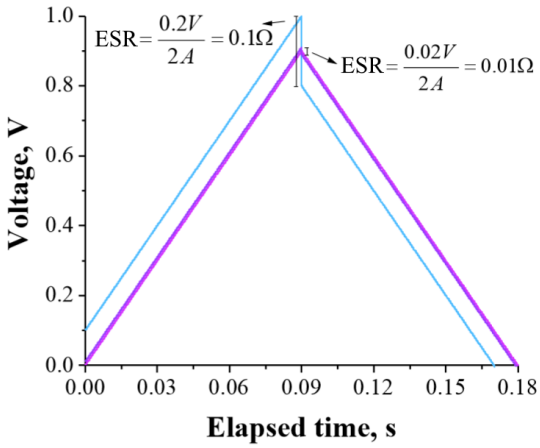

Figure 2.10: Simulated galvanostatic charge/discharge curve for ideal supercapacitors having $R_{\mathrm{ESR}} = 0.1$ and 0.01 Ω[152].

switching from charging to discharging. The capacitance can be determined from the gradient of the linear sections, while the cell resistance (or equivalent series resistance - ESR) is proportional to the magnitude of the Ohmic drop. C and R_{ESR} are given by [11, 21, 150, 152],

$$C = \frac{I_{\mathrm{cc}}}{dV/dt}, \tag{2.15}$$

and

$$\mathrm{ESR} = \frac{V_{\mathrm{drop}}}{2I_{\mathrm{cc}}}, \tag{2.16}$$

where I_{cc} is the applied (constant) current, dV/dt is the gradient of the top half of the linear section of the GCD curve, and V_{drop} is the magnitude of the Ohmic drop.

The energy input and output to the cell can be calculated by integrating the product of the current and potential over time [151]. For the simple RC model discussed above this is given by:

$$E = I_{\mathrm{cc}} \int \left[V_{+} \Delta I R_s t + I_{\mathrm{cc}} \frac{t}{C} \right] dt \; = I_{\mathrm{cc}} \left[V_0 t + \Delta I R_{\mathrm{s}} t + I_{\mathrm{cc}} \frac{t^2}{2C} \right], \tag{2.17}$$

However, as a real device cannot be assumed to behave as an ideal RC circuit, it is more accurate to calculate the input/output energy by directly integrating the experimental data:

$$E = i \int_{t_1}^{t_0} V(t)dt, \tag{2.18}$$

where i is the current, t_0 is the time at the start of the linear region of the charging or discharging part of the cycle, t_1 time at the end of the linear region of the charging or discharging part of the cycle and $V(t)$ is the instantaneous potential at time t.

The power as a function of time for this simple RC circuit is given by [151],

$$p(t) = V_0 I_{\mathrm{cc}} + R_{\mathrm{s}} I_{cc}^2 + \frac{I_{cc}^2 t}{C}, \tag{2.19}$$

however, as previously mentioned, for a real device it is more appropriate to determine the (average) power input/output from:

$$P = E/\Delta t, \tag{2.20}$$

where Δt is the time over which the linear region of the discharge curve extends.

Another important cell performance parameter which can be determined from GCD data is the Coulombic efficiency. This is the ratio of charge extracted during discharging to charge inserted during charging. Assuming that the discharging constant current is equal and opposite to the charging constant current, this can simply be found from the ratio of discharge to charge time. A reduced Coulombic efficiency can indicate the presence of irreversible Faradaic processes or self discharge, which are undesirable in a device. Although these processes also result in a decrease in energy efficiency, a high ESR will also reduce this making it a less useful indicator compared to the Coulombic efficiency.

2.2.4 Electrochemical Impedance Spectroscopy

In electrochemical impedance spectroscopy (EIS) a small alternating perturbation potential is applied to the cell. Such an alternating potential of the form $v = V\cos(\omega t)$ results in an alternating current $i = I\cos(\omega t + \phi)$ through the electrochemical cell. By measuring the current in response to an applied alternating potential (or vice versa) both its magnitude (I) and phase shift (ϕ) can be determined, which is then recorded as the frequency of the applied signal is varied.

The measured voltage and current are the real parts of $\boldsymbol{V} = Ve^{-j\omega t}$ and $\boldsymbol{I} = Ie^{-j(\omega t+\phi)}$, where $j = \sqrt{-1}$. The complex impedance, $\boldsymbol{Z}$, is then given by $\boldsymbol{Z} = \frac{V}{I}e^{-j\phi}$ which is the general form of Ohm's law. The complex impedance may then be separated into real and imaginary parts, expressed as Z' and Z'', respectively [18].

The resulting data can be plotted in a variety of ways, two of the most common being the Nyquist plot, which plots Z'' against Z', and the Bode plots, in which ϕ and Z are plotted against frequency [18]. EIS data is then commonly interpreted by fitting or comparing an equivalent circuit model to the Nyquist or Bode plots. A wide variety of such models are used, ranging from simple RC circuits, through to multi-branched transmission line models, as described in section 1.4.

Such modelling is enabled by the fact that individual circuit elements used to model and characterise supercapacitors each are responsible for distinct phase shifts, and therefore have unique impedances associated with them. In the case of a pure resistance, R, ϕ is zero and the impedance is simply $\boldsymbol{Z} = R$ [17]; while for an ideal capacitor, C, $\phi = \pi/2$ and its impedance is given by $\boldsymbol{Z} = -j\frac{1}{\omega C} = jX_C$ where X_C is known as the capacitive reactance [17]. This allows for the derivation of a

complex capacitance, $\boldsymbol{C}$, given by $\boldsymbol{C} = -j\frac{1}{\omega \boldsymbol{Z}}$. In terms of impedance, the real and imaginary parts of the capacitance are given by [24]:

$$C' = \frac{Z''}{\omega(Z'^2 + Z''^2)}, \tag{2.21}$$

$$C'' = \frac{Z'}{\omega(Z'^2 + Z''^2)}. \tag{2.22}$$

An alternative way of expressing the same information is through the complex admittance ($\boldsymbol{Y}$), which is the reciprocal of the complex impedance, and is related to electrical conductivity in the same way that impedance relates to resistivity [18].

In addition to resistors and capacitors such models may also incorporate constant phase elements (CPEs), having an impedance $\boldsymbol{Z} = \frac{1}{Q\omega^n} e^{-j\frac{\pi}{2}n}$ where Q and n are frequency independent constants [153, 154]. It is worth noting that the CPEs do not correspond to any real circuit elements and their exact physical meaning is poorly understood [154].

The Warburg element is a special case of CPE in which $\phi = \pi/4$, giving rise to an impedance of $\boldsymbol{Z} = \frac{A_\mathrm{W}}{\sqrt{\omega}} - j\frac{A_\mathrm{W}}{\sqrt{\omega}}$, where A_W is known as the Warburg coefficient [155]. This can be used to model semi-infinite diffusion processes, or the formation of the EDL in semi-infinite pores, as mentioned in Chapter 1 [33]. In the case of finite length diffusion, two versions of the Warburg element are possible; the Warburg short (W_s) and Warburg open (W_o).

W_s corresponds to finite-length diffusion with a transmissive boundary, which in the case of electrochemistry would be associated with a Faradaic process (i.e., charge trasfer occurring at the electode/electrolyte interface). The impedance of this element is given by $\boldsymbol{Z} = \frac{A_\mathrm{W}}{\sqrt{j\omega}} \tanh B\sqrt{j\omega}$ [156].

W_o, meanwhile, corresponds to finite-length diffusion with a reflective boundary, (i.e., capacitor-like behaviour). Its impedance is given by $\boldsymbol{Z} = \frac{A_W}{\sqrt{j\omega}} \coth B\sqrt{j\omega}$. In both cases $B = \delta/\sqrt{D}$, where δ is the thickness of the diffusion layer and D the diffusion coefficient of the system in question [156].

Impedances can be combined in the same way as resistors, so for a series RC circuit, the magnitude of the complex impedance is given by:

$$Z = \sqrt{R^2 + \left(\frac{1}{\omega C}\right)^2}. \tag{2.23}$$

As $\omega \to \infty, Z \to R$, and as $\omega \to 0, Z \to \frac{1}{\omega C}$ [17]. Meanwhile, for a parallel RC circuit, the complex impedance is

$$\boldsymbol{Z} = \frac{R}{1 + (\omega CR)^2} + j\frac{-\omega CR^2}{1 + (\omega CR)^2}, \tag{2.24}$$

which gives rise to the characteristic semicircle seen on many Nyquist plots (Figure 2.11) [17].

There is no clear consensus in the literature how the equivalent circuit elements or the features of the Nyquist plot which they model correspond to physical processes within an electrochemical cell [157]. Figure 2.11 shows a typical Nyquist plot for an EDLC[157].

Experimental results reported in the literature have attributed the semicircle labelled R_{AB}, referred to as the charge transfer resistance (CTR), which is attributed by Mei *et al.* to 'electrolyte resistance' instead to the electrode/current collector interfacial resistance [158–160], and it has even been linked to the shape of pores in the electrode [161]. It is possible that this feature is associated with a combination of the impedances of several of the interfaces in the cell (including the electrolyte resistance). Nonetheless, the section of the plot in Figure 2.11

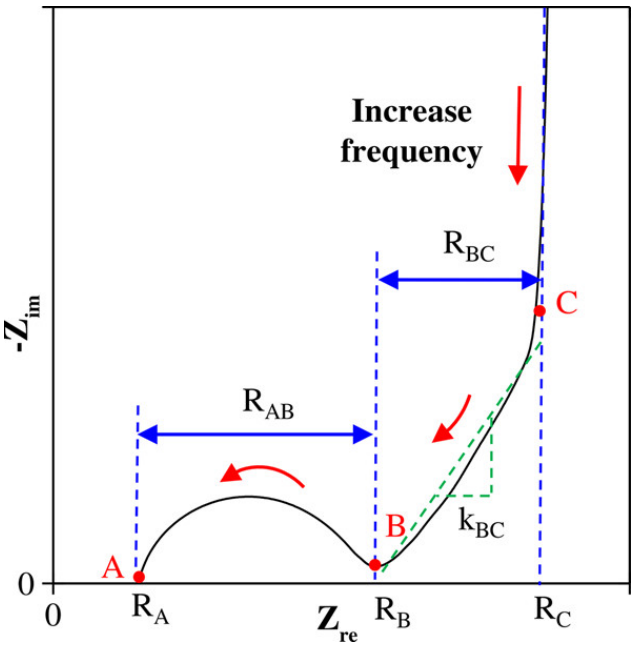

Figure 2.11: Typical Nyquist plot for an EDLC, reproduced from [157].

between 0 and R_A can still be taken as the ESR of the cell [157]. The section of Figure 2.11 labelled as R_{BC} corresponds to a Warburg element and, rather than corresponding to the diffuse layer, may instead correspond to the formation of the EDL within the pores of the electrode material [33, 109]. Together, these regions up to the vertical line comprise the *equivalent distributed resistance* (EDR) of the device [11, 157].

To find capacitance, the real part of the complex capacitance (C') can be plotted against frequency. At low frequencies C' should tend to a constant value – the equilibrium differential capacitance – corresponding to the vertical line on an idealised Nyquist plot. Unfortunately, in a real device, Faradaic processes and self discharge mean that the vertical section of the Nyquist plot, and corresponding horizontal section of the capacitance plot are rarely observed. In this instance, the EDL capacitance can be found using the plot of the imaginary parts of $\boldsymbol{Y}$ or $\boldsymbol{C}$ against frequency. These should show a local maximum, which corresponds to a characteristic frequency, f_0. The EDL capacitance is then given by $C = \frac{1}{2\pi \mathrm{ESR} f_0}$

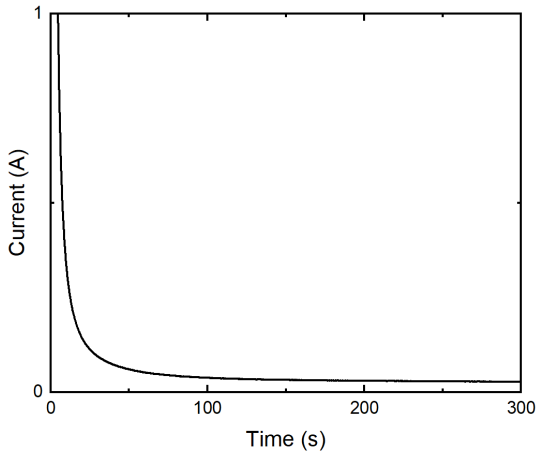

Figure 2.12: A typical chronoamperometric response showing current against time for a two-electrode cell with AC electrodes in aqueous 0.1 M KCl electrolyte, having been stepped from 0 V to 0.9 V.

[24].

An alternate way to estimate the capacitance and EDR from EIS data is to plot Z against ω^{-1}. At low frequencies (high ω^{-1}) this should approximate a straight line with its slope equal to the reciprocal of C. Meanwhile at high frequencies ($\omega^{-1} \to 0$), the intercept with the Z axis should be equal to the EDR of the cell.

2.2.5 Chronoamperometry

In a chronoamperometry (CA) experiment, a time varying transient current across a cell is measured in response to a change in potential. In this thesis, two variations of CA are employed; in the first, the current response to a step change in potential is measured [18]; while in the second, the potential is gradually increased to the target potential via charging at constant current, before the current evolution is measured as the cell is held at the target potential [162].

A typical chronoamperometry response for an EDLC with AC electrodes in aqueous 0.1 M KCl electrolyte, which has been stepped from 0 V to 0.9 V, is shown in Figure 2.12. For an ideal EDLC, the decay in transient current after a step change in potential is that of an RC circuit,

$$i(t) = I_0 e^{\frac{-t}{R_s C}}, \tag{2.25}$$

where I_0 is the initial current, R_s is the ESR of the cell, and C the capacitance. In the case of single pulse chronoamperometry, I_0 is given by V/R_s; i.e. the potential step divided by the ESR. If a parallel shunt resistance, R_p, is included (as in the case of a simplified Randles circuit) this equation becomes,

$$i(t) = \frac{V}{R_s} e^{-\frac{t}{\tau}} + \frac{V}{R_s + R_p}(1 - e^{-\frac{t}{\tau}}), \tag{2.26}$$

where $\tau = \frac{C R_s R_p}{R_s + R_p}$ [163] is the characteristic decay time associated with the circuit.

When considering Faradaic processes, provided they are diffusion limited the current instead evolves according to the Cottrell equation [17],

$$i(t) = \frac{nFAc_j^0\sqrt{D_j}}{\sqrt{\pi t}}, \tag{2.27}$$

where n is the number of electrons transferred during the Faradaic reaction, F the Faraday constant, A the area of the electrode, c_j^0 is the initial concentration of the reactive species j, and D_j the diffusion coefficient for j, all of which can be combined into a single constant, k. In this instance, i is purely limited by mass transport, and is entirely independent of potential [18]. There are limitations to this equation; for example the function is undefined at $t = 0$; meanwhile as $t \to \infty$, $i(t) \to 0$, whereas in practise an equilibrium will form at which the rate of diffusion of dissolved species to the electrode will equal the rate at which they are

consumed, resulting in a constant non-zero current [17].

In the case of a supercapacitor, equations 2.26 and 2.27 are not generally sufficient to describe the behaviour of the device in a CA experiment. For example, even in an EDLC there will be Faradaic processes such as pseudocapacitance and corrosion [23], which may render equation 2.26 inadequate. These Faradaic processes cannot even necessarily be described by equation 2.27; as mentioned in section 1.3.2, pseudocapacititive processes such as adsorption or intercalation will reduce the number of sites available for further ion storage [23], equivalent to reducing A in equation 2.27 as the reaction progresses, or alternatively, oxidative processes may etch the electrode material [164], thus increasing A with time.

Chapter 3

Experimental

3.1 Materials and Electrode Preparation

Throughout this work Supelco Activated carbon (AC), obtained from Sigma-Aldrich, was used as the active material for electrodes. In the studies reported in chapters 4 and 5 this was used with no pretreatment. 60 wt% PTFE in water (Sigma-Aldrich) was used as a binder and, where relevant, Timcal Super C65 carbon black (CB) was used as a conductive additive.

To produce basic electrode material as used throughout this thesis, the CB and AC were added to a beaker with 5 ml ethanol. This was then mixed using a magnetic stir bar on a 50 °C hotplate until most of the ethanol had evaporated. At this point the temperature was reduced to 30 °C and the stir bar removed, before the PTFE binder was added. The mixture was combined into a stiff paste using a spatula before being transferred to the pestle and mortar and mixed on a hotplate at 30 °C, for ten minutes until a cohesive paste was formed. This then rolled out thinly on the hotplate – still held at 30 °C – before being folded in half, flipped over and rotated 90°. This process was repeated ten times, giving a strong, uniform and flexible thin sheet of material which was then transferred to a worktop at room temperature and rolled to ≈75 μm, using metal shims to

regulate the thickness. The thickness of the resulting electrodes was measured by cutting a small piece of material and mounting it side-on, allowing cross-sectional imaging in the SEM. Electrodes produced in this way were typically measured to be $\approx 120\mu$m thick due to the elasticity of the material, causing it to rebound slightly after rolling out.

Electrochemical testing was carried out in 6 M aqueous KOH, or 0.1 M aqueous KCl, prepared using dry flakes or powder from Sigma-Aldrich without further purification. All ultra high purity (UHP) water used in this project was supplied by an Elga/Millipore PureLab Option-Q with DV-25 reservoir and had a resistivity of 15 MΩ cm. In chapter 6, Triton X-100 (Sigma-Aldrich), Tween-20, and Oleic acid were used to modify the behaviour of the electrolyte and were used as-recieved.

In chapter 5, the addition of Few-Layer Graphene (FLG) to AC electrodes was investigated. FLG was produced by liquid phase high shear exfoliation as described in reference [99]. This is summarised as follows: natural graphite flakes (Alfa Aesar) were combined in a vessel with ultra high purity water and Triton x-100 (Sigma-Aldrich) surfactant. These were mixed at 9000 rpm for 4 hours using a Silverson L5 laboratory mixer, corresponding to a shear rate, $\dot{\gamma}$, of $\approx 10^5$ s^{-1}. Centrifugation of the resulting mixture was performed with an Eppendorf 7500 centrifuge using 50 ml centrifuge tubes. Three different centrifuging protocols: a 'moderate' centrifugation at 2000 pm for 20 minutes (referred to as mFLG); a 'high' centrifugation at 7500 rpm for 1 hour (hFLG); and a third batch was left uncentrifuged (uFLG). After centrifuging, the top 40 ml of the suspension was extracted using a pipette to be used in electrodes as described below.

AC electrodes were prepared without any conductive additive, and with FLG as a conductive additive. To produce electrode material without any conductive additive, the AC, PTFE suspension, and $\approx$ 1 ml of ethanol were added directly

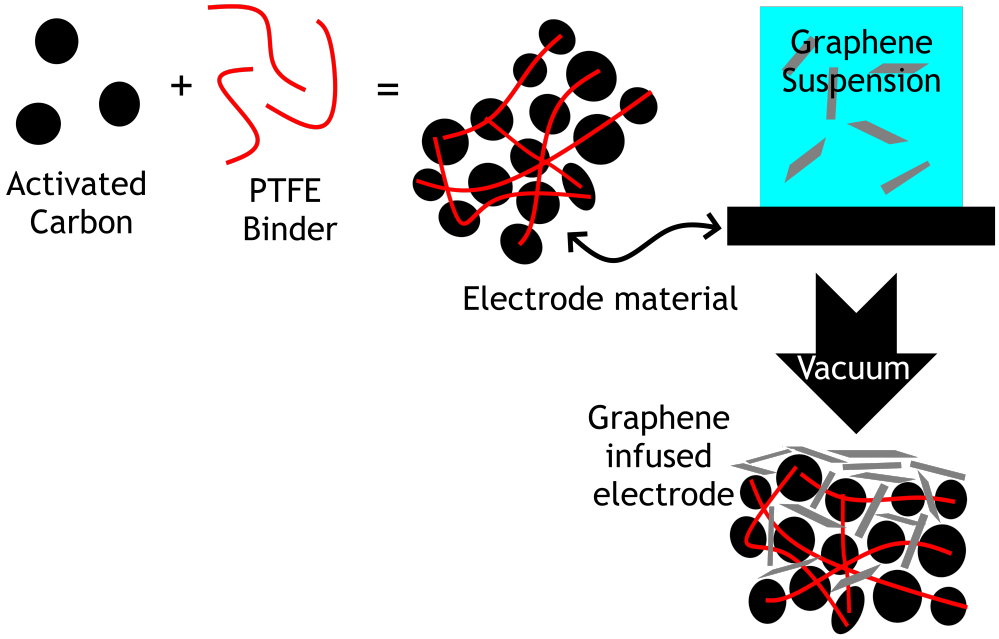

Figure 3.1: Diagram illustrating the method by which FLG infused electrodes were produced.

to the pestle and mortar and then formed into electrodes via the same method as described above. The method for producing electrodes using FLG as a mixed-in conductive additive is similar to the method using CB, except that as the FLG is suspended in water, no ethanol is added in the initial stages.

The method by which the vacuum infused FLG electrodes were produced is illustrated in figure 3.1; a sheet of activated carbon electrode material with no conductive additive (made as described above) was loaded into a vacuum filtration apparatus in lieu of a filter membrane. The FLG suspension was mixed with deionized water up to 150 ml and filtered through the AC material, resulting in a composite electrode. The concentration of FLG in the suspension was measured by filtering a known quantity of suspension onto a filter membrane and weighing the quantity of FLG deposited once dry. This concentration was used to guide the quantity of suspension used in making the composite electrodes, and the mass of FLG was confirmed by weighing the electrode material before and after the addition of FLG. The quantity of AC was held constant as

the amount of graphene added was varied, resulting in a variation in electrode mass.

Free-standing FLG electrodes were produced by filtering FLG suspension onto 0.4 μm pore cellulose nitrate membranes (Whatman) and washing with an excess of UHP water. The resulting film was dried at ambient temperature overnight before being peeled from the membrane.

The average electrode mass loading for the 'standard' electrodes made either with Timcal C65, or with no additive was 4.8±0.7 mg cm^{-2}, where the error given is the standard deviation. For the electrodes with vacuum-infused FLG, the mass loading varied from a comparable 4.24±0.04 mg cm^{-2} for those with approximately 5 wt% FLG, to 9.4±0.8 mg cm^{-2} for those containing over 50 wt% FLG. The electrodes with 50 wt% FLG showed a significantly greater variation in mass loading, leading to a much higher error. Electrodes were cut into varying sizes depending on test cell configuration (discussed below). Those cut into 15 mm discs had sheet resistance measured using a 4-point Van der Pauw method prior to electrochemical testing, using a custom-built apparatus.

For the work reported in chapter 6, both AC material and AC electrodes (the fabrication of which is described above) were oxidised by soaking in 10 ml of concentrated (70 %) nitric acid (Fisher) at ambient temperature for 48 hours. Following this, the bulk AC material was washed with UHP water in a vacuum filtration apparatus until the pH of the filtrate was measured to be 5 or higher. The whole electrodes that had been oxidised were instead left to soak in a bottle of UHP water; the water was changed every 24 hours, again until the pH was 5 or above. Thermally-treated AC (referred to as 'annealed AC'), also used for the experiments discussed in chapter 6, was prepared by placing AC in a custom-made glass furnace boat and loading it into a tube furnace (Carbolite). The furnace tube was purged with 900 cm^3 s^{-1} N_2 for 1 hour before the furnace was switched

on. The samples were heated to ≈1000 °C at a ramp rate of 10 °C s^{-1}, and held at ≈1000 °C for 15 minutes, before being allowed to cool naturally to room temperature, whilst maintaining the 900 cm^3 s^{-1} flow of N_2. These procedures were derived by trial and error with reference to appropriate literature [49, 54, 165, 166].

To better understand the impact of Triton X-100, Tween 20, and Oleic acid, electrodes made with the unmodified AC, electrodes made with the annealed AC, and the oxidised electrodes were soaked in these additives for 45 minutes, before being soaked in UHP water for a further 45 minutes to rinse off excess surfactant/oil. The electrodes were then dried in air on a hotplate, held at 100 °C, overnight prior to being tested.

3.2 Materials Characterisation

3.2.1 Electrolyte Characterisation

Electrolyte conductivity was measured at room temperature using a Jenway 4510 Conductivity/TDS Meter, capable of recording conductivities between 0 mS cm^{-1} and 19,999 mS cm^{-1}, with an accuracy of ±0.5 %. This was calibrated at 25 °C using conductivity standard solutions supplied by Oakton. pH measurements were carried out at room temperature using a Oakton EcoTestr pH1 Waterproof Pocket Tester, which can measure pH values between 0 and 14 with an accuracy of ±0.1, and was calibrated at 25 °C using pH buffer solutions (Oakton).

3.2.2 SEM

Scanning electron microscopy was used to examine morphology of both the AC and FLG, and of the complete electrodes used in chapter 5, and was used in conjunction

Figure 3.2: The Zeiss Sigma 300 VP SEM in the G.J. Russell Electron Microscopy Facility at Durham University.

with EDX to examine the surface chemistry of the modified ACs used in chapter 6. Backscattered electron images of the FLG were used to determine platelet size distribution. Imaging was carried out on a Zeiss Sigma 300 VP SEM, shown in Figure 3.2. This microscope has a FEG source, capable of accelerating voltages of 0.2 to 30 kV and beam currents of 0.5 pA to 5 μA. The microscope is equipped with a standard Everhart-Thornley detector for secondary electron imaging, a backscattered electron detector, a Zeiss Smart EDS silicon drift x-ray detector, and can be operated in a variable pressure mode which, in the experiments reported in this thesis, allowed imaging samples supported by non-conductive substrates.

In the studies described in chapter 5, imaging of ELDC electrodes was carried out using an incident beam energy of 3 keV and secondary electron detection. In a separate set of experiments used to determine the size distribution of the FLG platelets, small quantities of surfactant-stabilised aqueous FLG suspension

were diluted in UHP water and filtered onto anodic alumina (AA) membranes (Anodisc). These were imaged using backscattered electrons with primary beam energies of 3.2 keV or 5 keV. Imaging of these samples was performed in variable pressure mode in air at $\leq$ 10 Pa to neutralise charge build up on the AA membranes. A lower beam energy was used in the case of the electrode imaging in order to avoid damaging the highly delicate PTFE binder, while in the case of imaging the FLG platelets, a lower beam energy was necessary to avoid beam electrons passing straight through the thinnest platelets. Imaging and EDX analysis were carried out on the AC powder in chapter 6 with an incident beam energy of 12 keV. Here a higher beam energy was selected to induce not only the low-energy carbon and oxygen $K\alpha$ emissions, but also to cause the emission of characteristic X-rays from any higher atomic number contaminants that may have been present.

3.2.3 BET Measurements

The porosity of the AC powder and moderately centrifuged FLG material was measured using a Micromeritics Tri-star adsorption analyser at 77 K. Prior to measurements the sample was held under vacuum at 80 °C overnight, followed by 2 hours at 300 °C in a nitrogen environment, in a Micromeritics Flowprep system. As described in section 2.1.3, the Brunauer-Emmett-Teller (BET) equation was used to analyse the isotherms for surface area determination, while Barrett-Joyner-Halenda (BJH) theory was used for pore size analysis.

3.2.4 Raman Spectroscopy

Raman spectroscopy was used to examine the quality of the FLG material, and to determine the thickness of the FLG platelets. Spectra were acquired using an

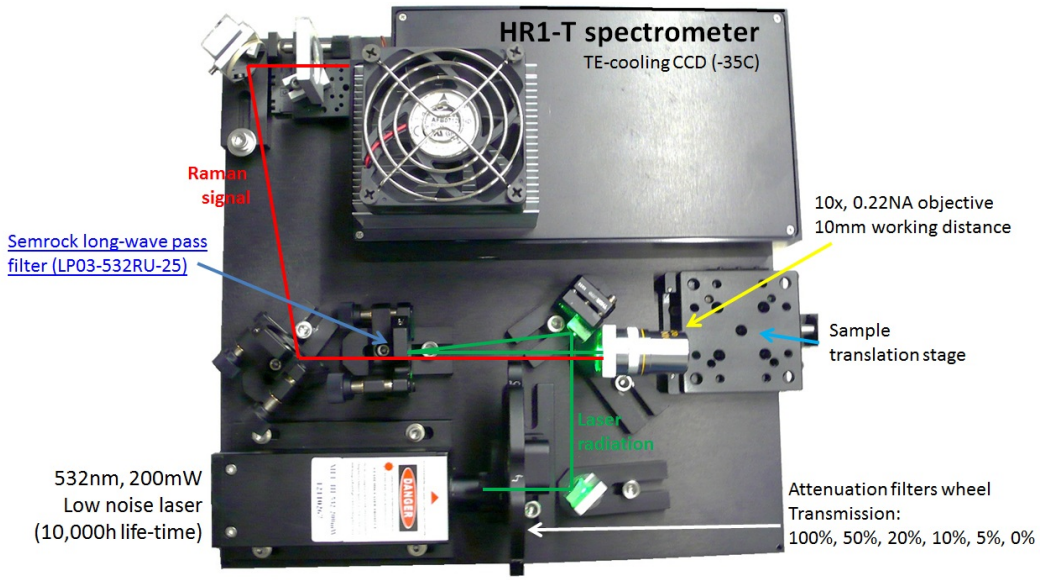

Figure 3.3: The interior of the ASEQ Instruments RM1, with key components annotated, and the path of the laser and Raman signals shown [167].

ASEQ Instruments RM1 Raman Spectrometer. This uses a 200 mW, low noise, 532 nm green laser (Opto Engine LLC); a 10x objective lens with 10 mm working distance; a Semrock LP03-532RU-25 long pass filter; and a Toshiba TCD1304AP linear array detector, thermoelectrically cooled to -35 °C, allowing a spectral resolution of between 8.5 and 16 cm^{-1}. Figure 3.3 shows the interior of the spectrometer and the position of these components in relation to the beam path. The thermoelectric cooling system was switched on one hour prior to using the spectrometer, to ensure adequate cooling and a stable temperature. The laser was operated at a beam power density of 15 W cm^{-2} in order to avoid damaging the sample surface. The energy of the spectra were calibrated using spectra from samples of silicon and SiC, and the Raman peaks were fitted to Lorentzian functions using Fityk [168], allowing for FLG platelet thicknesses to be calculated using a spectroscopic metric developed by Backes and co-workers, which compares the shape of the $2D$ peak of the parent graphite and that of the resultant FLG [145]. This is expanded upon in chapter 5.

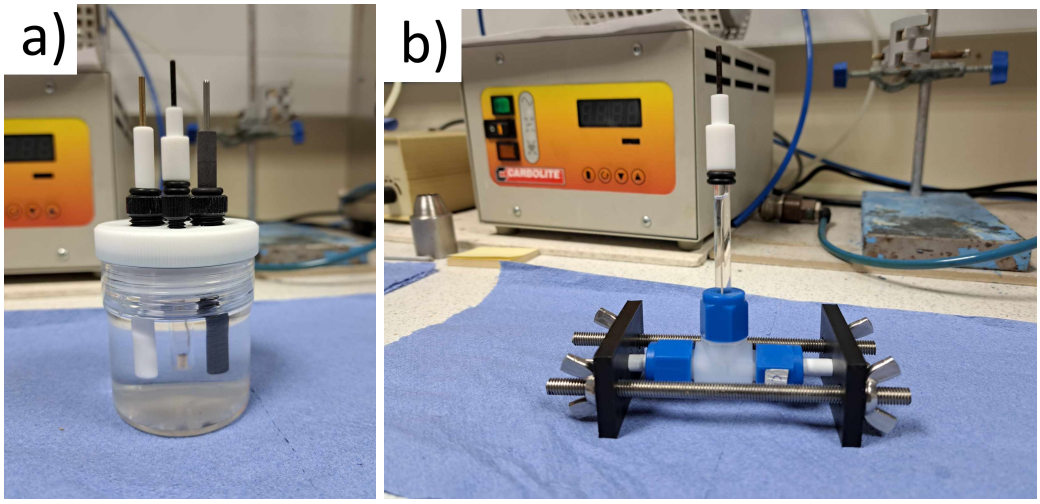

Figure 3.4: Two configurations used for three-electrode electrochemical testing: a) 'beaker' cell, b) 'Swagelok' cell.

3.3 Electrochemical Characterisation

3.3.1 Test Cell configuration

A number of different test cell configurations were employed for the work reported in this thesis. These include a simple glass beaker-based cell, as shown in Figure 3.4 (a), with either a 3 mm glassy carbon or 2 mm platinum disc working electrode (WE), an Ag/AgCl reference electrode (RE) (Ossila), and a 5 mm graphite rod as a counter electrode (CE) (Olmec). Between each test, the WEs were polished with diamond paste (RS) and polishing alumina (MetPrep) in order to remove surface contamination and oxides.

An alternative three-electrode configuration consisted of PTFE connectors and is commonly termed a 'Swagelok cell' (Figure 3.4(b)). In this cell a 1/4 inch PFA tee union (Swagelok) was used as the cell body, with 6 mm graphite or stainless steel rods (wrapped in PTFE tape) as contacts. As before, an Ag/AgCl reference electrode was used (Ossila), with a 5 mm disc of standard AC electrode material (described above) as a counter electrode, and 7 mm glass fibre disc (Sartorius)

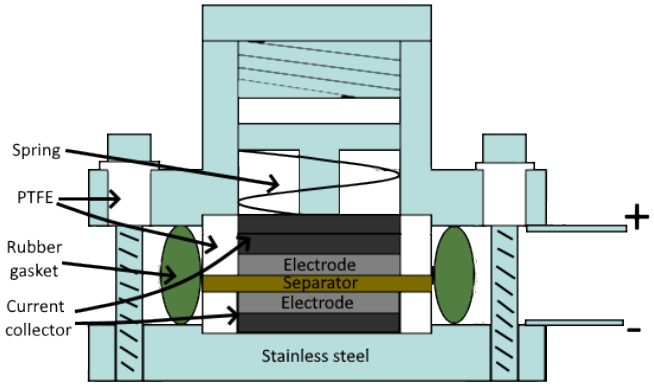

Figure 3.5: Schematic drawing of the two-electrode stainless steel electrochemical test cell.

as separator. The WE was cut to a 3 mm disc. A simple clamping apparatus consisting of two 3D-printed plastic pieces along with stainless steel studding and wingnuts was used to ensure a consistent cell pressure. This is important, as cell performance can vary significantly with pressure [169]. Following each test, the steel or graphite rods were polished with 15 μm microfinishing film (Cousins UK).

The Ag/AgCl reference electrode was filled with saturated (≈4 M) KCl solution, giving it a standard electrode potential of 0.197 V vs a standard hydrogen electrode. Prior to three electrode testing in either test cell, the electrolyte was purged of O_2 by sparging with N_2 for 45 minutes prior to testing. When using the Swagelok cell, the separator was soaked in the electrolyte for the duration of this period.

The majority of the two-electrode studies reported here, including all referred to in chapters 5 and 6, used a home-built stainless steel test cell, with type 316 stainless steel discs as contacts. A schematic of the construction this cell is shown in Figure 3.5. The cell was spring loaded, and designed so that the spring could not be compressed below a certain length in order to ensure a consistent pressure between tests, the spring force being set to 29 N when fully tightened. In most instances 25 mm diameter glass fibre filter membranes (Sartorius) were

used as separators and the electrodes were cut to 15 mm discs. The exceptions are the experiments used to derive the Ragone plot shown in chapter 5, Figure 5.17, in which 10 mm diameter electrodes were used in order to enable higher current loads, and in chapter 6.2.1, where a Celgard 2500 membrane was used as a separator. As with the three electrode cells, the steel contact discs were polished with 15 μm microfinishing film between tests. In the experiments presented here, 6 M KOH was used as the electrolyte, unless stated otherwise. In chapter 4, where 0.1 M KCl was used as an electrolyte, Swagelok cells with graphite electrodes were used for two-electrode testing. Both electrodes were cut to 5 mm discs and, where the reference electrode would have been inserted, the cell was instead capped and sealed.

3.3.2 Electrochemical Methods

Electrochemical characterisation was carried out using either a Palmsens 4 potentiostat, or a DIY USB-potentiostat as described by Dobbelaere and co-workers [170]. The Palmsens 4 has a DC potential range of ±5 V, and a maximum current of ±30 mA. Controlled by the PSTrace software, it can be used for a variety of electrochemical techniques including CV, LSV, GCD, EIS, and CA, or can be programmed to perform any combination of these. The USB potentiostat has a DC potential range of ±8 V, and a maximum current of ±25 mA, and can be operated in either a potentiostatic or galvanostatic mode for CV or GCD measurements.

For three-electrode testing, the cell was allowed to equilibrate for a half hour period, at the end of which the open circuit potential (OCP) was measured. EIS was performed with V_{DC} set to the OCP and V_{AC} = 0.02 V, for a range of frequencies between 0.005 and 100,000 Hz. Three-electrode CV was carried out with scan rates of 2 mV s^{-1} and 20 mV s^{-1}. In the case of CV performed at a 2 mV s^{-1} sweep rate, the electrode potential was initially swept in one direction

from the OCP until a target current density was reached, and then swept back to the OCP. Unless otherwise stated, the first cycle is presented in order to capture any irreversible processes present. When switching between tests at potentials below the OCP, and those at potentials above the OCP (i.e. negative and positive electrodes), the cell was reset with the electrolyte replaced, and in the case of the platinum and glassy carbon WEs, the WE was cleaned and polished, or in the case of AC WEs, these were replaced and the steel or graphite contacts, cleaned and polished. Conversely, voltammagrams measured at 20 mV s^{-1} sweep rates were performed over the whole stable range of the electrode, and the 10th cycle is presented by which time the shape of the CV curve no longer evolves significantly with cycling. For these voltammograms the potential was swept from the OCP to the positive potential limit, before being swept to the negative limit, and then back to the starting point. The procedure employed for LSV measurements was the same as that for a single three-electrode CV cycle performed at a sweep rate of 2 mV s^{-1}. As described in reference [171], the forward and backward sweeps were averaged together to remove any contribution arising from the double layer or pseudo-capacitance of the electrode.

Cyclic voltammetry on two-electrode cells was performed over a variety of scan rates across a specified working voltage for at least 25 cycles. Python code, presented in appendix A, was used to written to calculate C_{sp} and other parameters from the area under the discharge curve, according to the equations presented in chapter 2.2.2, and energy efficiency was calculated from the ratio of the area under the discharge curve to the area under the charge curve. In all instances, the twentieth cycle is presented in the figures, alongside the mean and standard error of performance parameters derived from the 15th to 25th cycles. Similarly, two-electrode GCD was performed for a variety of current loads over a specified working voltage range for 60 cycles for basic characterisation and 5,000 or more cycles for lifetime tests. Performance parameters were derived as described in chapter 2.2.3, using

python code presented in appendix B. As with the CV, the 20th cycle is presented in the figures, alongside the mean and standard error for the properties derived from the final ten cycles. In the case of the GCD data, the correct functioning of the python program in calculating ESR and C_{sp} could easily be checked by measuring the Ohmic drop and the gradients of the charging/discharging curves by hand. This could then be used to derive approximations of energy and power to verify that the code was working correctly. For the CV data, it was more complex to work out C_{sp} and other values by hand, but these could be approximated using the current during cycling, and data from the charging and discharging half-cycles could be checked against values derived from the whole area under the curve.

Chapter 4

Approaches for determining the maximum working voltage of aqueous supercapacitors

4.1 Introduction

One of the key drawbacks of supercapacitors is their low energy density [11, 12]. As energy stored is proportional to the square of the working voltage (equation 1.3), it is necessary to maximise the latter in order to achieve the highest possible energy density. The maximum working voltage (MWV) is limited by undesirable redox reactions which parasitically consume charge, reducing cell efficiency, and also cause irreversible damage to the cell leading to capacitance falling and/or ESR increasing with time [35, 172–175].

This problem is particularly acute for devices using aqueous electrolytes, which are generally viewed as being limited to a MWV of $\approx$ 1 V, due to the narrow electrochemical window (1.23 V) over which water is stable, as described in Chapter 1, section 1.5. However, the reality of the situation is slightly more complex than this. As discussed in Chapter 1, section 1.5, different electrode

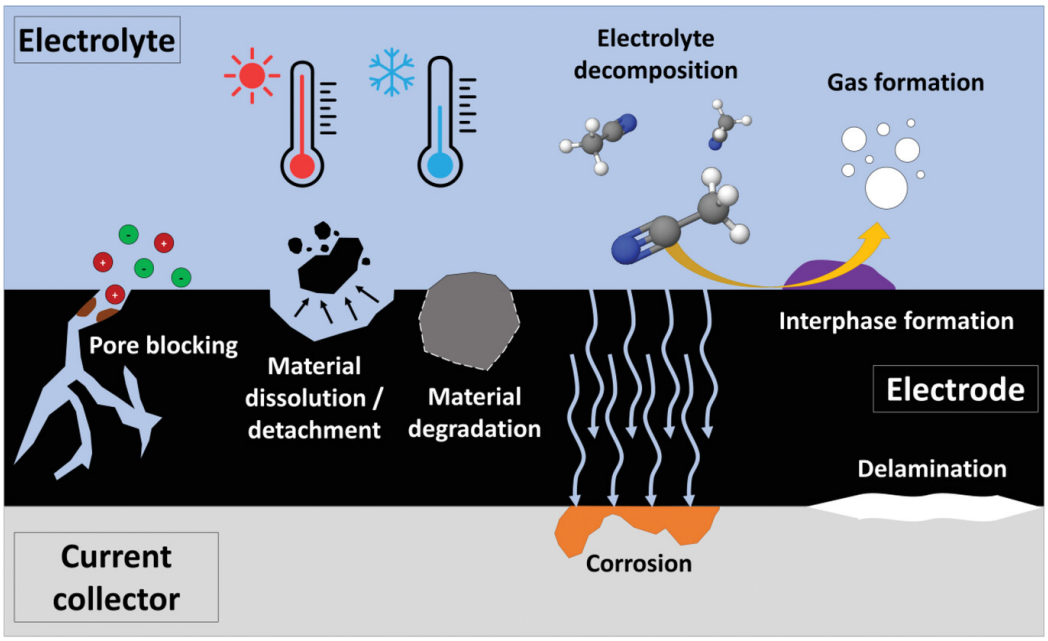

Figure 4.1: Overview of possible degradation processes in supercapacitors. Reproduced from Pamete *et al* [35].

materials will have different activation overpotentials for different reactions, but the electrolyte itself also has a role to play, with neutral sulphate electrolytes having been reported to have a greater stability than highly acidic or basic ones. Because of the variety of materials present in a real device, several different degradation processes are possible, illustrated in Figure 4.1 [35].

A number of studies have examined the failure at elevated voltages of EDLCs utilising aqueous sulphate electrolytes and activated carbon electrodes, and all have found that the MWV of the device is ultimately limited by the oxidation of water at the positive electrode. Gas evolution studies show that no O_2 is evolved, instead atomic oxygen is formed which corrodes the electrode surface, producing CO and CO_2 gas and forming surface functional groups (SFGs) which block the pores of the device, reducing capacitance [172–175]. As the cell degrades further, delamination may occur between the electrodes and current collectors, increasing equivalent series resistance (ESR) [35, 175], and ultimately, gas buildup may lead to the cell body rupturing, and the catastrophic failure of the device [35, 176].

Despite maximising the MWV of aqueous supercapacitors therefore being a major focus of research, accurately determining the MWV is itself no straightforward task. The first issue is that the definition of MWV is somewhat arbitrary: any cell will eventually fail regardless of the operating potential, and so the MWV is defined as the potential at which the cell can operate for a certain length of time, sustaining only a certain level of performance degradation. One of the more common criteria is 1,000 hours of operation with no more than a 20% drop in capacitance or a doubling of ESR [35, 174, 177, 178], although commercial supercapacitors can have lifespans much greater than this [11, 12, 179]. The rate of degradation can also be accelerated at high temperatures, so it is important that temperature be controlled for reliable results.

In light of this definition, the most reliable method is to subject the device to a large number of galvanostatic charge/discharge (GCD) cycles and measure the evolution of capacitance and ESR, but this can be extremely time consuming, especially bearing in mind that electric double layer capacitors (EDLCs) can in the extreme cases withstand around 1,000,000 cycles before significant degradation. For example, Rizoug *et al.* tested an EDLC device for over 500,000 cycles, taking almost a year to do so [179]. The 'voltage hold method', in which the supercapacitor is held at the test MWV for several hours and subject to occasional GCD cycles to monitor changes in performance, can provide accelerated aging [180]. Nonetheless, this approach can still take a third of the time that GCD cycling would take [7, 177], and hence does not fully address the requirement for an extended evaluation time.

Due to this, it is common for researchers to attempt to determine the MWV using more rapid approaches, to try and pinpoint the redox reactions which lead to cell failure. This is itself complicated by the fact that the processes leading to redox

currents are not known, and it is difficult to determine the magnitude of redox current density that will lead to cell failure. One of the most common approaches to be found in the literature is the visual inspection of the cyclic voltammogram, with an increase in current at high cell potentials (referred to as a 'tail') being associated with destructive redox processes [50, 181]. This method suffers from being highly subjective – not only can the the magnitude, and therefore visibility, of the tail can vary with scan rate, it can even be diminished with cycle number [182, 183]. Moreover, the extent of the tail and its acceptability or otherwise is usually evaluated by eye, using the judgement of the researcher, rather than on any quantitative basis. Other methods suggested in the literature include GCD [184–186], electrochemical impedance spectroscopy (EIS) [182, 186], and chronoamperometry [162, 175, 182], but there is no real consensus on the most effective and efficient method. This chapter will evaluate a number of two and three electrode techniques for determining the MWV of supercapacitor devices. In particular, short-term techniques will be compared with longer term GCD cycling, in order to determine the most appropriate and consistent methods for finding the MVW in aqueous EDLC devices.

As outlined above, the processes by which supercapacitors decay are highly complex, poorly understood, and can vary significantly between different cell constructions. To account for this, activated carbon electrodes in two distinct electrode structures will be investigated using two and three-electrode configurations. In particular, electrodes consisting of 90% activated carbon, 5% conductive carbon black and 5% PTFE, as described in Chapter 3, are employed, since these have been well-characterised in the course of the doctoral work reported in this thesis and display reproducible behaviour. The (free-standing, flexible) electrodes are placed either on stainless steel contacts using 6 M aqueous KOH as an electrolyte or on graphite contacts using a 0.1 M KCl electrolyte. Both two and three-electrode cells, with structures discussed in Chapter 3, have been

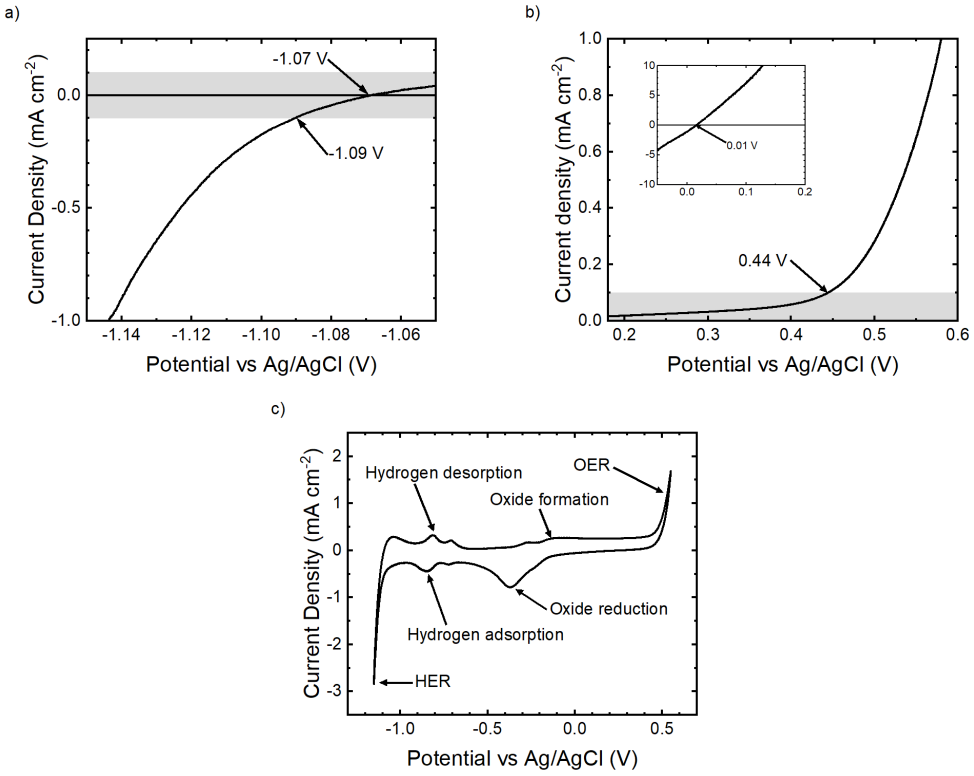

Figure 4.2: Three-electrode voltammetry data for a 2 mm platinum disc electrode in 6 M KOH: a,b) Linear sweep voltammograms captured at 2 mV s^{-1} of the HER and OER, and c) a cyclic voltammogram at 20 mV s^{-1}. The shaded regions in a) and b) correspond to current densities of $\leq$ 0.1 mA cm^{-2}. Annotations in c) are based on those given in [187, 188].

used. The 6 M KOH electrolyte is strongly alkaline, with a pH of 14, and due to its high ionic concentration was measured to have a very high conductivity of 571±3 mS cm^{-1}; while the 0.1 M KCl is a neutral (pH 7) electrolyte, with a much poorer measured conductivity of 13.95±0.07 mS cm^{-1}.

4.2 Results

4.2.1 Three-electrode linear sweep voltammetry and cyclic voltammetry

Three-electrode linear sweep voltammetry (LSV) and cyclic voltammetry (CV) were initially performed on platinum and glassy carbon working electrodes to gain a perspective on the stability of the aqueous 6 M KOH electrolyte independent of the oxidation of the electrodes or other cell components, which can themselves undergo reactions and limit the MWV, as described in [35]. Figure 4.2 shows LSV and CV data for the hydrogen and oxygen evolution reactions (abbreviated henceforth as HER and OER, respectively) on a platinum disc electrode. The chemical equations for these reactions are given in Chapter 1, section 1.5 (equations 1.7 and 1.8). The region of the HER is shown in Figure 4.2 (a). It can be seen that the equilibrium potential (i.e., the potential at which the current density is zero) occurs at -1.07 ± 0.02 V, possibly corresponding to where hydrogen adsorption and desorption are balanced; from here the current density (j) becomes negative and increases steeply in magnitude, to reach 0.1 mA cm^{-2} at -1.09 ± 0.02 V, this current density having been used in the literature to indicate the breakdown of the electrolyte [36, 189]. These values are close to the standard reduction potential of hydrogen in highly alkaline media (-1.03 V va Ag/AgCl [17]). The region of the OER is shown in Figure 4.2 (b), and here the picture is more complex. The equilibrium potential occurs at 0.01 ± 0.05 V, but from this point the current density increases slowly to reach 0.1 mA cm^{-2} at 0.44 ± 0.04 V. The OER is known to be a relatively sluggish reaction [171], and so the slow increase in current observed is in good agreement with expectations, but the equilibrium current occurs well before the standard reduction potential (SRP) of the OER (0.2 V). The equilibrium potential observed in Figure 4.2 (b) may therefore correspond to oxide formation occurring alongside the OER, which is balanced by oxide reduction.

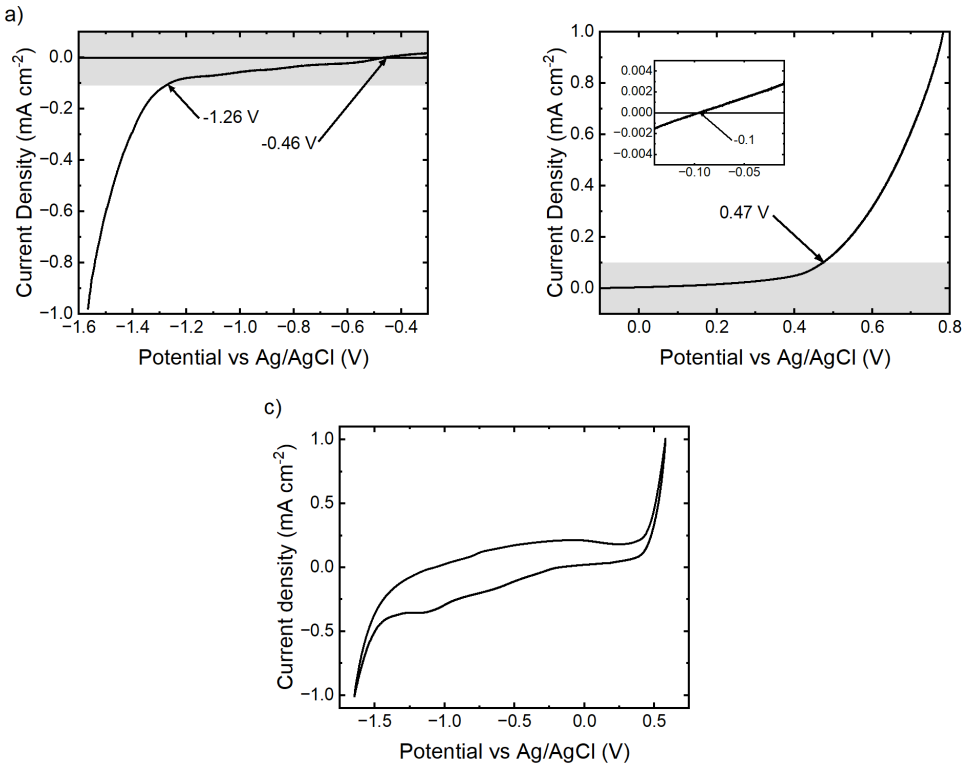

Figure 4.3: a,b) Linear sweep voltammograms captured at 2 mV s^{-1} of the HER and OER, and c) a cyclic voltammogram at 20 mV s^{-1} showing the whole stability window of aqueous 6 M KOH in a three-electrode electrochemical cell with a 3 mm glassy carbon disc working electrode. The shaded regions in a) and b) correspond to current densities of ≤ 0.1 mA cm^{-2}.

The regions of these reactions are indicated on the cyclic voltammogram shown in Figure 4.2 (c) [187, 188]. The sharp increases in current which can be assigned to the HER and OER are clearly visible at around -1.1 V and 0.4 V, showing the approximate 1.5 V stability window for aqueous 6 M KOH on Pt, given by the cut-off current density of $j = 0.1$ mA cm^{-2}.

Figure 4.3 shows corresponding data for a glassy carbon electrode in 6 M KOH. Compared with the Pt electrode, the equilibrium voltage of -0.46 ± 0.16 V at the negative electrode is closer to 0 V than that for the Pt electrode. This difference may be in part due to the suppression of the highly reversible hydrogen adsorption/desorption reaction owing to the high overpotential for H^+ reduction

on glassy carbon [36], with the current close to the Open Circuit Potential (OCP) instead being dominated by the reduction of trace quantities of oxygen in the electrolyte or on the electrode surface. At more negative potentials, j increases slowly, reaching 0.1 mA cm^{-2} at -1.26 ± 0.03 V, consistent with the HER having a higher overpotential on this electrode material in comparison with Pt [36]. In contrast, at positive biases, the electrode potentials at which $j = 0$ mA cm^{-2} and $j = 0.1$ mA cm^{-2} are measured (-0.1 ± 0.03 V and 0.47 ± 0.05 V, respectively) are very similar to those observed for Pt, showing that while the HER is suppressed on platinum the OER progresses at a similar rate on both materials, consistent with observations in the literature [36]. A CV sweep at 20 mV s^{-1} is shown in Figure 4.3. The downwards slope of the voltammagram at negative bias is typical of the reverse oxygen reduction reaction [190], which can arise from oxygen and oxide groups evolved at the positive bias limit being reduced during the negative sweep, or from the reduction of dissolved O_2 due to incomplete purging of O_2 from the test cell. Slight reduction and oxidation peaks are visible at approximately -1.1 V and -0.8 V, corresponding to hydrogen adsorption and desorption. These are much less prominent than their counterparts observed on platinum due to the relative unfavourability of these reactions on glassy carbon. The significant increase in the magnitude of j beyond potentials of -1.25 V and 0.4 V shows the stability window of 6 M KOH with glassy carbon electrodes to be around 1.65 V, slightly greater than that observed on platinum.

Whilst the LSV and CV data presented in Figures 4.2 and 4.3 can help to understand the stability of 6 M KOH on simple surfaces, the real devices used in this work consist of activated carbon electrodes on stainless steel contacts, which can have a significantly more complex surface chemistry and surface morphologies. In order to better understand the limits of a more realistic system, three electrode cyclic voltammetry was also performed using activated carbon electrodes, the results of which are shown in Figure 4.4. Due to the high surface area of the activated

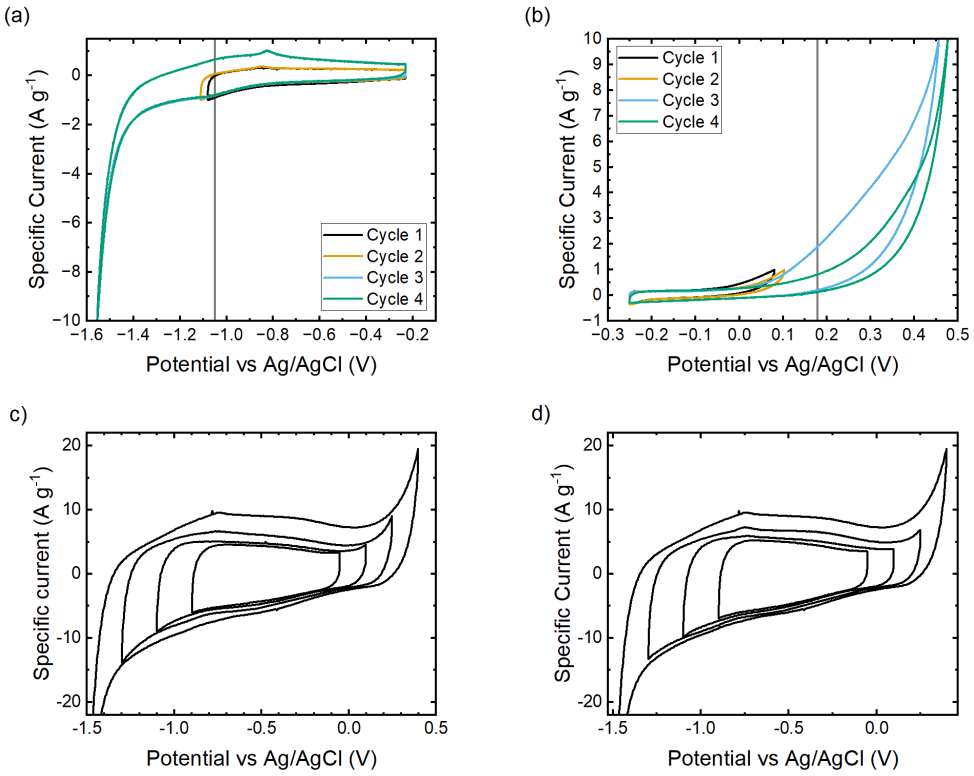

Figure 4.4: Cyclic voltammograms of a three-electrode electrochemical cell with an activated carbon working electrode in 6 M KOH electrolyte. a,b) those at 2 mV s^{-1} of the negative and positive electrode ranges, respectively; cyclic voltammograms at 20 mV s^{-1} across the entire stability window with increasing c) and decreasing d) potential limits.

carbon electrodes (the specific surface are of the activated carbon was measured to be 870 m^2 g^{-1}), the background capacitive current was high (0.25 A g^{-1}) compared with that observed on the planar Pt and glassy carbon electrodes, and a large degree of hysteresis was observed between the forward and backward sweeps. This could introduce large uncertainties into any LSV measurements, making it a less appropriate technique, compared with CV, which shows the entirety of the behaviour of the electrode. In light of this, CV was employed instead. Although the BET surface area of the activated carbon material is known, it is not possible to determine exactly how this corresponds to the electrochemically active surface area of the electrodes. This is due to the larger size of the solvated electrolyte ions and limited wettability of the AC, which mean that pores accessible to the N_2 molecules used in BET may not be accessible to the ions in the electrolyte. Because of this

the gravimetric specific current was used instead of the areal current density. This means that caution must be exercised when comparing the results obtained on the platinum and glassy carbon electrodes with those obtained on activated carbon.

Figure 4.4 (a,b) shows cyclic voltammograms obtained at a sweep rate of 2 mV s^{-1}: two cycles in which the scan was reversed at a specific current (I_{sp}) of 1 A g^{-1}, and then two more at 10 A g^{-1}. These cutoff specific currents were chosen to be larger than the capacitive current, whilst attempting to avoid significant damage to the electrodes. The results of a negative bias with respect to the OCP of the electrode are shown in Figure 4.4 (a). It can be seen that there is very little change in the shape of the voltammograms across each cycle within the same specific current limits, showing that the electrode is stable in the short term over the voltage range investigated. I_{sp} is first observed to reach 1 A g^{-1} at around -1.08 V, in good agreement with the standard reduction potential, and interestingly coinciding with the behaviour observed on platinum. However, upon scanning to 10 A g^{-1}, it becomes clear that this initial increase in current is in fact a shoulder on the HER peak, corresponding to another reaction, and possibly masking the onset of significant H_2 evolution. This shoulder may correspond to hydrogen adsorption, with the corresponding desorption peak visible at around -0.8 V [172], analogous to the behaviour observed on glassy carbon at similar potentials, Figure 4.3 . By the time the current reaches 10 A g^{-1} at -1.55 V, the evolution of H_2 gas may be assumed to dominate.

The results obtained from a positively biased working electrode are shown in Figure 4.4 (b). In this instance a specific current of 1 A g^{-1} is initially obtained at a potential 0.08 V, 0.12 V earlier than the standard OER potential. In contrast to those obtained from the negatively biased electrode, the cyclic voltammograms obtained from the positively biased electrode change significantly across the four cycles, with a specific current of 1 A g^{-1} being observed at biases of 0.1 V,

0.12 V and 0.21 V in successive cycles. This behaviour may originate from the electrooxidation of SFGs such as anhydrides (chapter 1.6.2.1), lactones, quinones and carbonyls, which occurs at potentials above 0.06 V vs Ag/AgCl, as described in reference [172]. As these SFGs are oxidised without being regenerated the current associated with this process decreases with each subsequent cycle. As the potential is increased further to 0.46 V, it might be expected that O_2 would be evolved, however, as described above, gas analysis studies of activated carbon electrodes with aqueous Li_2SO_4 electrolyte detected no O_2 – instead CO and CO_2 were formed by the oxidisation of the electrode, this process leading to the degradation of the cell [172, 175].

Figure 4.4 (c) and (d), shows cyclic voltammograms obtained at a sweep rate of 20 mV s^{-1} for activated carbon electrodes in a 6 M KOH electrolyte across a range of potential windows as the window is increased (Figure 4.4 (c)) and subsequently decreased (Figure 4.4(d)). The negative potential limits were −0.9 V, −1.1 V, −1.3 V, and −1.5 V, and the positive limits were −0.05 V, 0.1 V, 0.25 V, and 0.4 V, all vs Ag/AgCl, which were chosen so as to cover similar potential ranges to the scans at 2 mV s^{-1}. In the case of Figure 4.4 (c), small increases in anodic and cathodic current are visible at the positive and negative limits at even the smallest potential window, which increase monotonically in magnitude as the breadth of the window is increased. When the window increases to cover the potential range of −1.3 V to 0.25 V versus Ag/AgCl, the hydrogen desorption peak (as observed in Figure 4.4 (a)) begins to develop at −0.8 V, demonstrating significant breakdown of the electrolyte. At the broadest range of −1.5 V to 0.5 V the anodic and cathodic currents are large, demonstrating significant Faradaic processes, and the hydrogen desorption peak is sharper. This confirms, that as would be expected, 2.0 V would be beyond the stable operating potential of the device, but it might be argued that these Faradaic processes begin at a range of below even 1.0 V.

Decreasing the range, as seen in Figure 4.4 (d), tells a slightly different story. Although the sloped profile of the reduction current makes the onset of the sharp increase in hydrogen evolution current hard to determine, it can be seen that the oxidation current is at least temporarily suppressed at 0.1 V and below. In part, this is likely to be due to the oxidation of surface functional groups discussed above; but may also be due in part to the H^+ and OH^- ions generated by water splitting leading to localised changes in pH, thus altering the Nernst potentials of the half reactions [191]. These results, would seem to support operating voltage limits of approximately -1.1 ± 0.1 V and $+0.1 \pm 0.08$ V.

From these experiments alone, it is difficult to determine the operating window of the system in any more detail, the exponential increase in current means that the MWV measured can vary significantly depending on the range of specific currents measured, and it is unknown what magnitude of corrosion current will cause the cell to degrade over its lifetime. Furthermore, as shown in Figure 4.4 (b), the current response observed can vary significantly as the surface chemistry of the electrodes are altered over repeated testing.

A further problem which arises in trying to relate the three electrode CV data to the MWV of the cell comes from the . In the voltammograms above this is shown to be around -0.251 ± 0.001 V, nearer to the onset of the OER than that of the HER. This could limit the MWV to as low as 0.7 V (in agreement with some of the lower estimates for activated carbon (AC) in KOH shown in the literature [113]), necessitating mass balancing to exploit the full stable voltage of the cell [183]. On the other hand, it has been shown in the literature that in some systems such as carbon nanotube-polymer composites in HCl and KCl the OCP migrates (not only during cycling, but also while the electrodes are immersed in electrolyte), to a point nearer the centre of the stability window, allowing it to be more fully exploited [192], and it is possible

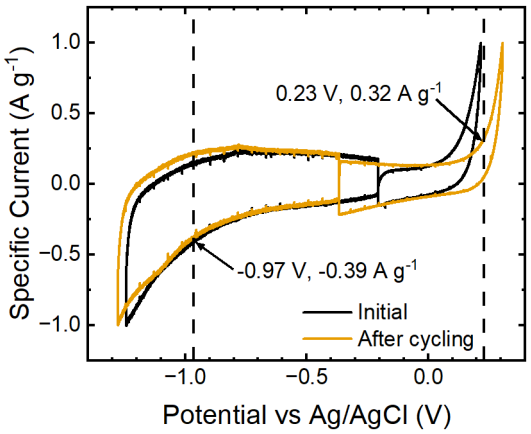

Figure 4.5: Three-electrode cyclic voltammograms at 2 mV s^{-1} of the positive and negative working electrodes in a symmetric cell before (black) and after (orange) 25 cycles in two electrode configuration over a window of 1.2 V. The electrode material is activated carbon and the electrolyte 6 M KOH. The dashed vertical lines indicate the approximate positive and negative potential limits of the electrodes during two-electrode cycling.

that the oxidation of SFGs on the surface of the AC may have a similar effect [164].

In order to investigate this, a three electrode cell was assembled having working and counter-electrodes of equal mass. The OCP of this cell was measured immediately after setup, and 20 hours later. The reference electrode was then disconnected and the cell, now operating in a two-electrode configuration, was subject to 25 CV cycles at 10 mV s^{-1} over a range of 1.2 V, before the reference electrode was reconnected and the OCP measured again. At each stage, the positive and negative working electrodes were individually cycled at 2 mV s^{-1} to a I_{sp} of 1 A g^{-1}. The results of this are shown in Figure 4.5. Initially, the OCP was measured to be -0.205 ± 0.001 V. After 24 hours, this had moved slightly more negative, to -0.227 ± 0.001 V, and after the cell was cycled in two electrode configuration the OCP moved further to -0.365 ± 0.001 V, closer to the midpoint of the -1.1 V to 0.1 V range observed in Figure 4.4.

Looking to the voltammograms in Figure 4.5, it can also be seen that while

the negative working electrode appears very stable, the voltammogram of the positive working electrode evolves significantly after cycling, in keeping with the trends observed in Figure 4.4. Initially, a specific current of 1 A g^{-1} is observed at 0.2 V on the positive working electrode, with a specific current of 1 A g^{-1} being measured at −1.2 V on the negative working electrode. This is a broader range than that observed for the AC electrodes in Figure 4.4, this may be because the electrodes being of equal mass means that the counter electrode is less effectively able to balance the current at the working electrode, or may be due to the larger diameter of the working electrode meaning less of the stainless steel contact is exposed to electrolyte, reducing any impact it may have had on performance. In either case, this demonstrates that these experiments are not perfectly replicable across different test cell setups – varying by 0.1 V at each electrode – an important caveat to note. After cycling, the voltage at which a specific current of 1 A g^{-1} is achieved at the positive working electrode moves to 0.3 V. This puts the OCP of −0.365 V even closer to the midpoint of potentials at which specific currents of ±1 A g^{-1} are realised, and means rather than the positive working electrode exceeding specific currents of 1 A g^{-1} during two-electrode cycling, the current at the positive working electrode is instead limited to 0.32 A g^{-1}, similar to the specific current of 0.39 A g^{-1} observed at the negative working electrode. These results show that it should be possible to exploit the full MWV for AC in 6 M KOH without the need to mass-balance the electrodes.

As mentioned in the introduction to this chapter, AC electrodes on graphite contacts in a 0.1 M KCl electrolyte were also investigated as a contrasting system. Figure 4.6 shows three-electrode cyclic voltammograms for this system, obtained at a higher scan rate of 100 mV s^{-1}. This higher scan rate significantly expedites measurements, and was chosen in order to understand whether useful data may still be obtained from quicker tests. Due to this high scan rate, the onset of the HER and OER will be less pronounced than in the 20 mV s^{-1} scans shown in

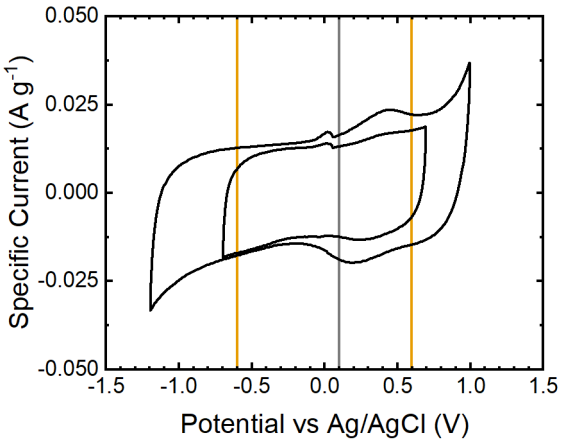

Figure 4.6: Three-electrode cyclic voltammograms of activated carbon electrodes on graphite current collectors in 0.1 M KCl electrolyte, obtained with a scan rate of 100 mV s^{-1}. The vertical grey line indicates the measured open circuit voltage, and the vertical orange lines indicate the theoretical potentials at which H_2 and O_2 evolution are expected to occur.

Figure 4.4 (c) [182]. Nonetheless, the peaks corresponding to these reactions are still clearly discernible at the positive and negative potential limits, showing that the 2.2 V range of this scan exceeds the MWV of such a cell. The OCP, measured to be 0.08 V, is illustrated with a grey vertical line; whilst orange vertical lines are used to indicate the expected onset of the HER in neutral electrolyte at -0.62 V, and the expected onset of the OER in neutral electrolyte at 0.61 V. The anodic current begins to increase steeply from around 0.65 ± 0.05 V, while the cathodic current begins to increase at -0.85 ± 0.05 V giving an expected MWV of the cell of 1.5 ± 0.07 V. As discussed in reference [182], such increases in current can be obscured at higher scan rates, and as such these measurements at 100 mV s^{-1} will be less accurate for observing the growth of Faradaic currents than the measurements at 2 mV s^{-1} and 20 mV s^{-1} used to investigate the AC electrodes in 6 M KOH. Nonetheless, this method may provide a useful initial rough estimate of MWV, and is advantageous as measurements can be performed and an estimate obtained in a matter of minutes.

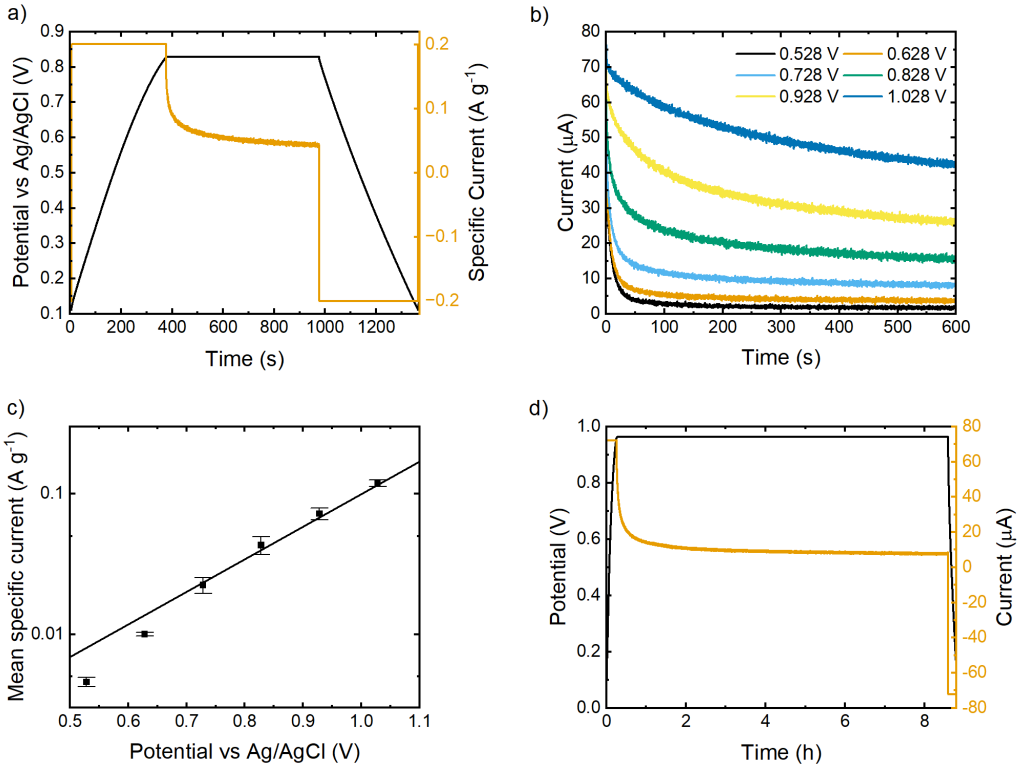

Figure 4.7: Data for potentiostatic analysis from activated carbon electrodes in 0.1 M KCl. a) example cycle: the charging specific current is 0.2 A g^{-1}, the cell is charged to 0.8 V (relative to Ag/AgCl), and held for 600 s. b) current response over 600 s as the dwell potential is varied from 0.5 V to 1.0 V vs Ag/AgCl. c) log plot of mean values of dwell current at 600 s plotted against working electrode potential. The mean is calculated from three consecutive cycles, and the standard deviation is given as an error. The grey line is a guide to the eye. d) example cycle in which dwell time is increased to 30,000 s.

4.2.2 Three-electrode potentiostatic analysis

A three-electrode potentiostatic analysis, as described Le Fevre *et al.* [162], was tested on a positively biased AC working electrode in 1 M KCl. A constant specific current of 0.2 A g^{-1} was used to charge the working electrode from the OCP to the test potential. The electrode was then held at this potential for 600 s and the current response measured, before the electrode was discharged to back to the OCP with a constant specific current of 0.2 A g^{-1} The change of current and potential over time for one cycle of this method are shown in Figure 4.7(a).

The change in current over 600 s for potentials from 0.528 V (below 0.61 V, which is the potential of the OER in neutral media) to 1.028 V is shown in of Figure 4.7 (b). In each case the decrease in current cannot be adequately fitted to either the exponential form of the RC equation (equation 2.26) or to the $1/\sqrt{t}$ form of the Cottrell equation (2.27). Also shown in Figure 4.7 (c) is a log plot of discharge I_{sp} at 600 s averaged over three consecutive cycles as a function of the test potential. It can be seen that the data becomes more linear at higher potentials, as illustrated by the grey line, having a shape similar to that given by the Butler-Volmer (equation 1.13) or Tafel (equation 1.12) equations. This transition occurs at around 0.73 ± 0.05 V, similar to the onset of the increase in anodic current shown in Figure 4.6. The OCP in this case was measured to be 0.128 V. If this value were fixed this would suggest a lower limit of the MWV of 1.2 ± 0.1 V for this cell.

The decay in current across all potentials is in disagreement with the trends observed by Le Fevre *et al.* and indeed elsewhere in the literature [162, 193]. Instead, they observe that at low potentials the current will initially drop to near zero and remain constant, but for higher potentials a subsequent increase in current is observed. Similar trends have been observed for glassy carbon in aqueous electrolytes, but at high voltages and over longer timescales of 1-2 hours [193]. To determine if the dwell time chosen for this experiment was insufficient to observe this behaviour, the electrode was held a high potential of 0.9 V vs Ag/AgCl for a high dwell time of 30,000 s. Even over this long dwell, no increase in current corresponding to oxidation was observed, as shown in Figure 4.7 (d).

4.2.3 Two-electrode CV and GCD

As discussed in Chapter 2, Section 2.2.1, although three-electrode tests are more useful for examining the behaviour of each electrode in isolation, two-electrode

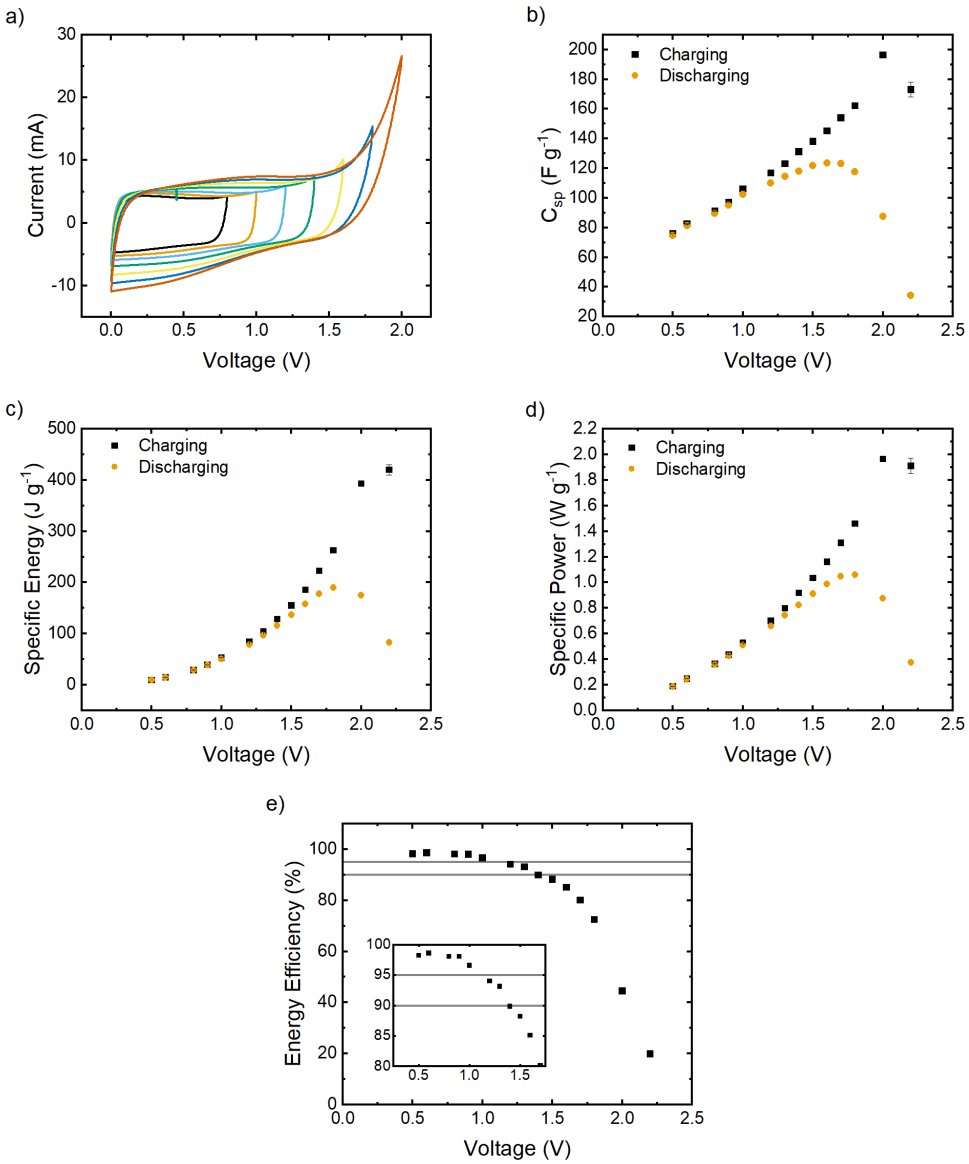

Figure 4.8: Two-electrode cyclic voltammetry data for activated carbon electrodes in 6 M KOH electrolyte measured at a voltage sweep rate of 10 mV s^{-1} as the upper potential limit is varied. Evolution of: a) voltammogram; b) charging and discharging specific capacitances; c) charging and discharging specific energy; d) charging and discharging specific power; e) energy efficiency, with 95% and 90% efficiencies indicated. In e) error bars are too small to be visible.

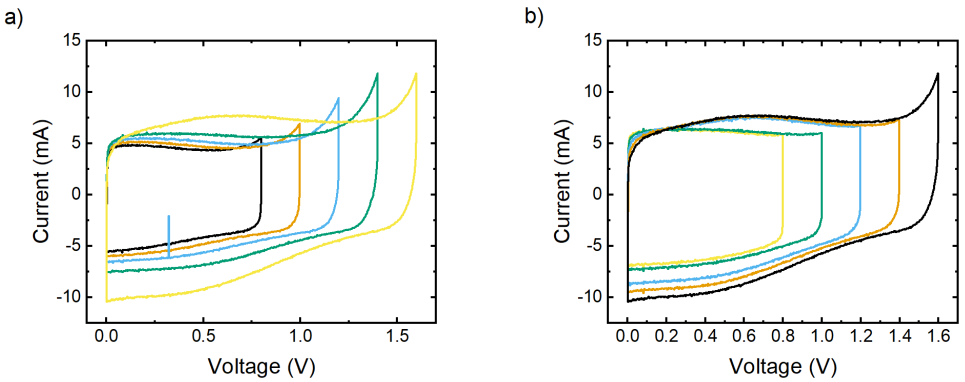

Figure 4.9: Two-electrode cyclic voltammograms for activated carbon electrodes in 6 M KOH at 10 mV s^{-1} as the upper potential limit is a) increased, and b) decreased.

tests more closely resemble the behaviour of 'real-world' devices. As such, a variety of two-electrode methods were also examined in order to investigate whether the MWV could be determined from two-electrode testing alone. This would be advantageous given that a two-electrode cell more closely resembles a real device, helping to understand how a given system would stand up to real-world usage. Two electrode CV and GCD are commonly used in the literature to determine the MWV of supercapacitor devices, often by visual inspection alone [50, 181–184]. In this section, this approach will be considered alongside more quantitative numerical analysis of the CV and GCD data.

Figure 4.8 shows CV data obtained at a voltage sweep rate of 10 mV s^{-1} for two-electrode stainless steel cells containing activated carbon electrodes in 6 M KOH electrolyte as the operating voltage is increased. The voltammograms are shown in Figure 4.8 (a); at high operating voltages these show a large tail at high voltages, but closer inspection of the low voltage voltammograms shows a small tail to be visible even there. The origin of this tail is poorly understood, but is likely to correspond to one or more of the following phenomena: oxidation/reduction of surface functional groups, water splitting, or the corrosion of the electrode materials/current collectors [172, 183, 194]. This increases relatively smoothly

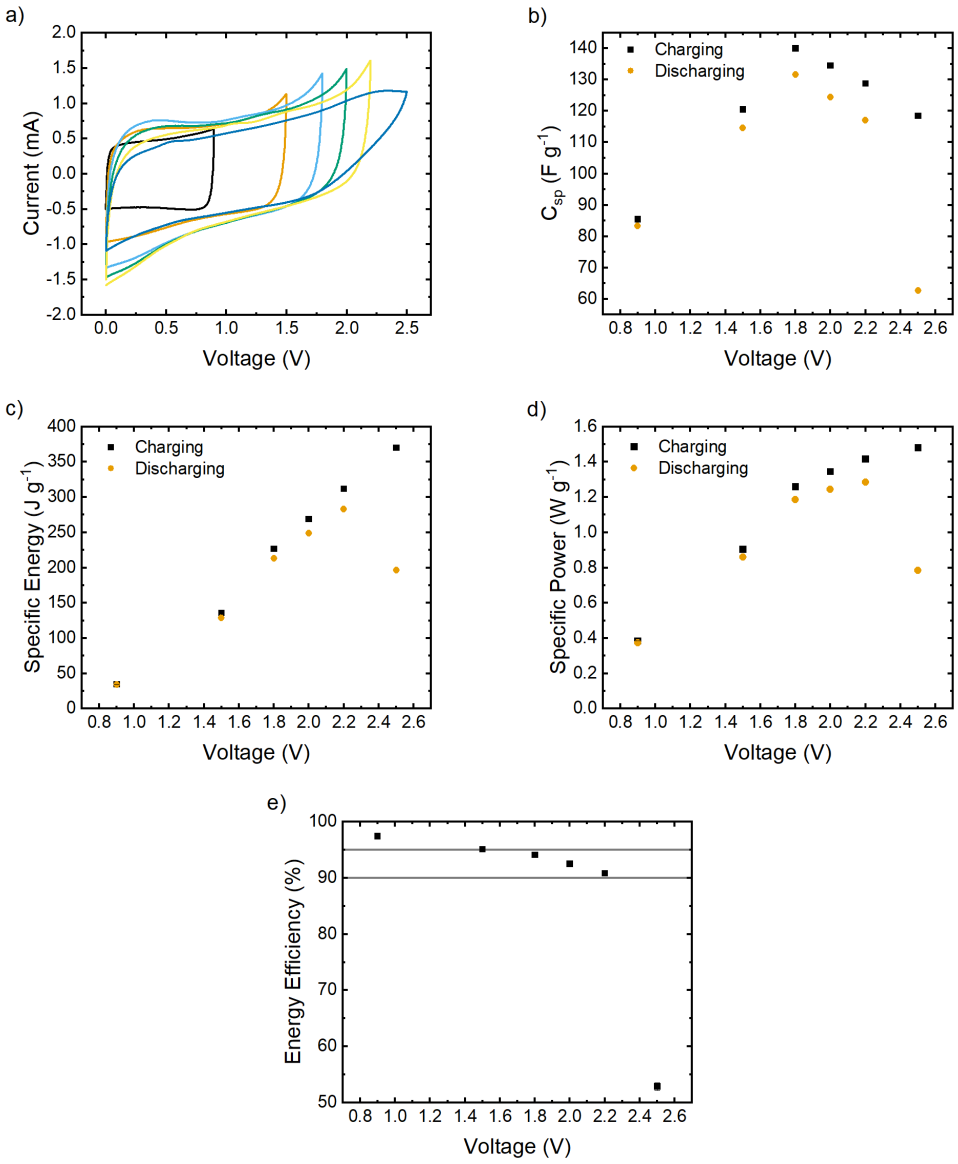

Figure 4.10: Two-electrode cyclic voltammetry data for activated carbon electrodes in 0.1 M KCl measured at a sweep rate of 10 mV s^{-1} as the upper potential limit is varied. Evolutions of: a) the voltammogram; b) charging and discharging specific capacitances; c) charging and discharging specific energy; d) charging and discharging specific power; e) energy efficiency, with 95% and 90% efficiencies indicated. In e) error bars are too small to be visible.

with increasing voltage, making it difficult to ascertain a maximum working voltage from visual inspection alone. Figures 4.8 (b,c,d) show the charging and discharging specific capacitance, energy and power, respectively, and how they vary with voltage. Up to 1.0 V the charging and discharging capacitances increase and remain very similar to one another, resulting in an energy efficiency of over 95%, as shown in Figure 4.8(e). Beyond this, they continue to increase, but begin to diverge from one another, indicating that a significant amount of charge is being lost. This leads to the energy efficiency falling below 90% by 1.4 V. The discharge capacity peaks at 1.6 V, perhaps indicating that the cell is beginning to degrade, and the charging capacitance decreases when the cell voltage is pushed to 2.0 V, indicating that the cell has been significantly degraded [173–175, 182].

This degradation of the cell at 2.0 V corresponds to the range over which significant specific currents (approx. 10 A g^{-1}) were observed on the positive and negative electrodes during three-electrode testing (Figure 4.4). Similar trends to this are observed in the energy and power inputs and outputs of the electrodes, however decreases in input/output energy and power are at a cell voltage 0.2 V higher. The initial increase in the capacitance, energy, and power at lower cell voltages may be attributed to steric effects, with ions both forming a more compact diffuse layer and more effectively filling the pores of the activated carbon at higher voltages [22, 173, 174]. Meanwhile, increases in capacitance at higher voltages may be pseudocapacitance due to Faradaic processes such as the adsorption and desorption of hydrogen (as was observed in Figure 4.4) [195, 196], or due to the oxidation of the material (as described in sections 4.1 and 4.2.1) leading to the formation of oxygen-containing SFGs which improve the wettability of the electrodes and contribute to pseudocapacitance, as was described in Chapter 1 section 1.6.2.1 [165, 174].

Figure 4.9 shows voltammograms from a similar experiment in which the working

voltage was stepped from 0.8 V to 1.6 V (Figure 4.9(a)), and then stepped back down to 0.8 V (Figure 4.9(b)). 1.6 V was selected as the maximum working voltage investigated in order to avoid damage to the electrodes. As with the data in Figure 4.8, a positive current tail is visible on all voltammograms, even at low working voltages. Analogous to the behaviour observed in Figure 4.4(d), and as has been noted elsewhere in the literature [183], this is not the case for the voltammograms recorded as the the MWV is decreased (shown in Figure 4.9 (b)). In that instance, no tail is observed at 1.2 V or below, and between 1.2 V and 1.6 V the positive current regions of the voltammograms are near identical. This is likely due to the same oxidative processes responsible for the evolution of the positive voltammograms shown in Figure 4.4.

Figure 4.10 shows CV data obtained at a voltage sweep rate 10 mV s^{-1} for two-electrode cells containing activated carbon electrodes in 0.1 M KCl electrolyte, and the evolution of these data with increasing operating voltage. As with the KOH, a small tail is seen on the voltammograms (Figure 4.10 (a)), even at low voltages. Interestingly, this is not observed when the cell is pushed to 2.5 V, leading to an immediate collapse in performance. The specific capacitance is shown in Figure 4.10 (b): unlike the data from cells with a 6 M KOH electrolyte (Figure 4.8) the C_{sp} values for both charging and discharging peak at 1.8 V. Meanwhile, unlike the capacitance, the input specific energy (Figure 4.10 (c)) and power (Figure 4.10 (d)) continue to increase with the cell voltage as the latter increases up to 2.5 V, while the output specific energy and power peak at a cell voltage of 2.2 V. These data would suggest that this cell can be operated to a slightly higher working voltage than a cell with the same electrodes and structure using a 6 M KOH electrolyte, which is corroborated by the energy efficiency (Figure 4.10 (e)) remaining above 95% to a cell voltage of approximately 1.5 V.

Figure 4.11 shows GCD profiles and parameters derived from them for a cell with

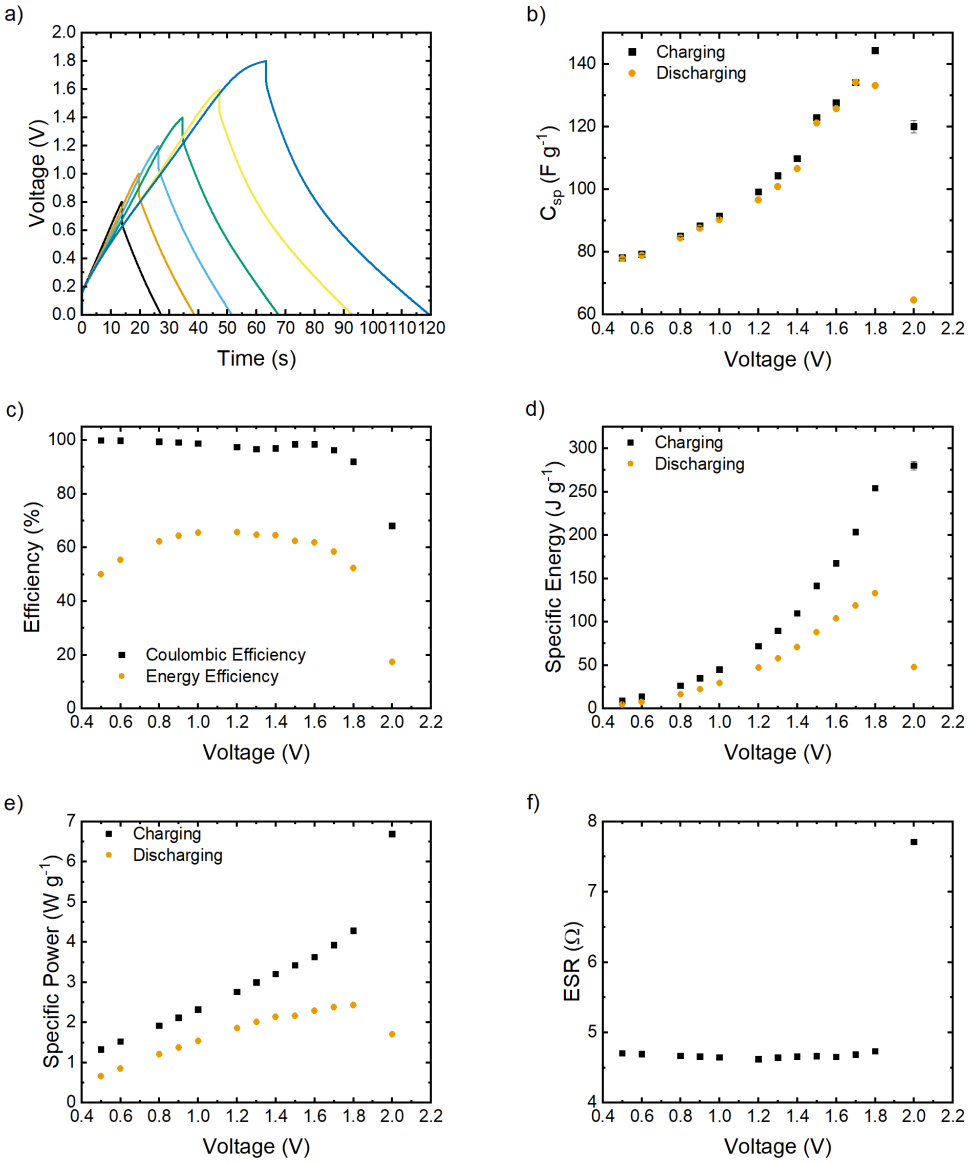

Figure 4.11: GCD data over a range of working voltages for AC electrodes in 6 M KOH in a stainless steel cell. a) GCD profiles, b)C_{sp}, c) Coulombic and energy efficiencies, d) specific energy, e) specific power, and f) ESR. Error bars are too small to be visible.

activated carbon electrodes in a 6 M KOH electrolyte measured over a range of operating voltages, with an applied current loading of 1 A g^{-1}. The GCD profiles (Figure 4.11 (a)) can be seen to flatten out towards the top, even at low working voltages. As with the tail seen in the CV data (Figures 4.8 and 4.9) this is often interpreted as a sign of the undesirable redox reactions which lead to cell damage [185, 186]. Similar to the CV-derived C_{sp}, the GCD-derived C_{sp} (Figure 4.11 (b)) is shown to increase up to a cell voltage of 1.8 V. However, unlike the CV data, the charging and discharging C_{sp} remain similar to one another, resulting in a high (>90%) Coulombic efficiency up to 1.8 V (Figure 4.11 (c)). This difference may occur due to the applied current during charging/discharging being ≈20 mA, more than double the ≈5-10 mA observed during CV, meaning that cycling would progress at a higher rate, which is known to obscure the Faradaic processes investigated here [182], hence reducing the loss in Coulombic efficiency. Figure 4.11 (d) shows the evolution of specific energy and Figure 4.11 (e) specific power, with increasing cell voltage. The charging specific energy and power increase across the entire range tested, while the discharging specific energy and power increase more slowly, and decline at cell voltages above 1.8 V. Examination of the energy efficiency in Figure 4.11 (c), shows an initial increase, as the energy losses are dominated by the Ohmic drop associated with the ESR, before peaking at a cell voltage of 1.2 V, and then falling off due to energy losses caused by an increasing rate of Faradaic reactions. The ESR is shown in Figure 4.11 (f) and shows very little change until sharply rising above a cell voltage of 1.8 V as the cell is degraded.

Figure 4.12 shows GCD profiles and parameters derived from them over the same range of voltages for activated carbon electrodes in Swagelok cells using a 0.1 M KCl electrolyte and graphite contacts. Similarly to the cells made using a 6 M KOH electrolyte, the GCD profiles for these cells show a flattening towards the top, which again may be indicative of Faradaic processes [185, 186]. The evolution of C_{sp} with working voltage is shown in Figure 4.12 (b); rather than

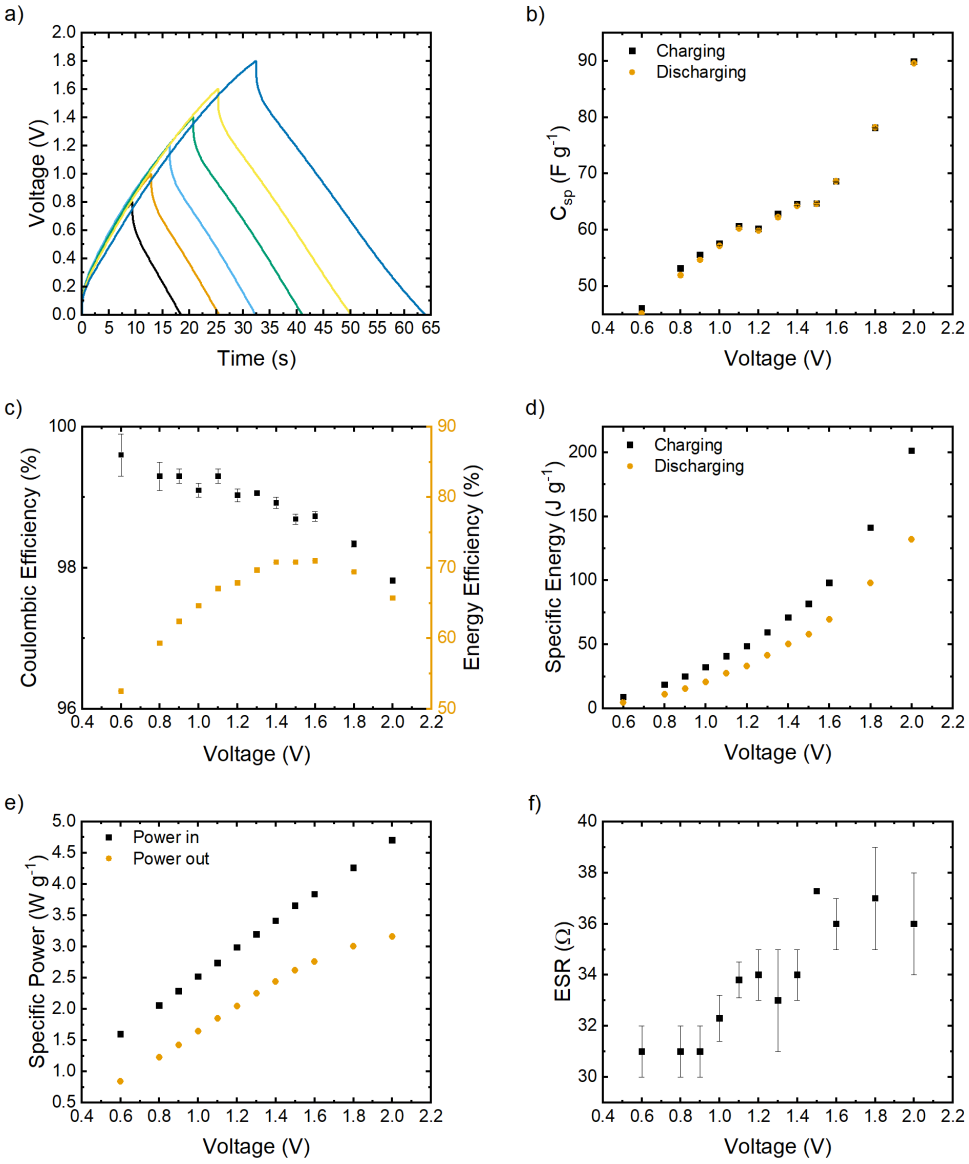

Figure 4.12: GCD data measured over a range of working voltages for AC electrodes in 0.1 M KCl in a Swagelok cells with graphite current collectors. a) GCD profiles, b) C_{sp}, c) Coulombic and energy efficiencies, d) specific energy, e) specific power, and f) ESR. Error bars are too small to be visible.

rising smoothly this appears to almost plateau between 1.2 V and 1.6 V before rising sharply to 2.0 V. Unlike the data obtained with 6 M KOH electrolyte, the charging and discharging capacitances remain close together, resulting in a high Coulombic efficiency ($> 97\%$) across the entire range of voltages investigated. It is worth noting that the Coulombic efficiency of cells using the 6 M KOH electrolyte only began to decrease significantly at cell voltages above 1.8 V, and as the two and three electrode CV data suggested that the MWV of the KCl should be approximately 200 mV greater than that of the KOH, a significant degradation in performance would not be expected until above 2.0 V. The evolution of specific energy and specific power with cell voltage are shown in Figure 4.12 (d,e). The input and output specific energy and power both appear to rise smoothly over the whole range investigated. Looking at the energy efficiency (shown in Figure 4.12 (c)), it can be seen to follow the same trend as in the cell using the 6 M KOH electrolyte, but with a peak at 1.6 V. The ESR is shown in Figure 4.12 (f); this shows the general trend of increasing with cell voltage, however the magnitude of these changes is not very large compared with the experimental uncertainties, making it hard to define a point at which the ESR definitively increases. It is worth noting that the differences in cell setup may account for some differences with the data from the cell containing 6 M KOH, for example the more resistive graphite contacts may account in part for the greater ESR observed, while the corrosion resistance of the graphite contacts and PTFE Swagelok cell body may account in part for the apparently higher MWV.

When considering the two electrode CV and GCD data as a whole it is clear that, despite being a common approach in the literature, visual inspection of the voltammograms and GCD profiles alone cannot reliably determine the MWV of the cell. In addition, the shape of the voltammogram and the voltage at which any tails become visible is largely dependent on scan rate, as is discussed in reference [182]. It is clear that of the parameters derived from CV and GCD data, many

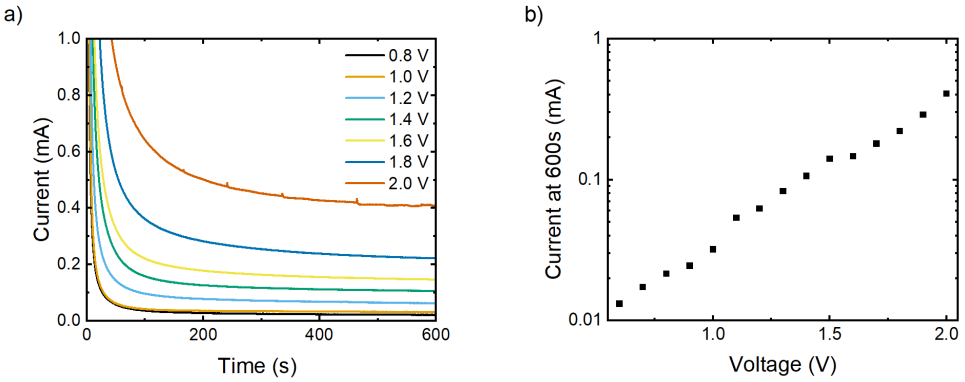

Figure 4.13: a) Single pulse chronoamperometry responses for a two electrode cell measured at pulse voltages between 0.8 V and 2.0 V. b) Current measured at 600 s after the end of the pulse for the same cell at a range of voltages between 0.6 and 2.0 V.

are unhelpful, even commonly-used metrics such as ESR and Coulombic efficiency [182]. The energy efficiency, conversely, shows promise: there is good (but not complete) agreement between the point at which 95% energy efficiency is observed in CV, and the peak energy efficiency in GCD (1.0 ± 0.08 V and 1.2 ± 0.08 V for the cells using 6 M KOH electrolyte, and 1.5 ± 0.2 V and 1.6 ± 0.05 V for cells using 0.1 M KCl electrolyte). These are also in good, but again imperfect, agreement with the MWV implied by the three-electrode CV data.

4.2.4 Two-electrode chronoamperometry

Two-electrode single-pulse chronoamperometry data for a cell using a 0.1 M KCl electrolyte are shown in Figure 4.13. As described in chapter 2, section 2.2.5, this technique involves applying a potential 'step' to the cell, from 0 V to the test voltage, and recording the resultant evolution of the current. This method was positively identified in the literature [175, 182] as a reliable method to identify the MWV of a cell through a sudden increase in dwell current once the MWV had been exceeded. The results shown in Figure 4.13 (a) are ostensibly similar to those in Figure 4.7 (b), with the current initially decaying rapidly, before beginning to level out. Moreover, at cell voltages of 0.8 V and 1.0 V the dwell currents are

of similar magnitude to one another, noticeably increasing voltages of 1.2 V and above. However, plotting the dwell current, measured at 600 s after the pulse, on a logarithmic axis against voltage (Figure 4.13 (b)) shows an approximately linear (i.e., exponential on a linear scale) increase across the entire voltage range tested with no discernible onset. This is in contrast to the Tafel-like behaviour shown in Figure 4.7 and in contrast to the behaviour shown in reference [175], where the dwell current increases exponentially due to non-Faradaic self discharge, before increasing super-exponentially as Faradaic processes begin.

4.2.5 Two-electrode electrochemical impedance spectroscopy

Figure 4.14 shows EIS data for a cell with 6 M KOH electrolyte using a constant (DC) voltage offset (V_{DC}) varying between 0.8 V and 2.0 V. Here and throughout the thesis, equivalent circuit models were not used in the analysis of EIS data, in part because of limitations in the software available, and in part the because of the difficulty of linking such models to physical processes in a cell [154, 157]. Instead, a more qualitative analysis was performed. All plots show that as V_{DC} varies the high frequency behaviour of the devices remains similar, but that significant variations open up in the low frequency region. At $V_{\mathrm{DC}} = 0.8$ V, the Nyquist plot, Figure 4.14 (a), shows behaviour approximating an ideal capacitor, with the low frequency data showing a slight curve (associated with charge transfer across the electrode-electrolyte interface [182]) rather than the vertical line indicative of ideal capacitive behaviour. This response is reflected in the 80° phase angle shown in the phase plot of Figure 4.14 (b), where a purely capcitive response would display a 90° phase angle. At low DC voltages, well within the stable window of water, this charge transfer might be linked to more benign processes, such as the initial oxidation of SFGs (as described in section 4.2.1). However, as V_{DC} is increased the curvature of the Nyquist plot increases and the peak phase decreases further, indicative of increased charge transfer, which may be due to an increasing rate of Faradaic processes. The inset of the phase plot (Figure 4.14) shows the

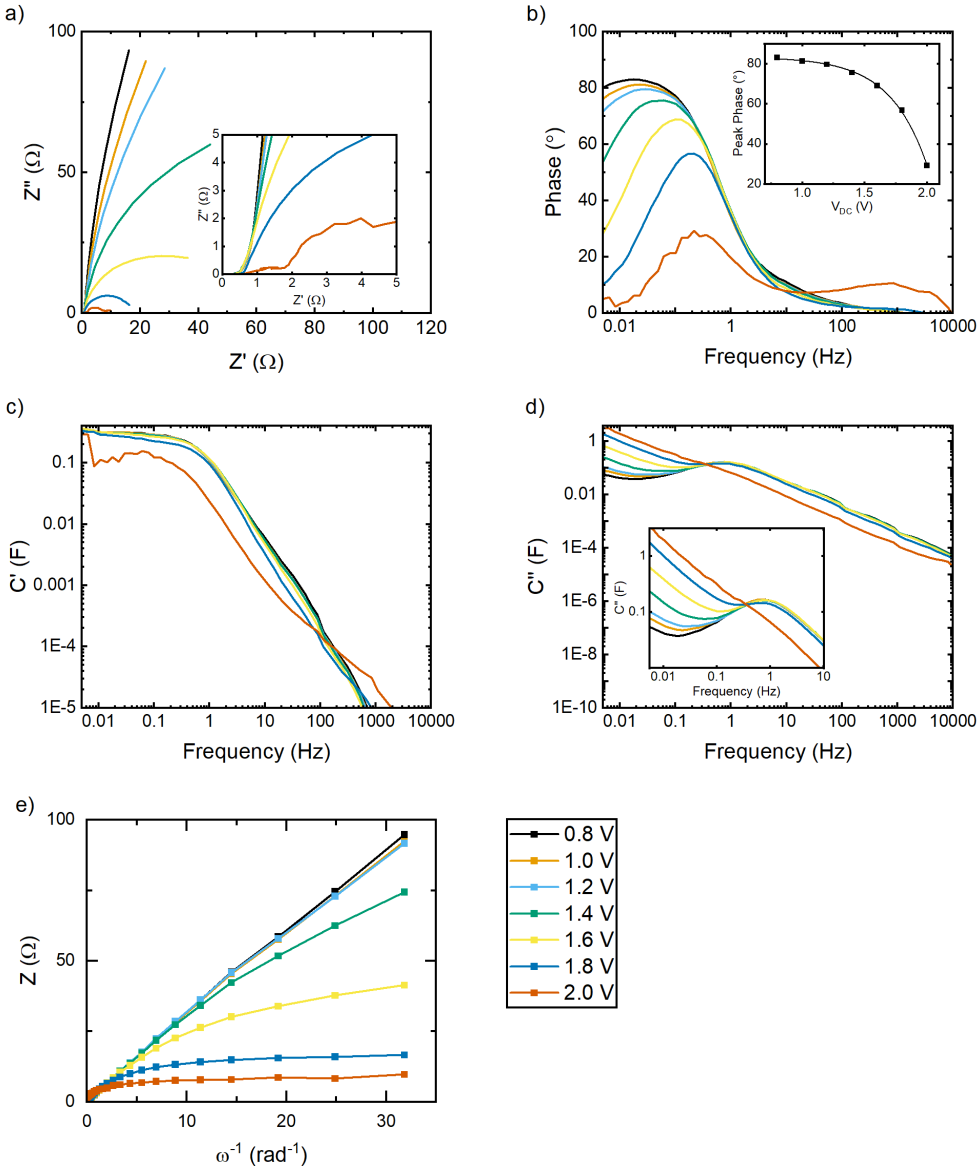

Figure 4.14: EIS data for activated carbon electrodes in a stainless steel test cell with 6 M KOH electrolyte for a range of DC voltages between 0.8 V and 2.0 V. a) Nyquist plots; b) phase plots; the c) real and d) imaginary parts of the complex capacitances (C' and C'', respectively); and e) Z plotted against ω^{-1}. Insets on the Nyquist and imaginary capacitance plots show the high and low frequency regions in greater detail, while the inset on the phase plot shows the evolution of the peak phase angle with V_{DC}. Error bars are too small to be seen.

evolution of the peak phase with increasing V_{DC}; the line shown is an exponential fit, showing that the peak phase varies with $V_0 - Ae^{\frac{V_{\mathrm{DC}}}{t}}$ (where $V_0 = 83.4 \pm 0.5$ V, $A = 0.06 \pm 0.02$, and $t = 0.30 \pm 0.01$ V^{-1}) in keeping with the exponential increase in Faradaic current observed in both cyclic voltammetry and chronoamperometry.

Considering the real part of the capacitance, C' (Figure 4.14 (c)), the behaviour of the device appears unchanged up to 2.0 V, plateauing at a capacitance of 0.34 ± 0.01 F, corresponding to a specific capacitance of 83 ± 3F g^{-1}. At 2.0 V the line becomes irregular, with large jumps in the real capacitance as ω is varied, which may indicate significant degradation of the device during the duration of the test. This constant capacitance suggests that the intrinsic capacitance of the device doesn't significantly vary with V_{DC}, and that the increases in capacitance seen in the CV and GCD tests may be due to Faradaic effects, which present in the EIS data as resistive rather than capacitive processes [197]. In contrast, the imaginary part of the capacitance (Figure 4.14 (d)), the low frequency region of which is shown as an inset, displays considerable evolution with V_{DC}. At $V_{\mathrm{DC}} = 0.8$ V there is a local maximum in C'' at approximately 1 Hz, followed by a local minimum and a small rise in C'' as the frequency decreases, indicating a pseudo-blocking electrode behaviour (i.e., no charge transfer at the electrode surface)[24]. As V_{DC} increases, the increase in C'' at low frequencies develops, until at $V_{\mathrm{DC}} = 1.4$ V, the imaginary capacitance exceeds the real capacitance, indicating that the electrodes are becoming reactive (Faradaic) rather than blocking [24]. Above $V_{\mathrm{DC}} = 1.6$ V, the local maximum and minimum vanish, with the electrodes instead showing an increase in C'' with decreasing f across the whole frequency range examined.

Figure 4.14 (e) shows the magnitude of the complex impedance (Z), plotted against the reciprocal of the angular frequency (ω^{-1}). For an ideal capacitor this should be a straight line, with the gradient of the line being the reciprocal of the

capacitance. For DC voltages up to $V_{\mathrm{DC}} = 1.2$ V such a linear relationship is observed, with an almost constant slope, corresponding to $C_{\mathrm{sp}} = 80.5 \pm 0.2$ F g^{-1} at 0.8 V, and 82.2 ± 0.2 F g^{-1} at 1.0 V and 1.2 V. This supports the assertion that the double layer capacitance does not significantly increase with V_{DC} in this range. As V_{DC} is increased further the data diverge from linear behvaiour, tending towards a horizontal plateau, as observed at and above $V_{\mathrm{DC}} = 1.8$ V, indicating that Faradaic behaviour dominates the device response. These observations suggest a MWV for this cell of 1.2 V, reflecting the limit of capacitor-like behaviour, and is broadly in agreement with the values of MWV derived from the methods described above.

Figure 4.15 shows EIS data for a cell with 0.1 M KCl electrolyte. As would be expected the Nyquist plot Figure 4.15 (a), and phase plot Figure 4.15 (b) show the same trends of decreasing capacitive and increasing reactive behaviour. However, unlike cells with 6 M KOH electrolyte, the peak phase does not vary according to $V_0 - Ae^{\frac{V_{\mathrm{DC}}}{t}}$, and instead decays proportionally to $V_0 + Ae^{-\frac{V_{\mathrm{DC}}}{t}}$ (where $V_0 = 49 \pm 3$ V, $A = 56 \pm 1$, and $t = 1.1 \pm 0.2$ V^{-1}) up to $V_{\mathrm{DC}} = 1.8$ V, where it falls off sharply. Again, like the cells with KOH electrolyte, the real part of the capacitance Figure 4.15 (c) shows little change with increasing V_{DC}, while the imaginary part of the capacitance Figure 4.15 (d) shows the same transition from pseudo-blocking to reactive behaviour as observed for the KOH electrolyte, Figure 4.14 (d).

The variation of the magnitude of impedance, Z,with ω^{-1} Figure 4.15 (e) does not conform to the trends observed for the cell with 6 M KOH electrolyte, Figure 4.14 (e). Whilst there is an approximately linear relationship present at $V_{\mathrm{DC}} = 0.8$ V, the data begin to show a curvature as V_{DC} is increased to 1.0 V. Then, for V_{DC} between 1.2 V and 1.8 V the behaviour shows little change: interestingly, this corresponds to the same region in which the GCD-derived capacitance appeared to plateau. When V_{DC} is increased to 2.0 V, the line again increases in curvature,

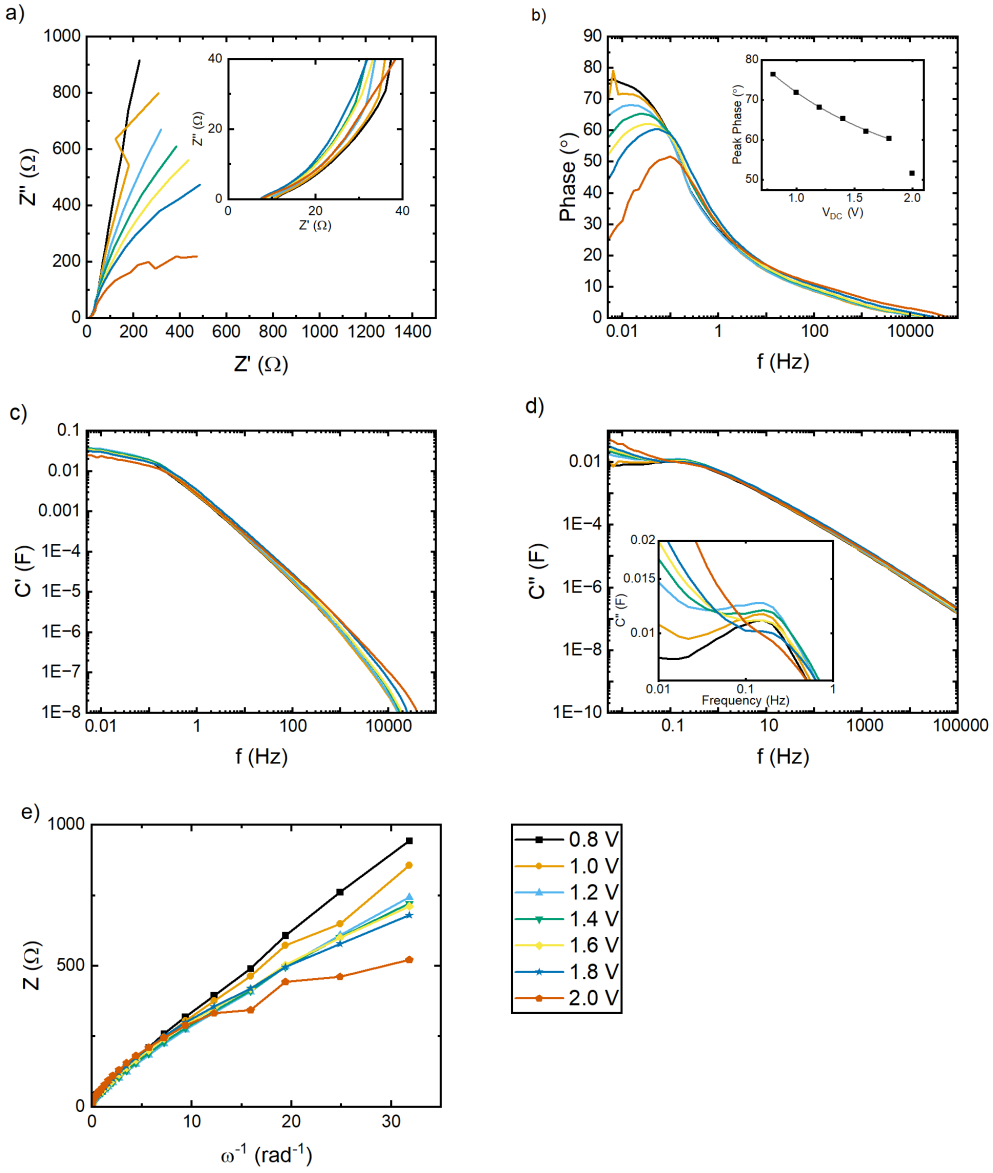

Figure 4.15: EIS data for AC electrodes obtained using a Swagelok test cell with graphite current collectors and 0.1 M KCl electrolyte for a range of DC voltages between 0.8 V and 2.0 V. a) Nyquist plots; b) phase plots; the c) real and d) imaginary parts of the complex capacitances (C' and C'', respectively); e) impedance, Z, plotted against ω^{-1}. Insets on the Nyquist plot and that of the imaginary part of the capacitance show the high and low frequency regions in greater detail, while the inset on the phase plot shows the evolution of the peak phase angle with V_{DC}. Error bars are too small to be seen.

although not to the same extent as is observed in cells with 6 M KOH electrolyte. From this data, there is no clear way to determine the MWV of the cell, suggesting that although the plot in Figure 4.14 (e) allowed the MWV of the cell with KOH electrolyte to be approximately determined, this result is not generalisable. This difference may arise in part due to a degree of Faradaic charge storage on the AC electrodes when 0.1 M KCl is used as an electrolyte. Looking back to the three electrode CV data shown in Figure 4.6, redox peaks indicative of a reversible reaction are visible at 0.2 V and 0.4 V. Although more prominent when the electrodes were pushed to greater polarities, they are still present within the suggested stable range of the electrodes. These peaks may be linked to the redox activity of the SFGs on the AC, discussed in Chapter 1, section 1.6.2.1. As these occur beyond the stable limits of the electrodes (≈1 V) when operating in 6 M KOH, they are not observed for those devices, but are observed in neutral and acidic electrolytes [198]. If this latter explanation is the case, it may mean that EIS cannot easily be used for measuring the MWV of activated carbon electrodes in neutral or acidic electrolytes, and may not be transferable to other electrode compositions with a high degree of Faradaic charge storage [186].

4.2.6 Chronopotentiometry

Figure 4.16 shows the results of a chronopotentiometry experiment for activated carbon electrodes measured in a stainless steel test cell with 6 M KOH electrolyte. This involved applying a constant current to the cell and measuring the evolution of the cell voltage with time. The cell voltage is plotted against charge inserted in Figure 4.16 (a), and the maximum voltage observed at each specific current is plotted in Figure 4.16 (b). Cyclic voltammetry was performed over a narrow range of 0.5 V. This range was chosen so as to be not only within the 'safe' range of operation of the device, but also to be below the voltages reached during testing, preventing the CV tests from affecting the results of the chronopotentiometry. CV was performed at a scan rate of 10 mV s^{-1} for 10 cycles before and after each test;

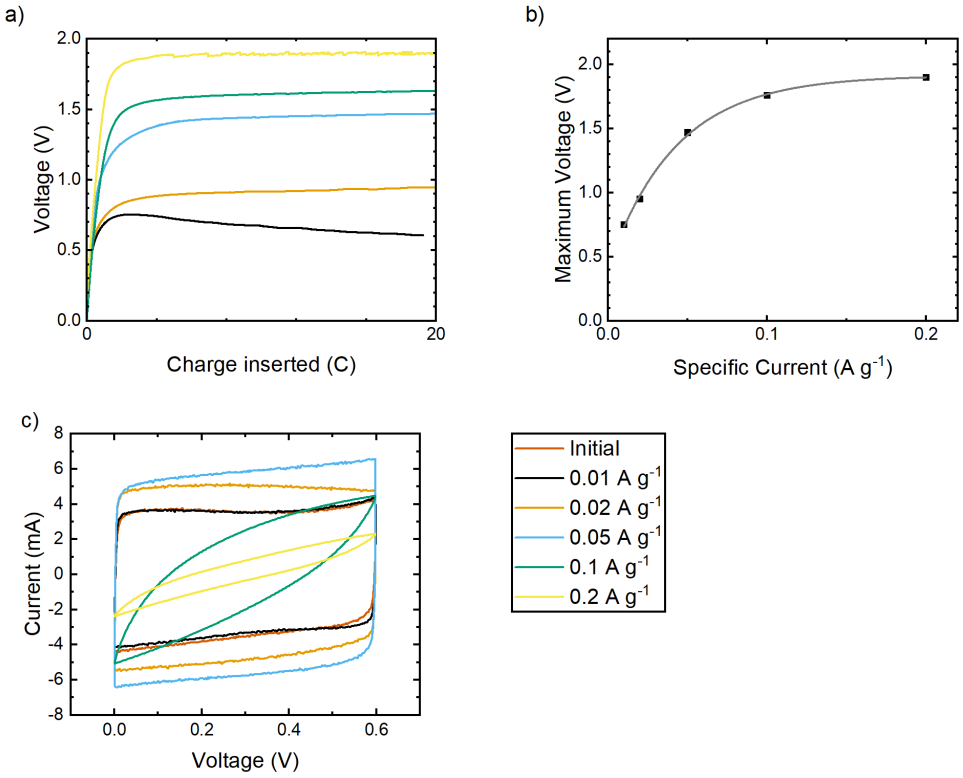

Figure 4.16: Chronopotentiometry data for activated carbon electrodes in 6 M KOH using a stainless steel cell: a) evolution of voltage against charge inserted for different values of specific current; b) maximum voltage observed during each measurement against specific current applied; c) cyclic voltammograms produced using a sweep rate of 10 mV s^{-1} measured before the chronopotentiometry and then after each test. The line in (b) is an exponential function fitted to the data.

the 10th cycle of each is presented in Figure 4.16(c).

At the lowest specific current, I_{sp}, of 0.01 A g^{-1}, the cell is able to charge to a voltage of 0.75 V, but after this the voltage decreases. This may be due to some degree of oxidation or similar changes to surface chemistry which can occur at low voltages (as discussed in section 4.2.1), but from the voltammograms presented in Figure 4.16 (c) this test appears to have little to no impact on the cell performance. As the specific specific current applied to the cell is increased the cell voltage plateaus at sucessively higher voltages. Plotting the maximum cell voltage against specific current Figure 4.16 (b) gives an approximate exponential variation of the form $V_0 - Ae^{-\frac{I_{sp}}{t}}$ (where $V_0 = 1.91 \pm 0.03$ V, $A = 1.49 \pm 0.05$, and

$t = 0.043 \pm 0.004$ V^{-1}), indicated by the grey fit line, in keeping with the trend that would be expected for both Faradaic and non-Faradaic leakage currents. After testing at $I_{sp} = 0.02$ A g^{-1} and 0.05 A g^{-1}, at which the cell is charged to voltages above 0.9 V and 1.4 V, respectively, the CV curve shows that the capacitance of the cell increases, as was observed in the CV and GCD data discussed in section 4.2.3. After the test at $I_{sp} = 0.1$ A g^{-1}, during which the cell charged to a voltage beyond 1.6 V, the shape of the voltammogram suggested a significant increase in ESR, indicating that the cell is degraded under these conditions. After the test at $I_{sp} = 0.2$ A g^{-1}, during which the cell voltage reaches 1.9 V, this degradation is even more severe. During this test the voltage signal is observed to become noisy, which may be indicative of significant gas evolution and corrosion of the electrodes, leading to the formation of bubbles on the electrode surface, the dissipation of which may cause jumps in voltage. These tests indicate an upper limit on the MWV of 1.4 V, which is higher than the limit of around 1.0 V-1.2 V suggested by the two-electrode and three-electrode methods examined above (sections 4.2.1, 4.2.3, and 4.2.5), which may be in part because this is in effect a short term voltage-hold method, and is therefore only sensitive to short term, more aggressive failure modes which manifest themselves at higher cell voltage.

4.2.7 Cycle life

The most reliable ways to test the MWV of a device are to either subject it to a high number of GCD cycles, or to hold it at the test voltage for several hundred hours whilst periodically testing the performance. Although the voltage-hold method is often considered to be more time efficient and effective [174, 180], it was found to be impractical with the laboratory resources available. In this work 5,000 GCD cycles were used instead, which had the advantage of allowing the performance to be monitored on a cycle-by-cycle basis. The relative change in discharge capacity

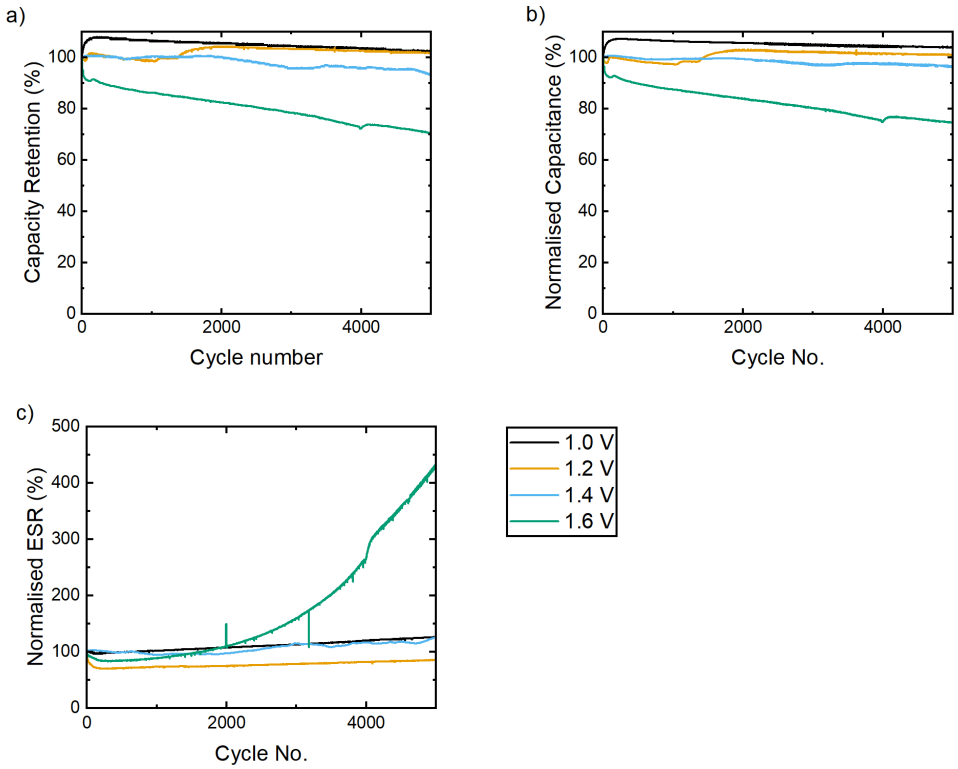

Figure 4.17: Performance of two electrode cells with steel current collectors and 6 M KOH electrolyte, after 5,000 GCD cycles at 1 A g^{-1} over a range of working cell voltages. a) Discharge capacity retention; b) normalised discharge specific capacitance; and c) normalised ESR. All values are shown as a percentage of the first cycle.

for 5,000 GCD cycles at 1 A g^{-1} of cells with a 6 M KOH electrolyte was measured at cell voltages of 1.0 V, 1.2 V, 1.4 V, and 1.6 V and is shown in Figure 4.17 (a). At cell voltages of 1.0 V and 1.2 V the discharge capacity increases to 102% of the initial value, while at cell voltages of 1.4 V and 1.6 V it falls to 93% and 71% of the intial value, respectively. As described in the introduction, failure for a supercapacitor is usually understood as being a 20% loss of capacitance or a doubling of ESR over 1,000 hours of operation [35, 174, 177, 178]. The 5,000 GCD cycles only took approximately 100 hours, so in this instance failure was taken to be *any* measurable decrease in capacity, showing the MWV to be 1.2 V, which is in good agreement with the conclusions drawn from several of the techniques presented above. Indeed, assuming a constant rate of electrode degradation, we would expect that over an approximately 10× greater cycle time that the capacity

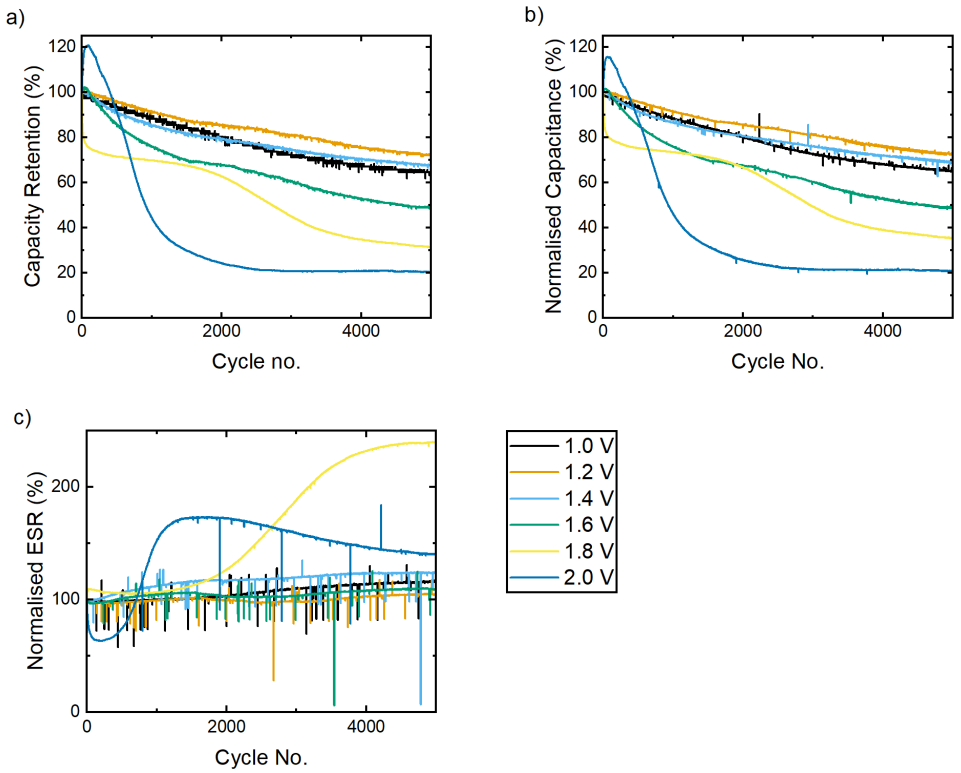

Figure 4.18: Evolution in performance over 5000 GCD cycles at 1 A g^{-1} for AC electrodes in 0.1 M KCl in swagelok cells with graphite current collectors. a) Discharge capacity retention; b) normalised discharge capacitance; c) normalised ESR. The origin of the experimental noise in this data is unknown and is likely to originate from the environment.

using a cell voltage of 1.4 V would reduce to $(93\%)^{10} = 48.4\%$, a loss in performance significantly in excess of 20%.

In order to better understand the changes in capacity, the changes in discharge capacitance and ESR are shown in Figure 4.17 (b) and (c). Similar to the discharge capacity, the capacitance shows no decrease over 5,000 cycles at cell voltages of 1.0 V and 1.2 V, but decreases to 96% and 75% of the initial value when cycled to cell voltages of 1.4 V and 1.6 V. The ESR was found to increase by 25% at cell voltages of 1.0 V and 1.4 V and to decrease by 25% at 1.2 V, before increasing to 431% of the initial value at a cell voltage of 1.6 V. This may suggest that different corrosion processes are occurring when the cell voltage is at 1.4 V compared with 1.6 V, with the increase in ESR at 1.6 V possibly being due to corrosion of the

stainless steel contacts, or a worsening of the contact between the electrodes and contacts due to gas evolution [173–175].

Figure 4.18 contains corresponding data for cells using a 0.1 M KCl electrolyte. Even at the lowest cell voltage of 1.0 V the cell fails, losing around 30% of discharge capacity, within 5,000 cycles. However, the rate of degradation at cell voltages of 1.2 V and 1.4 V proceeds at the same rate, suggesting that this loss of capacity is inherent to the device independent of voltage. As the cell voltage is increased beyond 1.4 V, the capacity loss increases to 50%, 70% and 80% at 1.6 V, 1.8 V, and 2.0 V, respectively, suggesting the MWV of cells with 0.1 M KCl electrolyte to be 1.4 V. This value is in approximate agreement with the MWV derived from the three-electrode data, but lower than that implied by the Coulombic and energy efficiencies of the two-electrode CV and GCD data, demonstrating that aging tests are necessary to confirm the MWV of a cell. The normalised discharge capacitance Figure 4.18 (b) shows similar trends to the capacity. The ESR, Figure 4.18 (c), does not show any significant increase with cycling until a cell voltage of 1.8 V. As with the cells with KOH electrolyte, this is 0.2 V greater than the voltage at which the capacity and C_{sp} are observed to degrade.

4.3 Conclusions

This chapter has examined various approaches to determine the MWV of aqueous EDLCs, comparing short-term approaches with longer-term GCD cycling. Three-electrode cyclic voltammetry with a low scan rate of 2 mV s^{-1} was found to be accurate for determining the onset of irreversible Faradaic processes at each electrode, provided an appropriate cut-off value of specific current is used. Despite the evolution of the electrochemical behaviour of the electrodes with cycling, it was still found that the initial cycles could provide a good estimate of the MWV. A three-electrode chronoamperometric method was also examined, and shown to

potentially give similar information on the onset of irreversible Faradaic processes.

A variety of two electrode techniques were also investigated. Although visual inspection of CV curves has been shown to be inadequate, the energy efficiency from CV data was examined and found to give good estimates of the MWV, though not in exact agreement with the results of long-term GCD cycling. Similarly, although the Coulombic efficiency derived from short-term GCD cycling proved not to be useful, the energy efficiency showed a peak where both energy losses due to Ohmic dissipation arising from the ESR of the cell and energy losses due to irreversible Faradaic processes were minimised. This again was in reasonable, but not exact, agreement with the results of long-term GCD cycling.

The use of two-electrode chronoamperometry, chronopotentiometry, and EIS was also investigated. Chronoamperometry and chronopotentiometry were found to be of little use, with both showing an approximately exponential relationship between dwell current and cell voltage. In the case of cells employing a 6 M KOH electrolyte, EIS appeared to be useful showing significant changes in the Nyquist and $Z - \omega^{-1}$ plots once the MWV of 1.2 V was exceeded, however these trends did not prove transferable to the cells with 0.1 M KCl electrolyte. This may have been due to the redox activity of SFGs occurring outside of the operating window of alkaline electrolytes but within the operating window of neutral or acidic electrolytes, which would prevent EIS from being easily used to determine the MWV of neutral or acidic systems, or of more strongly redox-active electrodes [198].

In conclusion, two electrode techniques of CV, GCD, and EIS can provide rough indications of the MWV of a device but they are far from exact. The suggested best practice for rapid evaluation of MWV would be instead to estimate it from three-electrode techniques, preferentially CV, and to verify exact values with long term GCD cycling, or accelerated aging, if practical.

Chapter 5

Few-layer graphene as a conductive additive for aqueous supercapacitors

5.1 Introduction

As discussed in Chapter 1, activated carbon (AC) is widely used as an electrode material for electric double layer capacitors (EDLCs) due to its low cost, high specific surface area (SSA), and controlled hierarchical pore size distribution, which allows for high specific capacitances [12, 39, 199]. Unfortunately, without the inclusion of a conductive additive, activated carbon electrodes are excessively resistive, leading to poor measured capacitance at higher charge/discharge rates and limiting the maximum power output of the device [11]. Carbon black (CB) is widely used as a conductive additive, which helps to substantially improve electrode conductivity. However, its low specific capacitance (C_{sp}) compared to activated carbon means that its inclusion reduces the overall C_{sp} of an electrode.

A variety of carbon materials including carbon nanotubes (CNTs), carbon fibres, expanded graphite, carbon onions, and graphene materials have been investigated

as alternatives [43, 200–202]. Wang *et al.* [200], for example, compared multiwall carbon nanotubes (MWCNTs), vapour grown carbon fibres (VGCF), and CB in AC electrodes with 5 wt% polytetrafluoroethylene (PTFE) binder, in 1.0 M $LiClO_4$/ethylene carbonate–diethyl carbonate electrolyte. In this instance MWCNTs were found to perform best at 5 wt%, VGCF at 7 wt%, and CB at 9 wt% loading. For all concentrations the performance of the MWCNTs exceeded that of the VGCFs which in turn exceeded the CBs.

A contrasting approach was taken by Kiseleva *et al.* [201], who investigated using single wall carbon nanotubes (SWCNTs) as both a binder and conductive additive for activated carbon-based electrodes. Using an acetonitrile (ACN) electrolyte, it was found that electrodes containing only 0.005 wt% SWCNTs had a comparable C_{sp} (123 F g^{-1}) and ESR (0.18 Ω) to AC electrodes containing 10 wt% CB and 8 wt% PTFE binder (122 F g^{-1} and 0.18 Ω) and performance improved further as the proportion of SWCNTs was increased to 0.012 wt% (152 F g^{-1} and 0.13 Ω).

Jäckel *et al.* examined an alternative form of nanostructured carbon – carbon onions – as additives. These are essentially concentric fullerenes, having smaller particle sizes ($<$ 10 nm) and higher SSAs ($>$ 300 m^2 g^{-1}), than more commonly used carbon blacks (30 - 50 nm and $<$ 100 m^2 g^{-1}). When tested in an ACN-based electrolyte, AC electrodes containing carbon onions at the optimum concentration of 5 wt% showed a drop in C_{sp} only by around 10 % (from 103 F g^{-1}) as specific current density increased from 0.1 to 10 A g^{-1}. Overall, this was similar to the performance observed when using CB as an additive tested under the same conditions (102 F g^{-1} and a 12 % capacitance loss) [202].

Of all these materials, carbon nanotubes were shown to offer the best performance compared to CB [200, 201]. They are, however, unsuitable as a replacement for CB, due to both their high cost and serious concerns surrounding the risks they

pose to human health [71], as discussed in chapter 1.

It has also been shown that in selecting a conductive additive it is important to consider more than just conductivity and surface area. Pandolfo *et al.* studied the role of the conductive additive in more detail, comparing CB to micrographite flakes [43]. It was found that CB has a resistivity similar to activated carbon (approximately 40 mΩ cm), four times that of the the graphite flakes. In spite of this, the CB was found to be a superior conductive additive. This was attributed to the structure of the CB, which consists of agglomerations of small ($\approx$20 nm) particles, allowing it to more effectively fill voids and improve conductivity between activated carbon particles, indicating the importance of the dimensions and structure of the additive.

This consideration is illustrated further in a study by Jäckel *et al.* [203], comparing three different CBs: high SSA Cabot BP2000, medium SSA Ensaco 350, and lower SSA Timcal Super C65. These were added in varying quantities to electrodes made with two different activated carbons: YP-50F and YP-80F, both steam-activated and derived from coconut. The first had a lower SSA (1681 m^2 g^{-1}) and smaller pore radius (0.9 nm), than the other (2347 m^2 g^{-1} and 1.6 nm, respectively). These were formed into electrodes with 5 wt% PTFE binder and tested in an electrolyte of 1 M TEA BF_4 in ACN. Electrodes made from the two activated carbons without any additives had similar sheet resistances, but the effect of adding conductive additive varied not just between the three CBs but also between the two ACs. All three CBs strongly decreased sheet resistance of the electrodes made with YP-50F at low concentrations (2.5 wt%), but had less of an effect on those made with YP-80F . The highest capacitance (87 F g^{-1}) was measured for the YP-50F with 2.5 wt% Ensaco 350, however for the YP-80F this composition saw a decrease in capacitance, with the highest value instead being observed for 5 wt% Cabot BP2000. These differences in performance were

suggested to arise due to differences in pore structure between the two ACs (YP-50F having slit-like pores, while YP-80F has branching, hierarchical pores) and their interactions with the different particle sizes and morphologies of the CBs.

The high conductivity and specific surface area of graphene has made it a promising material for EDLCs [204]. When used as a stand alone electrode material, performance is limited by restacking of the graphene sheets, reducing available surface area. However, graphene materials have potential as conductive additives, and have been explored as such in the past. For example, Wang *et al.* [205] investigated commercially available few-layer graphene as a conductive additive in conjunction with a graphene coated current collector in 6 M KOH aqueous electrolyte. An AC electrode with 5 wt% graphene additive was found to have a superior specific capacitance of 123 F g^{-1} compared to 96 F g^{-1} for 10 wt% CB. Beyond 5 wt%, EIS data suggested that the graphene increased the electrolyte diffusion resistance of the electrodes, limiting performance slightly.

Niu *et al.* [206] investigated graphene quantum dots (GQDs) as a conductive additive. GQDs consist of few ($\lesssim 10$) layer graphene with a particle size below 100 nm. The electrodes tested were based on AC with 8 wt% PTFE binder, and were characterised in a PC-based electrolyte. Electrodes less than 5 wt% GQD were found to perform better, with higher C_{sp} (110 F g^{-1} from GCD at 0.1 A g^{-1}) and better rate capability than 10 wt% CB (100 F g^{-1} in the same conditions), with performance being optimised at 1 wt% GQD.

Xu *et al.* [82] investigated using reduced graphene oxide (rGO) as a binder and conductive additive. AC electrodes containing 20 wt% rGO were compared with reference AC electrodes containing 10 wt% PTFE and 10 wt% CB. The AC + rGO electrodes were found to have a greater surface area and greater micro-porosity than the conventional electrodes, and almost double the conductivity

(0.337 S cm^{-1} compared with 0.177 S cm^{-1}). When tested in 6 M KOH, this led to a 25 % increase in capacitance (from 251 F g^{-1} to 321 F g^{-1} at a current density 0.5 A g^{-1}), and a superior rate capability, retaining 70 % capacitance at 50 A g^{-1} compared with 58 % for conventional electrodes.

In this chapter, few-layer graphene (FLG) platelets, produced by high-shear exfoliation [74] into an aqueous suspension stabilised by a surfactant [99, 100] are explored as a conductive additive for AC EDLC electrodes. As detailed in chapter 1, the use of water, rather than organic solvents as the liquid phase makes this an environmentally friendly approach to produce FLG, and furthermore avoiding the dangerous chemicals used in the production of rGO [82], makes FLG produced by this method an attractive material for use in supercapacitor applications [101].

5.2 Results

5.2.1 Material Characterisation

Sample	SSA (m^2 g^{-1})	V_{total} (cm^3 g^{-1})	D_{av} (nm)
Activated Carbon	870	0.73	3.4
Few-layer graphene	13	0.141	44

Table 5.1: Specific surface area (SSA), pore volume (V_{total}), and average pore diameter (D_{av}) for the activated carbon and FLG materials.

The SSA and pore size distributions (PSD) of the AC and FLG used to construct the EDLC electrodes were determined from N_2 adsorption/desorption isotherms shown in Figure 5.1, and are reported in table 5.1. The AC displays a type IV isotherm (Figure 5.1 (a)), indicative of a hierarchical pore structure. The significant intake of N_2 at low pressures corresponds to capillary condensation and consequently indicates the presence of micropores, while the high-pressure hysteresis loop is indicative of mesoporosity [207]. The FLG sample (Figure 5.1

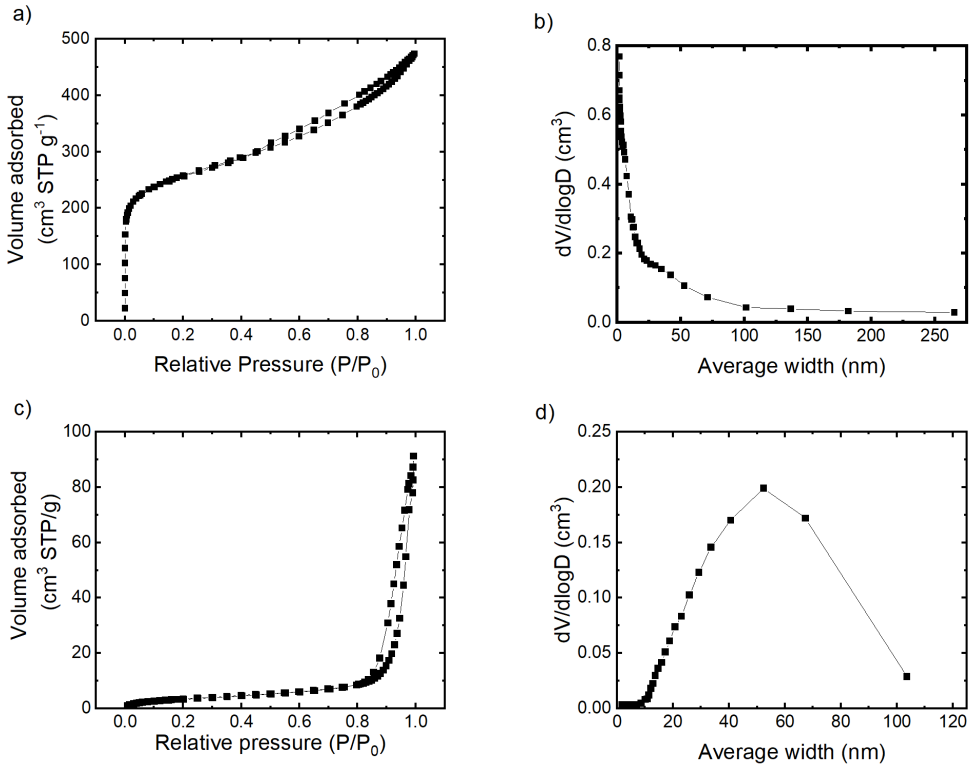

Figure 5.1: a) Nitrogen adsorption isotherm of the activated carbon; b) Pore size distribution of the activated carbon; c) Nitrogen adsorption isotherm of the few layer graphene electrodes; d) Pore size distribution of the few layer graphene electrodes

(c)) also shows a type IV isotherm, however the low intake of N_2 at low pressures indicates a purely mesoporous pore structure with an absence of microporosity. The SSA of the activated carbon is in the typical range observed for such a material [47]. However the measured SSA of the FLG, obtained from a vacuum filtered film, is much smaller than that which would be expected from isolated FLG platelets, and is indicative of considerable re-stacking of the platelets in the absence of any external 'scaffold'. This is reflected in the cross sectional SEM micrographs shown in Figure 5.2.

Size (planar area) distributions of the FLG platelets are given by the histograms in Figure 5.3 (a, c, e). These were determined from backscattered electron SEM images; typical examples of these for each of the three FLG materials are shown

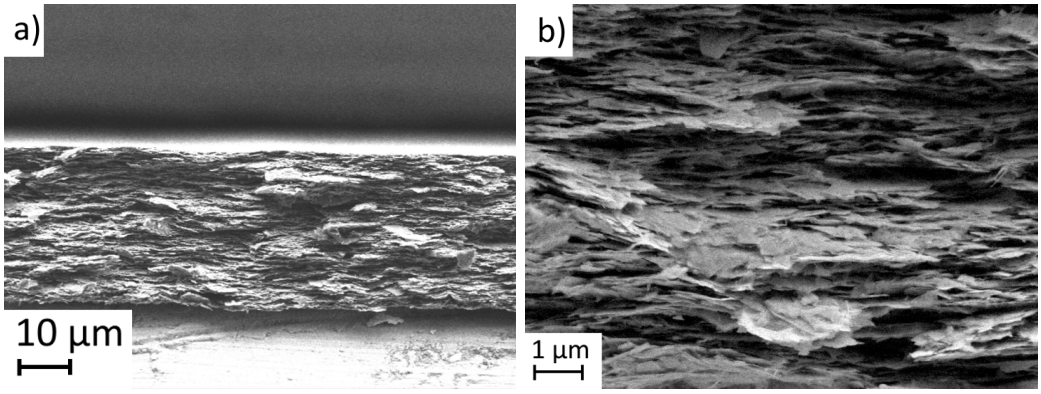

Figure 5.2: a) cross sectional SEM image of moderately centrifuged FLG electrode; b) higher magnification image of the same, showing restacking of FLG platelets in greater detail.

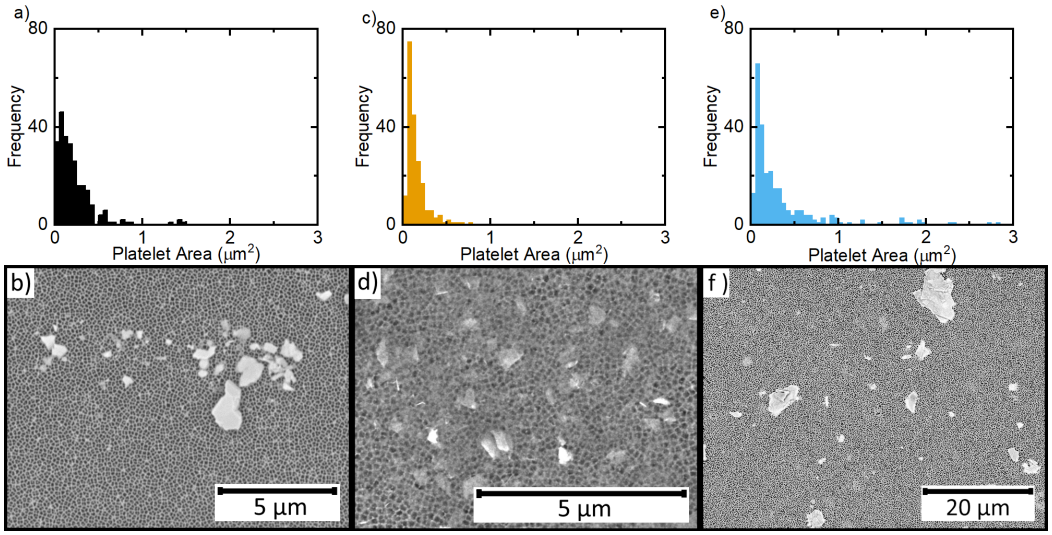

Figure 5.3: a,c,e) FLG platelet size (area) distributions, and b,d,f) typical SEM images obtained using backscattered electrons of platelets deposited on anodic alumina (chapter 3.2.2) for the three centrifuging protocols used: a,b) mFLG, c,d) hFLG, and e,f) uFLG.

alongside. The highly centrifuged few-layer graphene (hFLG) (Figure 5.3 (c,d)) consists largely of graphene platelets of small lateral size, while the moderately centrifuged few-layer graphene (mFLG) (Figure 5.3 (a,b)), and uncentrifuged few-layer graphene (uFLG) (Figure 5.3 (e,f)) material also contain small platelets but alongside a number of significantly larger platelets. The histograms show the narrow size distribution of the highly centrifuged material, and the broader size distributions of the moderately and uncentrifuged materials. In order to

FLG	μ ($\ln \mu m^2$)	σ ($\ln \mu m^2$)	mean (μm^2)	s.d. (μm^2)
mFLG	-1.9 ± 0.1	0.90 ± 0.08	0.22 ± 0.03	0.25 ± 0.06
hFLG	-2.1 ± 0.09	0.66 ± 0.06	0.15 ± 0.01	0.11 ± 0.02
uFLG	-1.6 ± 0.1	1.0 ± 0.08	0.33 ± 0.04	0.4 ± 0.1

Table 5.2: μ and σ, and means and standard deviations (s.d.) derived from them, obtained from fitting log-normal distributions to the platelet size data for mFLG, hFLG, and uFLG.

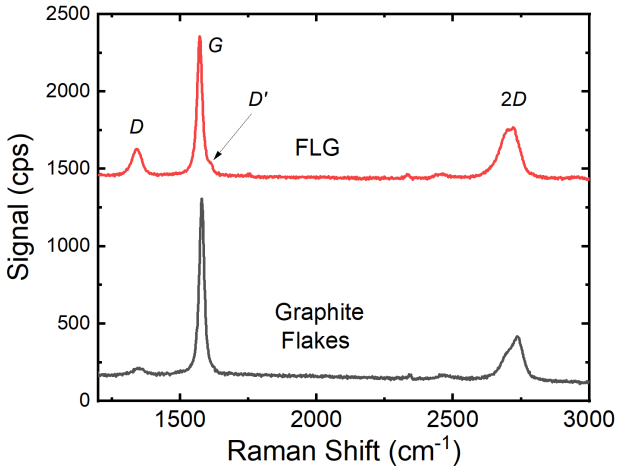

Figure 5.4: Raman spectra of graphite flakes (grey) and mFLG produced from them (red). D, G, $D^{'}$, and $2D$ peaks are labelled.

better understand the size distributions of the platelets, the data were fitted to a log-normal distribution $X = e^{\mu+\sigma Z}$, where Z is the platelet size, and μ and σ are the mean and standard deviation of $\ln Z$. These parameters are given in table 5.2, alongside the mean and standard deviation of the platelet size data derived from them. As expected, the highly centrifuged graphene has the smallest platelet size (0.15±0.01 μm^2) and smallest standard deviation (0.11±0.02 μm^2), while the uncentrifuged material has the greatest platelet size and standard deviation (0.33±0.04 μm^2 and 0.4±0.1 μm^2, respectively).

Figure 5.4 shows a Raman spectrum for a film of mFLG (red), alongside a spectrum for the graphite flakes from which the FLG was produced. Three peaks are clearly visible at approximately 1350 cm^{-1}, 1580 cm^{-1}, and 2700 cm^{-1}, labelled as D, G, and $2D$ respectively. In addition, the G peak displays a small shoulder, labelled

as *D'*. The ratio of the intensities of the *D* and *D'* peaks gives information on the nature of the defects in the material. Here, $I_D/I_{D'}$ is observed to increase from 2±1 for the as-supplied graphite flakes to 7 ± 1 for the FLG. This is characteristic of a transition from domination by grain-boundary defects in the polycrystalline graphite material to vacancy-like defects in the graphene platelets [208]. The shape of the *2D* band is indicative of a few-layer graphene material; graphite will display a broad *2D* peak with a distinct shoulder, and monolayer graphene displays a single sharp peak, whereas the peak observed here is instead broader than that typical of monolayer graphene, and lacks the clear shoulder typical of graphite [209].

By comparing the shape of the *2D* peaks of the parent graphite and the resultant FLG, it is possible to derive the average number of layers of the FLG platelets, N using the relation derived empirically by Backes *et al.*[145];

$$N = 10^{0.84M+0.45M^2}. \tag{5.1}$$

Here M is given by;

$$M = \frac{[I_{\omega_1}/I_{\omega_2}]_{Graphene}}{[I_{\omega_1}/I_{\omega_2}]_{Graphite}}, \tag{5.2}$$

where ω_1 is the position of the graphite maximum, and $\omega_2 = \omega_1 - 30$ (i.e. equation 5.2 uses the intensities of the two spectra at these two Raman shifts defined from the graphite spectrum). Using these equations the average platelet thickness for the moderately centrifuged graphene material was found to be 4 ± 1.5 layers, where the magnitude of the error is suggested by Backes *et al.* [145, 210].

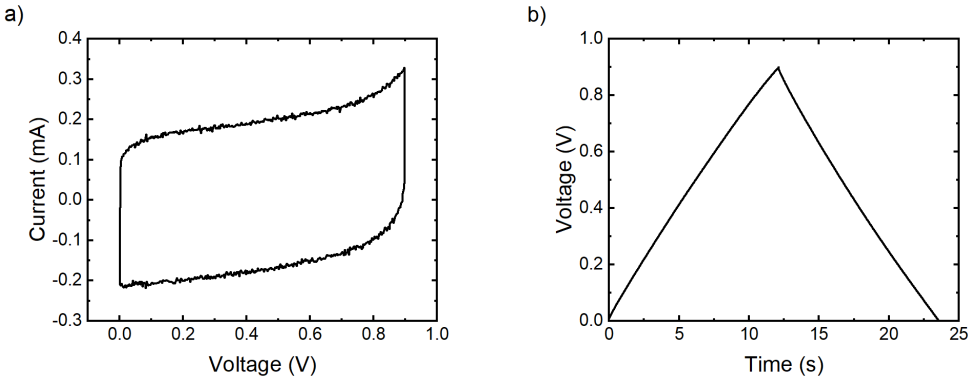

Figure 5.5: Electrochemical data of moderately centrifuged FLG electrodes in 6 M KOH in a stainless steel test cell. a) Cyclic voltammogram at 10 mV s^{-1}; b) GCD profile at 0.1 A g^{-1}.

5.2.2 Electrochemical Characterisation

5.2.2.1 Moderately centrifuged FLG as an electrode material

Figure 5.5 shows a cyclic voltammogram and GCD profile of the moderately centrifuged FLG electrodes. The square shape of the cyclic voltammogram, and small ohmic drop on the GCD profile are indicative of the low ESR, which was measured as $4.1 \pm 0.5\ \Omega$. The low CV current and short GCD charge/discharge time lead to low C_{sp} values of 5.7 ± 0.2 F g^{-1} and 5.06 ± 0.05 F g^{-1}, derived from the two respective techniques. This is to be expected, given the low SSA of the material.

5.2.2.2 FLG as a conductive additive

Figure 5.6 shows typical cyclic voltammagrams measured at a voltage sweep rate of 10 mV s^{-1} (Figure 5.6 (a)), and GCD curves measured at 0.1 A g^{-1} (Figure 5.6 (b)) of AC electrodes produced without conductive additive (black curve), 5 wt% Timcal C65 (orange curve), and 5 wt% uFLG directly mixed from suspension with AC (blue curve). The limited efficacy of the uFLG directly mixed into the AC electrodes as a conductive additive is reflected in the relatively small area

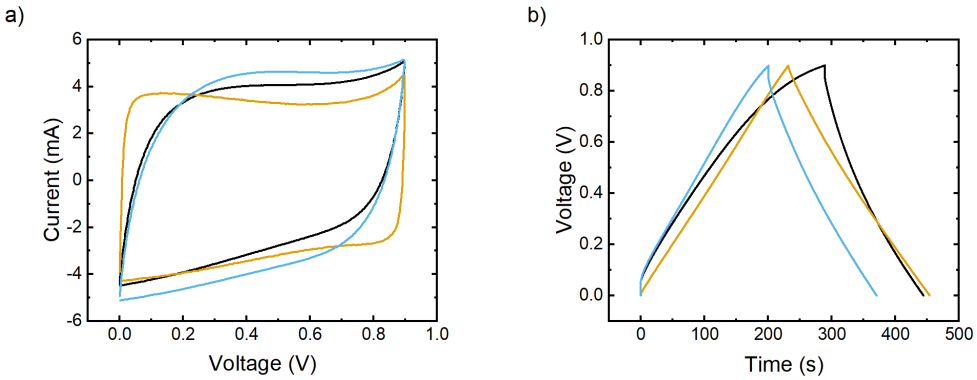

Figure 5.6: a): Cyclic voltammograms obtained at a scan rate of 10 mV s^{-1}, and b): GCD profiles obtained at a specific current of 0.1 A g^{-1}, of activated carbon electrodes (black), AC electrodes with 5% CB (orange), and AC electrodes with 5% uFLG directly mixed in (blue). Electrodes were tested in 6 M KOH in a stainless steel test cell.

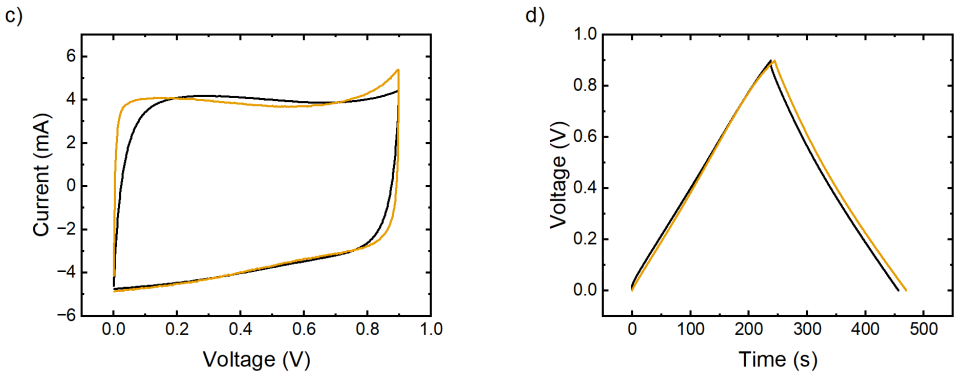

Figure 5.7: a): Cyclic voltammograms obtained at a scan rate of 10 mV s^{-1}, and b): GCD profiles obtained at a specific current of 0.1 A g^{-1}, of activated carbon electrodes with 5 wt% uFLG mixed in, which have subsequently been washed (black); and electrodes with 5 wt% uFLG added by vacuum filtration (orange). Electrodes were tested in 6 M KOH in a stainless steel test cell.

Sample	C_{sp} from CV (F g^{-1})	ESR from GCD (Ω)	C_{sp} from GCD (F g^{-1})	Sheet Resistance (Ω $\square^{-1}$)
AC	52±5	35±9	73.6±0.1	5800±500
AC + 5% CB	95.49±0.03	2.22±0.02	99.7±0.1	1700±90
AC + 5% FLG (uncentrifuged, mixed)	53±8	19±8	77.5±0.8	3700±100
AC + 5% FLG (uncentrifuged, mixed & washed)	81±6	10±4	89±5	2800±200
AC + 5% FLG (uncentrifuged, vacuum filtered)	102.9±0.1	1.4±0.1	99.06±0.03	1700±60

Table 5.3: Mean values of specific capacitance (C_{sp}), equivalent series resistance (ESR), and sheet resistance data for a variety of electrodes. The C_{sp} and ESR values were derived from CV at 10 mV s^{-1} and GCD at 0.1 A g^{-1} measured over a potential window of 0.9 V. The mean and standard errors are derived from multiple cells measured for each electrode type.

enclosed by the CV curve and large voltage drop visible in GCD. Table 5.3 shows mean values of C_{sp} and ESR derived from multiple CV and GCD curves obtained from several cells. Not only does the ESR vary with the different compositions, the error on the ESR is also seen to be much greater for the cells with worse performance, showing that not only does the absence of an effective conductive additive lead to excessive resistance, but also to poor reproducibility. It can be seen that direct mixing of uFLG into the activated carbon electrodes leads to only a modest improvement in cell metrics, with both C_{sp} and ESR values comparing poorly with those of electrodes containing 5 % CB.

The mediocre behaviour of electrodes produced by directly mixing uFLG with activated carbon can be attributed to the presence of Triton X-100. This surfactant, which is required to ensure that the FLG remains in suspension, assembles at the water/FLG interface potentially presenting a barrier to conduction and blocking access to both the few-layer graphene and AC surface area when the

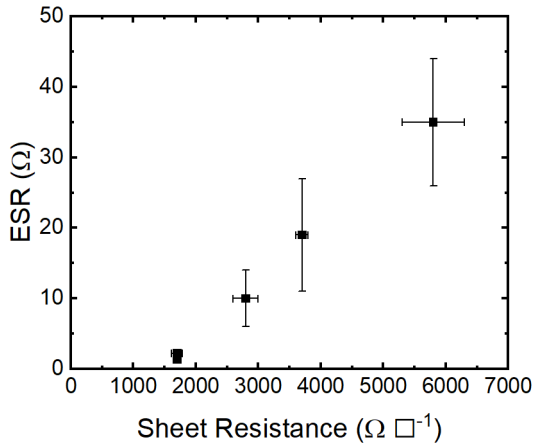

Figure 5.8: Sheet resistance plotted against ESR for the data shown in table 5.3.

FLG is incorporated into the electrode. This effect is demonstrated by the improvement when electrodes produced by direct mixing of the uFLG suspension are subsequently washed with 500 ml of UHP water, as shown by the CV and GCD curves in Figure 5.7 and the data in Table 5.3. After washing, the C_{sp}, measured by GCD at 0.1 A g^{-1}, increases from 77.5 ± 0.8 to 89 ± 5 F g^{-1}, which is closer to that of the electrodes produced with CB (see table 5.3). This increase in specific capacitance most likely arises from an enhancement in the surface area accessible to ions after the removal of the surfactant. However, despite the improvement in specific capacitance, the ESR remains relatively high and hence direct mixing of 5 % uFLG produces an inferior electrode material to that produced by the same loading of CB. We attribute the high ESR of electrodes produced from uFLG by mixing and subsequent washing to poor contact between AC and FLG. Removal of the surfactant increases the surface area accessible to ions but does not lead to structural re-arrangement improving contact between the additive and the active material.

In order to overcome the poor performance of the FLG additive when directly mixed into the electrode materials, a novel approach of using vacuum filtration to infuse the FLG suspension directly into pre-formed AC electrodes was employed,

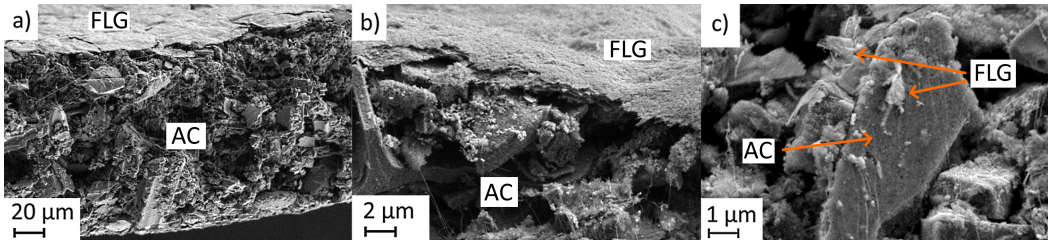

Figure 5.9: SEM images showing; a) a cross section of an electrode with vacuum infiltrated FLG additive; b) a magnified image showing the FLG layer on the back of the electrode; c) magnified image showing FLG platelets deposited on an activated carbon particle.

termed 'vacuum infiltration'. The enhanced electrochemical performance of the electrodes prepared by this method is readily apparent from the CV and GCD plots shown in Figure 5.7. The C_{sp} of the uFLG 'infused' electrodes is found to increase to 102.9 ± 0.1 F g^{-1} when derived from CV and to increase to 99.06 ± 0.3 F g^{-1} from GCD, similar to that of the 5 wt% electrodes, while the ESR decreases to 1.4 ± 0.1 Ω. This is reflected in a sheet resistance which agrees with that of the CB-containing electrode to within experimental error. Figure 5.8 shows ESR plotted against sheet resistance for the data presented in table 5.3. It can be seen that a sheet resistance correlates strongly with ESR.

Figure 5.9 shows SEM images of typical electrodes prepared by this vacuum infiltration of FLG. The interior of the electrode is shown to be composed of AC particles with a wide variety of shapes and sizes. The FLG material is visible as a layered material atop the electrode (the layer of re-stacked platelets is more clearly visible in Figure 5.9(b)). Figure 5.9(c) shows FLG platelets deposited on a grain of activated carbon in the body of the electrode, although this may demonstrate the penetration of the FLG into the body of the electrode, this may also be an artefact of sample preparation – platelets being knocked into the interior of the electrode when the material was cut. In order to more conclusively understand the distribution of the FLG platelets, Raman spectroscopy was performed on the electrodes.

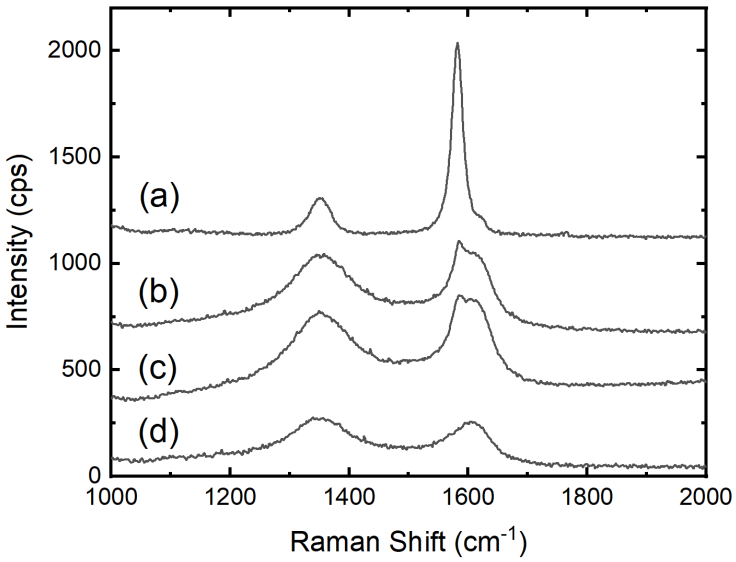

Figure 5.10: Raman spectra showing the D and G band region for a) FLG, b) the 'upper' side of a FLG-infused AC electrode, c) the 'lower' side of a FLG-infused AC electrode and d) a standard electrode made with AC.

The resulting Raman spectra are provided in Figure 5.10. AC electrodes without FLG (Figure 5.10 (d)) have spectra displaying features typical of amorphous carbons; with broad D and G bands at $\approx$1350 cm^{-1} and $\approx$1600 cm^{-1}, respectively. Upon infiltration of FLG, the Raman spectra obtained from both the graphene-rich 'upper' and graphene-poor 'lower' faces (referring to orientation within the vacuum filtration apparatus) of the electrodes (Figure 5.10 (b) and (c), respectively) consist of a superposition of the spectra from the purely-AC electrodes, and from the FLG 'paper' (Figure 5.10 (a)). This is particularly apparent for the G band of the FLG-infused electrode, where a sharp feature, corresponding to the narrow G band of the FLG at $\approx$1581 cm^{-1} is visible on the low energy side of the peak. This feature is strongest on the FLG-rich 'upper' side of the electrode (5.9(b)), but is also clearly present in spectra obtained from the FLG-poor 'lower' surface. As the penetration depth of the laser used is ≤ 1.5 μm, this indicates that the FLG is present across the entire thickness of the electrode,

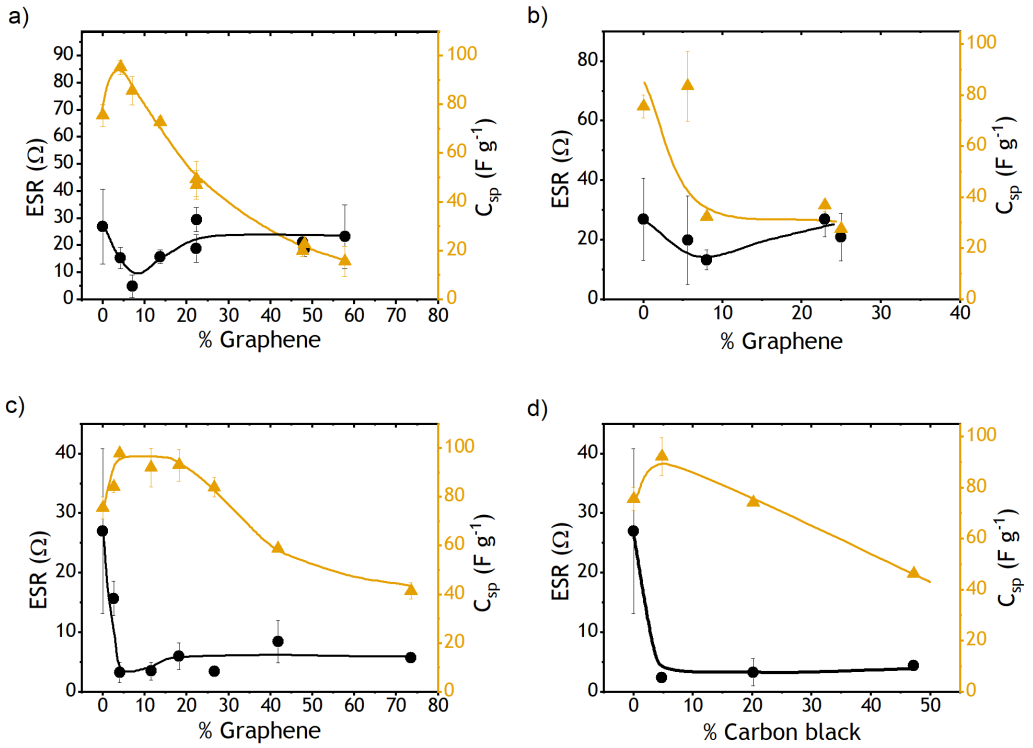

Figure 5.11: Mean values of C_{sp} (orange triangles) and ESR (black circles) derived from GCD at a specific current of 0.1 A g^{-1} over a working voltage of 0.9 V for AC electrodes with varying quantities (by wt%) of vacuum infiltrated: a) moderately centrifuged FLG, b) highly centrifuged FLG, and c) uncentrifuged FLG; compared with d) varying levels of conventionally-incorporated CB conductive additive. The lines are a guide to the eye.

and consistent with the SEM observations.

The small size of the FLG platelets used makes it difficult if not impossible to discern their exact quantity and distribution throughout the electrode material. However the Raman spectra shown in Figure 5.10, and the considerable decrease in ESR, which cannot solely be attributed to a reduction in contact resistance between the electrode and current collector, implies that enough platelets must penetrate the bulk of the electrode to significantly improve conductivity. It can therefore be concluded that, when incorporated into the electrodes through a route that removes excess surfactant, the FLG can act as an effective conductive additive.

5.2.2.3 Variations in performance with size and mass-loading

In order to determine the extent to which FLG size distribution and mass loading influenced the performance of the FLG-infiltrated AC electrodes, a broad range of electrochemical characterisations including GCD, CV, and EIS were performed on electrodes infiltrated with mFLG, hFLG, and uFLG over a broad range of mass loadings. Equivalent characterisations were also performed on conventional electrodes with varying quantities of CB, in order to provide a baseline against which to evaluate the effectiveness of the different size distributions of FLG.

Figure 5.11 (a) shows how the C_{sp} and ESR, as derived from GCD, varied with the quantity of mFLG. Performance is optimised at 7 wt% FLG, with a C_{sp} derived from CV of 82 ± 9 F g^{-1}, and C_{sp} and ESR derived from GCD of 86 ± 6 F g^{-1} and 5 ± 4 Ω, respectively. As the quantity of FLG is increased the specific capacitance decreased sharply to 11.9 F g^{-1} for 58 wt% FLG per electrode. To a certain extent this is to be expected; as shown in the SEM image in Figure 5.9, a significant amount of FLG stacks up on the back of the electrode which adds mass without contributing capacitance. This behaviour could be expected to lead to a linear decrease in capacitance, which the real data significantly diverges from, instead falling off steeply at first, then more gently at higher concentrations. More unusual behaviour is observed in the ESR: although performance is good at around 7 wt% mFLG, as the amount of mFLG increases further, so too does the ESR before plateauing at ≈20 Ω. This is in sharp contrast to sheet resistance measurements, which having fallen sharply from 5800 ± 500 Ω □$^{-1}$ with no conductive additive to 50 ± 4 Ω □$^{-1}$ at 7 wt% mFLG, decrease further to 7.9 ± 0.9 Ω □$^{-1}$ at 50 wt% mFLG. The relationship between sheet resistance and ESR for the electrodes containing mFLG is shown in figure 5.12. Unlike the data shown in figure 5.8, no correlation between sheet resistance and ESR is observed. This is attributed to the graphene forming a high conductivity layer on the back of the electrode, which

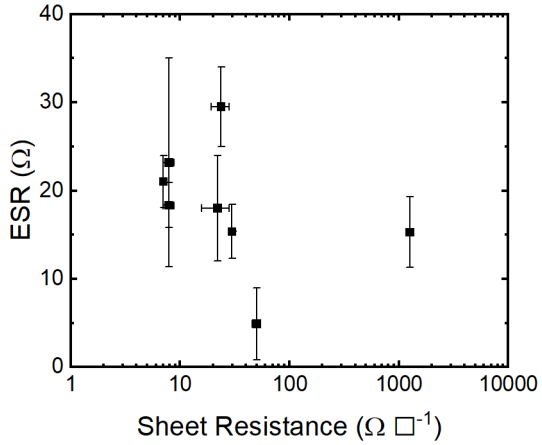

Figure 5.12: Sheet resistance plotted against ESR for electrodes with varying quantities of mFLG.

means that the sheet resistance cannot be directly related to the ESR associated with a cell produced from that electrode material.

Figure 5.11 (b) shows the efficacy of the hFLG. Compared to that of the moderately centrifuged graphene, the samples show a comparable or decreased performance across all mass loadings. Figure 5.11 (c) shows the performance of electrodes incorporating varying percentages of uFLG. Performance is optimised at approximately 4-20 wt% FLG; a wider range of mass loadings than that of other materials. Moreover, the ESR, after initially dropping rapidly remains low with increased mass loading, unlike the variation observed for the mFLG additive. C_{sp} (as derived from GCD) remains above 90 F g^{-1} up to 20 wt% FLG, before decreasing slowly. This is superior even to electrodes with CB conductive additive (Figure 5.11 (d)), in which the capacitance displays the expected linear decrease as the loading of CB increases above 5 wt%. A similar trend in ESR and C_{sp} is observed for both CB and uFLG, with the peak value of C_{sp} slightly lower in the case of the CB.

Figure 5.13(a-c) shows how the C_{sp} of FLG-infused AC electrodes varies with CV scan rate. For the most part these results are as would be expected based on

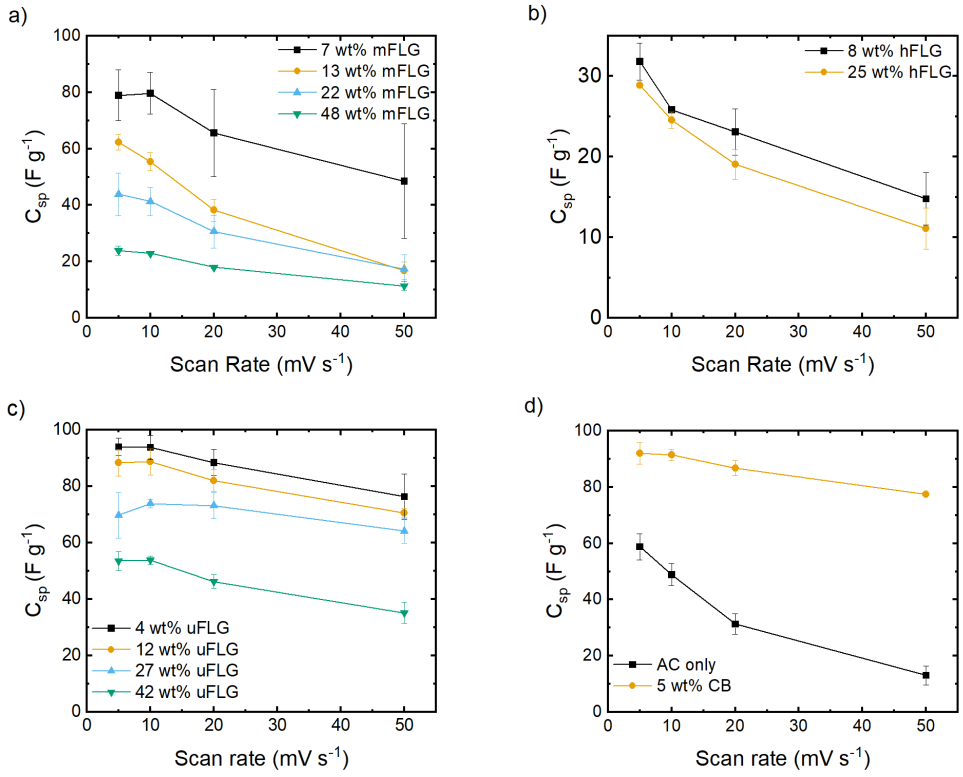

Figure 5.13: Variations of specific capacitance with cyclic voltammetry scan rate for AC electrodes with varying quantities (by wt%) of vacuum infiltrated: a) moderately centrifuged FLG, b) highly centrifuged FLG, and c) uncentrifuged FLG; compared with d) varying levels of conventionally-incorporated CB conductive additive. The lines are a guide to the eye.

the GCD data presented in Figure 5.11: the C_{sp} of the mFLG samples (Figure 5.13 (a)) can be seen to drop with increasing FLG mass loading across almost all scan rates, with the exception of at 50 mV s^{-1} the devices containing 13 wt% and 22 wt% mFLG show the same C_{sp}, perhaps suggesting an increased diffusion resistance for the 13 wt% sample. Figure 5.13(b) shows data for the hFLG at 8 wt% and 25 wt% loadings; the C_{sp} is shown to be similar across all scan rates, in agreement with GCD data (Figure 5.11 (b)), which also shows performance to be almost invariant across these mass loadings. Data for the uFLG-infused electrodes is shown in Figure 5.13 (c). Again in keeping with the GCD data, the C_{sp} of 4 wt% uFLG and 12 wt% uFLG are in agreement to within experimental error across all scan rates, only decreasing at loading 27 wt% and above. Furthermore, these low mass loading values of C_{sp} are shown to be superior to those of AC

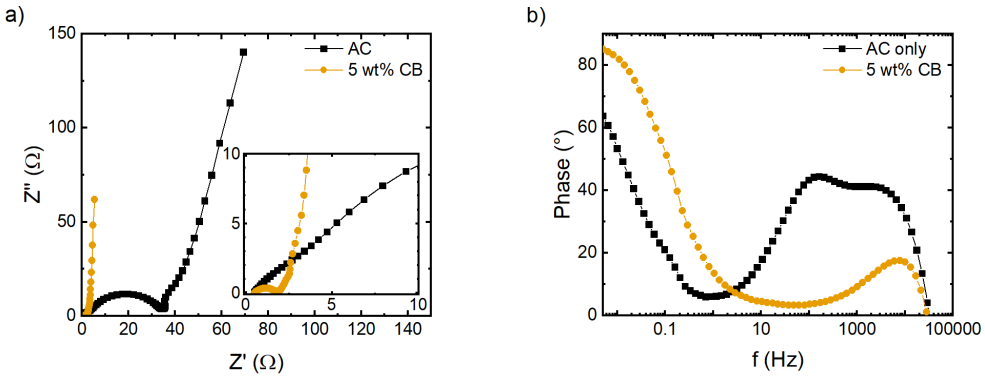

Figure 5.14: a) Nyquist plots, and b) Phase plots for control devices containing no conductive additive (black), and 5 % CB (orange).

electrodes without conductive additive.

5.2.2.4 Electrochemical Impedance Spectroscopy

Figure 5.14 shows Nyquist (Figure 5.14(a)) and phase (Figure 5.14(b)) plots for AC electrodes with (orange circles) and without (black squares) 5 wt% CB conductive additive. The interpretation of Nyquist plots as they relate to EDLCs is discussed in Chapter 2, section 2.2.4, and illustrated in Figure 2.11. Generally, the ESR of a device is understood to correspond to the sum of a series resistance (corresponding to the section of the Nyquist plot labelled 'electrode resistance' in Figure 2.11), and that of the semicircular region of the Nyquist plot, referred to sometimes as the 'charge transfer resistance' (CTR) (labelled 'electrolyte resistance' in Figure 2.11). In both plots shown in Figure 5.15, the series resistance is small, however the Nyquist plot of the AC electrode is dominated by a large CTR (the diameter of the semicircular region of the Nyquist plot) of approximately 35 Ω, in agreement with the ESR determined from GCD (table 5.3). For the device containing 5 wt% CB, the CTR region shrinks to around 2 Ω, again in good agreement with the ESR determined from GCD. As discussed in Chapter 2, the interpretation of Nyquist plots for supercapacitors is not an exact science; the CTR is sometimes attributed to the resistance of the electrolyte [157], however from its dramatic decrease with

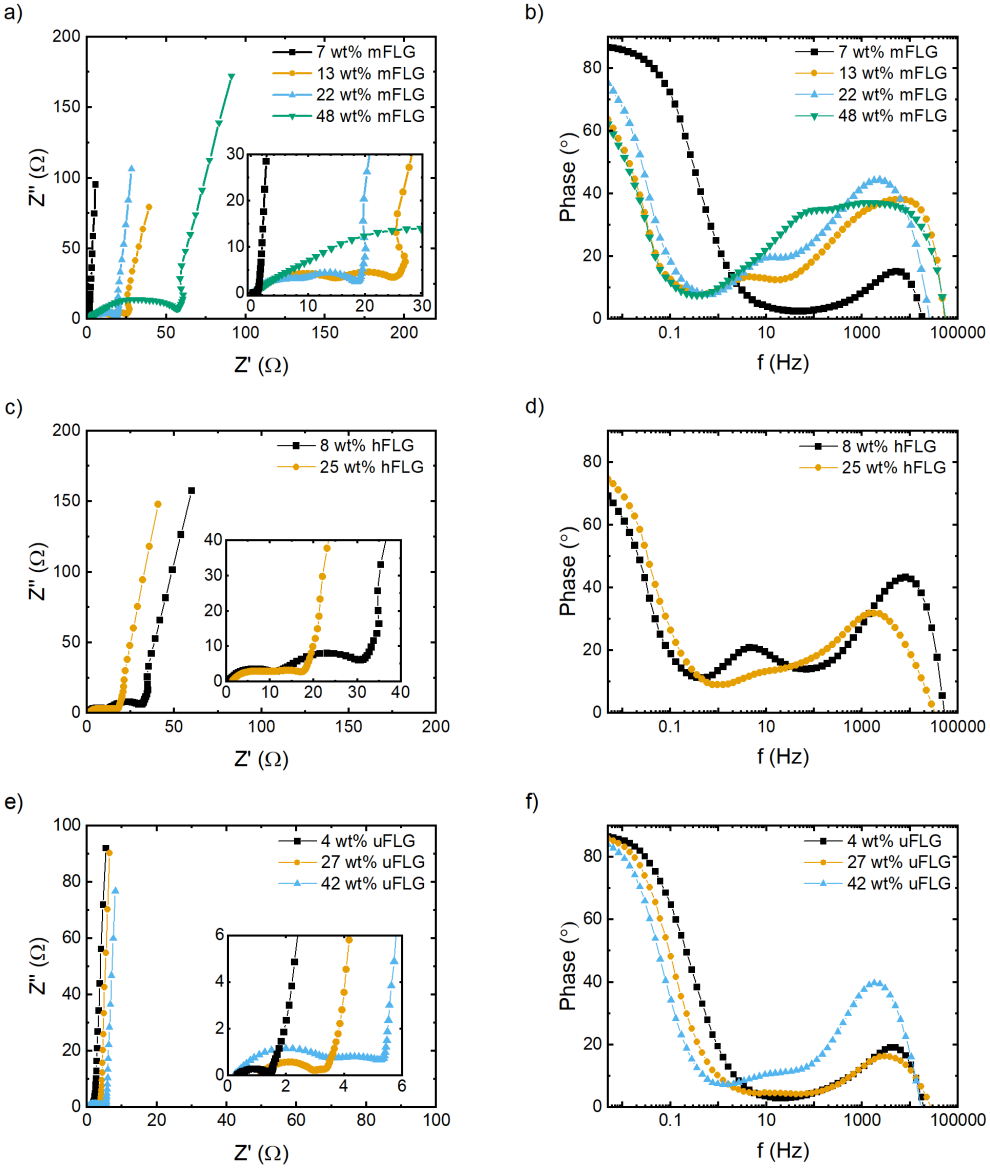

Figure 5.15: a, c, e) Nyquist plots, and b, d, f) phase Plots for EDLCs containing varying quantities of: a, b) mFLG, c, d) hFLG, and e, f) uFLG.

the inclusion of conductive additive it is clear that in this case it is dominated by the resistivity of the electrodes.

Phase plots for the two devices are shown in Figure 5.14(b). The device with 5 wt% CB shows typical behaviour for a supercapacitor, with a low phase angle (ϕ) at high frequencies as the system behaves like a resistor; then, as the frequency decreases, ϕ increases, before at the very lowest frequencies ϕ reaches close to 90°, indicative of capacitor-like behaviour due to the formation of the EDL. In contrast, the AC-only device shows a large increase in ϕ at the higher frequencies, indicating poor charge-carrier transport into and through the device. This appears to consist of a superposition of two peaks, perhaps suggesting two distinct sources of impedance of different magnitudes. The nadir of ϕ, corresponding to good charge-carrier transport comes at lower frequencies than it does for the CB-containing device, and the subsequent increase in ϕ as the EDL forms also occurs at lower frequencies, not actually reaching a high value corresponding to good capacitive behaviour within the range of frequencies measured.

Figure 5.15 shows Nyquist (Figures 5.15 (a, c, e)) and phase (Figures 5.15 (b, d, f)) plots for devices with varying mass loadings of the three different sizes of FLG. Data for the mFLG is shown in Figure 5.15 (a, b). At a mass loading of 7 wt% (black squares), where the performance was optimised, the data is comparable to that of the CB-containing device shown in Figure 5.14, with a small CTR of around 1 Ω diameter corresponding to the low ESR of the device (0.8±0.2 Ω). As the quantity of mFLG is increased, the CTR region is distorted and enlarged. At the very highest mass loading of 48 wt% (green triangles) this resembles the data from the AC only electrode (Figure 5.14), however at the intermediate mass loadings of 13 and 22 wt% (orange circles and blue triangles, respectively), the CTR region takes on a double-hump shape, reflected in the high-frequency peak on the phase plot showing a distinct shoulder in the mid-frequency range. In

these instances the CTR no longer corresponds to the ESR of the devices (as measured by GCD) however, in the case of the double humped Nyquist plots (13 and 22 wt% mFLG), the diameter of the first hump does approximate the ESRs of 12.3±0.5 Ω and 12±1 Ω measured for the two samples (the >50 Ω CTR of the device containing 48 wt% mFLG is simply much larger than the 23±1 Ω measured by GCD). This observation may suggest that the second hump is linked to the the diffusion of electrolyte ions into the electrode pores. Although this diffusion resistance is often assumed to behave as a constant phase element (CPE) – which would manifest as a straight, sloped line on the Nyquist plot – when pores are pear-shaped with a narrow opening relative to their internal diameter, instead of being unrestricted at their entrance, a semicircle in the Nyquist plot can result [157, 161, 211–213]. For electrodes with intermediate mFLG loading, this effect may have been caused by FLG platelets partially obstructing the entrance to pores, in a similar manner to the increased diffusion resistance observed by Wang *et al.* [205].

More extreme manifestations of the same trends are seen in the Nyquist and phase plots for 8 wt% hFLG (Figure 5.15 (c, d)). The ESR derived from GCD was found to be 15.36±0.06 Ω, which roughly aligns with the first hump of the CTR-region of the Nyquist plot, however the second hump extends the region to over 30 Ω, before the onset of capacitor-like behaviour. In the phase plot, this is reflected by a mid-frequency peak in the phase angle. Looking to the uFLG data (Figure 5.15 (e, f)), its clear that alongside the ESR remaining low, the development of this second hump is suppressed. As the quantity of uFLG increases, a small plateau is observed in the Nyquist plot, in between the semicircular CTR region and the vertical capacitive region, however the overall equivalent distributed resistance (EDR) of the cell remains low. In the phase plot (Figure 5.15 (f)), only a slight hint of the mid-frequency peak observed for the hFLG is visible. This difference in behaviour may be due to the presence of the larger micrographite platelets in the uFLG; their large size will mean that they take up a significant proportion of

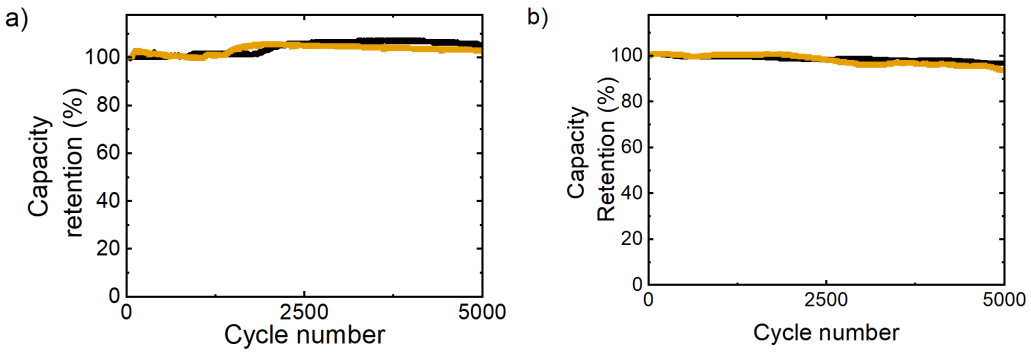

Figure 5.16: Discharge capacity retention over 5000 cycles of galvanostatic charge/discharge with a current density of 1 A g^{-1}. a) data obtained with a working voltage of 1.2 V, b) 1.4 V. In both figures, data from a device with 5 wt% vacuum infiltrated uncentrifuged FLG are shown in black, and data from a 5 wt% CB electrode are shown in orange.

the mass of FLG, so that fewer small platelets are available to block the pores of the AC; and even as the mass loading is increased they may plug the macro-pores, helping to prevent the infiltration of excessive quantities of FLG into the device.

5.2.2.5 Lifetime and Ragone plot

Initial electrode characterisation was carried out at a working voltage of 0.9 V, below the threshold for water splitting and electrolyte degradation [214], in order to ensure good stability for comparative measurements of C_{sp} and ESR. However, in order to maximise energy and power density, it is necessary to utilise the highest possible working potential without compromising the long term stability of the device. Hence, the stability of electrodes produced with the optimal combination of FLG mass loading and size distribution (≈4-20 wt% vacuum infiltrated uFLG) was tested over 5,000 GCD cycles and and compared to that of standard electrodes containing 5 wt% CB.

Figure 5.16 compares the cyclability of a 5 wt% uncentrifuged FLG device, with a standard device containing 5 wt% CB, over 5000 GCD cycles at 1.2 V (Figure 5.16

(a)) and 1.4 V (Figure 5.16 (b)), each with a specific current of 1 A g^{-1}. At 1.2 V, which was determined to be the MWV of the standard electrodes in Chapter 3, the FLG-containing device also displays excellent stability, with the capacity increasing to 105 % of the original value, compared to 103 % for the standard electrodes. At 1.4 V, where the standard electrodes show a slight decrease in capacity to 94 % of the initial value, the FLG-containing device also shows a slight decrease in capacity to 97 %. This demonstrates that the inclusion of uFLG in no way compromises the stability of the device, allowing it to safely operate at a MWV of 1.2 V, equivalent to that of the conventionally prepared electrodes.

Figure 5.17 (a) shows a Ragone plot comparing a series of devices produced from electrodes with 8 wt% and 4 wt% vacuum infiltrated uFLG conductive additive (within the range of optimal mass loadings) with those having 5 wt% and 10 CB wt% conductive additive, all operating at a working cell potential of 1.2 V. From the data it can be seen that across all tests the FLG-containing electrodes show a greater energy density than the CB-containing electrodes across the full range of power densities tested. The graphs also demonstrate both the reproducibility of devices of differing compositions, with the 5 wt% CB electrodes having a variation of around 5% in specific energy, while the 8 wt% FLG electrodes have a variation of around 6%. The relative invariance of performance with uFLG loadings is shown by how the results for 4 wt% FLG (orange squares) lie within the range covered by the results for 8 wt% FLG (orange circles). The consistent performance of the uFLG devices with additive loading stands in sharp contrast to the CB devices, where the energy density of the device containing 10 wt% CB falls off sharply with increasing specific current. The average performance across all electrodes containing 8 wt% uFLG and 5 wt% CB is shown in Figure 5.17 (b); the energy storage for both compositions was optimised at a power density of around 200 W kg^{-1} (a specific current of 0.1 A g^{-1}), corresponding to an average specific energy of 23.1 ± 0.9 Wh kg^{-1} for the electrodes containing 8 wt%

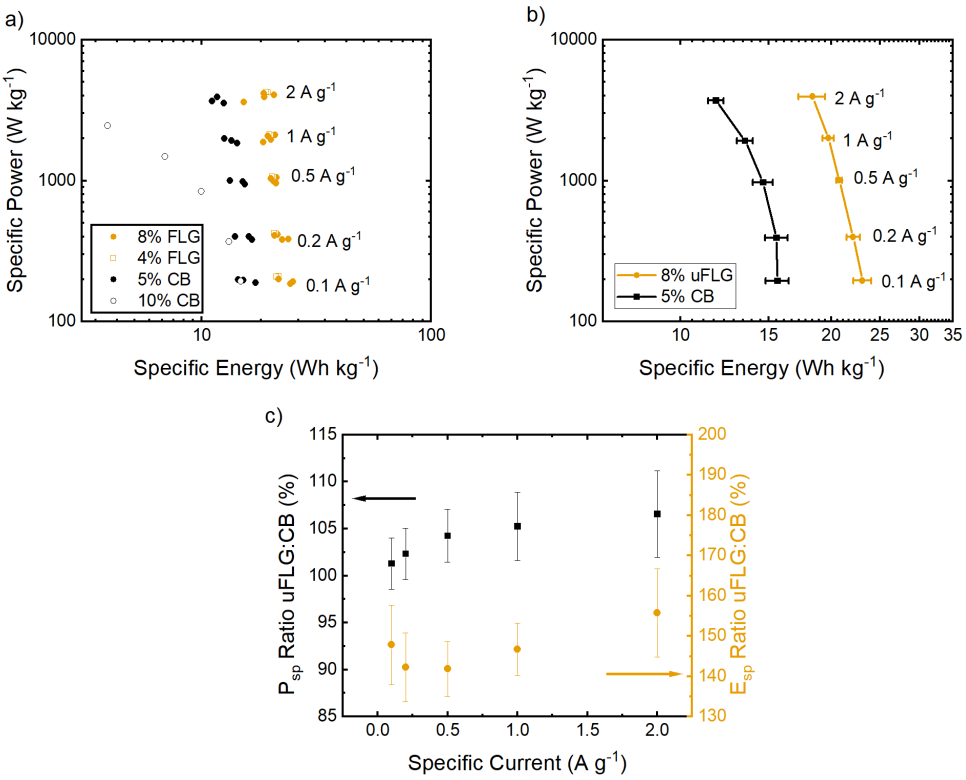

Figure 5.17: a) Ragone plot comparing the performance of four devices with 8 wt% vacuum infiltrated uFLG (filled orange circles), two devices with 4 wt% vacuum infiltrated uFLG (hollow orange squares), three devices with 5 wt% carbon black (filled black circles), and a device with 10 wt% carbon black (hollow black circles). b) Ragone plot comparing the average performance of electrodes with 8 wt% vacuum infiltrated uFLG (orange circles), and 5 wt% carbon black (black squares). c) Plot showing the ratios of average values of specific power (P_{sp}) (black squares), and specific energy (E_{sp}) (orange circles), for electrodes with 8 wt% vacuum infiltrated uFLG, and electrodes with 5 wt% carbon black as a function of specific current. Power and energy densities are derived from GCD data collected between 0.1 and 2 A g^{-1} at a cell potential of 1.2 V. The averages in b) and c) are derived from three different cells for each composition, and the error bars given are the standard error in the mean.

uFLG, and 15.6±0.8 Wh kg^{-1} for those containing 5 wt% carbon black. Over the range of specific currents tested the specific energy of electrodes containing 8 wt% uFLG was on average 47 ± 3 % greater than those containing CB. This improved specific energy arises due to the uFLG infiltrated electrodes having a greater average C_{sp} of 142.3 ± 0.1 F g^{-1} over the 1.2 V working potential, compared with 96.81 ± 0.02 F g^{-1} for the electrodes containing CB (both at a specific current of 0.1 A g^{-1}). The ESRs of the devices were found to be comparable at 1.3 ± 0.4 Ω and 3 ± 1 Ω, for the uFLG and CB devices, respectively. It is important to note that although these values appear large relative to those in figure 1.2, those refer to whole device specific energies, whereas those given here are only electrode specific energies.

Figure 5.17 (c) shows the ratio of the specific power density (P_{sp}) of 8 wt% uFLG loaded electrodes to 5 wt% conductive black loaded electrodes measured by GCD (black squares) and the ratio of specific energy density (E_{sp}) between the two materials (orange circles), both plotted against specific current. It can be seen that both ratios are constant to within experimental error. The similar power densities of the two electrode materials arises from the ESRs being the same to within error, whereas the increased energy density of the 8% uFLG electrodes over those with 5% carbon black loading reflects the increased specific capacitance of the former. This gain in C_{sp} obtained for the optimal mass loading of uFLG, while the ESR remains comparable, suggests that the improved performance of the uFLG-containing devices arises from the uFLG making an active contribution to the double layer capacitance.

5.3 Conclusions

Few-layer graphene produced by the environmentally friendly approach of high shear exfoliation into a surfactant-stabilised aqueous solution was investigated as a conductive additive for activated carbon based EDLCs operating in aqueous electrolyte. Three different centrifuging protocols were used to produce suspensions of FLG platelets with varying lateral size distributions; moderately centrifuged mFLG, highly centrifuged hFLG, and uncentrifuged uFLG.

Directly mixing the FLG into the electrodes in the manner of a conventional conductive additive showed poor performance, with only a slight decrease in ESR and little change in C_{sp} when compared to a device made without any conductive additive. Both C_{sp} and ESR were shown to improve when the electrodes were washed, suggesting that residual Triton X-100 left over from the shear exfoliation process may have been in part responsible for the poor performance, perhaps blocking access to pores and reducing electrical contact between the AC grains and FLG platelets. In spite of this improvement, the performance remained inferior to conventional CB-containing electrodes.

Prompted by this, a novel vacuum infiltration approach was developed to incorporate FLG into the electrodes. mFLG-infiltrated electrodes were observed to perform well at a 7 wt% concentration, however counter-intuitively, the ESR was observed to increase alongside the concentration of FLG beyond this point, while hFLG, with the smallest platelet dimensions, performed poorly across all mass-loadings tested. In contrast the uncentrifuged uFLG was shown to facilitate good performance over a broad range of concentrations, maintaining a C_{sp} of over 90 F g^{-1} and a low ESR at mass loadings of between 4 wt% and 20 wt%.

Electrodes containing uFLG within this optimal range of mass loadings were compared to those containing 5 wt% CB, and were found to have comparable stability, leading to an equal MWV of 1.2 V. Furthermore, when operating at their MWV, the uFLG-infused electrodes were shown to have superior specific energy density (23.1 ± 0.9 Wh kg^{-1}) to those containing 5 wt% carbon black (15.6 ± 0.8 Wh kg^{-1}), when measured at comparable power densities. This demonstrates that the uFLG can provide better performance as a conductive additive than commercially-available CB, but only if added via the novel vacuum infiltration technique shown here.

Chapter 6

The impact of electrolyte additives on the performance of aqueous EDLCs.

6.1 Introduction

As discussed in chapter 1, the high specific surface area (SSA), defined as the total surface area per unit mass, of activated carbon enables high specific capacitances, making it a popular electrode material for electric double layer capacitors (EDLCs). However, the relationship between capacitance and SSA is not linear, with the observed capacitance being generally lower than that implied by the high surface area of the activated carbon [50, 215, 216]. It has been suggested that, in aqueous devices, the hydrophobic nature of the activated carbon surface leads to incomplete wetting and is therefore at least partially responsible for this. Indeed, the introduction of surface functional groups (SFGs) which increase the hydrophilicity of the activated carbon surface is observed to improve capacitance (although this may be also be attributed, all or in part, to pseudocapacitive effects) [50–54]. Reducing the surface tension of aqueous electrolytes through the addition of ethanol or isopropanol has similarly demonstrated improved performance [217,

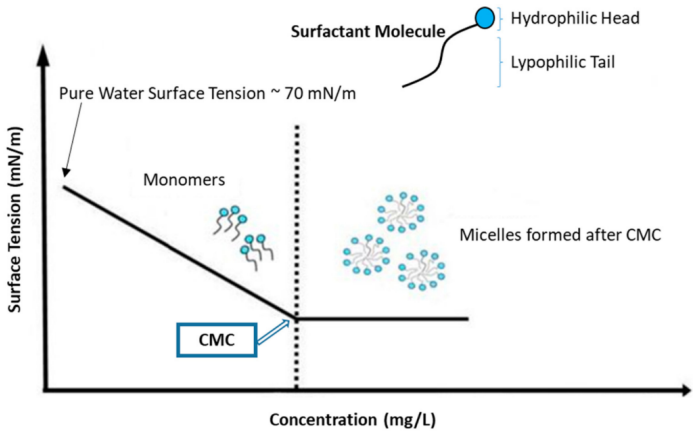

Figure 6.1: Schematic showing how increasing the concentration of surfactant lowers surface tension up to the critical micellar concentration, at which point large agglomerations, referred to as micelles, are formed. Reproduced from [219].

218].

Improved wetting of activated carbon surfaces may also be achieved by the use of surfactants. Surfactants are molecules having both hydrophilic and hydrophobic functional moieties. Their amphiphilic nature reduces interfacial tension [220] which allows for oils [181], and hydrophobic materials such as carbon nanotubes [221] and the few-layer graphene, described in chapter 5, to be dispersed in water. Surfactants can be ionic, carrying a charge at the hydrophilic head, with an oppositely charged ion to ensure the overall charge neutrality, or non-ionic. Moreover, ionic surfactants can be subdivided into three further catergories: anionic (negatively charged), cationic (positively charged), or zwitterionic (having two opposite charges at the head) [216]. As the concentration of surfactant molecules is increased the surface tension of the system decreases until the *critical micellar concentration* (CMC) is reached. Above this point, the surface tension remains constant while the surfactant molecules are no longer uniformly dispersed in the host liquid but, instead, tend to form large agglomerations known as micelles. This process is illustrated in Figure 6.1, which provides an approximate representation of the evolution of surface tension with surfactant concentration, alongside a diagram depicting micelles.

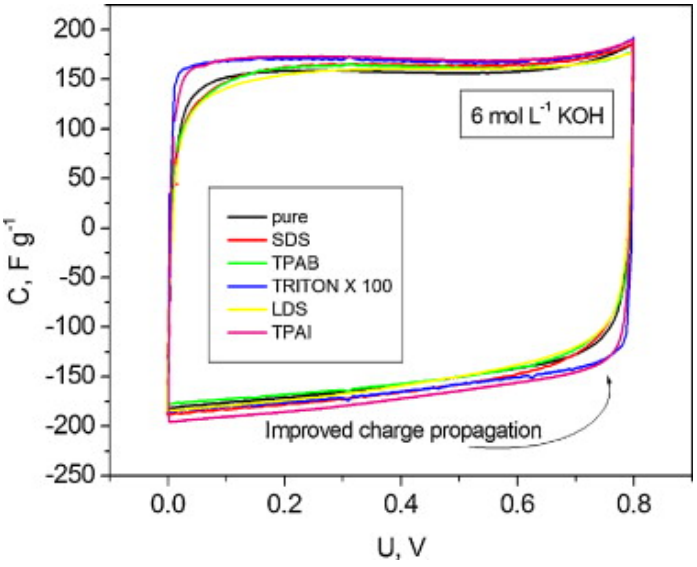

Figure 6.2: Cyclic voltammetry at 10 mV s^{-1} for activated carbon electrodes in 6 M KOH with and without various surfactants. Reproduced from [50].

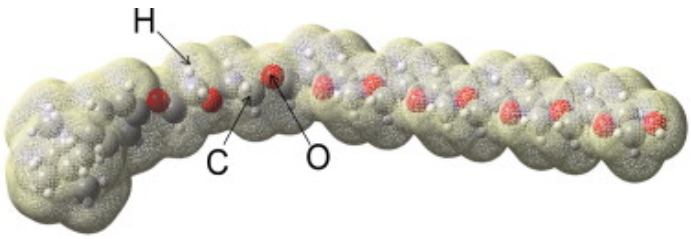

Figure 6.3: Molecular structure of Triton X-100 [50].

Fic *et al.* investigated the addition of surfactants to aqueous electrolytes and consequently reported a decrease in ESR and improved capacitance with the addition of 5 mM Triton X-100 to aqueous 6 M KOH [50, 216]. Figure 6.2 presents cyclic voltammetry data from reference [50]. It can be seen that with the addition of Triton X-100, the voltammogram becomes more rectangular, indicating improved charge propagation, while the larger area would lead to a greater measured capacitance (although the capacitance values derived from these data are not presented). Triton X-100 is a non-ionic surfactant, the structure of which is shown in Figure 6.3, with a diameter of 0.525 nm and length of 3.621 nm. This improved performance was attributed to the Triton molecules forming so-called 'ion channels', which facilitate the movement of ions from the

bulk electrolyte to the electrode/electrolyte interface [50, 216]. Triton X-100 was compared with both anionic and cationic surfactants, which were on the whole found to be ineffective, with the exception of a single cationic surfactant, tetrapropylammonium iodide (TPAI), the improved capacitance of which may be due to the pseudocapacitive contribution of the iodide ion [50, 222]. Meanwhile Ghasemi and Ahmadi observed a significant improvement in C_{sp} for rGO-Fe_3O_4 electrodes operating in Na_2SO_4 with 5 mM Triton X-100 [223].

Interestingly, Fic *et al.* also reported an increased maximum working voltage (MWV) from 1.23 V to 1.6 V with the addition of Triton X-100, which was attributed to the electrolyte effectively coating electrode surfaces and filling pores, increasing the partial pressure of evolved gases and therefore suppressing their further evolution. However, this behaviour was not observed for the other surfactants tested [50]. This result is at odds with reports of an anionic surfactant, sodium dodecyl sulfate (SDS), improving the MWV of aqueous sodium ion batteries [224] and inhibiting the corrosion of zinc-aluminium-hydrotalcite (used as an anode in zinc/nickel batteries) in alkaline electrolytes [225]. In both instances the observed effect of SDS has been attributed to the hydrophilic head of the SDS molecules adhering to the hydrophilic electrode surface – the hydrophobic tails of the surfactant then prevent the electrolyte from reaching the electrode surface. In the case of the sodium ion batteries, this prevents the water molecules from undergoing reduction/oxidation [224], while in the case of the zinc-based electrodes this reduces the concentration of OH^- ions which would otherwise corrode the electrode [225].

As was discussed in chapter 4, the narrow MWV of aqueous electrolytes is a significant limitation to the energy density of EDLCs, hence many studies have attempted to increase this voltage window by modifying the electrolyte [35, 181, 189, 226, 227]. One approach is through the use of water-in-salt electrolytes (WiSEs), which utilise

highly soluble salts, such as lithium bis(trifluoromethanesulfonyl)imide (LiTFSI), at high concentrations (often over 20 M) and have demonstrated MWVs of up to 3.0 V. The high salt concentration means that there are almost no free water molecules, reducing their chemical activity and, in addition, the $TFSI^-$ anions decompose at the electrode surface leading to the formation of a LiF-containing solid-electrolyte interphase (SEI), which acts to prevent water molecules from reaching the electrode surface, both preventing the decomposition of the electrolyte, and shielding the electrode from corrosion [35, 224, 226, 228, 229].

An alternative approach to the modification of aqueous electrolytes has been to use the principle of molecular-crowding, in which high concentrations of additives such as polyethylene glycol (PEG) or dimethyl sulfoxide (DMSO) are added to the electrolyte. This has the effects of reducing the effective concentration of water molecules and partially replacing them in the solvation shells of ions, thus reducing the chemical activity of water, alongside disrupting the hydrogen bonding between water molecules. These effects together have been reported to allow aqueous supercapacitors to operate at cell voltages as high as 2.8 V [189, 226, 227, 230].

A modification of the molecular crowding approach is to use a microemulsion electrolyte. Hughson *et al.* [181] reported a supercapacitor employing a microemulsion electrolyte composed of water, SDS, *n*-butanol and cyclohexane with MWV of 2.7 V. As with the SDS-containing electrolyte discussed above, this was attributed to the formation of an additive (in this case, surfactant and oil) rich layer at the electrode surface [181]. In contrast to the use of SDS in reference [224], the microemulsion electrolyte required a hydrophobic electrode surface in order to have the desired effect [181].

Although WiSE, molecular crowding electrolytes and microemulsions appear to significantly broaden the MWV of aqueous EDLCs, this usually comes at

a cost of lower ionic mobility and subsequently increased ESR and lower C_{sp}, which may in extreme cases compromise any improvement in MWV relative to conventional aqueous electrolytes. As the simple addition of Triton X-100 has, contrastingly, been observed by Fic *et al.* to improve MWV, ESR, and C_{sp} [50, 216], this makes it a highly attractive approach, worthy of further investigation.

In this chapter a series of experiments are detailed, the intial aim of which was to replicate the work of Fic *et al* and use the lessons of chapter 4 to more accurately determine any increase in the MWV. In particular, Fic *et al.* used the development of the tail in CV curves to estimate MVW, which has been shown in this work to be an unreliable approach (see chapter 4.2.3). The improvement in EDLC performance with the simple addition of 5 mM Triton X-100 observed in the literature could not be reproduced in this work. The effect of other surfactants and the surface chemistry of the electrodes is investigated to try and understand why the results reported here diverge from those previously reported.

6.2 Results and Discussion

6.2.1 Triton X-100 as an electrolyte additive

In order to understand the impact of the addition of 5 mM Triton X-100 to an aqueous 6 M KOH electrolyte, as previously reported by Fic *et al.* [50], CV, GCD and EIS measurements were performed on two-electrode devices with a fixed electrode mass (10.9 ± 0.1 mg corresponding to an areal mass loading of 3.084 ± 0.002 mg cm^{-2}) in stainless steel test cells. Additional CV measurements carried out on devices with a broader range of electrode areal mass loading to determine if increased areal mass, and hence electrode thickness, influenced the observed results. Such measurements were undertaken as typical electrodes used

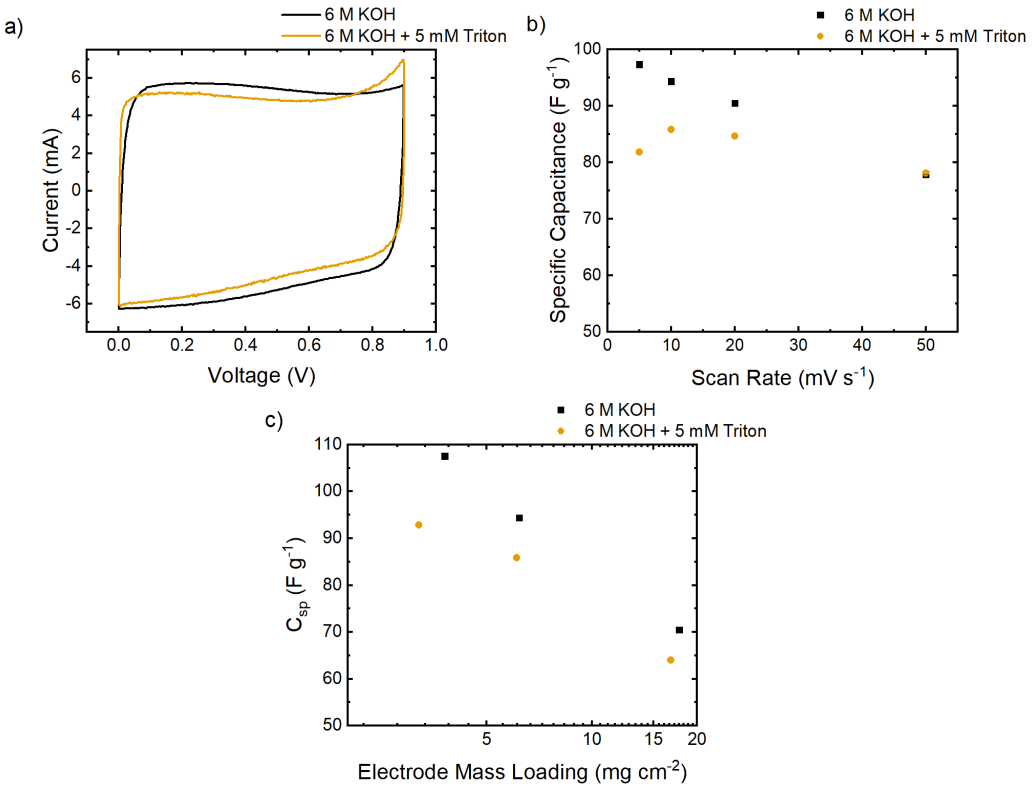

Figure 6.4: Cyclic voltammetry data comparing the performance of activated carbon electrodes in a two-terminal cell with a 6 M KOH electrolyte with and without the addition of Triton X-100 to 5 mM concentration over a working voltage of 0.9 V. a) Cyclic voltammograms measureed at a sweep rate of 10 mV s^{-1}, b) variation of C_{sp} with CV scan rate, c) variation of C_{sp} derived from CV at 10 mV s^{-1} with electrode mass loading. Error bars are too small to be visible.

in the work reported in this thesis are around 120 μm thick (see Chapter 5, Figure 5.9), which are thinner than the 300 μm thick electrodes used in the previously reported work [50, 216]. Differences in electrode thickness may influence the efficacy of a surfactant-based electrolyte as, in the case of a hydrophobic material, thicker electrodes will show less penetration of electrolyte into the bulk.

Figure 6.4 compares cyclic voltammetry data for two sets of AC-based electrodes, one measured in 6 M KOH electrolyte (data presented in black) and the other in 6 M KOH electrolyte with Triton X-100 added to an overall concentration of 5 mM (data presented in orange). Cyclic voltammograms at 10 mV s^{-1} are shown in 6.4 (a): from these the C_{sp} was calculated to be 85.85 ± 0.05 F g^{-1} and

94.31 ± 0.04 F g^{-1} for the cells with and without Triton, respectively. The loss in capacitance is clearly reflected in the decrease in measured current across most of the sweep. However, the shape of the voltammogram for the cell containing the Triton additive is notably more rectangular in shape, which is consistent with the expected decrease in ESR. It can also be observed that the cell containing the Triton as an additive displays a tail at high voltages. This tail is indicative of the presence of Faradaic reactions but, as was discussed in Chapter 4, its exact origin is unclear. Although the improvement in ESR resulting from the addition of Triton to the 6 M KOH electrolyte to 5 mM concentration observed in these measurements agrees well with the results reported by Fic *et al.*[50, 216] the reduction of specific capacitance is at odds with the data they present.

The variation of C_{sp} with scan rate is shown in Figure 6.4 (b). The electrolyte with added Triton X-100 is shown to deliver inferior specific capacitance at low scan rates but at a scan rate of 50 mV s^{-1} the performance of the two devices converges, a result of the reduced resistance in the cell containing the Triton. The performance of this cell peaks at 10 mV s^{-1}, with C_{sp} decreasing as the scan rate is lowered further, which is likely to originate from a a leakage current, related to the tail in the voltammogram shown in Figure 6.4 (a).

The efficacy of wetting agents has previously been shown to depend in part on electrode areal mass density [218], which is investigated by the measurements presented in Figure 6.4 (c), which shows how the discharge capacitance of two electrode cells varies with electrode mass loading with and without Triton additive. It can be seen that the C_{sp} of the Triton-containing cell is inferior across the full range of areal mass loading examined. The measured values of C_{sp} for cells containing each electrolyte converge as the mass loading increases, perhaps due to the lowered surface tension of the Triton-containing electrolyte allowing better electrolyte penetration throughout the full thickness of the electrode, however this

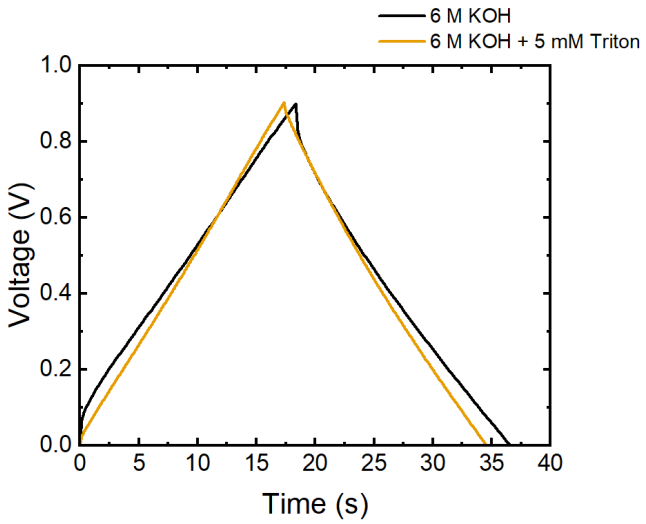

Figure 6.5: GCD profile measured at 1 A g^{-1} showing the performance of cells containing 6 M KOH with and without the addition of Triton X-100 at 5 mM concentration.

effect is slight, and even at a mass loading of almost 20 mg cm^{-2} its capacitance remains worse than that of the unadulterated 6 M KOH.

GCD profiles for two-electrode devices with the standard areal mass loading given in chapter 3, and 6 M KOH electrolyte with and without Triton X-100 are shown in Figure 6.5. It is immediately clear that the Ohmic drop of the Triton-containing device as the current reverses direction is smaller than that of the device without any additive. From multiple GCD cycles an ESR of 0.6 ± 0.03 Ω can be determined when the Triton is added to the electrolyte compared with 2.13 ± 0.003 Ω without. C_{sp}, calculated from the slope of the discharge curve is found to be 77.8 ± 0.1 F g^{-1} for former case, compared to 89 ± 1 F g^{-1} for the latter. Both of these results are in agreement with the trends in the CV data presented in Figure 6.4 above. This loss of capacitance is at odds with data presented in references [50, 216], in which no significant change in capacitance is observed at low current densities (0.2-2 A g^{-1}).

EIS data comparing two-electrode EDLCs with and without added Triton are

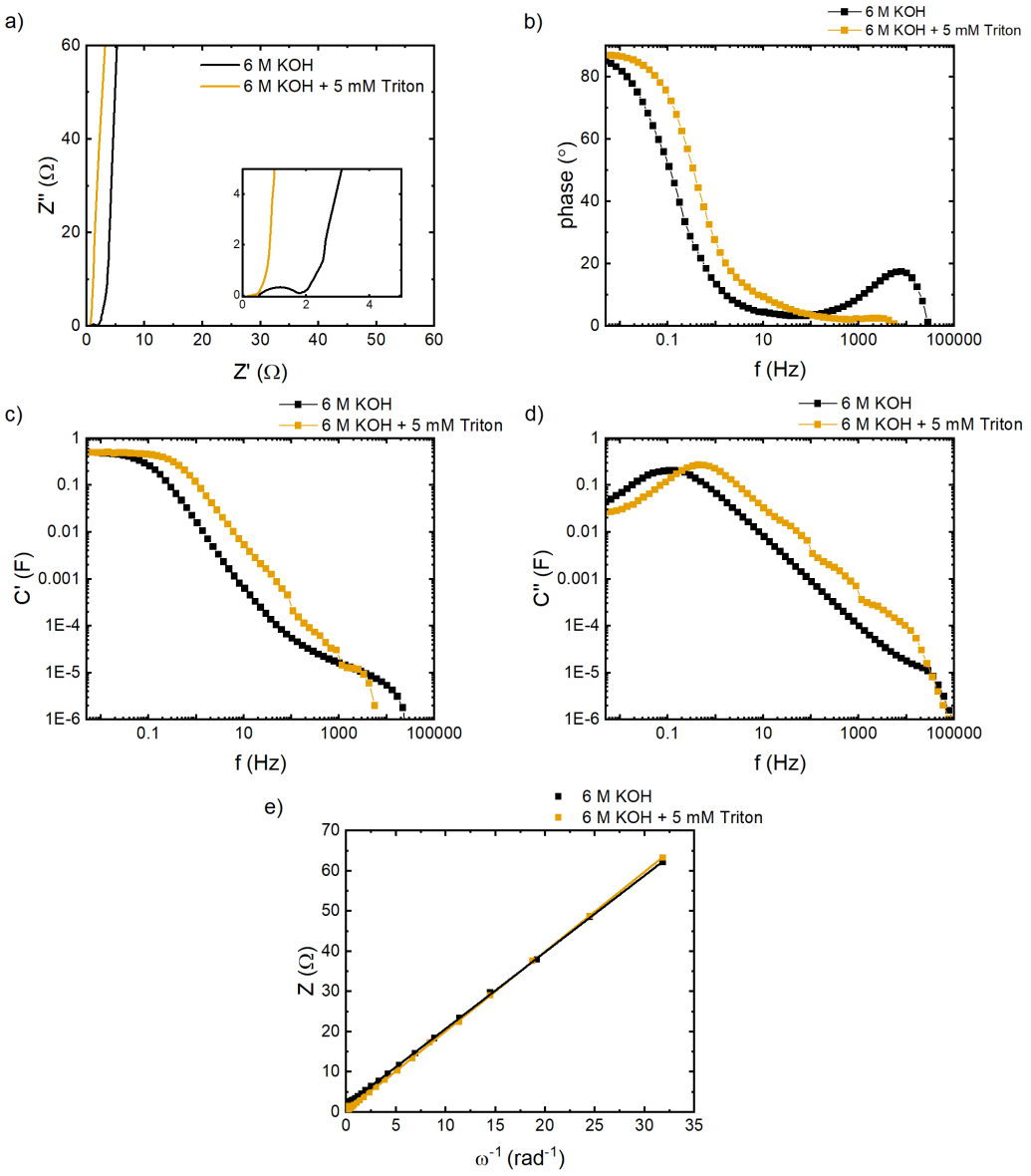

Figure 6.6: EIS data comparing the performance of cells containing 6 M KOH with and without the addition of Triton X-100 to 5 mM concentration. a) Nyquist plot; b) phase plot; c) real part of complex capacitance (C') against frequency; d) imaginary part of complex capacitance (C'') against frequency; e) magnitude of complex impedance (Z) plotted against the reciprocal of the angular frequency ω^{-1}. The lines shown in e) are lines of best fit. Discontinuities can be seen in the data in c) and d), the origin of which are not obvious and may be caused by vibrations or electrical noise.

shown in Figure 6.6. A Nyquist plot of the data is presented in Figure 6.6 (a) and it can be seen that with the addition of Triton to the electrolyte, the semi-circular region of the Nyquist plot shrinks from $\approx 2\ \Omega$ to $\approx 0.5\ \Omega$. As discussed in Chapter 2, section 2.2.4 this region (labelled as 'Internal Resistance' on Figure 2.11) corresponds to the ESR of the cell, encompassing contributions to ESR from both electrode and electrolyte resistivity, and is sometimes referred to as the 'charge transfer resistance' (CTR). This decrease in ESR is in agreement with the GCD data and is reflected in the phase plot (Figure 6.6 (b)), where the high frequency peak visible for the device without additive is absent when electrolyte containing Triton is used. Moreover, it can be seen that, as the frequency decreases, the phase angle more rapidly increases to over 80°, indicative of a transition to behaviour closer to that of an ideal capacitor.

The real and imaginary parts of the capacitance (C' and C'', respectively) are shown in Figures 6.6 (c, d). In spite of the significant reduction in capacitance observed in CV and GCD, both devices show a plateau in C' at similar values at low frequencies. This implies that both devices have similar double layer capacitances, confirmed by plotting Z against ω^{-1} (Figure 6.6 (e)), with almost identical slopes observed for both devices. C_{sp} calculated from the Z against ω^{-1} plot was determined to be 96.8 ± 0.2 F g^{-1} and 93.3 ± 0.2 F g^{-1} for the devices without and with Triton, respectively. This result, measured for an applied alternating (AC) voltage centred at a cell potential of 0 V suggests that there may be a voltage dependence to the differences in capacitance between the two devices – the variation of capacitance with operating voltage was discussed in depth in chapter 4, and includes variation in the double layer capacitance as well as pseudocapacitive and other Faradaic effects, hence it is not possible from EIS data about a single cell potential to conclude whether the addition of Triton impedes the formation of the double layer, suppresses Faradaic processes, or both. The variation of C'' is shown in Figure 6.6 (d). Both devices can be

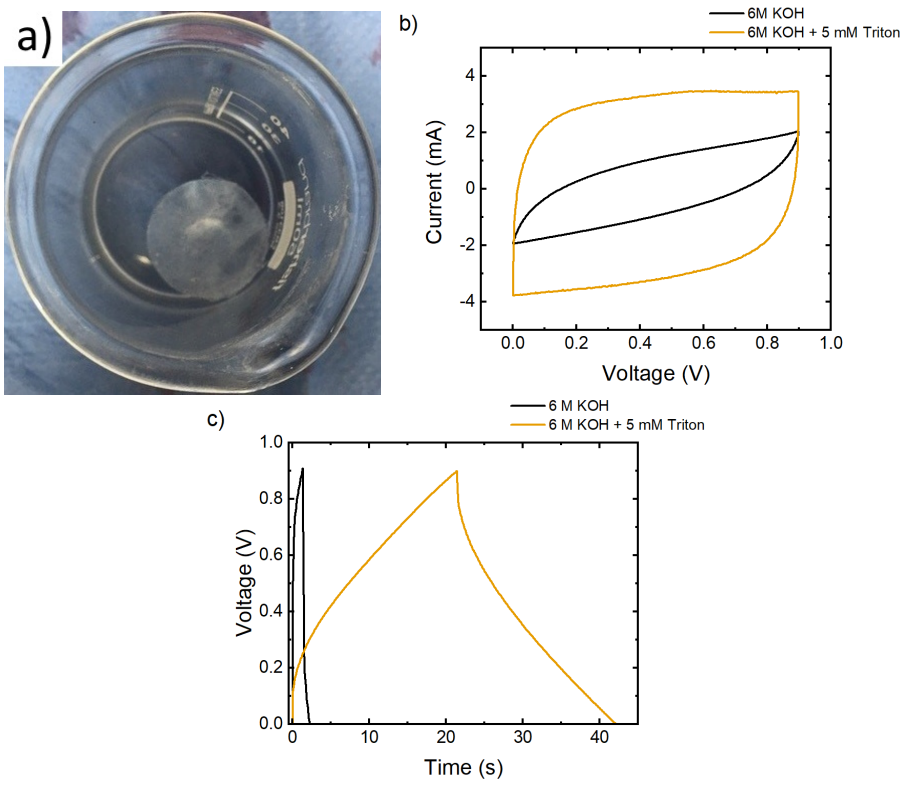

Figure 6.7: Effects of Triton on a hydrophobic Celgard separator: a) photograph showing the wetting of the Celgard after immersion in 6 M KOH with Triton addedat 5 mM concentration for 48 hours; b) cyclic voltammograms measured at a sweep rate 10 mV s^{-1}, and c) GCD profiles measured at a specific current of 0.5 A g^{-1} showing the performance of a Celgard separator in 6 M KOH compared with a Celgard separator soaked in 6 M KOH with 5 mM Triton.

seen to demonstrate pseudo-blocking behaviour, with a low frequency maximum in C'', in the case of the Triton-containing device this appears to transition to a local minimum at the very lowest frequencies investigated, suggestive of an increase in reactive behaviour at lower frequencies. This indicates the presence of a leakage current, which links to the decrease in C_{sp} observed at low CV scan rates.

6.2.2 Effect of Triton X-100 on hydrophobic separators.

One aspect in which the addition of Triton X-100 to the electrolyte was shown to improve the performance of EDLCs was in enabling the use of separators

based on hydrophobic materials. The voltammograms and GCD profiles in Figure 6.7 (b, c), show the behaviour of a two-terminal cell assembled with activated carbon electrodes, a Cellgard 2500 polymeric separator and aqueous 6 M KOH electrolyte. The hydrophobic nature of the Celgard separator severely impedes cell performance, as can be seen from the high ESR, $38 \pm 1\ \Omega$, and low C_{sp}, 30.7 ± 0.2 F g^{-1}, as determined from GCD at 0.1 A g^{-1}. The corresponding C_{sp} determined from CV measured at a sweep rate of 10 mV s^{-1} was even worse, at 19.26 ± 0.02 F g^{-1}.

Figure 6.7 (a) shows a Celgard separator soaked in 5 mM Triton in 6 M KOH for 24 hours. During this time, the Triton allows the separator to wet out completely and uniformly, changing from opaque white to translucent. When a Celgard separator soaked in the Triton-containing electrolyte prior to use is employed in a cell, the electrochemical behaviour dramatically improves, with the ESR decreasing to $2.41 \pm 0.09\ \Omega$, which is comparable to that observed when using the glass fibre separators utilised in the majority of the work presented here. Moreover, the C_{sp} increases to 55.9 ± 0.1 F g^{-1} when calculated from GCD measured at 0.5 A g^{-1} or 63.20 ± 0.04 F g^{-1}, when calculated from CV measured at a sweep rate of 10 mV s^{-1}. This result demonstrates that the addition of the surfactant to the electrolyte can allow a broader range of separator materials to be used, enabling the use of alternative electrolytes which may dissolve some separator materials and facilitating flexible devices, for which the glass fibre material used elsewhere in this thesis would be unsuitable.

6.2.3 Influence of Triton X-100 additive on the MWV of activated carbon electrodes in 6 M KOH.

6.2.3.1 Effect of Triton X-100 as an electrolyte additive on MWV

As discussed above, the addition of Triton X-100 to aqueous 6 M KOH electrolyte has been reported to increase the MWV of the EDLCs with activated carbon electrodes [50, 216] as some other electrolyte formulations have been reported to do, but without compromising either ESR and C_{sp}. To investigate this possible effect linear sweep voltammagrams were measured for three-electrode cells with glassy carbon disc electrodes in 6 M KOH and with the addition of Triton X-100 to 5 mM or 0.5 mM concentration, Figure 6.8. It can be seen that the inclusion of Triton X-100 does indeed slightly extend the stability window of the electrolyte, from ≈1.7 V to ≈1.8 V, and the extent of this change seems to increase with the quantity of Triton X-100. In both instances, the concentration of surfactant is well above the CMC (0.22 mM L^{-1} [231]), so this is in contrast with observations in the literature that increasing the concentration of surfactant beyond the CMC does not further increase stability [224].

Figure 6.9 shows three electrode cyclic voltammograms obtained at a sweep rate of 2 mV s^{-1} for AC electrodes in 6 M KOH electrolyte either in pure form or with the addition of 0.5 mM and 5 mM of Triton X-100. Using a specific current limit of 1 A g^{-1} , it can be seen that with the addition of 5 mM of Triton X-100, the increases in cathodic and anodic current are delayed by 60 ± 30 mV and 10 ± 30 mV, respectively. While the overpotential for the HER is comparable to that measured on glassy carbon, the oxidation overpotential of 10 ± 30 mV is small enough to be within experimental error. Meanwhile, a device produced with 0.5 mM Triton X-100 as an additive appears to suffer a small decrease in MWV. However, in both cases the changes in MWV are slight. It can also be observed that the peak at around -0.8 V vs Ag/AgCl is suppressed with the addition of

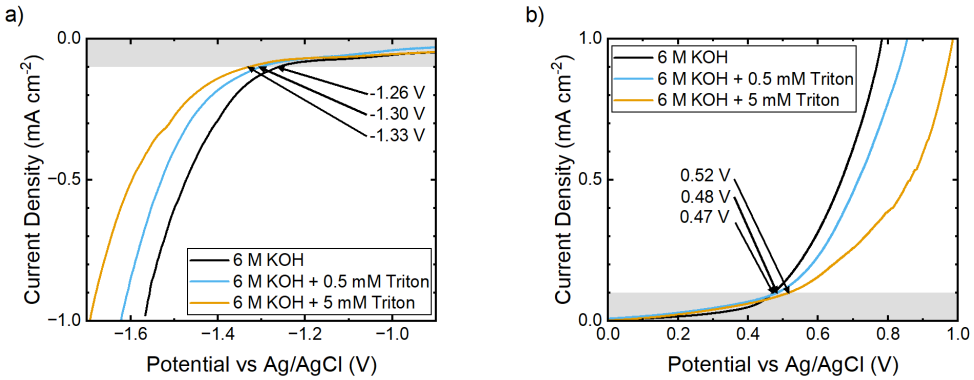

Figure 6.8: Three-electrode LSV data obtained at a sweep rate of 2 mV s^{-1} from a glassy carbon working electrode in 6 M KOH with varying quantities of Triton X-100. a) Negatively biased, b) positively biased. The electrode was cleaned and polished and the electrolyte replaced between each test. The point at which each dataset surpasses a current density 0.1 mA cm^{-2} is indicated as the approximate onset of electrolyte breakdown.

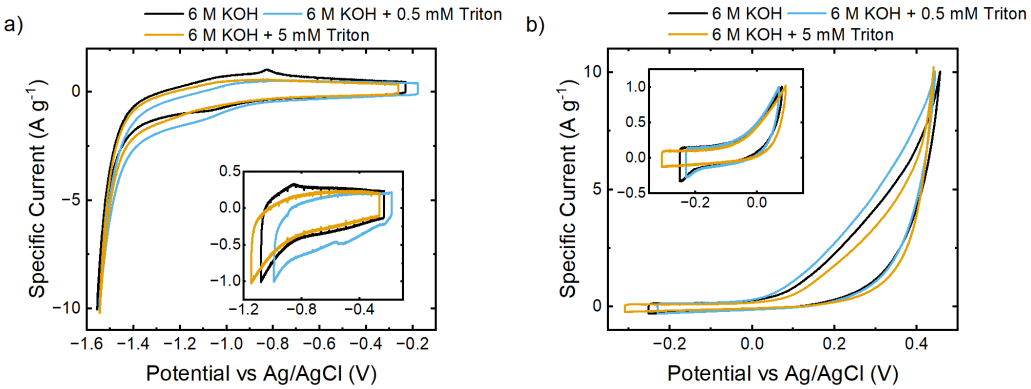

Figure 6.9: Three-electrode cyclic voltammetry data obtained at 2 mV s^{-1} potential swepp rate for AC electrodes in 6 M KOH electrolyte and with the addition of varying concentrations of Triton X-100. A different electrode was used for each test. a) Negatively biased working electrode, b) positively biased working electrode. The main graphs show the cyclic voltammograms with the scan reversed at $j = 10$ A g^{-1}, while the insets show voltammograms reversed at $j = 1$ A g^{-1}. The data for electrodes in 6 M KOH without Triton X-100 are reproduced from Chapter 4.

Triton X-100. This peak is attributed to hydrogen adsorption/desorption [172], and its suppression may be due to the Triton X-100 coating the electrode surface, hence preventing the adsorption of hydrogen.

To verify that MWV did indeed remain unchanged with the addition of Triton X-100, in disagreement with the work of Fic *et al.* [50, 216], 5,000 GCD cycles

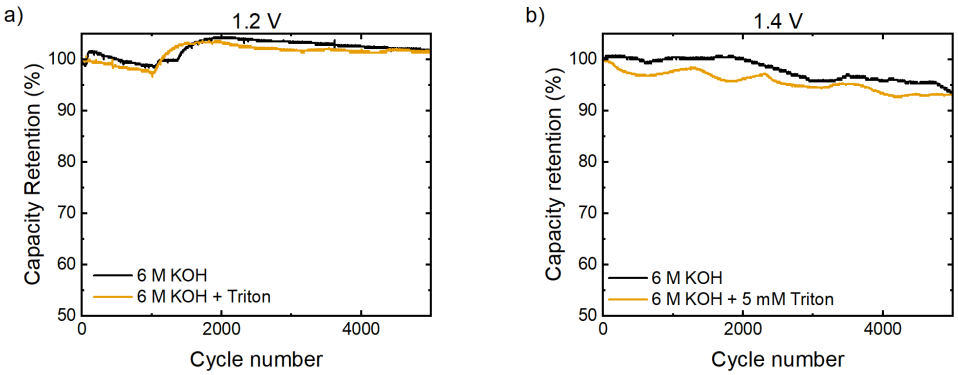

Figure 6.10: Capacity retention measured over 5,000 GCD cycles at 1 A g^{-1} for AC electrodes in 6 M KOH and 6 M KOH with 5 mM Triton X-100, operating at a) 1.2 V and b) 1.4 V.

measured at a specific current of 1 A g^{-1} were carried out on a two electrode device containing 5 mM Triton at working potentials of 1.2 V and 1.4 V. These data are shown in Figure 6.10, alongside data for a cell with a conventional 6 M KOH electrolyte, reproduced from chapter 4. As expected, the Triton X-100 containing EDLC behaves in a similar manner to that of a cell without the additive when the working potential is 1.2 V, recording a slight increase in capacity to 101% of the initial value. Similarly, at a working potential 1.4 V it shows a similar decrease in capacity to 93%, compared to the 94% capacity decrease observed for the device without Triton X-100. Both cells display a number of peaks in the data, which may be attributed to temperature fluctuations in the laboratory.

6.2.3.2 Pre-soaking electrodes in Triton X-100.

As the addition of Triton X-100 to 5 mM concentration was not found to measurably extend the MWV of the EDLCs used in the experiments above, it was initially decided to increase the concentration of Triton X-100 in the electrolyte. This was not possible as beyond a concentration of 5 mM, as it was not possible to completely dissolve the surfactant in the electrolyte, so an alternative approach of soaking the electrodes in Triton in order to ensure a high concentration at the

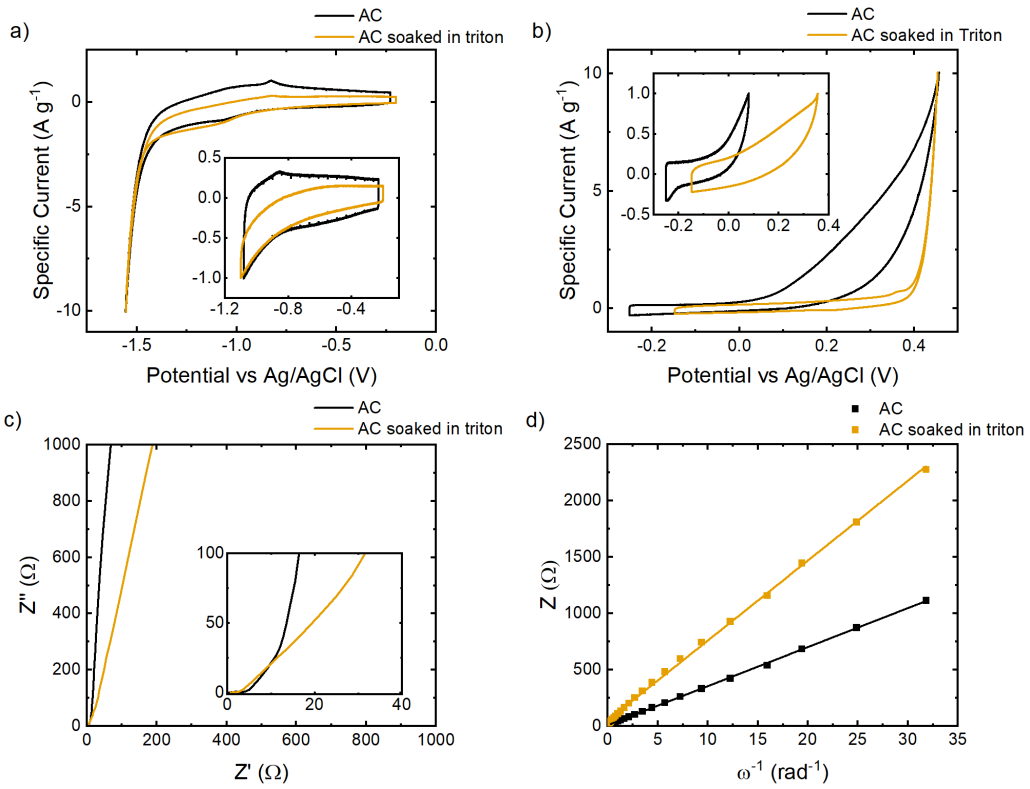

Figure 6.11: a), b) Three-electrode cyclic voltammetry data obtained at a sweep rate of 2 mV s^{-1} for AC electrodes in 6 M KOH compared with AC electrodes which were soaked in Triton X-100 prior to cell assembly: a) negatively biased working electrode, b) positively biased working electrode. The main graphs show the cyclic voltammograms with the scan reversed at $j = 10$ A g^{-1}, while the insets show voltammograms where the cycle was reversed at $j = 1$ A g^{-1}. Three electrode EIS data for the same configuration: c) Nyquist plots, with the high frequency region shown as an inset, d) Z plotted against ω^{-1}.

electrode surface was adopted.

Figure 6.11 shows data from a three-electrode cell assembled with activated carbon electrodes soaked in Triton X-100 prior to assembly. From the voltammograms shown in Figure 6.11 (a,b), it can be seen that although the cathodic current corresponding to hydrogen evolution when the working electrode is negatively biased is almost unchanged, the onset of the anodic oxidation current at the positively biased working electrode is significantly delayed, suggesting an increase in MWV from ≈1.2 V to ≈1.4 V.

This apparent improvement in MWV, however, comes at a cost, as can be determined from the EIS data shown in Figure 6.11 (c, d). The Nyquist plot (Figure 6.11 (c)) shows that although the CTR region is essentially unchanged at around 1.5 Ω, the diffusion/pore resistance increases significantly, from ≈10 Ω to >20 Ω. Meanwhile, the C_{sp}, as calculated from the Z-ω^{-1} plot, falls dramatically from 96.9 ± 0.6 F g^{-1} to 32.8 ± 0.4 F g^{-1}. Using this method to determine C_{sp} comes with the caveats that three-electrode measurements can significantly overstate C_{sp}, and that as this measurement was performed at a single potential (the OCP) it neglects any possible voltage dependence of the capacitance, both of which mean that such C_{sp} values cannot be compared quantitatively with those obtained from two-electrode data. Nonetheless, this method provides an estimate of C_{sp} which can be combined with the estimated MWV obtained from CV to provide qualitative information regarding the specific energy density of the electrodes via equation 1.3, which is particularly valuable in understanding the trends resulting from electrode/electrolyte treatments. The results of this show that in spite of the increased MWV, the estimated specific energy density of the electrodes falls from 19.4 ± 0.1 Wh kg^{-1} (69.7 ± 0.4 J g^{-1}) to 8.9 ± 0.1 Wh kg^{-1} (32.1 ± 0.4 J g^{-1}).

Two electrode CV and GCD data, comparing Triton X-100 soaked activated carbon electrodes with those which did not undergo this pretreatment, both operating in 6 M KOH are shown in Figure 6.12. Performance over a working voltage of 0.9 V for CV obtained at a 10 mV s^{-1} sweep rate and GCD at a specific current of 1 A g^{-1} is shown in 6.12 (a, b). As is obvious from a visual inspection of the plots, soaking the electrodes in Triton X-100 significantly reduces electrochemical energy storage performance, with the C_{sp}, obtained from CV at a 10 mV s^{-1} sweep rate falling to 25.6 ± 0.02 F g^{-1} compared with 95.59 ± 0.03 F g^{-1} for untreated electrodes. Likewise, the C_{sp} and ESR calculated from GCD at a current of 1 A g^{-1} was measured as 9.8 ± 0.2 F g^{-1} and 7.7 ± 0.4 Ω, respectively,

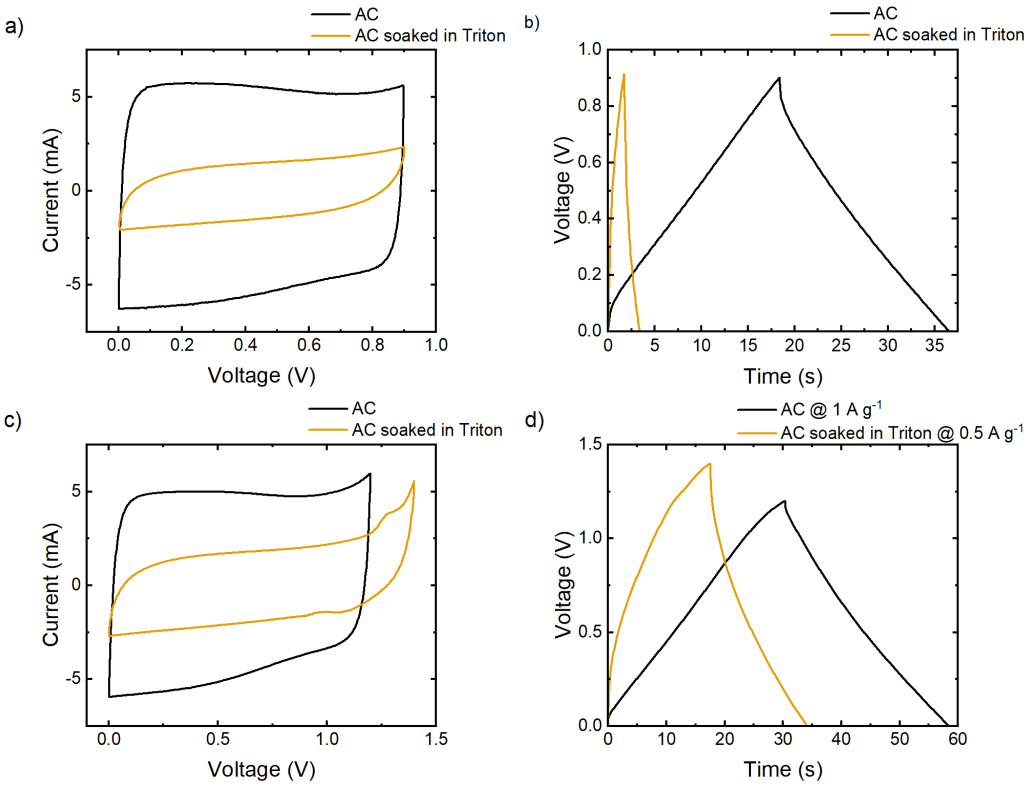

Figure 6.12: CV and GCD profiles for Triton X-100 soaked activated carbon electrodes in a two-electrode cell compared with electrodes without soaking: a) cyclic voltammograms obtained at a sweep rate of 10 mV s^{-1} over a 0.9 V window; b) GCD profiles measured at 1 A g^{-1} over a 0.9 V window; c) cyclic voltammograms measured at a sweep rate of 10 mV s^{-1} for activated carbon over the full MWV of 1.2 V, and for the Triton X-100 soaked acticated carbon at the prevously determined MWV of 1.4 V; d) GCD profiles for activated carbon electrodes obtained at a specific current of 1 A g^{-1} over the full MWV of 1.2 V, and for the Triton X-100 soaked activated carbon electrodes at a specific current of 0.5 A g^{-1} over their MWV of 1.4 V.

for the treated electrodes compared with 99.7 ± 0.1 F g^{-1} and 2.01 ± 0.21 Ω for the untreated electrodes.

Figure 6.12 (c, d) shows behaviour at the 1.4 V MWV of the Triton soaked electrodes determined from three-terminal measurements, compared to the untreated electrodes operating at their MWV of 1.2 V (as determined in chapter 4). Cyclic voltammograms measured at a sweep rate of 10 mV s^{-1} are shown in Figure 6.12 (c). Once the potential exceeds 1.2 V, the Triton X-100 soaked

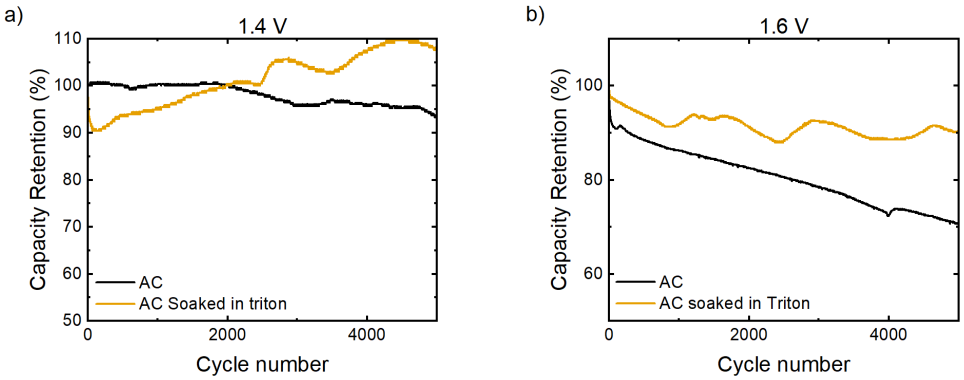

Figure 6.13: Capacity retention over 5,000 GCD cycles at a) 1.4 V, and b) 1.6 V for untreated electrodes cycled at 1 A g^{-1}, and Triton X-100 soaked activated electrodes cycled at 0.5 A g^{-1}.

electrodes show an oddly-shaped tail containing a shoulder, in contrast the more usual tails developed by untreated electrodes at elevated voltages. The specific capacitance of the Triton X-100 soaked electrodes at 1.4 V remains low at only 32.00 ± 0.02 F g^{-1}, compared with 109.86 ± 0.08 F g^{-1} measured for the untreated electrodes operating at 1.2 V. GCD profiles are shown in Figure 6.12 (d): in this instance the Triton X-100 soaked electrodes were tested at a lower specific current of 0.5 A g^{-1}, compared with the usual 1 A g^{-1} used for the untreated electrodes. At this lower current loading and greater working voltage, C_{sp} increased slightly to 30.18 ± 0.03 F g^{-1}, in line with the value derived from CV, while the ESR remains high at 7.031 ± 0.003 Ω. This is far inferior to the values of 99.409 ± 0.005 F g^{-1} and 1.607 ± 0.006 Ω measured for the conventional electrodes over a working voltage of 1.2 V with a current density of 1 A g^{-1}.

In order to verify the expanded MWV, the Triton X-100 soaked electrodes were subject to 5,000 GCD cycles in a two-terminal configuration over the potential window of 1.4 V determined by the three-terminal measurements described above. A lower specific current of 0.5 A g^{-1} was selected in order to ensure this test was comparable to the conventional electrodes being tested at 1 A g^{-1}: the lower current means that in spite of the inferior capacitance, the charge/discharge time

remains comparable, thus ensuring that the device spends a comparable amount of time at the test voltage. Moreover, the lower specific current also helps to minimise the Ohmic drop and thus the impact of resistance overpotential on the measurements of cells using the treated electrodes. Capacity retention for the Triton X-100 soaked electrodes at 1.4 V and 1.6 V is shown alongside data obtained from cells using untreated electrodes in Figure 6.13. As with the data presented in figure 6.10, the data shows a number of peaks and troughs which may be attributable to temperature fluctuations in the laboratory.

At a working cell potential of 1.4 V the conventional electrodes suffer a small drop in capacity to 93% of the original value whereas the Triton X-100 soaked electrodes see a capacity increase to 108% of the original value. At 1.6 V, the Triton X-100 soaked electrodes see a small decrease in capacitance to 90% of the original value after 5,000 GCD cycles, while the untreated electrodes suffer a much more significant decrease to 71% of their original capacity.

These results would appear to confirm that the Triton X-100 soaked electrodes have an improved MWV of 1.4 V. However, it is important to note that in spite of the reduced current density, the Ohmic drop in cells made with the treated electrodes remained higher than that of measured for the cells assembled with untreated electrodes, at ≈150 mV compared to ≈50 mV. This means that up to half of the improved MWV may be attributable to additional Ohmic drop resulting from the increased ESR of the treated electrodes alone.

6.2.3.3 Additives beyond Triton X-100.

To understand if the behaviour described above is unique to Triton X-100, two other electrolyte additives were considered: Tween-20, which is another non-ionic

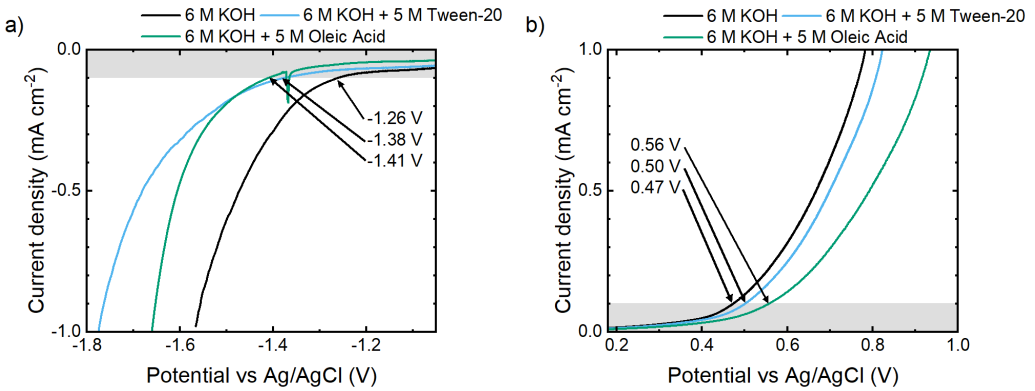

Figure 6.14: Three-electrode LSV data obtained at a sweep rate of 2 mV s^{-1} for a glassy carbon working electrode in 6 M KOH, 6 M KOH with 5 mM Tween-20 and 6 M KOH with 5 mM oleic acid: a) negatively biased working electrode, b) positively biased working electrode. The point at which each dataset surpasses a current density 0.1 mA cm^{-2} is indicated as an approximate onset of electrolyte degradation. The spike in the oleic acid data at −1.4 V in a) is an artefact which may result from external vibration or electrical noise.

surfactant [232], and oleic acid, a fatty acid which will react with the KOH in the electrolye to form potassium oleate, an anionic surfactant [233, 234].

Figure 6.14 shows the behaviour of three-electrode cells using glassy carbon working electrodes and 6 M KOH alone or with the addition of either Tween-20 or oleic acid to 5 mM concentration. At negative potentials (Figure 6.14 (a)), the two additives delay the onset of the HER current by similar amounts (0.12 V and 0.15 V for the Tween-20 and Oleic acid, respectively). However, beyond this initial onset, the current can be seen to increase much more rapidly in the case of the electrode using oleic acid as an additive. For the positively biased working electrode, the Tween-20 has little effect on the onset of the oxidation current, delaying it by only 0.03 V, in contrast to the larger overpotential of 0.09 V recorded for the use of oleic acid. This difference may be due to the negative charge of the oleate molecules: as the electrode is polarised more negatively they are repelled from the electrode surface, and their influence reduced, but they are strongly attracted to the electrode when a positive bias is applied, increasing their effect. As the failure of aqueous capacitors has been linked to the oxidation of the posit-

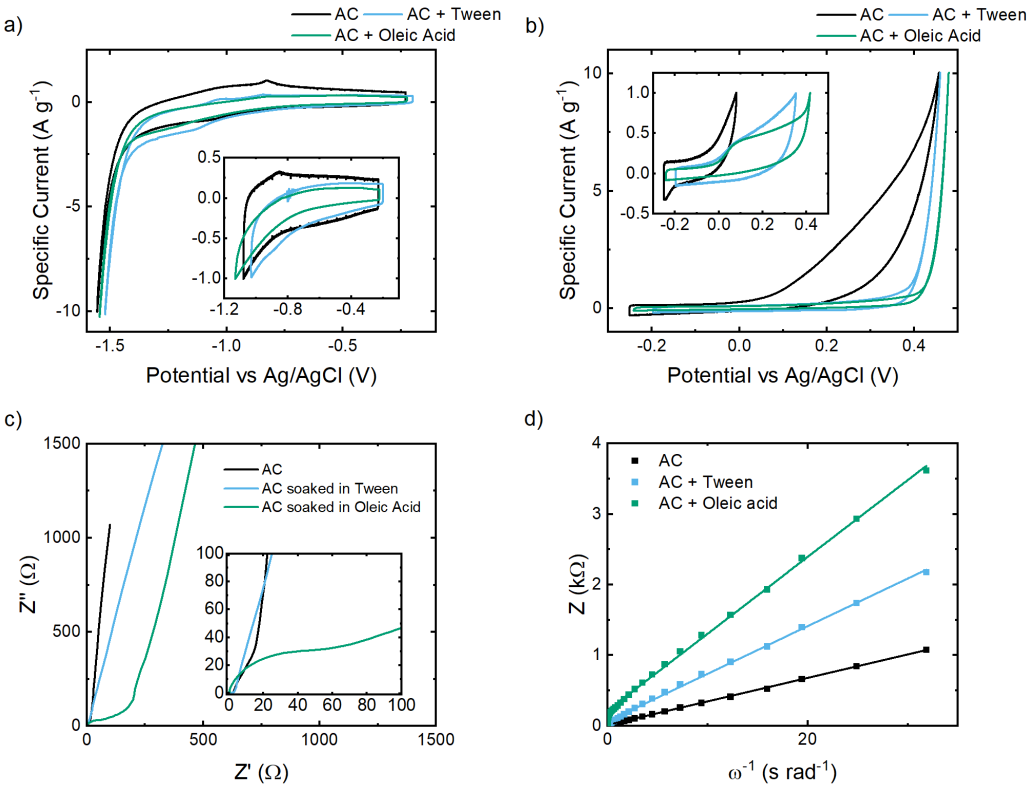

Figure 6.15: a), b) Three-electrode cyclic voltammetry data measured at 2 mV s^{-1} sweep rate for activated electrodes in 6 M KOH compared with activated carbon electrodes soaked in either Tween-20 and oleic acid: a) negatively biased working electrode, b) positively biased working electrode. The main graphs show cyclic voltammograms with the scan reversed at $j = 10$ A g^{-1}, while the insets show voltammograms reversed at $j = 1$ A g^{-1}. Three electrode EIS data were obtained for the same configurations: c) Nyquist plots, with the high frequency region shown as an inset, d) Z plotted against ω^{-1}.

ive electrode [35, 172–174], this may make the use of oleic acid of particular interest.

Figure 6.15 compares three-electrode CV and EIS data for activated carbon electrodes soaked in Tween-20 and oleic acid with data for untreated electrodes. As was observed when electodes were soaked in Triton X-100 (Figure 6.11), the increase in cathodic current at the negatively biased working electrode is essentially unchanged (Figure 6.15 (a)), while the onset of the oxidation current when the working electrode is positively biased is delayed (Figure 6.15 (b)). For the Tween-20, this results in an apparent MWV of ≈1.4 V, the same as that measured for electrodes soaked in Triton X-100, while the use of oleic acid sees

the apparent MWV increased to ≈1.6 V.

EIS data were used to give an estimate of how the electrodes soaked in Tween-20 or oleic acid might perform in real devices. The Nyquist plot shown in Figure 6.15 (c), demonstrates that, like the Triton X-100 soaked electrodes, the CTR is unchanged with the addition of Tween-20, however it is also likely that in practice the ESR would be seen to increase in a two-electrode cell, as was observed with Triton X-100. Z-ω^{-1} plots were used to estimate C_{sp}: for the device produced with Tween-20 soaked electrodes this was found to be 41.2 ± 0.5 F g^{-1}, leading to an estimated specific energy density of 11.2 ± 0.1 Wh kg^{-1} (40.3 ± 0.5 J g^{-1}). This value is superior to that found for the Triton X-100 soaked electrodes, but still much lower than that obtained for untreated electrodes, in spite of their lower MWV. The oleic acid was shown to have a significantly deleterious effect on electrode performance, with the CTR increasing from ≈ 1.5 Ω to ≈ 50 Ω, while the C_{sp} decreased to 25.5 F g^{-1}, leading to an estimated specific energy density of only 9.06 ± 0.08 Wh kg^{-1} (32.6 ± 0.3 J g^{-1}).

6.2.4 Influence of Surface Chemistry on the effectiveness of Triton X-100

A potential cause of the inability to replicate the results of Fic *et al.* [50, 216], may originate in differences between the activated carbon used in the studies reported here (Supelco) and that used in the work reported in the literature. Fic *et al.* used Norit SX-2, which was 'reactivated' in KOH. The reactivation treatment significantly altered the properties of the activated carbon, including decreasing surface oxygen [50, 216, 235]. Since the primary role which the surfactant plays involves the electrode-electrolyte interface, it is reasonable to assume that this may be significantly influenced by the surface chemistry of the activated carbon. To this end, the surface composition of the activated carbon used in this study,

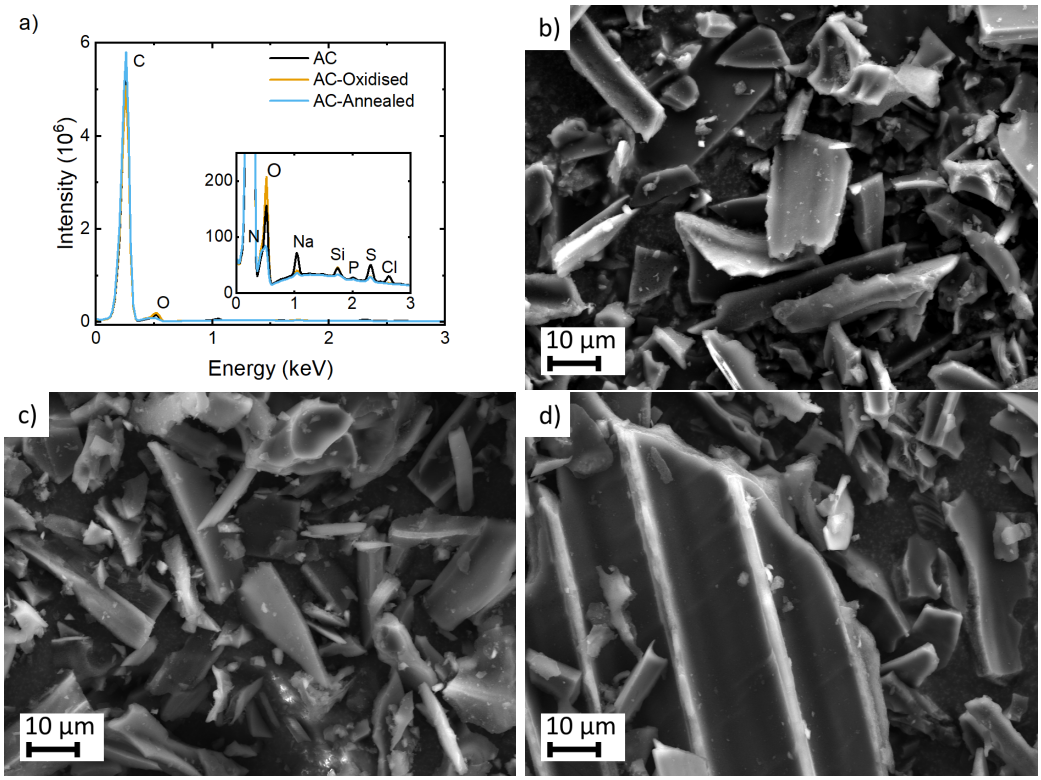

Figure 6.16: a) EDX spectra for as-received activated carbon (black), annealed activated carbon (blue), and HNO_3-treated activated carbon (orange). SEM micrographs obtained using secondary electrons of b) as-recieved activated carbon, c) annealed activated carbon, and d) HNO_3-treated activated carbon.

particularly the concentration of oxygen-containing (and hence, polar) SFGs was modified by simple techniques. Activated carbon was oxidised by immersion in concentrated (70%) HNO_3 for 48 hours, and reduced by annealing in a nitrogen atmosphere at ≈1000 °C for 15 minutes. More volatile SFGs such as carboxyls can decompose at temperatures below 370 °C whereas more stable SFGs such as carbonyls and quinones may survive to almost 1000 °C, hence a high annealing temperature was necessary to remove as many of the oxygen-containing SFGs as possible [49, 166]. EDX was used to provide a qualitative assessment of how these treatments altered the surface concentrations of oxygen and nitrogen in the acid-treated and annealed activated carbons. Electrodes were produced from the annealed activated carbon for electrochemical analysis whereas the effects of HNO_3 treatment was assessed by soaking pre-made electrodes in the acid, under

the assumption that surface functional groups produced in this process would be the same as those created by similarly treating the as-received material.

EDX spectra obtained from as-recieved and modified activated carbons are shown in Figure 6.16 (a), alongside SEM images of the same samples, Figure 6.16 (b,c,d). From the SEM images, it is clear that neither the oxidation nor the annealing process noticeably affects sample morphology, but the EDX spectra reveal changes to the surface chemistry of the samples. In all cases, the spectrum is dominated by a large carbon peak, as expected. The next most prominent peak is the oxygen peak; this is significantly larger in the oxidised sample, indicating an increase in surface oxygen which, although diminished, is still clearly present in the annealed sample. The presence of a clear oxygen peak after annealing indicates the presence of oxygen-containing SFGs which were not fully decomposed, but may also partly be due to atmospheric oxygen adsorbed on the sample surface. Any nitrogen peak would be expected to be visible between the carbon and oxygen peaks, but is not discernible in any samples, demonstrating than annealing the activated carbon under a nitrogen atmosphere did not introduce a detectable quantity of nitrogen-containing SFGs, which would influence the electrochemical properties of the annealed material, although we cannot rule our the presence of a small signal buried in the 'tail' of the carbon x-ray line. Also visible in spectra from the as-received activated carbon are peaks corresponding to sodium, silicon, potassium sulphur and chlorine – all of these trace contaminants appear to be removed by annealing, and all but the silicon are removed by the oxidation treatment.

Raman spectroscopy was used to investigate whether the annealing process had any effect on the structure of the AC. High temperature annealing can significantly alter the structure and defects of carbon materials: in highly ordered materials such as CNTs, annealing can introduce defects and disorder [166], whereas in less ordered materials such as activated carbon fibres, the annealing process can lead

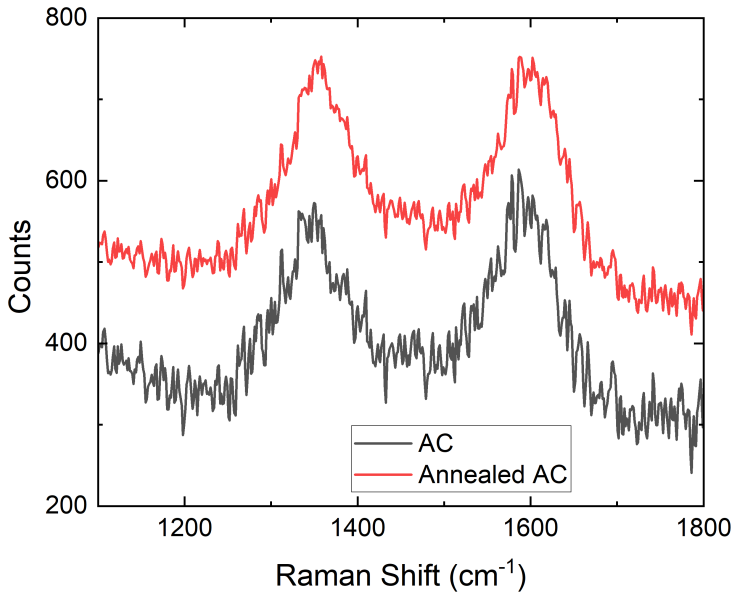

Figure 6.17: Raman spectra comparing the region of the D and G peaks for as-received (black) and annealed (red) AC.

to graphitization of the material. Raman spectra of the regions of the D and G peaks as-received and annealed AC are shown in Figure 6.17. It can be seen that there is little difference between the two samples, both showing the broad peaks of equal height typical of AC, verifying that this short anneal does not significantly alter the structure of the material [236].

Figure 6.18 compares cyclic voltammograms and EIS data of electrodes containing oxidised and annealed activated carbons with those produced from the as-received material. Based upon the cyclic voltammograms (figure 6.18 (a,b)), the annealed activated carbon shows little change relative to the as-recieved activated carbon suggesting a similar MWV of 1.2 V. In contrast, the HNO_3-treated electrodes shows significantly altered performance at negative potentials (figure 6.18 (a)), with the development of a large irreversible redox peak at ≈ -0.6 V and an increase of the hydrogen evolution potential by 0.1 - 0.2 V. Although the redox peak disappears on the second cycle (orange dashed line), the potential at which a large specific current of 10 A g^{-1} is measured is unchanged. If this irreversible redox peak is linked to

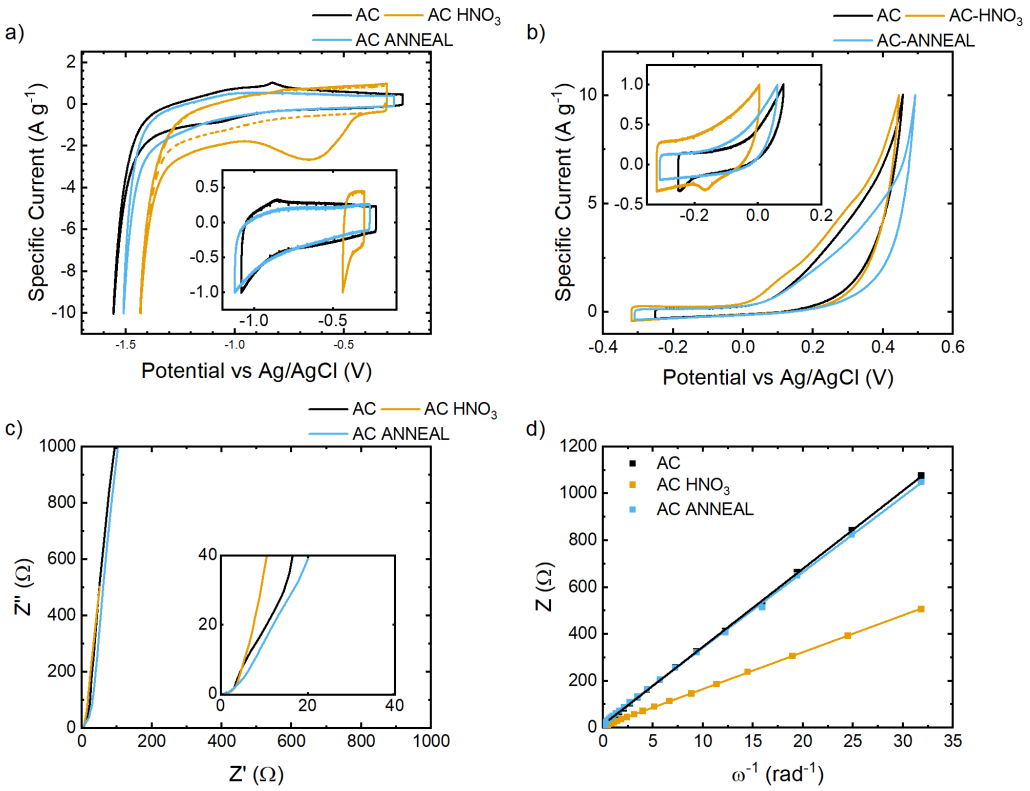

Figure 6.18: Three-electrode characterisation of electrodes prepared with as-received activated carbon (reproduced from Chapter 4) (black), HNO_3-treated activated carbon electrodes (orange), and electrodes prepared with annealed activated carbon (blue). (a, b) Cyclic voltammograms: a) negative potentials, and b) positive potentials (relative to OCP). The main graphs show the cyclic voltammograms with the scan reversed at $j = 10$ A g^{-1}, while the insets show voltammograms reversed at $j = 1$ A g^{-1}. The first cycle over each current range is shown with a solid line, while in a) second cycle to 10 A g^{-1} for the HNO_3-treated electrode is shown with a dashed line. (c, d) EIS data: c) Nyquist plots, and d) Z-ω^{-1} plots.

degradation and capacity loss, it could limit the MWV of the device to below 0.5 V.

Nyquist plots are shown in Figure 6.18 (c). All three samples appear to have similar ESRs, as defined by the CTR, of around 1.5 Ω. However, it appears that relative to electrodes made with the as-received activated carbon, oxidised electrodes have a reduced diffusion resistance, while electrodes made with annealed activated carbon show a slightly increased diffusion resistance, likely to be linked to changes in hydrophobicity. The linear nature of the Z-ω^{-1} plots shown in Figure 6.18 (d), confirms the good capacitor-like behaviour of all three activated

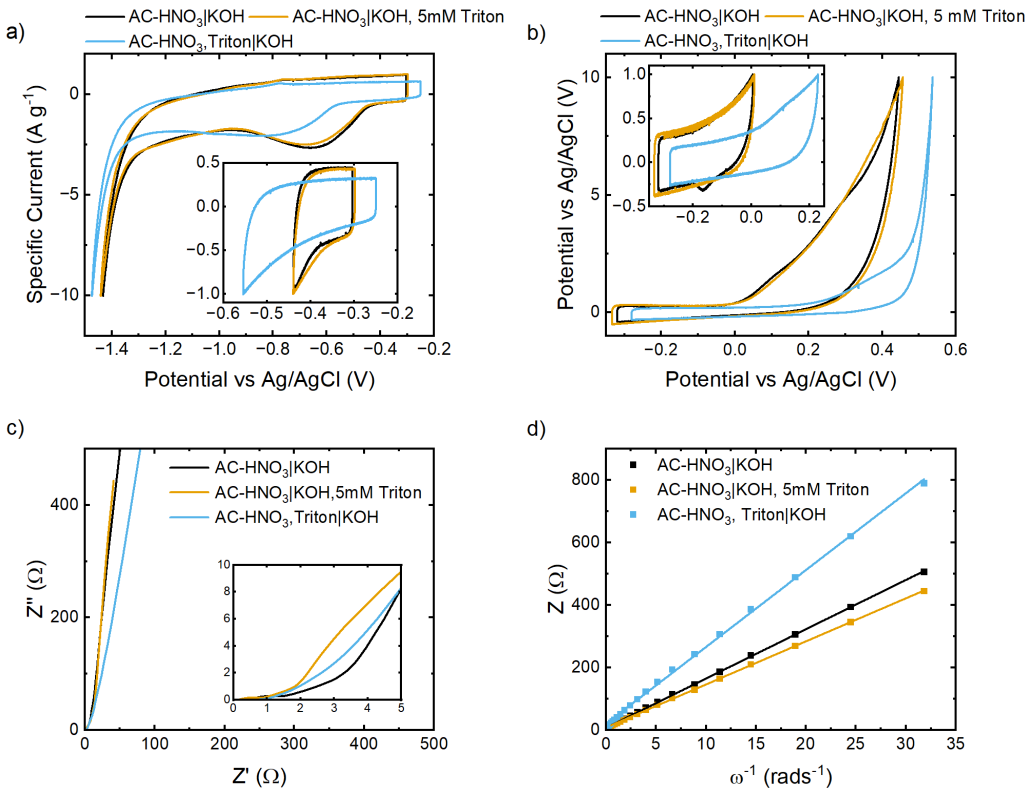

Figure 6.19: Cyclic voltammograms in the a) negative, and b) positive ranges, and c) Nyquist and d) Z-ω^{-1} plots, of HNO_3-treated electrodes tested in 6 M KOH (black), tested in 6 M KOH with 5 mM Triton (orange), and soaked in Triton X-100 before testing in 6 M KOH (blue). The main graphs show the cyclic voltammograms with the scan reversed at $j = 10$ A g^{-1}, while the insets show voltammograms reversed at $j = 1$ A g^{-1}. The first cycle over each current range is presented.

carbons and was used to estimate C_{sp}. Electrodes containing oxidised activated carbon were found to have a significantly enhanced C_{sp} of 154.8 ± 0.5 F g^{-1}. Although the annealed activated-carbon based electrodes had a similar gradient (indicating a similar capacitance) to the those produced from as-recieved activated carbon, the mass loading of the former electrode was ≈30 % higher, leading to a reduced C_{sp} of 73.9 ± 0.5 F g^{-1}. These changes in performance may be due to oxygen-containing SFGs (increased in coverage by acid treatment) enhancing the wettability of the activated carbon [51–53] while also providing Faradaic charge storage [54].

Figure 6.19 shows three electrode cyclic voltammetry (a, b) and EIS (c, d) data for the HNO_3-treated electrodes tested in 6 M KOH (labelled AC-HNO_3|KOH), with the addition of 5 mM Triton X-100 (labelled AC-HNO_3|KOH, 5 mM Triton), and with acid treated electrodes soaked in Triton X-100 prior to cell assembly (labelled AC-HNO_3, Triton|KOH). With regard to the CV data, like the untreated AC, the addition of Triton X-100 to the electrolyte to 5 mM concentration has little impact, while soaking the electrodes in Triton X-100 appears to extend their stable region by $\approx$ 0.2 V in the positive direction. However, unlike electrodes produced from the as-received activated carbon, soaking these electrodes in Triton X-100 also appears to extend the stable region by $\approx$ 0.2 V in the negative bias direction by suppressing the redox peak observed at -0.8 V.

Nyquist and Z-ω^{-1} plots are shown in Figure 6.19 (c) and (d), respectively. All three electrodes show similar CTRs of between 1 Ω and 2 Ω, with the electrodes in plain KOH and with 5 mM Triton X-100 in KOH showing slightly better capacitor-like behaviour than the Triton X-100-soaked electrodes, indicated by the more vertical capacitive region of the Nyquist plot. All three devices demonstrated good enough capacitor-like behaviour to show linear relationships on the Z-ω^{-1} plot, allowing their capacitance to be estimated. The electrodes tested in KOH with 5 mM Triton X-100 appeared to show an increase in capacitance to 177 ± 0.8 F g^{-1}, while the Triton X100-soaked electrodes saw their capacitance fall by around 30 % to 99.1 ± 0.8 F g^{-1}.

Figure 6.20 shows two-electrode CV and GCD data for the HNO_3-treated activated carbon based electrodes compared with similar electrodes soaked in Triton X-100. CV data obtained at a sweep rate of 10 mV s^{-1} over a working potential range of 0.9 V are shown in Figure 6.20 (a). As was indicated by the EIS data, the oxidised activated carbon based electrodes show a significant increase in C_{sp} to 119.1 ± 0.1 F g^{-1}, compared to 95.49 ± 0.1 F g^{-1} for those made with untreated AC

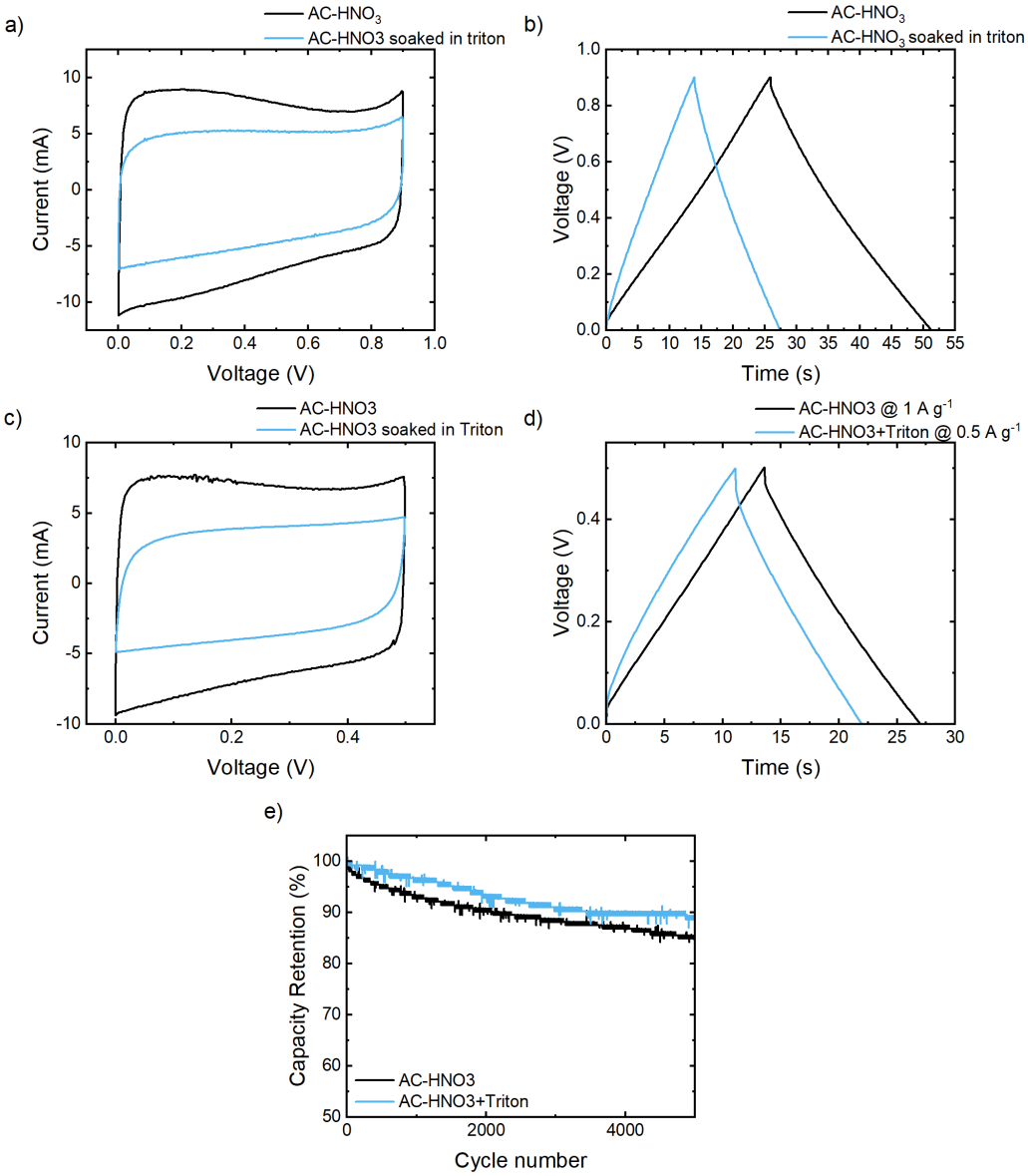

Figure 6.20: Two-electrode data for HNO_3-treated electrodes (black) and HNO_3-treated electrodes soaked in Triton X-100 (blue). a, c) Cyclic voltammograms obtained at a sweep rate of 10 mV s^{-1} and working voltages of a) 0.9 V, and c) 0.5 V. b, d) GCD profiles at working voltages of b) 0.9 V, d) and 0.5 V. (e) capacity retention over 5,000 GCD cycles at a working voltage of 0.5 V. Both GCD datasets shown in (b) were obtained with a specific current of 1 A g^{-1}. In d) and e) the Triton X-100-soaked electrodes were instead cycled at 0.5 A g^{-1}.

(table 5.3). This is almost halved to 65.16 ± 0.03 F g^{-1} when electrodes are soaked in Triton X-100. GCD data over a working voltage of 0.9 V and with a specific current of 1 A g^{-1} are shown in Figure 6.20 (b). As with the CV data, a fall in C_{sp} is observed when comparing oxidised electrodes with the same material when soaked in Triton X-100, with a decline from 116.1 ± 0.1 F g^{-1} to 53 ± 0.1 F g^{-1} observed. Although this is a significant decrease it is nonetheless much less than the 90% decrease in C_{sp} observed for the untreated activated carbon electrodes soaked in Triton X-100 (see section 6.2.3.2). This behaviour may be explained by the ESR of the oxidised electrodes being almost unchanged by soaking in Triton X-100, having a value of 0.77 ± 0.04 Ω compared with 0.78 ± 0.02 Ω for the unsoaked electrodes.

Although electrodes treated with HNO_3 were observed to have a greater C_{sp} than those made with the as-received activated carbon, three-electrode cyclic voltammetry (Figure 6.20) also indicated that the MWV may be significantly curtailed to as low as 0.5 V. As a result, electrodes made with the HNO_3 treated material were also evaluated at this range. CV curves measured at a 10 mV s^{-1} sweep rate are shown in Figure 6.20 (a, c), while GCD profiles and capacity retention over 5,000 GCD cycles are shown in Figure 6.20 (b, d) and (e), respectively. As with the untreated activated carbon, the HNO_3-treated electrodes were tested at 1 A g^{-1}, while the Triton X-100 soaked electrodes were tested at 0.5 A g^{-1}, in order to compensate for the reduced C_{sp}. Even over this abridged window, the HNO_3 treated electrodes still demonstrate an impressive C_{sp} of 112.84 ± 0.09 F g^{-1}, as derived from CV, and 113.1 ± 0.2 F g^{-1}, as derived from GCD. These values are again approximately halved to 50.43 ± 0.1 F g^{-1} and 47.7 ± 0.1 F g^{-1}, respectively, when the electrodes are soaked in Triton X-100. Unfortunately, even over this reduced working voltage the electrodes are unstable, and soaking in Triton X-100 appears to do little to correct this, with the unsoaked and soaked electrodes retaining only 85% and 89% of their initial capcacities after 5,000 GCD cycles, respectively. This compares unfavourably to electrodes made with untreated AC,

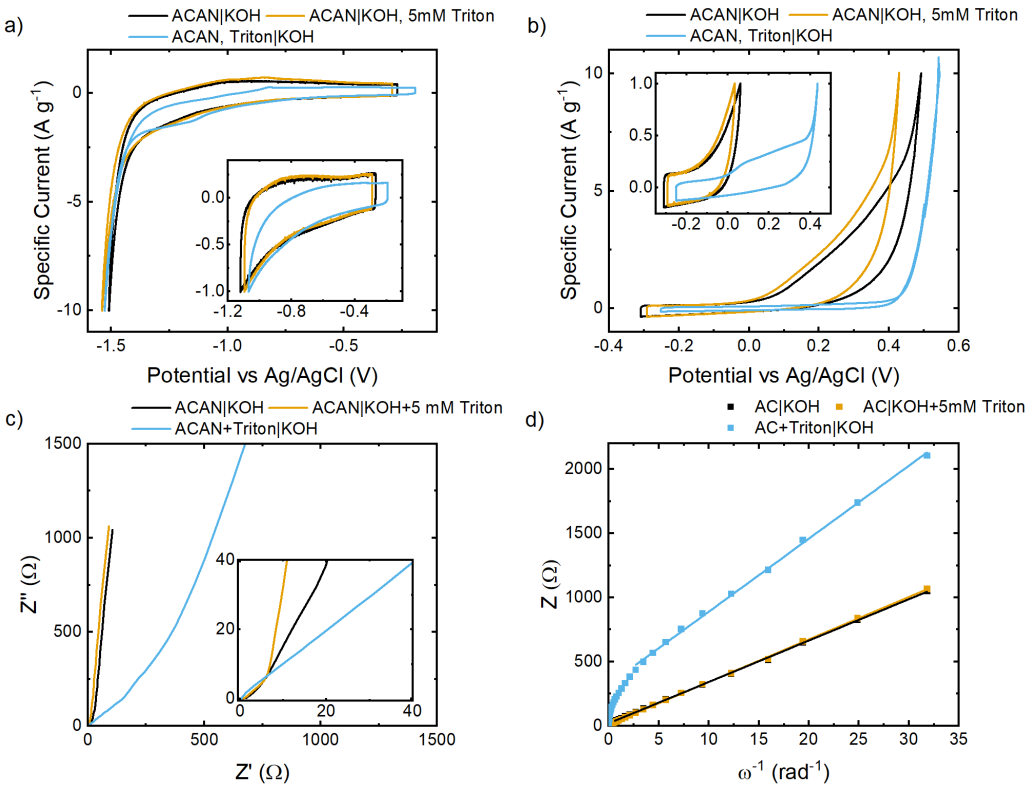

Figure 6.21: Cyclic voltammograms in the a) negative, and b) positive ranges. c) Nyquist and d) Z-ω^{-1} plots, of annealed AC electrodes with 6 M KOH electrolyte (black), measured in 6 M KOH with 5 mM Triton (orange), and soaked in Triton X-100 before testing in 6 M KOH electrolyte (blue). The main panels show the cyclic voltammograms with the scan reversed at $j = 10$ A g^{-1}, while the insets show voltammograms reversed at $j = 1$ A g^{-1}. The first cycle over each current range is presented.

which increased their capacity to 102 % of their initial value at a much higher working voltage of 1.2 V (chapter 4.2.7).

Cyclic voltammetry and EIS data for electrodes made from annealed activated carbon were performed in in 6 M KOH (labelled ACAN|KOH), 6 M KOH with 5 mM Triton (labelled ACAN|KOH, 5 mM Triton), and 6 M KOH after the electrodes were soaked in Triton X-100 (labelled $ACAN_3$, Triton|KOH) are shown in Figure 6.21. As with the oxidised and untreated activated carbon-based electrodes, the addition of 5 mM Triton X-100 to the electrolyte has little impact on the CV data (Figure 6.21 (a,b)). While the Nyquist plot in (Figure 6.21 (c))

suggests that the addition of 5 mM Triton reduces diffusion resistance from ≈20 Ω to ≈10 Ω. The Z-ω^{-1} plot demonstrates that the C_{sp} is almost unchanged at 71.9 ± 0.4 F g^{-1}. Again, in agreement with trends observed for the oxidised and untreated electrodes, soaking the electrodes in Triton X-100 has no impact on the onset of the HER current (Figure 6.21(a)), but significantly delays the onset of the oxidation current by around 0.4 V (Figure 6.21 (b)), resulting in a potential MWV of up to 1.6 V. Unfortunately, the EIS data shows a significant deviation from ideal capacitor behaviour for the Triton-soaked electrodes: in the Nyquist plot (Figure 6.21 (c)), no semicircular CTR region is visible, and the data instead shows a near perfect 45 ° line, corresponding to a Warburg element, up to around 200 Ω, indicating a significant diffusion resistance. This is reflected in the Z-ω^{-1} plot which does not tend to linear behaviour until 5 rad^{-1}, and this linear region corresponds to a reduced capacitance of 41.8 ± 0.5 F g^{-1}.

Figure 6.22 (a, b) shows two-electrode CV and GCD data for the electrodes made with annealed activated carbon with and without soaking in Triton X-100, over a potential window 0.9 V and at the MWVs determined from three-electrode measurements of 1.2 V and 1.6 V, respectively. In agreement with the EIS data, the capacitance of the electrodes made with annealed activated carbon is significantly lower than that of electrodes produced from the as-received material: 68.46 ± 0.06 F g^{-1} and 64.3 ± 0.2 F g^{-1} as derived from CV at a sweep rate of 10 mV s^{-1} and GCD at 1 A g^{-1}, respectively, over a working cell potential of 0.9 V. Mirroring the increase in capacitance of the oxidised activated carbon, this decrease in capacitance is likely due to a loss in pseudocapacitance and a reduced electrode wettability. Interestingly, in spite of this possibly reduced wettability, a low ESR of 0.67 ± 0.06 Ω was obtained (from GCD at 1 A g^{-1}), alongside a reduced sheet resistance of only 980 ± 20 Ω □$^{-1}$ (measured using a four-point probe), compared with 1540 ± 80 Ω □$^{-1}$ for those electrodes made with unmodified material, which may be due to better electrical contact between the

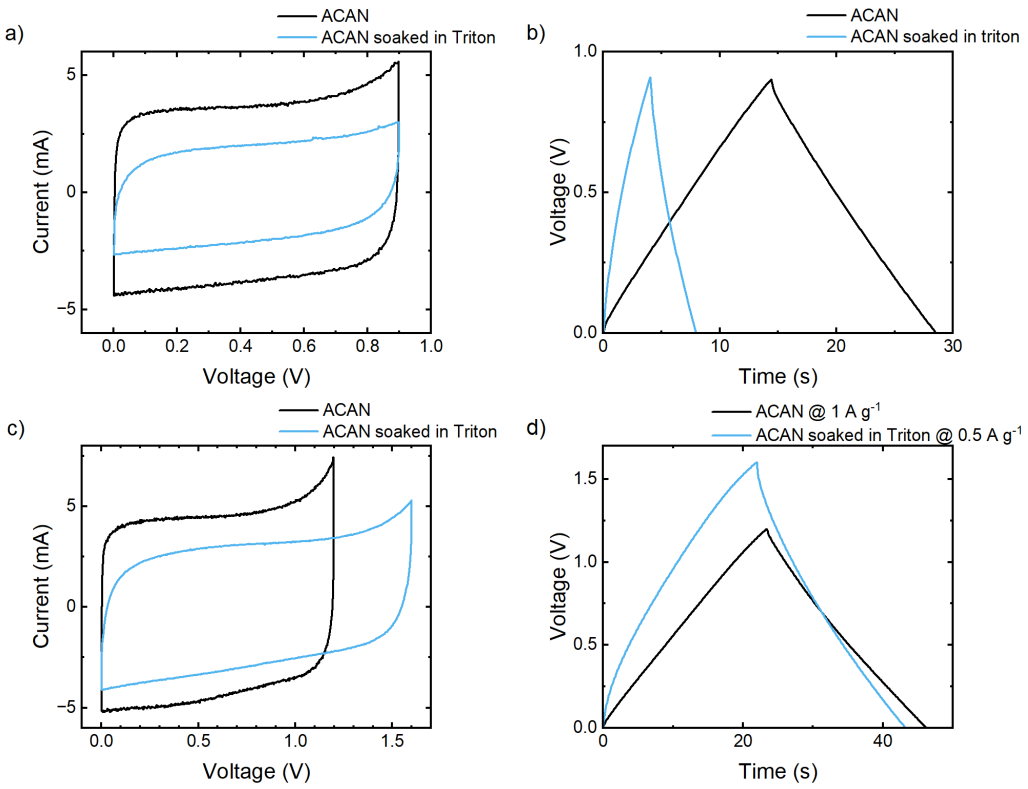

Figure 6.22: Two-electrode data for electrodes prepared with annealed AC (black) and electrodes prepared with annealed AC and subsequently soaked in Triton X-100 (blue). a, c) Cyclic voltammograms obtained at a sweep rate of 10 mV s^{-1}. In a), the working voltage of both electrodes was 0.9 V. In c) the electrodes prepared with annealed AC were tested at 1.2 V, while those that had been soaked in Triton X-100 were tested at 1.6 V. b, d) GCD profiles. As with the CV data, in b), the working voltage of both electrodes was 0.9 V, while in d) the electrodes prepared with annealed AC were tested at 1.2 V, whereas those that had been soaked in Triton X-100 were tested at 1.6 V. at working voltages of b) 0.9 V, d) and 0.5 V. Both GCD datasets shown in (b) were obtained with a specific current of 1 A g^{-1}. In (d) the Triton X-100-soaked electrodes were instead cycled at 0.5 A g^{-1}.

activated carbon particles in the absence of SFGs [237]. As with the unmodified and oxidised electrodes, soaking the electrodes in Triton X-100 was significantly detrimental to their performance, causing a decrease in C_{sp} to 23.84 ± 0.05 F g^{-1} as measured from CV at a 10 mV s^{-1} sweep rate, or 14.75 ± 0.02 F g^{-1}, as measured from GCD at a specific current of 1 A g^{-1}. Alongside this, the ESR increased to 1.933 ± 0.003 Ω, although the sheet resistances of the electrodes were unchanged.

When operating at the MWVs derived from three-electrode analysis, the specific capacitances, as measured by CV at a sweep rate of 10 mV s^{-1} (Figure 6.22 (c)) increase to 80.3 ± 0.1 F g^{-1} for the electrodes containing annealed material, and 43.78 ± 0.05 F g^{-1} for similar electrodes soaked in Triton X-100. Despite its significantly increased MWV of 1.6 V, the low C_{sp} means that the specific energy density of the Triton X-100-soaked annealed activated carbon-based electrodes (as determined from CV at 10 mV s^{-1} sweep rate) remains low, at 12.16 ± 0.01 Wh kg^{-1} (43.78 ± 0.05 J g^{-1}), compared with 16.06 ± 0.03 Wh kg^{-1} (57.8 ± 0.1 J g^{-1}) for the unsoaked electrodes operating over 1.2 V, and 21.97 ± 0.02 Wh kg^{-1} (79.1 ± 0.06 J g^{-1}) for electrodes made with as-recieved activated carbon operating at 1.2 V. GCD profiles are shown in Figure 6.22 (d). As with the electrodes made with the as-received and oxidised materials; the Triton X-100-soaked electrodes were tested at a lower specific current of 0.5 A g^{-1}, compared to the usual 1 A g^{-1} used for the 'conventional' electrodes. At this lower current draw and greater working voltage, C_{sp} increased slightly to 28.66 ± 0.02 F g^{-1}, while the ESR was unchanged at 2.609 ± 0.001 Ω. As would be anticipated, these values are inferior to the C_{sp} of 77.19 ± 0.003 F g^{-1} and 0.6796 ± 0.0008 Ω measured for analogous electrodes without soaking in Triton X-100 tested over a working voltage of 1.2 V with a current density of 1 A g^{-1}. Although increased compared to the electrodes treated with Triton X-100, the relatively low ESR of the Triton X-100-soaked electrodes means that the Ohmic potential drop is limited to below 100 mV, allowing any increase in MWV to be attributed to genuine suppression of the

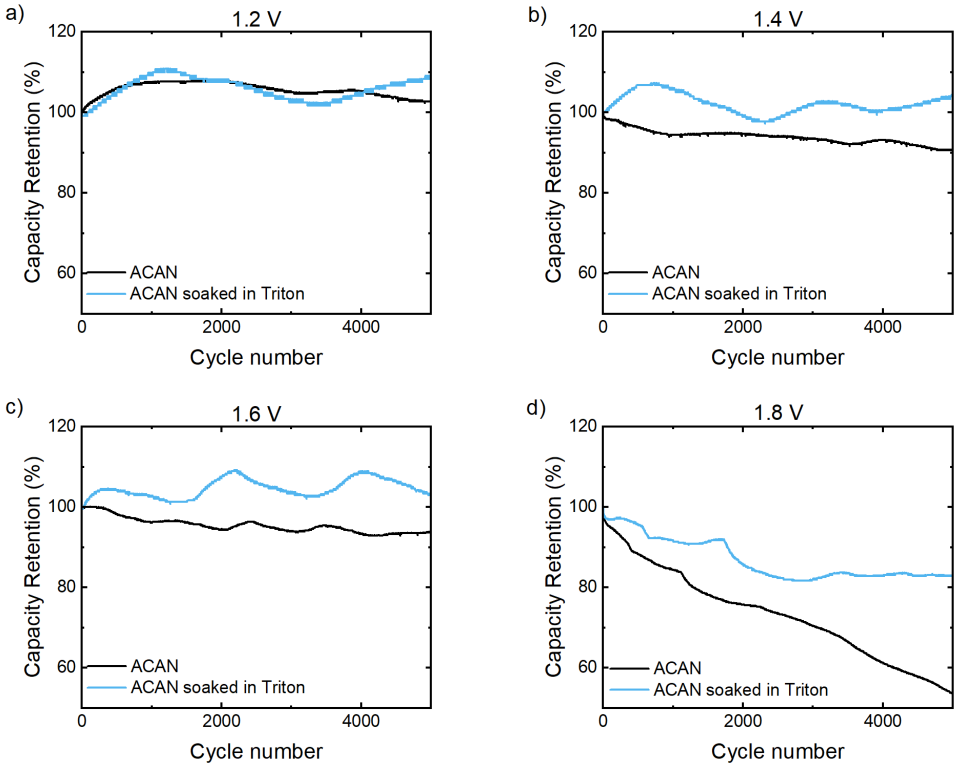

Figure 6.23: Capacity retention over 5,000 GCD cycles of annealed AC (black) and annealed AC soaked in Triton X-100 (blue) at working voltages of a) 1.2 V, b) 1.4 V, c) 1.6 V, and d) 1.8 V. The annealed AC was cycled at a current density of 1 A g^{-1}, while the Triton-soaked electrodes were tested at 0.5 A g^{-1}.

electrode oxidation and not merely to resistance overpotential.

To confirm this increased MWV, the Triton X-100-soaked annealed activated carbon-based electrodes were subject to 5,000 GCD cycles at cell potentials of 1.2 V, 1.4 V, 1.6 V and 1.8 V at specific currents of 0.5 A g^{-1}. The capacity retention during these tests are shown in Figure 6.23, alongside data for their counterparts without Triton X-100 treatment operating at 1 A g^{-1}. As with the data shown earlier in the chapter (figures 6.10 and 6.13), peaks and troughs in the data may correspond to temperature fluctuations in the laboratory. Both electrode sets show an increase in capacity to 103 % of the initial value for electrodes without the pre-treatment in Triton X-100 and 109 % for the Triton X-100-soaked electrodes, when operating at 1.2 V. When the working cell potential

Experiment	MWV (V)	Capacity retention over 5000 cycles (%)
6 M KOH + 5 mM Triton [50]	1.6	≈ 100%
6 M KOH + 5 mM Triton	1.2	101
6 M KOH + 5 mM Triton	1.4	193
AC soaked in Triton	1.4	108
AC soaked in Triton	1.6	90
AC-HNO_3 soaked in Triton	0.5	89
ACAN soaked in Triton	1.6	103

Table 6.1: Table comparing long-term cycling data from reference [50], with those from this chapter.

was increased to 1.4 V, the electrodes without a Triton X-100 soak saw a decrease in capacity to 91 % of their initial value after 5,000 cycles, confirming their working voltage to be limited to 1.2 V, the same as the electrodes made with unmodified activated carbon. In contrast, the Triton X-100-soaked electrodes demonstrated an increase in capacity to 104 % and 103 % of their initial values when cycling at 1.4 V and 1.6 V, respectively, only decreasing to 83 % when the working voltage was increased to 1.8 V, confirming the significant increase in MWV.

The results from this chapter are compared to those of Fic *et al.* in table 6.1. Theses results suggest that the effect of Triton X-100 is very strongly dependent on the surface chemical composition of the electrode material, and is significantly reduced by the presence of oxygen containing SFGs. That the results of Fic *et al.* could not be replicated completely may be in part due to the limitations of the simple annealing process used in this work: the EDX data presented in Figure 6.16 suggests that not all surface oxygen was removed upon annealing. Furthermore, although the annealing treatment used here did not alter the the structure of the AC (Figure 6.17), a longer more aggressive treatment, of the kind necessary to remove more SFGs, may have a noticeable effect.

Another factor, which is rather more difficult to investigate in a systematic fashion, is the relationship between pore size in the active material, the dimensions of

the surfactant molecules, and those of the electrolyte anions and cations. The activated carbon material used by Fic *et al.* had an average pore diameter of $\approx$ 1 nm [50, 216], which although larger than the diameter of the Triton X-100 molecules (0.525 nm) is smaller than their length (3.621 nm), restricting the ability of the Triton to enter the pores and limiting its orientation to be parallel to the pore length. Not only would this make it less likely for pores to be blocked by Triton X-100, but a pore of 1 nm diameter containing a 0.525 nm Triton molecule would not be able to fit a solvated K^+ ion (diameter 0.662 nm [238, 239]) but would be able to accommodate desolvated K^+ ions due to their smaller diameter (0.302 nm [240]). Such behaviour would have the effect of reducing the concentration, and therefore chemical activity, of water molecules at the electrode surface. In contrast, the AC used in this project had an average pore diameter of 3.4 nm, meaning that the Triton X-100 would more easily be able to enter the pores and with a greater variety of orientations. This may lead to more pores being unavailable for ion storage and hence to the observed loss of capacitance, and would not cause any selectivity towards desolvated ions.

6.3 Conclusions

In this chapter the effect of surfactants, principally Triton X-100, but also Tween-20 and oleic acid, on the performance of EDLCs with aqueous 6 M KOH electrolyte was investigated. In disagreement with positive results reported by Fic *et al.* [50, 216], although the addition of 5 mM of Triton X-100 to the electrolyte was found to decrease the ESR of an EDLC from $2.13 \pm 0.003\ \Omega$ to $0.6 \pm 0.03\ \Omega$, it was also found to reduce C_{sp} by over 10 % from 89 ± 1 F g^{-1} to 77.8 ± 0.1 F g^{-1}, as calculated from GCD at 1 A g^{-1}.

Fic *et al.* also reported an increase of the MWV of EDLCs using 6 M KOH

electrolyte with the addition of 5 mM Triton. This could not be replicated, with the MWV remaining at 1.2 V. Soaking the AC electrodes in Triton X-100 was found to increase the MWV to 1.4 V, however, this came at the expense of a significantly reduced C_{sp} of 30.18 ± 0.03 F g^{-1}, as derived from GCD at 0.5 A g^{-1}. Moreover, the increased cell MWV could in part be caused by a large ohmic drop of $\approx$150 mV owing to the increase of ESR to 7.031 ± 0.003 Ω.

In order to investigate whether surface chemistry might determine the efficacy of the surfactant, samples of activated carbon were either oxidised using HNO_3 or annealed under nitrogen at 1000 °C to remove surface oxygen. In neither case was the addition of 5 mM of Triton X-100 to the electrolyte found to improve C_{sp}, ESR, or MWV, but it was found that the extent to which soaking in Triton X-100 improved the MWV did vary; being reduced for the HNO_3-treated activated carbon, but allowing the MWV to increase to 1.6 V in the case of the annealed activated carbon. Unfortunately, as with the unmodified activated carbon, soaking the annealed activated carbon electrodes in Triton X-100 significantly reduced their C_{sp}, to the extent that the specific energy of the Triton X-100-soaked annealed activated carbon electrodes operating at 1.6 V was smaller (12.16 ± 0.01 Wh kg^{-1}) than that of their unsoaked counterparts operating at only 1.2 V (16.06 ± 0.03 Wh kg^{-1}). These results do, however, indicate that the surface chemistry of the electrodes can have a substantial influence on the behaviour of surfactant additives, and hence give hope that by appropriately designing the active materials of the electrodes it may be possible to realise an increased MWV without compromising energy storage.

Chapter 7

Summary and Further Work

This thesis has examined various approaches towards improving the energy density of aqueous EDLCs. First, several electrochemical methods for determining the MWV of an EDLC device were investigated; maximising the MWV is essential for maximising the energy stored by an EDLC, but overestimating this comes at the cost of a shortened lifespan. Next, the role of the conductive additive was explored. An effective conductive additive such as carbon black was shown to be essential for minimising ESR and improving capacitance, specific energy, and specific power. When incorporated via a novel 'vacuum infiltration' technique, uncentrifuged FLG was shown to be a highly effective conductive additive, improving specific energy by up to 50% compared to carbon black. Lastly the effect of adding surfactant to electrolyte and modifying the surface chemistry of the activated carbon electrodes was investigated. The addition of 5 mM Triton X-100 to 6 M KOH was shown to reduce ESR, but at the expense of a 10% loss of capacitance. Going further and soaking the electrodes in Triton X-100 was shown to allow the MWV to increase to 1.4 V, but at the expense of ESR and capacitance, leading to a net loss of specific energy. The role of surface chemistry was also investigated; increasing surface oxygen led to improved capacitance but resulted in electrodes which were unstable even at low voltages and when soaked in Triton. In contrast, reducing surface oxygen allowed Triton-soaked electrodes to operate stably at 1.6 V, but with a significant loss of capacitance compared to untreated AC, again leading to

a net loss of specific energy.

The experiments presented in this thesis give rise to several further questions about the phenomena observed and prompt various ideas for further work in this area. This chapter will present some of the most obvious lines of enquiry for better understanding the behaviour of aqueous EDLCs and further improving their performance.

In chapter 4, various electrochemical methods were tested in an attempt to determine the MWV of EDLCs. Due to the range of experimental apparatus available in Durham and limited opportunities to visit other laboratories as a result of Covid-19, the electrochemical data could only be compared to long-term cycle life, and no information was directly available on the detailed processes leading to device failure. By understanding the precise mechanism of electrode degradation under a range of conditions, such as electrolyte composition, valuable insight can be gained on how to engineer future devices which have a higher MWV and, hence, energy density. Potential approaches might mirror studies reported in the literature [172, 175] which have used *in operando* analysis of gases evolved to provide this information, for example. Other approaches could involve the use of *in-situ* Raman and Fourier-transform infra-red spectroscopy to monitor the real time evolution of the electrode surface chemistry during the process of cell evolution. A cell does not consist only of the electrodes and a thorough cell post-mortem examining morphological and chemical changes not just to the electrodes but also to the current collectors would also be of interest to determine any role they may play in performance loss.

In chapter 5, a novel vacuum infiltration technique was reported for adding few-layer graphene to activated carbon electrodes as a conductive additive. A variety of 2D materials, such as MoS_2 [241], WS_2 [242, 243], black phosphorus

[244] and SnS_2 [245] have been shown to have potential for applications in supercapacitors and batteries. These materials may also be produced by the same shear exfoliation technique [246–249] into an aqueous suspension and incorporated into activated carbon-based electrodes in the same way as for FLG in order to boost energy storage and to incorporate other functionalities into the electrodes such as improved hydrogen evolution [250] or selective capacitive deionisation [251]. The aforementioned materials contain elements with higher atomic numbers than carbon, so could be more clearly differentiated from the activated carbon of the host electrodes than FLG when using backscattered electron detection in the SEM, or EDX mapping. This would help in gaining a detailed understanding how the vacuum infused additives are distributed throughout the electrodes, and may help to elucidate why excessive quantities of platelets of small dimension and with a narrow size distribution had, in the case of FLG, a deleterious effect not only on C_{sp} but also on ESR.

In chapter 6, inspired by promising results reported in the literature [50, 216], the effect of Triton X-100 surfactant on the performance of aqueous EDLC devices was investigated. The results demonstrate that surface chemistry does indeed affect the efficacy of the surfactant, at least to some extent, and this ought be explored further. Although annealing the AC was not found to alter its structure and defect density, this also varies between different varieties of AC, and may affect the impact that the Triton X-100 and other additives have. By using graphite samples with a low defect density (for example, producing electrodes from large pieces of highly oriented pyrolytic graphite – HOPG), and introducing defects and SFGs separately through annealing and electrooxidation, the impact of carbon defects and SFGs on the HER and OER potentials/overpotentials can be decoupled, allowing for greater insight into the corrosion of carbon electrodes and the impact of surfactants upon this.

Another factor which may affect the efficacy of surfactants is the interplay between the pore size of the active material and the size of the surfactant molecules. Fic *et al.* used an activated carbon with an average pore diameter of around 1 nm. This is greater than the 0.525 nm diameter of the Triton X-100 molecule, but smaller than its 3.621 nm length. In contrast, the activated carbon used in this work had an average pore diameter of 3.2 nm, comparable to the length of the Triton X-100 molecule, and therefore creating fewer restrictions on the ability of the Triton X-100 molecules to access the pores. Future work may be undertaken to compare activated carbons with different pore sizes to surfactants of different sizes and structures to better understand how the interplay between these factors might influence MWV and overall cell performance. Alongside work examining the effect of surface chemistry in greater detail, such a study should allow the properties of the electrode material to be tuned in such a way as to optimize performance when used in conjunction with appropriately selected surfactants.

References

[1]IPCC, *Climate Change 2013: The Physical Science Basis. Contribution of Working Group I to the Fifth Assessment Report of the Intergovernmental Panel on Climate Change*, edited by D. Qin, G.-K. Plattner, M. Tignor, S. K. Allen, J. Boschung, A. Nauels, Y. Xia, V. Bex and P. M. Midgley (Cambridge University Press, Cambridge, United Kingdom and New York, NY, USA, 2013), p. 1535.

[2]California Independent Systems Operator, *Today's Outlook*, 2023.

[3]International Energy Authority, *Data and Statistics*, 2020.

[4]I. A. G. Wilson, P. G. McGregor and P. J. Hall, "Energy Storage in the UK Electrical Network: Estimation of the Scale and Review of Technology Options", Energy Policy **38**, 4099–4106 (2010).

[5]M. Hiremath, K. Derendorf and T. Vogt, "Comparative Life Cycle Assessment of Battery Storage Systems for Stationary Applications", Environmental Science & Technology **49**, 4825–4833 (2015).

[6]J. J. Quintana, A. Ramos, M. Diaz and I. Nuez, "Energy Efficiency Analysis as a Function of the Working Voltages in Supercapacitors", Energy **230**, 120689 (2021).

[7]J. Zhao and A. F. Burke, "Review on Supercapacitors: Technologies and Performance Evaluation", Journal of Energy Chemistry **59**, 276–291 (2021).

[8]B. Dyatkin, V. Presser, M. Heon, M. R. Lukatskaya, M. Beidaghi and Y. Gogotsi, "Development of a Green Supercapacitor Composed Entirely of Environmentally Friendly Materials", ChemSusChem **6**, 2269–2280 (2013).

[9]M. M. Archuleta, "Toxicity of Materials Used in the Manufacture of Lithium Batteries", Journal of Power Sources **54**, 138–142 (1995).

[10]S. Lee and A. Manthiram, "Can Cobalt Be Eliminated from Lithium-Ion Batteries?", ACS Energy Letters **7**, 3058–3063 (2022).

[11]A. González, E. Goikolea, J. A. Barrena and R. Mysyk, "Review on Supercapacitors: Technologies and Materials", Renewable and Sustainable Energy Reviews **58**, 1189–1206 (2016).

[12]M. Mirzaeian, Q. Abbas, A. Ogwu, P. Hall, M. Goldin, M. Mirzaeian and H. F. Jirandehi, "Electrode and Electrolyte Materials for Electrochemical Capacitors", International Journal of Hydrogen Energy **42**, 25565–25587 (2017).

[13]A. Burke, "Ultracapacitors: Why, How, and Where is the Technology", Journal of Power Sources **91**, 37–50 (2000).

[14]J. Xu, N. Yuan, J. M. Razal, Y. Zheng, X. Zhou, J. Ding, K. Cho, S. Ge, R. Zhang, Y. Gogotsi and R. H. Baughman, "Temperature-Independent Capacitance of Carbon-Based Supercapacitor from 100 to 60 °C", Energy Storage Materials **22**, 323–329 (2019).

[15]B. E. Conway and W. G. Pell, "Double-Layer and Pseudocapacitance Types of Electrochemical Capacitors and their Applications to the Development of Hybrid Devices", Journal of Solid State Electrochemistry **7**, 637–644 (2003).

[16]X. Li and B. Wei, "Supercapacitors Based on Nanostructured Carbon", Nano Energy **2**, 159–173 (2013).

[17]W. R. Browne, *Electrochemistry*, Oxford chemistry primers (Oxford University Press, New York, NY, 2018).

[18]A. J. Bard, L. R. Faulkner and H. S. White, *Electrochemical Methods : Fundamentals and Applications*, Third edition. (Wiley, Hoboken, NJ, 2022).

[19]L. L. Zhang and X. S. Zhao, "Carbon-Based Materials as Supercapacitor Electrodes", Chemical Society Reviews **38**, 2520–2531 (2009).

[20]A. Yu, *Electrochemical Supercapacitors for Energy Storage and Delivery: Fundamentals and Applications*, Electrochemical Energy Storage and Conversion (Taylor & Francis, Boca Raton, Florida, 2013).

[21]N. Devillers, S. Jemei, M.-C. Péra, D. Bienaimé and F. Gustin, "Review of Characterization Methods for Supercapacitor Modelling", Journal of Power Sources **246**, 596–608 (2014).

[22]A. Szewczyk, J. Sikula, V. Sedlakova, J. Majzner, P. Sedlak and T. Kuparowitz, "Voltage Dependence of Supercapacitor Capacitance", Metrology and Measurement Systems **23**, 403–411 (2016).

[23]B. E. Conway, *Electrochemical Supercapacitors: Scientific Fundamentals and Technological Applications* (Springer, New York, 1999).

[24]M. Khademi and D. P. J. Barz, "Structure of the Electrical Double Layer Revisited: Electrode Capacitance in Aqueous Solutions", Langmuir **36**, 4250–4260 (2020).

[25]O. Barbieri, M. Hahn, A. Herzog and R. Kötz, "Capacitance Limits of High Surface Area Activated Carbons for Double Layer Capacitors", Carbon **43**, 1303–1310 (2005).

[26]H. Shi, "Activated Carbons and Double Layer Capacitance", Electrochimica Acta **41**, 1633–1639 (1996).

[27]Y. J. Kim, Y. Horie, S. Ozaki, Y. Matsuzawa, H. Suezaki, C. Kim, N. Miyashita and M. Endo, "Correlation Between the Pore and Solvated Ion Size on Capacitance Uptake of PVDC-Based Carbons", Carbon **42**, 1491–1500 (2004).

[28]J. Chmiola, G. Yushin, R. Dash and Y. Gogotsi, "Effect of Pore Size and Surface Area of Carbide Derived Carbons on Specific Capacitance", Journal of Power Sources **158**, 765–772 (2006).

[29]C. Vix-Guterl, E. Frackowiak, K. Jurewicz, M. Friebe, J. Parmentier and F. Béguin, "Electrochemical Energy Storage in Ordered Porous Carbon Materials", Carbon **43**, 1293–1302 (2005).

[30]E. Frackowiak, V. Khomenko, K. Jurewicz, K. Lota and F. Béguin, "Supercapacitors Based on Conducting Polymers/Nanotubes Composites", Journal of Power Sources **153**, 413–418 (2006).

[31]G. Wang, L. Zhang and J. Zhang, "A Review of Electrode Materials for Electrochemical Supercapacitors", Chemical Society Reviews **41**, 797–828 (2012).

[32]P. Kurzweil, J. Schottenbauer and C. Schell, "Past, Present and Future of Electrochemical Capacitors: Pseudocapacitance, Aging Mechanisms and Service Life Estimation", Journal of Energy Storage **35**, 102311 (2021).

[33]R. de Levie, "On Porous Electrodes in Electrolyte Solutions: I. Capacitance Effects", Electrochimica Acta **8**, 751–780 (1963).

[34]L. Zubieta and R. Bonert, "Characterization of Double-Layer Capacitors for Power Electronics Applications", IEEE Transactions on Industry Applications **36**, 199–205 (2000).

[35]E. Pameté, L. Köps, F. A. Kreth, S. Pohlmann, A. Varzi, T. Brousse, A. Balducci and V. Presser, "The Many Deaths of Supercapacitors: Degradation, Aging, and Performance Fading", Advanced Energy Materials **13**, 2301008 (2023).

[36]D. M. Heard and A. J. J. Lennox, "Electrode Materials in Modern Organic Electrochemistry", Angewandte Chemie International Edition **59**, 18866–18884 (2020).

[37]C. G. Zoski, *Handbook of Electrochemistry*, 1st ed. (Elsevier, San Diego, 2006).

[38]A. K. Samantara and S. Ratha, *Materials Development for Active/Passive Components of a Supercapacitor: Background, Present Status and Future Perspective* (Springer Singapore, Singapore, 2018).

[39]A. G. Pandolfo and A. F. Hollenkamp, "Carbon Properties and their Role in Supercapacitors", Journal of Power Sources **157**, 11–27 (2006).

[40]P. Simon and A. F. Burke, "Nanostructured Carbons: Double-Layer Capacitance and More", The Electrochemical Society Interface **17**, 38 (2008).

[41]C. Zheng, W. Qian, C. Cui, G. Xu, M. Zhao, G. Tian and F. Wei, "Carbon Nanotubes for Supercapacitors: Consideration of Cost and Chemical Vapor Deposition Techniques", Journal of Natural Gas Chemistry **21**, 233–240 (2012).

[42]Z. Zhai, L. Zhang, T. Du, B. Ren, Y. Xu, S. Wang, J. Miao and Z. Liu, "A Review of Carbon Materials for Supercapacitors", Materials & Design **221**, 111017 (2022).

[43]A. G. Pandolfo, G. J. Wilson, T. D. Huynh and A. F. Hollenkamp, "The Influence of Conductive Additives and Inter-Particle Voids in Carbon EDLC Electrodes", Fuel Cells **10**, 856–864 (2010).

[44]P. Simon and Y. Gogotsi, "Materials for Electrochemical Capacitors", Nature Materials **7**, 845–854 (2008).

[45]K. Jurewicz, C. Vix-Guterl, E. Frackowiak, S. Saadallah, M. Reda, J. Parmentier, J. Patarin and F. Béguin, "Capacitance Properties of Ordered Porous Carbon Materials Prepared by a Templating Procedure", Journal of Physics and Chemistry of Solids **65**, 287–293 (2004).

[46]J. A. Fernández, T. Morishita, M. Toyoda, M. Inagaki, F. Stoeckli and T. A. Centeno, "Performance of Mesoporous Carbons Derived from Poly (Vinyl Alcohol) in Electrochemical Capacitors", Journal of Power Sources **175**, 675–679 (2008).

[47]L. Wei and G. Yushin, "Nanostructured Activated Carbons from Natural Precursors for Electrical Double-Layer Capacitors", Nano Energy **1**, 552–565 (2012).

[48]Y. Gao, Q. Yue, B. Gao and A. Li, "Insight into activated carbon from different kinds of chemical activating agents: a review", Science of The Total Environment **746**, 141094 (2020).

[49]J. L. Figueiredo, M. F. Pereira, M. M. Freitas and J. J. Órfão, "Modification of the Surface Chemistry of Activated Carbons", Carbon **37**, 1379–1389 (1999).

[50]K. Fic, G. Lota and E. Frackowiak, "Effect of Surfactants on Capacitance Properties of Carbon Electrodes", Electrochimica Acta **60**, 206–212 (2012).

[51]B. Li, F. Dai, Q. Xiao, L. Yang, J. Shen, C. Zhang and M. Cai, "Nitrogen-Doped Activated Carbon for a High Energy Hybrid Supercapacitor", Energy & Environmental Science **9**, 102–106 (2016).

[52]M. Sevilla and R. Mokaya, "Energy Storage Applications of Activated Carbons: Supercapacitors and Hydrogen Storage", Energy & Environmental Science **7**, 1250–1280 (2014).

[53]J. Huang, X. Meng, G. Zhu, Y. Song, S. Zhu, M. Chen, Q. Li, Y. Zhou and M. C. Lin, "Thermally Oxidized Activated Carbon with High Specific Surface Area to Boost Electrochemical Performance for Supercapacitor", Applied Surface Science **619**, 156684 (2023).

[54]G. Moussa, C. Matei Ghimbeu, P.-L. Taberna, P. Simon and C. Vix-Guterl, "Relationship Between the Carbon Nano-Onions (CNOs) Surface Chemistry/Defects and their Capacitance in Aqueous and Organic Electrolytes", Carbon **105**, 628–637 (2016).

[55]M. Inagaki, H. Konno and O. Tanaike, "Carbon Materials for Electrochemical Capacitors", Journal of Power Sources **195**, 7880–7903 (2010).

[56]L.-Z. Fan, T.-T. Chen, W.-L. Song, X. Li and S. Zhang, "High Nitrogen-Containing Cotton Derived 3D Porous Carbon Frameworks for High-Performance Supercapacitors", Scientific Reports **5**, 15388 (2015).

[57]D. Kalderis, S. Bethanis, P. Paraskeva and E. Diamadopoulos, "Production of Activated Carbon from Bagasse and Rice Husk by a Single-Stage Chemical Activation Method at Low Retention Times", Bioresource Technology **99**, 6809–6816 (2008).

[58]C.-S. Yang, Y. S. Jang and H. K. Jeong, "Bamboo-Based Activated Carbon for Supercapacitor Applications", Current Applied Physics **14**, 1616–1620 (2014).

[59]S. Yu, D. Liu, S. Zhao, B. Bao, C. Jin, W. Huang, H. Chen and Z. Shen, "Synthesis of Wood Derived Nitrogen-Doped Porous Carbon–Polyaniline Composites for Supercapacitor Electrode Materials", RSC Advances **5**, 30943–30949 (2015).

[60]X. He, P. Ling, J. Qiu, M. Yu, X. Zhang, C. Yu and M. Zheng, "Efficient Preparation of Biomass-Based Mesoporous Carbons for Supercapacitors with both High Energy Density and High Power Density", Journal of Power Sources **240**, 109–113 (2013).

[61]M Raja, B. Sadhasivam, J. Naik R, D. R and K. Ramanujam, "A Chitosan/-Poly(ethylene glycol)-ran-poly(propylene glycol) Blend as an Eco-benign Separator and Binder for Quasi-Solid-State Supercapacitor Applications", Sustainable Energy & Fuels **3**, 760–773 (2019).

[62]T. W. Ebbesen, H. J. Lezec, H. Hiura, J. W. Bennett, H. F. Ghaemi and T. Thio, "Electrical Conductivity of Individual Carbon Nanotubes", Nature **382**, 54–56 (1996).

[63]A. Izadi-Najafabadi, S. Yasuda, K. Kobashi, T. Yamada, D. N. Futaba, H. Hatori, M. Yumura, S. Iijima and K. Hata, "Extracting the Full Potential of Single-Walled Carbon Nanotubes as Durable Supercapacitor Electrodes Operable at 4 V with High Power and Energy Density", Advanced Materials **22**, E235–E241 (2010).

[64]O. Bohlen, J. Kowal and D. U. Sauer, "Ageing Behaviour of Electrochemical Double Layer Capacitors: Part I. Experimental Study and Ageing Model", Journal of Power Sources **172**, 468–475 (2007).

[65]T. Hiraoka, A. Izadi-Najafabadi, T. Yamada, D. N. Futaba, S. Yasuda, O. Tanaike, H. Hatori, M. Yumura, S. Iijima and K. Hata, "Compact and Light Supercapacitor Electrodes from a Surface-Only Solid by Opened Carbon Nanotubes with 2,200 m^2 g^{-1} Surface Area", Advanced Functional Materials **20**, 422–428 (2010).

[66]H. Dai, "Carbon Nanotubes: Synthesis, Integration, and Properties", Accounts of Chemical Research **35**, 1035–1044 (2002).

[67]N. Arora and N. N. Sharma, "Arc Discharge Synthesis of Carbon Nanotubes: Comprehensive Review", Diamond and Related Materials **50**, 135–150 (2014).

[68]C. Emmenegger, P. Mauron, A. Züttel, C. Nützenadel, A. Schneuwly, R. Gallay and L. Schlapbach, "Carbon Nanotube Synthesized on Metallic Substrates", Applied Surface Science **162**, 452–456 (2000).

[69]J. H. Chen, W. Z. Li, D. Z. Wang, S. X. Yang, J. G. Wen and Z. F. Ren, "Electrochemical Characterization of Carbon Nanotubes as Electrode in Electrochemical Double-Layer Capacitors", Carbon **40**, 1193–1197 (2002).

[70]F. Markoulidis, C. Lei, C. Lekakou, D. Duff, S. Khalil, B. Martorana and I. Cannavaro, "A Method to Increase the Energy Density of Supercapacitor Cells by the Addition of Multiwall Carbon Nanotubes into Activated Carbon Electrodes", Carbon **68**, 58–66 (2014).

[71]A. D. Maynard, "Are We Ready for Spray-On Carbon Nanotubes?", Nature Nanotechnology **11**, 490–491 (2016).

[72]D. B. Warheit, B. R. Laurence, K. L. Reed, D. H. Roach, G. A. Reynolds and T. R. Webb, "Comparative Pulmonary Toxicity Assessment of Single-wall Carbon Nanotubes in Rats", Toxicological Sciences **77**, 117–125 (2004).

[73]Z.-S. Wu, G. Zhou, L.-C. Yin, W. Ren, F. Li and H.-M. Cheng, "Graphene/Metal Oxide Composite Electrode Materials for Energy Storage", Nano Energy **1**, 107–131 (2012).

[74]K. R. Paton, E. Varrla, C. Backes, R. J. Smith, U. Khan, A. O'Neill, C. Boland, M. Lotya, O. M. Istrate, P. King, T. Higgins, S. Barwich, P. May, P. Puczkarski, I. Ahmed, M. Moebius, H. Pettersson, E. Long, J. Coelho, S. E. O'Brien, E. K. McGuire, B. M. Sanchez, G. S. Duesberg, N. McEvoy, T. J. Pennycook, C. Downing, A. Crossley, V. Nicolosi and J. N. Coleman, "Scalable Production of

Large Quantities of Defect-Free Few-Layer Graphene by Shear Exfoliation in Liquids", Nature Materials **13**, 624–630 (2014).

[75]A. K. Geim, "Graphene: Status and Prospects", Science **324**, 1530–1534 (2009).

[76]D. Chen, L. Tang and J. Li, "Graphene-Based Materials in Electrochemistry", Chemical Society Reviews **39**, 3157–3180 (2010).

[77]Y. Huang, J. Liang and Y. Chen, "An Overview of the Applications of Graphene-Based Materials in Supercapacitors", Small **8**, 1805–1834 (2012).

[78]J. Tian, S. Wu, X. L. Yin and W. Wu, "Novel Preparation of Hydrophilic Graphene/Graphene Oxide Nanosheets for Supercapacitor Electrode", Applied Surface Science **496**, 11 (2019).

[79]R. Tamilselvi, M. Ramesh, G. S. Lekshmi, O. Bazaka, I. Levchenko, K. Bazaka and M. Mandhakini, "Graphene Oxide-Based Supercapacitors from Agricultural Wastes: A Step to Mass Production of Highly Efficient Electrodes for Electrical Transportation Systems", Renewable Energy **151**, 731–739 (2020).

[80]J. Wang, H. Zhang, M. R. C. Hunt, A. Charles, J. Tang, O. Bretcanu, D. Walker, K. T. Hassan, Y. Sun and L. Siller, "Synthesis and Characterisation of Reduced Graphene Oxide/Bismuth Composite for Electrodes in Electrochemical Energy Storage Devices", ChemSusChem **10**, 363–371 (2017).

[81]M. Canal-Rodríguez, J. A. Menéndez, M. A. Montes-Morán, I. Martín-Gullón, J. B. Parra and A. Arenillas, "The Role of Conductive Additives on the Performance of Hybrid Carbon Xerogels as Electrodes in Aqueous Supercapacitors", Electrochimica Acta **295**, 693–702 (2019).

[82]B. Xu, H. Wang, Q. Zhu, N. Sun, B. Anasori, L. Hu, F. Wang, Y. Guan and Y. Gogotsi, "Reduced Graphene oxide as a Multi-Functional Conductive Binder for Supercapacitor Electrodes", Energy Storage Materials **12**, 128–136 (2018).

[83]S. Stankovich, R. D. Piner, S. T. Nguyen and R. S. Ruoff, "Synthesis and Exfoliation of Isocyanate-Treated Graphene Oxide Nanoplatelets", Carbon **44**, 3342–3347 (2006).

[84]S. Stankovich, D. A. Dikin, G. H. B. Dommett, K. M. Kohlhaas, E. J. Zimney, E. A. Stach, R. D. Piner, S. T. Nguyen and R. S. Ruoff, "Graphene-Based Composite Materials", Nature **442**, 282–286 (2006).

[85]G. Wang, X. Shen, B. Wang, J. Yao and J. Park, "Synthesis and Characterisation of Hydrophilic and Organophilic Graphene Nanosheets", Carbon **47**, 1359–1364 (2009).

[86]Y. Si and E. T. Samulski, "Synthesis of Water Soluble Graphene", Nano Letters **8**, 1679–1682 (2008).

[87]Z. Feng, C. Zhang, J. Chen, Y. Wang, X. Jin, R. Zhang and J. Hu, "An Easy and Eco-Friendly Method to Prepare Reduced Graphene Oxide with $Fe(OH)_2$ for Use as a Conductive Additive for $LiFePO_4$ Cathode Materials", RSC Advances **3**, 4408–4415 (2013).

[88]Z. Lei, L. Lu and X. S. Zhao, "The Electrocapacitive Properties of Graphene Oxide Reduced by Urea", Energy & Environmental Science **5**, 6391–6399 (2012).

[89]J. Shen, T. Li, Y. Long, M. Shi, N. Li and M. Ye, "One-step solid state preparation of reduced graphene oxide", Carbon **50**, 2134–2140 (2012).

[90]W. S. Hummers and R. E. Offeman, "Preparation of Graphitic Oxide", Journal of the American Chemical Society **80**, 1339 (1958).

[91]H. Bai, C. Li and G. Shi, "Functional Composite Materials Based on Chemically Converted Graphene", Advanced Materials **23**, 1089–1115 (2011).

[92]J. Xia, F. Chen, J. Li and N. Tao, "Measurement of the Quantum Capacitance of Graphene", Nature Nanotechnology **4**, 505–509 (2009).

[93]S. R. Vivekchand, C. S. Rout, K. S. Subrahmanyam, A. Govindaraj and C. N. Rao, "Graphene-Based Electrochemical Supercapacitors", Journal of Chemical Sciences **120**, 9–13 (2008).

[94]W. Lv, D.-M. Tang, Y.-B. He, C.-H. You, Z.-Q. Shi, X.-C. Chen, C.-M. Chen, P.-X. Hou, C. Liu and Q.-H. Yang, "Low-Temperature Exfoliated Graphenes: Vacuum-Promoted Exfoliation and Electrochemical Energy Storage", ACS Nano **3**, 3730–3736 (2009).

[95]E. Pohjalainen, S. Räsänen, M. Jokinen, K. Yliniemi, D. A. Worsley, J. Kuusivaara, J. Juurikivi, R. Ekqvist, T. Kallio and M. Karppinen, "Water Soluble Binder for Fabrication of $Li_4Ti_5O_{12}$ Electrodes", Journal of Power Sources **226**, 134–139 (2013).

[96]K. Zhang, J. Tang, J. Yuan, J. Li, Y. Sun, Y. Matsuba, D.-M. Zhu and L.-C. Qin, "Production of Few-Layer Graphene via Enhanced High-Pressure Shear Exfoliation in Liquid for Supercapacitor Applications", ACS Applied Nano Materials **1**, 2877–2884 (2018).

[97]E. S. Ferreira, D. S. da Silva, T. A. L. Burgo, B. C. Batista and F. Galembeck, "Graphite exfoliation in cellulose solutions", Nanoscale **9**, 10219–10226 (2017).

[98]P. Yu, X. Wang, K. Zhang, D. Zhou, M. Wu, Q. Wu, J. Liu, J. Yang and J. Zhang, "Aqueous Cellulose Solution Assisted Direct Exfoliation of Graphite to High concentration Graphene Dispersion", Materials Letters **285**, 129081 (2021).

[99]J. N. Coleman, "Liquid Exfoliation of Defect-Free Graphene", Accounts of Chemical Research **46**, 14–22 (2013).

[100]E. Varrla, K. R. Paton, C. Backes, A. Harvey, R. J. Smith, J. McCauley and J. N. Coleman, "Turbulence-Assisted Shear Exfoliation of Graphene Using Household Detergent and a Kitchen Blender", Nanoscale **6**, 11810–11819 (2014).

[101]R. Raccichini, A. Varzi, S. Passerini and B. Scrosati, "The Role of Graphene for Electrochemical Energy Storage", Nature Materials **14**, 271–279 (2015).

[102]T. Purkait, G. Singh, M. Singh, D. Kumar and R. S. Dey, "Large Area Few-Layer Graphene with Scalable Preparation from Waste Biomass for High-Performance Supercapacitor", Scientific Reports **7**, 15239 (2017).

[103]S. B. Hong, J. M. Jeong, H. G. Kang, D. Seo, Y. Cha, H. Jeon, G. Y. Lee, M. Irshad, D. H. Kim, S. Y. Hwang, J. W. Kim and B. G. Choi, "Fast and Scalable Hydrodynamic Synthesis of MnO_2/Defect-Free Graphene Nanocomposites with High Rate Capability and Long Cycle Life", ACS Applied Materials & Interfaces **10**, 35250–35259 (2018).

[104]M. Mirzaeian, A. A. Ogwu, H. F. Jirandehi, S. Aidarova, Z. Ospanova and N. Tsendzughul, "Surface Characteristics of Silver Oxide Thin Film Electrodes for Supercapacitor Applications", Colloids and Surfaces A: Physicochemical and Engineering Aspects **519**, 223–230 (2017).

[105]A. Krause, P. Kossyrev, M. Oljaca, S. Passerini, M. Winter and A Balducci, "Electrochemical Double Layer Capacitor and Lithium-Ion Capacitor Based on Carbon Black", Journal of Power Sources **196**, 8836–8842 (2011).

[106]W. G. Pell, B. E. Conway and N. Marincic, "Analysis of Non-Uniform Charge/Discharge and Rate Effects in Porous Carbon Capacitors Containing Sub-Optimal Electrolyte Concentrations", Journal of Electroanalytical Chemistry **491**, 9–21 (2000).

[107]H. Nishihara, T. Simura, S. Kobayashi, K. Nomura, R. Berenguer, M. Ito, M. Uchimura, H. Iden, K. Arihara, A. Ohma, Y. Hayasaka and T. Kyotani, "Oxidation-Resistant and Elastic Mesoporous Carbon with Single-Layer Graphene Walls", Advanced Functional Materials **26**, 6418–6427 (2016).

[108]C. Zhong, Y. Deng, W. Hu, J. Qiao, L. Zhang and J. Zhang, "A Review of Electrolyte Materials and Compositions for Electrochemical Supercapacitors", Chemical Society Reviews **44**, 7484–7539 (2015).

[109]R. Kötz and M. Carlen, "Principles and Applications of Electrochemical Capacitors", Electrochimica Acta **45**, 2483–2498 (2000).

[110]W. Qian, F. Sun, Y. Xu, L. Qiu, C. Liu, S. Wang and F. Yan, "Human Hair-Derived Carbon Flakes for Electrochemical Supercapacitors", Energy & Environmental Science **7**, 379–386 (2014).

[111]N. Böckenfeld, S. S. Jeong, M. Winter, S. Passerini and A. Balducci, "Natural, Cheap and Environmentally Friendly Binder for Supercapacitors", Journal of Power Sources **221**, 14–20 (2013).

[112]N. S. Nadiah, F. S. Omar, A. Numan, Y. K. Mahipal, S. Ramesh and K. Ramesh, "Influence of Acrylic Acid on Ethylene Carbonate/Dimethyl Carbonate Based Liquid Electrolyte and its Supercapacitor Application", International Journal of Hydrogen Energy **42**, 30683–30690 (2017).

[113]V. Ruiz, R. Santamaría, M. Granda and C. Blanco, "Long-Term Cycling of Carbon-Based Supercapacitors in Aqueous Media", Electrochimica Acta **54**, 4481–4486 (2009).

[114]A. Krause and A. Balducci, "High Voltage Electrochemical Double Layer Capacitor Containing Mixtures of Ionic Liquids and Organic Carbonate as Electrolytes", Electrochemistry Communications **13**, 814–817 (2011).

[115]L. Korson, W. Drost-Hansen and F. J. Millero, "Viscosity of Water at Various Temperatures", Journal of Physical Chemistry **73**, 34–39 (1969).

[116]W.-H. Jin, G.-T. Cao and J.-Y. Sun, "Hybrid Supercapacitor Based on MnO_2 and Columned FeOOH Using Li_2SO_4 Electrolyte Solution", Journal of Power Sources **175**, 686–691 (2008).

[117]J. Zhu, Y. Xu, J. Wang, J. Lin, X. Sun and S. Mao, "The Effect of Various Electrolyte Cations on Electrochemical Performance of Polypyrrole/RGO Based Supercapacitors", Physical Chemistry Chemical Physics **17**, 28666–28673 (2015).

[118]T. Abdallah, D. Lemordant and B. Claude-Montigny, "Are Room Temperature Ionic Liquids Able to Improve the Safety of Supercapacitors Organic Electrolytes Without Degrading the Performances?", Journal of Power Sources **201**, 353–359 (2012).

[119]A. Brandt, S. Pohlmann, A. Varzi, A. Balducci and S. Passerini, "Ionic Liquids in Supercapacitors", MRS Bulletin **38**, 554–559 (2013).

[120]S. Pohlmann, T. Olyschläger, P. Goodrich, J. Alvarez Vicente, J. Jacquemin and A. Balducci, "Azepanium-Based Ionic Liquids as Green Electrolytes for High Voltage Supercapacitors", Journal of Power Sources **273**, 931–936 (2015).

[121]F. B. Sillars, S. I. Fletcher, M. Mirzaeian and P. J. Hall, "Effect of Activated Carbon Xerogel Pore Size on the Capacitance Performance of Ionic Liquid Electrolytes", Energy & Environmental Science **4**, 695–706 (2011).

[122]A. Balducci, R. Dugas, P. L. Taberna, P. Simon, D. Plée, M. Mastragostino and S. Passerini, "High Temperature Carbon–Carbon Supercapacitor Using Ionic Liquid as Electrolyte", Journal of Power Sources **165**, 922–927 (2007).

[123]G. P. Pandey, A. C. Rastogi and C. R. Westgate, "All-Solid-State Supercapacitors with Poly(3,4-ethylenedioxythiophene)-Coated Carbon Fiber Paper Electrodes and Ionic Liquid Gel Polymer Electrolyte", Journal of Power Sources **245**, 857–865 (2014).

[124]K. S. Ngai, S. Ramesh, K. Ramesh and J. C. Juan, "A Review of Polymer Electrolytes: Fundamental, Approaches and Applications", Ionics **22**, 1259–1279 (2016).

[125]C. Chen, Y. Zhang, Y. Li, J. Dai, J. Song, Y. Yao, Y. Gong, I. Kierzewski, J. Xie and L. Hu, "All-Wood, Low Tortuosity, Aqueous, Biodegradable Supercapacitors with Ultra-High Capacitance", Energy & Environmental Science **10**, 538–545 (2017).

[126]X. Peng, H. Liu, Q. Yin, J. Wu, P. Chen, G. Zhang, G. Liu, C. Wu and Y. Xie, "A Zwitterionic Gel Electrolyte for Efficient Solid-State Supercapacitors", Nature Communications **7**, 11782 (2016).

[127]W. Zhou, R. Apkarian, Z. L. Wang and D. Joy, "Fundamentals of Scanning Electron Microscopy (SEM) ", in *Scanning microscopy for nanotechnology: techniques and applications*, edited by W. Zhou and Z. L. Wang (Springer, 2010).

[128]P. J. Goodhew, F. J. Humphreys and R. Beanland, *Electron Microscopy and Analysis* (CRC Press, 2014).

[129]J. I. Goldstein, D. E. Newbury, P. Echlin, D. C. Joy, C. Fiori and E. Lifshin, *Scanning Electron Microscopy and X-Ray Microanalysis* (Plenum Press, New York, 1981).

[130]B. J. Griffin, "A Comparison of Conventional Everhart-Thornley Style and In-Lens Secondary Electron Detectors – a Further Variable in Scanning Electron Microscopy", Scanning **33**, 162–173 (2011).

[131]R. E. Williams, "Microstructural Defects in Antimony Selenide Solar Cells", MSc Thesis (University of Durham, Durham, UK, 2020).

[132]G. Lawes, *Scanning Electron Microscopy and X-Ray Microanalysis*, edited by A. M. James (ACOL, London, 1987).

[133]R. Grissa, V. Fernandez, N. Fairley, J. Hamon, N. Stephant, J. Rolland, R. Bouchet, M. Lecuyer, M. Deschamps, D. Guyomard and P. Moreau, "XPS and SEM-EDX Study of Electrolyte Nature Effect on Li Electrode in Lithium Metal Batteries", ACS Applied Energy Materials **1**, 5694–5702 (2018).

[134]R. J. Keyse, A. J. Garratt-Reed, P. J. Goodhew and G. W. Lorimer, *Introduction to Scanning Transmission Electron Microscopy* (BIOS Scientific, 1998).

[135]I. P. Jones, *Chemical Analysis Using Electron Beams* (The Institute of Materials, 1992).

[136]F. Ambroz, T. J. Macdonald, V. Martis, I. P. Parkin, F. Ambroz, T. J. Macdonald, I. P. Parkin and V. Martis, "Evaluation of the BET Theory for the Characterization of Meso and Microporous MOFs", Small Methods **2**, 1800173 (2018).

[137]R. Bardestani, G. S. Patience and S. Kaliaguine, "Experimental Methods in Chemical Engineering: Specific Surface Area and Pore Size Distribution Measurements—BET, BJH, and DFT", The Canadian Journal of Chemical Engineering **97**, 2781–2791 (2019).

[138]S. Lowell and J. E. Shields, *Powder Surface Area and Porosity* (Springer Netherlands, Dordrecht, 1991).

[139]S. Brunauer, P. H. Emmett and E. Teller, "Adsorption of Gases in Multimolecular Layers", Journal of the American Chemical Society **60**, 309–319 (1938).

[140]K. Sing, "The Use of Nitrogen Adsorption for the Characterisation of Porous Materials", Colloids and Surfaces A: Physicochemical and Engineering Aspects **187-188**, 3–9 (2001).

[141]E. P. Barrett, L. G. Joyner and P. P. Halenda, "The Determination of Pore Volume and Area Distributions in Porous Substances. I. Computations from Nitrogen Isotherms", Journal of the American Chemical Society **73**, 373–380 (1951).

[142]M. S. Amer, *Raman Spectroscopy, Fullerenes and Nanotechnology* (Royal Society of Chemistry, Cambridge, 2010).

[143]M. S. Dresselhaus, A. Jorio and R. Saito, "Characterizing Graphene, Graphite, and Carbon Nanotubes by Raman Spectroscopy", Annual Review of Condensed Matter Physics **1**, 89–108 (2010).

[144]P. Vandenabeele, *Practical Raman spectroscopy: an Introduction* (Wiley, 2013).

[145]C. Backes, K. R. Paton, D. Hanlon, S. Yuan, M. I. Katsnelson, J. Houston, R. J. Smith, D. McCloskey, J. F. Donegan and J. N. Coleman, "Spectroscopic Metrics Allow In Situ Measurement of Mean Size and Thickness of Liquid-Exfoliated Few-Layer Graphene Nanosheets", Nanoscale **8**, 4311–4323 (2016).

[146]M. D. Stoller and R. S. Ruoff, "Best Practice Methods for Determining an Alectrode Material's Performance for Ultracapacitors", Energy & Environmental Science **3**, 1294–1301 (2010).

[147]P. T. Kissinger and W. R. Heineman, "Cyclic Voltammetry", Journal of Chemical Education **60**, 702 (1983).

[148]Q. Abbas, D. Pajak, E. Frąckowiak and F. Béguin, "Effect of binder on the performance of carbon/carbon symmetric capacitors in salt aqueous electrolyte", Electrochimica Acta **140**, Electrochemistry for a New Era, 132–138 (2014).

[149]P. Zaccagnini, M. Serrapede, A. Lamberti, S. Bianco, P. Rivolo, E. Tresso, C. F. Pirri, G. Barbero and A. L. Alexe-Ionescu, "Modeling of Electrochemical Capacitors Under Dynamical Cycling", Electrochimica Acta **296**, 709–718 (2019).

[150]J. W. Campos, M. Beidaghi, K. B. Hatzell, C. R. Dennison, B. Musci, V. Presser, E. C. Kumbur and Y. Gogotsi, "Investigation of Carbon Materials for Use as a Flowable Electrode in Electrochemical Flow Capacitors", Electrochimica Acta **98**, 123–130 (2013).

[151]A. Allagui, T. J. Freeborn, A. S. Elwakil and B. J. Maundy, "Reevaluation of Performance of Electric Double-layer Capacitors from Constant-current Charge/Discharge and Cyclic Voltammetry", Scientific Reports **6**, 38568 (2016).

[152]R. Vicentini, L. Morais, L. Da Silva, P. Junior, T. Alves, W. Nunes and H. Zanin, "How to Measure and Calculate Equivalent Series Resistance of Electric Double-Layer Capacitors", Molecules **24**, 1452 (2019).

[153]A. Lasia, "The Origin of the Constant Phase Element", Journal of Physical Chemistry Letters **13**, 580–589 (2022).

[154]M. R. Shoar Abouzari, F. Berkemeier, G. Schmitz and D. Wilmer, "On the Physical Interpretation of Constant Phase Elements", Solid State Ionics **180**, 922–927 (2009).

[155]W. Schmickler and E. Santos, *Interfacial Electrochemistry*, 2nd ed. (Springer, Heidelberg ; 2010).

[156]J. Huang, "Diffusion Impedance of Electroactive Materials, Electrolytic Solutions and Porous Electrodes: Warburg Impedance and Beyond", Electrochimica Acta **281**, 170–188 (2018).

[157]B.-A. Mei, O. Munteshari, J. Lau, B. Dunn and L. Pilon, "Physical Interpretations of Nyquist Plots for EDLC Electrodes and Devices", The Journal of Physical Chemistry C **122**, 194–206 (2018).

[158]Y. R. Nian and H. Teng, "Influence of Surface Oxides on the Impedance Behavior of Carbon-Based Electrochemical Capacitors", Journal of Electroanalytical Chemistry **540**, 119–127 (2003).

[159]T. Momma, X. Liu, T. Osaka, Y. Ushio and Y. Sawada, "Electrochemical Modification of Active Carbon Fiber Electrode and its Application to Double-Layer Capacitor", Journal of Power Sources **60**, 249–253 (1996).

[160]X. Liu and T. Osaka, "All-Solid-State Electric Double-Layer Capacitor with Isotropic High-Density Graphite Electrode and Polyethylene Oxide/ $LiClSO_4$ Polymer Electrolyte", Journal of the Electrochemical Society **143**, 3982–3986 (1996).

[161]J. Huang, Y. Gao, J. Luo, S. Wang, C. Li, S. Chen and J. Zhang, "Editors' Choice—Review—Impedance Response of Porous Electrodes: Theoretical Framework, Physical Models and Applications", Journal of The Electrochemical Society **167**, 166503 (2020).

[162]L. W. Le Fevre, R. Fields, E. Redondo, R. Todd, A. J. Forsyth and R. A. W. Dryfe, "Cell Optimisation of Supercapacitors Using a Quasi-Reference Electrode and Potentiostatic Analysis", Journal of Power Sources **424**, 52–60 (2019).

[163]N. Shirshova, H. Qian, M. S. Shaffer, J. H. Steinke, E. S. Greenhalgh, P. T. Curtis, A. Kucernak and A. Bismarck, "Structural Composite Supercapacitors", Composites Part A: Applied Science and Manufacturing **46**, 96–107 (2013).

[164]C. Moreno-Castilla, M. A. Ferro-García, J. P. Joly, I. Bautista-Toledo, F. Carrasco-Marín and J. Rivera-Utrilla, "Activated Carbon Surface Modifications by Nitric Acid, Hydrogen Peroxide, and Ammonium Peroxydisulfate Treatments", Langmuir **11**, 4386–4392 (1995).

[165]M. J. Bleda-Martínez, D. Lozano-Castelló, E. Morallón, D. Cazorla-Amorós and A. Linares-Solano, "Chemical and Electrochemical Characterization of Porous Carbon Materials", Carbon **44**, 2642–2651 (2006).

[166]S. A. Chernyak, A. S. Ivanov, N. E. Strokova, K. I. Maslakov, S. V. Savilov and V. V. Lunin, "Mechanism of Thermal Defunctionalization of Oxidized Carbon Nanotubes", Journal of Physical Chemistry C **120**, 17465–17474 (2016).

[167]ASEQ Instruments, *Equipment for Spectroscopy*.

[168]M. Wojdyr, "Fityk: A General-Purpose Peak Fitting Program", Journal of Applied Crystallography **43**, 1126–1128 (2010).

[169]X. Li, J. Rong and B. Wei, "Electrochemical Behavior of Single-Walled Carbon Nanotube Supercapacitors under Compressive Stress", ACS Nano **4**, 6039–6049 (2010).

[170]T. Dobbelaere, P. M. Vereecken and C. Detavernier, "A USB-Controlled Potentiostat/Galvanostat for Thin-Film Battery Characterization", HardwareX **2**, 34–49 (2017).

[171]J. G. Vos and M. T. Koper, "Measurement of Competition Between Oxygen Evolution and Chlorine Evolution Using Rotating Ring-Disk Electrode Voltammetry", Journal of Electroanalytical Chemistry **819**, 260–268 (2018).

[172]M. He, K. Fic, E. Frackowiak, P. Novák and E. J. Berg, "Ageing Phenomena in High-Voltage Aqueous Supercapacitors Investigated by In Situ Gas Analysis", Energy & Environmental Science **9**, 623–633 (2016).

[173]P. Ratajczak, K. Jurewicz, P. Skowron, Q. Abbas and F. Béguin, "Effect of Accelerated Ageing on the Performance of High Voltage Carbon/Carbon Electrochemical Capacitors in Salt Aqueous Electrolyte", Electrochimica Acta **130**, 344–350 (2014).

[174]P. Ratajczak, K. Jurewicz and F. Béguin, "Factors Contributing to Ageing of High Voltage Carbon/Carbon Supercapacitors in Salt Aqueous Electrolyte", Journal of Applied Electrochemistry **44**, 475–480 (2014).

[175]P. Przygocki, P. Ratajczak and F. Béguin, "Quantification of the Charge Consuming Phenomena under High-Voltage Hold of Carbon/Carbon Supercapacit-

ors by Coupling Operando and Post-Mortem Analyses", Angewandte Chemie International Edition **58**, 17969–17977 (2019).

[176]R. Kötz, M. Hahn, P. Ruch and R. Gallay, "Comparison of Pressure Evolution in Supercapacitor Devices Using Different Aprotic Solvents", Electrochemistry Communications **10**, 359–362 (2008).

[177]A. Platek, J. Piwek, K. Fic and E. Frackowiak, "Ageing Mechanisms in Electrochemical Capacitors with Aqueous Redox-Active Electrolytes", Electrochimica Acta **311**, 211–220 (2019).

[178]R. Kötz, P. W. Ruch and D. Cericola, "Aging and Failure Mode of Electrochemical Double Layer Capacitors During Accelerated Constant Load Tests", Journal of Power Sources **195**, 923–928 (2010).

[179]N. Rizoug, P. Bartholomeus and P. Le Moigne, "Study of the Ageing Process of a Supercapacitor Module Using Direct Method of Characterization", IEEE Transactions on Energy Conversion **27**, 220–228 (2012).

[180]D. Weingarth, A. Foelske-Schmitz and R. Kötz, "Cycle Versus Voltage Hold – Which is the Better Stability Test for Electrochemical Double Layer Capacitors?", Journal of Power Sources **225**, 84–88 (2013).

[181]F. R. Hughson, R. Borah and T. Nann, "A 2.7 V Aqueous Supercapacitor Using a Microemulsion Electrolyte", Batteries & Supercaps **4**, 1122–1125 (2021).

[182]W. G. Nunes, B. G. A. Freitas, R. M. Beraldo, R. M. Filho, L. M. Da Silva and H. Zanin, "A Rational Experimental Approach to Identify Correctly the Working Voltage Window of Aqueous-Based Supercapacitors", Scientific Reports **10**, 19195 (2020).

[183]J. H. Chae and G. Z. Chen, "1.9 V Aqueous Carbon–Carbon Supercapacitors with Unequal Electrode Capacitances", Electrochimica Acta **86**, 248–254 (2012).

[184]S. Zhang and N. Pan, "Supercapacitors Performance Evaluation", Advanced Energy Materials **5**, 1401401 (2015).

[185]V. Khomenko, E. Raymundo-Piñero and F. Béguin, "Optimisation of an Asymmetric Manganese Oxide/Activated Carbon Capacitor Working at 2 V in Aqueous Medium", Journal of Power Sources **153**, 183–190 (2006).

[186]R. Khayyam Nekouei, S. S. Mofarah, S. Maroufi, I. Tudela and V. Sahajwalla, "Determination of the Optimum Potential Window for Super- and Pseudocapacitance Electrodes via In-Depth Electrochemical Impedance Spectroscopy Analysis", Journal of Energy Storage **56**, 106137 (2022).

[187]D. W. Kumsa, N. Bhadra, E. M. Hudak, S. C. Kelley, D. F. Untereker and J. T. Mortimer, "Electron Transfer Processes Cccurring on Platinum Neural Stimulating Electrodes: a Tutorial on the $i(V_e)$ Profile", Journal of Neural Engineering **13**, 052001 (2016).

[188]M. Favaro, C. Valero-Vidal, J. Eichhorn, F. M. Toma, P. N. Ross, J. Yano, Z. Liu and E. J. Crumlin, "Elucidating the Alkaline Oxygen Evolution Reaction Mechanism on Platinum", Journal of Materials Chemistry A **5**, 11634–11643 (2017).

[189]M. Peng, L. Wang, L. Li, Z. Peng, X. Tang, T. Hu, K. Yuan and Y. Chen, "Molecular Crowding Agents Engineered to Make Bioinspired Electrolytes for High-Voltage Aqueous Supercapacitors", eScience **1**, 83–90 (2021).

[190]D. W. Wang and D. Su, "Heterogeneous Nanocarbon Materials for Oxygen Reduction Reaction", Energy & Environmental Science **7**, 576–591 (2014).

[191]K. Obata, R. Van De Krol, M. Schwarze, R. Schomä and F. F. Abdi, "In Situ Observation of pH Change During Water Splitting in Neutral pH Conditions: Impact of Natural Convection Driven by Buoyancy Effects", Energy and Environmental Science **13**, 5104 (2020).

[192]Z. Dai, C. Peng, J. H. Chae, K. C. Ng and G. Z. Chen, "Cell Voltage Versus Electrode Potential Range in Aqueous Supercapacitors", Scientific Reports **5**, 9854 (2015).

[193]Y. Yi, G. Weinberg, M. Prenzel, M. Greiner, S. Heumann, S. Becker and R. Schlögl, "Electrochemical Corrosion of a Glassy Carbon Electrode", Catalysis Today **295**, 32–40 (2017).

[194]M. P. Bichat, E. Raymundo-Piñero and F. Béguin, "High Voltage Supercapacitor Built with Seaweed Carbons in Neutral Aqueous Electrolyte", Carbon **48**, 4351–4361 (2010).

[195]L. Demarconnay, E. Raymundo-Piñero and F. Béguin, "A Symmetric Carbon/-Carbon Supercapacitor Operating at 1.6 V by Using a Neutral Aqueous Solution", Electrochemistry Communications **12**, 1275–1278 (2010).

[196]Q. Gao, L. Demarconnay, E. Raymundo-Piñero and F. Béguin, "Exploring the Large Voltage Range of Carbon/Carbon Supercapacitors in Aqueous Lithium Sulfate Electrolyte", Energy & Environmental Science **5**, 9611–9617 (2012).

[197]B. A. Mei, J. Lau, T. Lin, S. H. Tolbert, B. S. Dunn and L. Pilon, "Physical Interpretations of Electrochemical Impedance Spectroscopy of Redox Active Electrodes for Electrical Energy Storage", Journal of Physical Chemistry C **122**, 24499–24511 (2018).

[198]K. Okajima, K. Ohta and M. Sudoh, "Capacitance Behavior of Activated Carbon Fibers with Oxygen-Plasma Treatment", Electrochimica Acta **50**, 2227–2231 (2005).

[199]P. J. Hall, M. Mirzaeian, S. I. Fletcher, F. B. Sillars, A. J. R. Rennie, G. O. Shitta-Bey, G. Wilson, A. Cruden and R. Carter, "Energy Storage in Electrochemical Capacitors: Designing Functional Materials to Improve Performance", Energy & Environmental Science **3**, 1238–1251 (2010).

[200]G. Wang, Z. Shao and Z. Yu, "Comparisons of Different Carbon Conductive Additives on the Electrochemical Performance of Activated Carbon", Nanotechnology **18**, 205705 (2007).

[201]E. A. Kiseleva, S. A. Kochanova, E. J. Shkolnikov, A. B. Tarasenko, O. V. Zaitseva, O. V. Uryupina, G. V. Valyano and M. A. Zhurilova, "Influence of Carbon Conductive Additives on Electrochemical Double-Layer Supercapacitor Parameters", Journal of Physics: Conference Series **946**, 012030 (2018).

[202]N. Jäckel, D. Weingarth, M. Zeiger, M. Aslan, I. Grobelsek and V. Presser, "Comparison of Carbon Onions and Carbon Blacks as Conductive Additives for Carbon Supercapacitors in Organic Electrolytes", Journal of Power Sources **272**, 1122–1133 (2014).

[203]N. Jäckel, D. Weingarth, A. Schreiber, B. Krüner, M. Zeiger, A. Tolosa, M. Aslan and V. Presser, "Performance Evaluation of Conductive Additives for Activated Carbon Supercapacitors in Organic Electrolyte", Electrochimica Acta **191**, 284–298 (2016).

[204]M. D. Stoller, S. Park, Y. Zhu, J. An and R. S. Ruoff, "Graphene-Based Ultracapacitors", Nano Letters **8**, 3498–3502 (2008).

[205]R. Wang, Y. Qian, W. Li, S. Zhu, F. Liu, Y. Guo, M. Chen, Q. Li and L. Liu, "Performance-Enhanced Activated Carbon Electrodes for Supercapacitors Combining Both Graphene-Modified Current Collectors and Graphene Conductive Additive", Materials **11**, 799 (2018).

[206]Y. Niu, J. Wang, J. Zhang and Z. Shi, "Graphene Quantum Dots as a Novel Conductive Additive to Improve the Capacitive Performance for Supercapacitors", Journal of Electroanalytical Chemistry **828**, 1–10 (2018).

[207]K. V. Kumar, S. Gadipelli, B. Wood, K. A. Ramisetty, A. A. Stewart, C. A. Howard, D. J. Brett and F. Rodriguez-Reinoso, "Characterization of the Adsorption Site Energies and Heterogeneous Surfaces of Porous Materials", Journal of Materials Chemistry A **7**, 10104–10137 (2019).

[208]A. Eckmann, A. Felten, A. Mishchenko, L. Britnell, R. Krupke, K. S. Novoselov and C. Casiraghi, "Probing the Nature of Defects in Graphene by Raman Spectroscopy", Nano Letters **12**, 3925–3930 (2012).

[209]A. C. Ferrari and D. M. Basko, "Raman Spectroscopy as a Versatile Tool for Studying the Properties of Graphene", Nature Nanotechnology **8**, 235–246 (2013).

[210]S. Sukumaran, "Two-dimensional Materials For Use In Advanced Energy Storage", MSc Thesis (University of Durham, Durham, UK).

[211]C. L. Liu, W. S. Dong, G. P. Cao, J. R. Song, L. Liu and Y. S. Yang, "Influence of KOH Followed by Oxidation Pretreatment on the Electrochemical Performance of Phenolic Based Activated Carbon Fibers", Journal of Electroanalytical Chemistry **611**, 225–231 (2007).

[212]J. Gamby, P. L. Taberna, P. Simon, J. F. Fauvarque and M. Chesneau, "Studies and Characterisations of Various Activated Carbons Used for Carbon/Carbon Supercapacitors", Journal of power sources **101**, 109–116 (2001).

[213]B. Fang and L. Binder, "A Modified Activated Carbon Aerogel for High-Energy Storage in Electric Double Layer Capacitors", Journal of Power Sources **163**, 616–622 (2006).

[214]X. Zang, C. Shen, M. Sanghadasa and L. Lin, "High-Voltage Supercapacitors Based on Aqueous Electrolytes", ChemElectroChem **6**, 976–988 (2019).

[215]M. Sevilla, S. Álvarez, T. A. Centeno, A. B. Fuertes and F. Stoeckli, "Performance of Templated Mesoporous Carbons in Supercapacitors", Electrochimica Acta **52**, 3207–3215 (2007).

[216]K. Fic, G. Lota and E. Frackowiak, "Electrochemical Properties of Supercapacitors Operating in Aqueous Electrolyte with Surfactants", Electrochimica Acta **55**, 7484–7488 (2010).

[217]J. Xu, R. Zhang, P. Chen and S. Ge, "Effects of Adding Ethanol to KOH Electrolyte on Electrochemical Performance of Titanium Carbide-Derived Carbon", Journal of Power Sources **246**, 132–140 (2014).

[218]D. G. Gromadskyi, J. H. Chae, S. A. Norman and G. Z. Chen, "Correlation of Energy Storage Performance of Supercapacitor with Iso-Propanol Improved Wettability of Aqueous Electrolyte on Activated Carbon Electrodes of Various Apparent Densities", Applied Energy **159**, 39–50 (2015).

[219]B. Vafakish and L. D. Wilson, "A Review on Recent Progress of Glycan-Based Surfactant Micelles as Nanoreactor Systems for Chemical Synthesis Applications", Polysaccharides **2**, 168–186 (2021).

[220]G. Usha, R. Prakash, K. Karpagalakshmi, S. Ramalakshmi, L. Piramuthu, C. Yang and N. Selvapalam, "A Graphene Oxide-Based Fluorescent Sensor for Surfactants", Analytical Methods **11**, 5826–5832 (2019).

[221]W. H. Duan, Q. Wang and F. Collins, "Dispersion of Carbon Nanotubes with SDS Surfactants : a Study from a Binding Energy Perspective", Chemical Science **2**, 1407–1413 (2011).

[222]G. Lota and E. Frackowiak, "Striking Capacitance of Carbon/Iodide Interface", Electrochemistry Communications **11**, 87–90 (2009).

[223]S. Ghasemi and F. Ahmadi, "Effect of Surfactant on the Electrochemical Performance of Graphene/Iron Oxide Electrode for Supercapacitor", Journal of Power Sources **289**, 129–137 (2015).

[224]Z. Hou, X. Zhang, X. Li, Y. Zhu, J. Liang and Y. Qian, "Surfactant Widens the Electrochemical Window of an Aqueous Electrolyte for Better Rechargeable Aqueous Sodium/Zinc Battery", Journal of Materials Chemistry A **5**, 730–738 (2017).

[225]X. Xie, Z. Yang, Z. Feng and J. Huang, "Effect of Dodecyl Sulfate Anions on the Electrochemical Performances of Zinc-Aluminum-Hydrotalcite as Anode Material for Zinc/Nickel Secondary Batteries", Electrochimica Acta **149**, 101–107 (2014).

[226]J. Tan and J. Liu, "Electrolyte Engineering Toward High-Voltage Aqueous Energy Storage Devices", Energy & Environmental Materials **4**, 302–306 (2021).

[227]W. Wang, C. Yang, X. Chi, J. Liu, B. Wen and Y. Liu, "Small-Molecular Crowding Electrolyte Enables High-Voltage and High-Rate Supercapacitors", Energy Technology **9**, 2100684 (2021).

[228]L. Suo, O. Borodin, W. Sun, X. Fan, C. Yang, F. Wang, T. Gao, Z. Ma, M. Schroeder, A. von Cresce, S. M. Russell, M. Armand, A. Angell, K. Xu and C. Wang, "Advanced High-Voltage Aqueous Lithium-Ion Battery Enabled by "Water-in-Bisalt" Electrolyte", Angewandte Chemie International Edition **55**, 7136–7141 (2016).

[229]L. Suo, F. Han, X. Fan, H. Liu, K. Xu and C. Wang, ""Water-in-Salt" Electrolytes Enable Green and Safe Li-Ion Batteries for Large Scale Electric Energy Storage Applications", Journal of Materials Chemistry A **4**, 6639–6644 (2016).

[230]J. Xie, Z. Liang and Y. C. Lu, "Molecular Crowding Electrolytes for High-Voltage Aqueous Batteries", Nature Materials 2020 19:9 **19**, 1006–1011 (2020).

[231]G. E. Tiller, T. J. Mueller, M. E. Dockter and W. G. Struve, "Hydrogenation of Triton X-100 Eliminates its Fluorescence and Ultraviolet Light Absorption While Preserving its Detergent Properties", Analytical Biochemistry **141**, 262–266 (1984).

[232]M. Alkasrawi, T. Eriksson, J. Börjesson, A. Wingren, M. Galbe, F. Tjerneld and G. Zacchi, "The Effect of Tween-20 on Simultaneous Saccharification and Fermentation of Softwood to Ethanol", Enzyme and Microbial Technology **33**, 71–78 (2003).

[233]P. R. Paiva, M. B. Monte, R. A. Simão and J. C. Gaspar, "In Situ AFM Study of Potassium Oleate Adsorption and Calcium Precipitate Formation on an Apatite Surface", Minerals Engineering **24**, 387–395 (2011).

[234]L. Hu, G. Pan, H. Wang, X. Zhang, Z. Wang and T. Zhu, "The Synergy and DFT Study of TT-LYK and Potassium Oleate on Chemical Mechanical Polishing of Cobalt in Alkaline Medium", Materials Chemistry and Physics **256**, 123672 (2020).

[235]G. Lota, T. A. Centeno, E. Frackowiak and F. Stoeckli, "Improvement of the Structural and Chemical Properties of a Commercial Activated Carbon for its Application in Electrochemical Capacitors", Electrochimica Acta **53**, 2210–2216 (2008).

[236]A. Rao, A. Fung, M. Dresselhaus and M. Endo, "Structural Characterization of Heat-Treated Activated Carbon Fibers", Journal of Materials Research **7**, 1788–1794 (1992).

[237]D. Pantea, H. Darmstadt, S. Kaliaguine, L. Sümmchen and C. Roy, "Electrical Conductivity of Thermal Carbon Blacks: Influence of Surface Chemistry", Carbon **39**, 1147–1158 (2001).

[238]E. N. Guyes, T. Malka and M. E. Suss, "Enhancing the Ion-Size-Based Selectivity of Capacitive Deionization Electrodes", Environmental Science and Technology **53**, 8447–8454 (2019).

[239]M. E. Suss, "Size-Based Ion Selectivity of Micropore Electric Double Layers in Capacitive Deionization Electrodes", Journal of The Electrochemical Society **164**, E270–E275 (2017).

[240]R. D. Shannon, "Revised Effective Ionic Radii and Systematic Studies of Interatomic Distances in Halides and Chalcogenides", Acta Crystallographica Section A **32**, 751–767 (1976).

[241]I. T. Bello, A. O. Oladipo, O. Adedokun and S. M. Dhlamini, "Recent Advances on the Preparation and Electrochemical Analysis of MoS_2-Based Materials for Supercapacitor Applications: A Mini-Review", Materials Today Communications **25**, 101664 (2020).

[242]W. Chen, X. Yu, Z. Zhao, S. Ji and L. Feng, "Hierarchical Architecture of Coupling Graphene and 2D WS_2 for High-Performance Supercapacitor", Electrochimica Acta **298**, 313–320 (2019).

[243]T. W. Lin, T. Sadhasivam, A. Y. Wang, T. Y. Chen, J. Y. Lin and L. D. Shao, "Ternary Composite Nanosheets with MoS_2/WS_2/Graphene Heterostructures as High-Performance Cathode Materials for Supercapacitors", ChemElectroChem **5**, 1024–1031 (2018).

[244]M. Qiu, Z. T. Sun, D. K. Sang, X. G. Han, H. Zhang and C. M. Niu, "Current Progress in Black Phosphorus Materials and their Applications in Electrochemical Energy Storage", Nanoscale **9**, 13384–13403 (2017).

[245]X. Zhang, J. Xiang, C. Mu, F. Wen, S. Yuan, J. Zhao, D. Xu, C. Su and Z. Liu, "SnS_2 Nanoflakes Anchored Graphene obtained by Liquid Phase Exfoliation and MoS_2 Nanosheet Composites as Lithium and Sodium Battery Anodes", Electrochimica Acta **227**, 203–209 (2017).

[246]B. Adilbekova, Y. Lin, E. Yengel, H. Faber, G. Harrison, Y. Firdaus, A. El-Labban, D. H. Anjum, V. Tung and T. D. Anthopoulos, "Liquid Phase Exfoliation of MoS_2 and WS_2 in Aqueous Ammonia and their Application in Highly Efficient Organic Solar Cells", Journal of Materials Chemistry C **8**, 5259–5264 (2020).

[247]H. Yuan, X. Liu, L. Ma, P. Gong, Z. Yang, H. Wang, J. Wang and S. Yang, "High Efficiency Shear Exfoliation for Producing High-Quality, Few-Layered MoS_2 Nanosheets in a Green Ethanol/Water System", RSC Advances **6**, 82763–82773 (2016).

[248]C. Xing, J. Zhang, J. Jing, J. Li and F. Shi, "Preparations, Properties and Applications of Low-Dimensional Black Phosphorus", Chemical Engineering Journal **370**, 120–135 (2019).

[249]Z. Yang, H. Liang, X. Wang, X. Ma, T. Zhang, Y. Yang, L. Xie, D. Chen, Y. Long, J. Chen, Y. Chang, C. Yan, X. Zhang, X. Zhang, B. Ge, Z. Ren, M. Xue and G. Chen, "Atom-Thin SnS_2-xSe_x with Adjustable Compositions by Direct Liquid Exfoliation from Single Crystals", ACS Nano **10**, 755–762 (2016).

[250]Y. Chen, K. Yang, B. Jiang, J. Li, M. Zeng and L. Fu, "Emerging Two-Dimensional Nanomaterials for Electrochemical Hydrogen Evolution", Journal of Materials Chemistry A **5**, 8187–8208 (2017).

[251]Y. Cai, W. Zhang, R. Fang, D. Zhao, Y. Wang and J. Wang, "Well-Dispersed Few-Layered MoS_2 Connected with Robust 3D Conductive Architecture for Rapid Capacitive Deionization Process and its Specific Ion Selectivity", Desalination **520**, 115325 (2021).

Appendix A

Python Code for Analysing Cyclic Voltammetry Data

```
import numpy as np
import matplotlib.pyplot as plt
import csv
from shapely.geometry import Polygon
import scipy.integrate
from scipy.stats import sem


x = []
x0 = 0.0
x1 = 0.0
y = []
i = 1
d0 = 0.0
d1 = 0.0
t_1 = 0.0
t = 0.0
z = []
Caps = []
Energy = []
Power = []
CCsp = []
DCsp = []
```

```
CPsp = []
DPsp = []
CEsp = []
DEsp = []
Coulombic = []
EE = []

file = input('File name:')

filet = file + '.txt'
fileCsp = file + '_Capacities' + '.txt'
fileCspH = file + '_halfcycles_Capacities' + '.txt'

U_r = input('Voltage Range (V):')
rate = input('Scan Rate (mV/s):')
mass = input('Total Electrode Mass (mg):')

t_cycle = 2000*float(U_r)/float(rate)



with open(filet) as cv:
    data = csv.DictReader(cv, delimiter='\t')

    for row in data:

        x1 = float(row['Potential(V)'])

        time_step = float(row['Elapsed time(s)']) - t_1
        t_1 = float(row['Elapsed time(s)'])
        d_t = i*t_cycle - t_1

        if d_t < time_step:
            #print(t_cycle, time_step, d_t, t_1, x1)
            z.append(float(row['Elapsed time(s)']) - t)
            x.append(float(row['Potential(V)']))
            y.append(float(row['Current(A)']))
```

```
            fileit = file + '_cycle' + str(i) + '.txt'
            fileip = file + '_cycle' + str(i) + '.png'
            with open(fileit, mode='w') as target:
                writer = csv.writer(target, delimiter='\t', quotechar
                                                    ='"', quoting=csv.
                                                    QUOTE_NONNUMERIC)
                writer.writerow(['Time (s)', 'Potential(V)', 'Current
                                                    (A)'])
                j = len(x)
                k = 0
                data = []
                while k < j:
                    writer.writerow([z[k], x[k], y[k]])
                    data.append((x[k], y[k]))
                    k += 1
            target.close()
            plt.plot(x, y)
            plt.xlabel('Potential(V)')
            plt.ylabel('Current(A)')
            plt.savefig(fileip)
            plt.clf()

# Create a closed polygon from the data using shapely
            polygon = Polygon(data)

# Find area of closed loop (assuming units of current and voltage are
                                    A and V)
            area = polygon.area

            # print("Area", area)

            # Calculate the specific capacitance (F/g)
            # Factor of two, for two electrodes...
            C = (area)/(2*float(rate)*float(U_r)*(10**(-6)))
```

```
            Csp = 2.0*(area)/(float(rate)*float(mass)*float(U_r)*(10
                                                **(-6)))

            Caps.append(Csp)

            # Calculate average Power
            P = area/4
            Psp = area/(float(mass)*10**(-3))
            Power.append(Psp)

            # Calculate energy stored
            E = C*(float(U_r)**2)/2
            Esp = Csp*(float(U_r)**2)/2
            Energy.append(Esp)

            # for k in range(len(Caps)):
            #print(i, Caps[k])
            #print("Specific capacitance: ","%.2f" % Csp," F/g")

# now look at half cycles for charging/discharging

            halfcycle_length = int(len(data)/2)


            ##integrating under the charging curve to find Csp Psp
                                                and Esp
            charging_Csp = 4.0*scipy.integrate.trapezoid(y[0:
                                                halfcycle_length], x =
                                                 x[0:halfcycle_length]
                                                )/(float(rate)*float(
                                                mass)*float(U_r)*(10**
                                                (-6)))
            CCsp.append(charging_Csp)

            charging_charge = scipy.integrate.trapezoid(y[0:
                                                halfcycle_length], x =
```

```
                                        z[0:halfcycle_length]
                                        )

        charging_Psp = 2.0*scipy.integrate.trapezoid(y[0:
                                        halfcycle_length], x =
                                         x[0:halfcycle_length]
                                        )/(float(mass)*10**(-3
                                        ))
        CPsp.append(charging_Psp)

        charging_Esp = charging_Csp*(float(U_r)**2)/2
        CEsp.append(charging_Esp)

        ##integrating under the discharging curve to find Csp Psp
                                         and Esp
        discharging_Csp = 4.0*scipy.integrate.trapezoid(y[
                                        halfcycle_length:len(
                                        data)], x = x[
                                        halfcycle_length:len(
                                        data)])/(float(rate)*
                                        float(mass)*float(U_r)
                                        *(10**(-6)))
        DCsp.append(discharging_Csp)
        print(charging_Csp, discharging_Csp)

        discharging_charge = abs(scipy.integrate.trapezoid(y[
                                        halfcycle_length:len(
                                        data)], x = z[
                                        halfcycle_length:len(
                                        data)]))

        discharging_Psp = 2.0*scipy.integrate.trapezoid(y[
                                        halfcycle_length:len(
                                        data)], x = x[
                                        halfcycle_length:len(
                                        data)])/(float(mass)*
```

```
                                                10**(-3))
            DPsp.append(discharging_Psp)

            discharging_Esp = discharging_Csp*(float(U_r)**2)/2
            DEsp.append(discharging_Esp)

            #efficiencies
            coulombic_efficiency = 100*discharging_charge/
                                                charging_charge
            Coulombic.append(coulombic_efficiency)

            energy_efficiency = 100*discharging_Esp/charging_Esp
            EE.append(energy_efficiency)

            del x[:]
            del y[:]
            del z[:]
            del data[:]
            i += 1
            t = float(row['Elapsed time(s)'])

        else:
            z.append(float(row['Elapsed time(s)']) - t)
            x.append(float(row['Potential(V)']))
            y.append(float(row['Current(A)']))

cv.close()

cycles = []
n = len(Caps)

with open(fileCsp, mode='w') as Carget:
    Capwriter = csv.writer(Carget, delimiter='\t', quotechar='"',
                                        quoting=csv.QUOTE_NONNUMERIC)
    Capwriter.writerow(['Cycle No.', 'Specific Capacitance (F/g)',
```

```
                    'Specific Energy (J/g)', 'Specific Power (W/g)
                                                        '])
    for k in range(n):
        #print('!', Caps[k])
        Capwriter.writerow([k, Caps[k], Energy[k], Power[k]])
        cycles.append(k)
Carget.close()

with open(fileCspH, mode='w') as Carget:
    Capwriter = csv.writer(Carget, delimiter='\t', quotechar='"',
                                    quoting=csv.QUOTE_NONNUMERIC)
    Capwriter.writerow(['Cycle No.', 'Charging Specific Capacitance (
                                    F/g)','Discharging Specific
                                    Capacitance (F/g)',
                    'Charging Specific Energy (J/g)','Discharging
                                                    Specific
                                                    Energy (J/g
                                                    )', '
                                                    Charging
                                                    Specific
                                                    Power (W/g)
                                                    ',
                    'Discharging Specific Power (W/g)', 'Coulombic
                                                     Efficiency
                                                     (%)', '
                                                    Energy
                                                    Efficiency
                                                    (%)'])
    for k in range(n):
        #print('!', Caps[k])
        Capwriter.writerow([k, CCsp[k], DCsp[k], CEsp[k], DEsp[k],
                                        CPsp[k], DPsp[k],
                                        Coulombic[k], EE[k]])
Carget.close()
```

```
outputs = open((file + '_outputs.txt'), 'w')
if n > 10:
    outputs.write(
    'Specific Capacitance = ' + str(np.mean(Caps[(n-10):n])) + ' +/-
                                        ' + str(sem(Caps[(n-10):n])) +
                                         'F/g \n'
    'Specific Energy = ' + str(np.mean(Energy[(n-10):n])) + ' +/- ' +
                                         str(sem(Energy[(n-10):n])) +
                                        'J/g \n'
    'Specific Power = ' + str(np.mean(Power[(n-10):n])) + ' +/- ' +
                                        str(sem(Power[(n-10):n])) + 'W
                                        /g \n')
else:
    outputs.write(
    'Specific Capacitance = ' + str(np.mean(Caps[1:-1])) + ' +/- ' +
                                        str(sem(Caps[1:-1])) + ' F/g \
                                        n'
    'Specific Energy = ' + str(np.mean(Energy[1:-1])) + ' +/- ' + str
                                        (sem(Energy[1:-1])) + ' J/g \n
                                        '
    'Specific Power = ' + str(np.mean(Power[1:-1])) + ' +/- ' + str(
                                        sem(Power[1:-1])) + ' W/g \n')
outputs.close()

outputs = open((file + '_halfcycle_outputs.txt'), 'w')
if n > 10:
    outputs.write(
    'Charging Specific Capacitance = ' + str(np.mean(CCsp[(n-10):n]))
                                         + ' +/- ' + str(sem(CCsp[(n-
                                        10):n])) + ' F/g \n'
    'Charging Specific Energy = ' + str(np.mean(CEsp[(n-10):n])) + '
                                        +/- ' + str(sem(CEsp[(n-10):n]
                                        )) + ' J/g \n'
    'Charging Specific Power = ' + str(np.mean(CPsp[(n-10):n])) + '
                                        +/- ' + str(sem(CPsp[(n-10):n]
                                        )) + ' W/g \n'
```

```
    'Discharging Specific Capacitance = ' + str(np.mean(DCsp[(n-10):n
                                        ])) + ' +/- ' + str(sem(DCsp[(
                                        n-10):n])) + ' F/g \n'
    'Discharging Specific Energy = ' + str(np.mean(DEsp[(n-10):n])) +
                                         ' +/- ' + str(sem(DEsp[(n-10)
                                        :n])) + ' J/g \n'
    'Discharging Specific Power = ' + str(np.mean(DPsp[(n-10):n])) +
                                        ' +/- ' + str(sem(DPsp[(n-10):
                                        n])) + ' W/g \n'
    'Coulombic Efficiency = ' + str(np.mean(Coulombic[(n-10):n])) + '
                                         +/- ' + str(sem(Coulombic[(n-
                                        10):n])) + ' % \n'
    'Energy Efficiency = ' + str(np.mean(EE[(n-10):n])) + ' +/- ' +
                                        str(sem(EE[(n-10):n])) + ' % \
                                        n')


else:
    outputs.write(
    'Charging Specific Capacitance = ' + str(np.mean(CCsp[1:-1])) + '
                                         +/- ' + str(sem(CCsp[1:-1]))
                                        + ' F/g \n'
    'Charging Specific Energy = ' + str(np.mean(CEsp[1:-1])) + ' +/-
                                        ' + str(sem(CEsp[1:-1])) + ' J
                                        /g \n'
    'Charging Specific Power = ' + str(np.mean(CPsp[1:-1])) + ' +/- '
                                         + str(sem(CPsp[1:-1])) + ' W/
                                        g \n'
    'Discharging Specific Capacitance = ' + str(np.mean(DCsp[1:-1]))
                                        + ' +/- ' + str(sem(DCsp[1:-1]
                                        )) + ' F/g \n'
    'Discharging Specific Energy = ' + str(np.mean(DEsp[1:-1])) + '
                                        +/- ' + str(sem(DEsp[1:-1])) +
                                         ' J/g \n'
    'Discharging Specific Power = ' + str(np.mean(DPsp[1:-1])) + '
                                        +/- ' + str(sem(DPsp[1:-1])) +
                                         ' W/g \n'
```

```
    'Coulombic Efficiency = ' + str(np.mean(Coulombic[1:-1])) + ' +/-
                                        ' + str(sem(Coulombic[1:-1]))
                                        + ' % \n'
    'Energy Efficiency = ' + str(np.mean(EE[1:-1])) + ' +/- ' + str(
                                      sem(EE[1:-1])) + ' % \n')
outputs.close()

fileCp = file + '_capacities' + '.png'
plt.plot(cycles, Caps)
plt.xlabel('Cycle Number')
plt.ylabel('Specific Capacitance (F/g)')
plt.savefig(fileCp)
plt.clf()
```

Appendix B

Python Code for Analysing GCD Data

```
import numpy as np
import matplotlib.pyplot as plt
import csv
import random
import scipy.integrate as integrate
from scipy.stats import sem

file = input("GCD file name: ")
file_txt = file + '.txt'
file_data = file + '_data' + '.txt'

time = []
potential = []
current = []
current_smoothed = []

x = []
y = []
z = []

count = 0
cycle_number = 0
```

```
start_time = 0.0

with open(file_txt) as gcd:
    data = csv.DictReader(gcd, delimiter='\t')



    for row in data:
        time.append(float(row['Elapsed time(s)']))
        potential.append(float(row['Potential(V)']))
        current.append(float(row['Current(A)']))



gcd.close()

#smooths current data

i = 2
while i < len(current) - 3:
    window = current[i - 2 : i + 2]
    window_average = sum(window)/4
    print(window_average)
    current_smoothed.append(window_average)
    i += 1

#breaks up data into individual cycles and outputs these

while count < len(current_smoothed)-1  and cycle_number <= 100:
    x.append(time[count + 1] - start_time)
    y.append(potential[count + 1])
    z.append(current_smoothed[count])

    if current_smoothed[count] < 0 and current_smoothed[count+1] > 0
                                        and len(x) > 3:


        plt.plot(x,y)
        plt.savefig(file + '_gcd_cycle' + str(cycle_number) + '.png')
```

```
        plt.close()

        with open((file + '_gcd_cycle' + str(cycle_number) + '.txt'),
                                            mode='w') as target:
            writer = csv.writer(target, delimiter='\t', quotechar='"'
                                                , quoting=csv.
                                                QUOTE_NONNUMERIC)
            writer.writerow(['Time (s)','Potential(V)','Current(A)'])
            k = 0
            while k < len(x):
                writer.writerow([x[k],y[k],z[k]])
                k += 1
        target.close()

        x.clear()
        y.clear()
        z.clear()

        x.append(0.0)
        y.append(potential[count + 1])
        z.append(current_smoothed[count])
        start_time = time[count + 1]
        cycle_number += 1

    count += 1

count = 0

#breaks up data into halfcyles for analysis

mass = float(input('Total electrode mass (mg)'))/1000

charging_csp = []
discharging_csp = []
charging_esr = []
discharging_esr = []
```

```
charging_q = []
discharging_q = []
efficiency = []
charging_e = []
discharging_e = []
energy_efficiency = []
charging_p = []
discharging_p = []

constant_current = max(current)

charging = 0

# charging = 0, discharching = 1

while count < len(current_smoothed)-1:
    x.append(time[count + 1] - start_time)
    y.append(potential[count + 1])
    z.append(current_smoothed[count])

    if current_smoothed[count] > 0 and current_smoothed[count+1] < 0
                                        and len(x) > 3 and charging ==
                                         0:

        n = len(x)
        esr = abs(y[2]-y[0])/(2*constant_current)
        charging_esr.append(esr)

        print(y[n-1], y [2])
        if y[n-1] != y[2]:
            csp = 4*constant_current*(x[n-1]-x[2])/(abs(y[n-1]-y[2])*
                                                    mass)
            charging_csp.append(csp)

        q = max(x)*constant_current
        charging_q.append(q)
```

```
        energy = 4*constant_current*integrate.trapezoid(y, x = x)/
                                                mass
        charging_e.append(energy)

        power = energy/abs(x[n-1])
        charging_p.append(power)

        x.clear()
        y.clear()
        z.clear()

        x.append(0.0)
        y.append(potential[count + 1])
        z.append(current_smoothed[count])
        start_time = time[count + 1]
        charging = 1

    if current_smoothed[count] < 0 and current_smoothed[count+1] > 0
                                        and len(x) > 3 and charging ==
                                         1:

        n = len(x)
        esr = abs(y[2]-y[0])/(2*constant_current)
        discharging_esr.append(esr)

        if y[n-1] != y[2]:
            csp = 4*constant_current*(x[n-1]-x[2])/(abs(y[n-1]-y[2])*
                                                    mass)
            discharging_csp.append(csp)

        q = max(x)*constant_current
        discharging_q.append(q)

        energy = 4*constant_current*integrate.trapezoid(y, x = x)/
                                                mass
```

```
        discharging_e.append(energy)

        power = energy/abs(x[n-1])
        discharging_p.append(power)

        x.clear()
        y.clear()
        z.clear()

        x.append(0.0)
        y.append(potential[count + 1])
        z.append(current_smoothed[count])
        start_time = time[count + 1]
        charging = 0

    if current_smoothed[count] < 0 and current[count+1] > 0 and len(x
                                        ) > 3 and charging == 0:
        x.clear()
        y.clear()
        z.clear()

    if current_smoothed[count] > 0 and current[count+1] < 0 and len(x
                                        ) > 3 and charging == 1:
        x.clear()
        y.clear()
        z.clear()

    count += 1

print(len(charging_csp),len(discharging_csp),len(charging_esr),len(
                                    discharging_esr))

with open((file + '_data.txt'), mode='w') as target:
    writer = csv.writer(target, delimiter='\t', quotechar='"',
                                        quoting=csv.QUOTE_NONNUMERIC)
```

```
    writer.writerow(['Cycle No.','Charging Csp(F/g)','Discharging Csp
                                    (F/g','Charging ESR(Ohm)','
                                    Discharging ESR(Ohm)','Input
                                    charge (C)','Output charge (C)
                                    ','Coulombic efficiency(\%)','
                                    Specific Energy Input (J/g)','
                                    Specific Energy Output (J/g)',
                                    'Energy Efficiency (\%)','
                                    Average Specific Power Input (
                                    W/g)','Average Specific Power
                                    Output (W/g)'])
    k = 1
    while k < len(charging_csp) and k < len(discharging_csp):
        efficiency.append(100*discharging_q[k]/charging_q[k])
        energy_efficiency.append(100*discharging_e[k]/charging_e[k])
        writer.writerow([k,charging_csp[k],discharging_csp[k],
                                        charging_esr[k],
                                        discharging_esr[k],
                                        charging_q[k],
                                        discharging_q[k],
                                        efficiency[k-1],charging_e
                                        [k],discharging_e[k],
                                        energy_efficiency[k-1],
                                        charging_p[k],
                                        discharging_p[k]])
        k += 1
    target.close()

length = len(charging_csp)

if len(charging_csp) > 10:
    charging_csp_mean = np.mean(charging_csp[length - 10 : length])
    charging_csp_stdev = sem(charging_csp[length - 10 : length])
    print('Charging Csp = ',charging_csp_mean,'+/-',
                                    charging_csp_stdev)
```

```
discharging_csp_mean = np.mean(discharging_csp[length - 10 :
                                length])
discharging_csp_stdev = sem(discharging_csp[length - 10 : length]
                                )
print('Discharging Csp = ', discharging_csp_mean,'+/-',
                                discharging_csp_stdev)

charging_esr_mean = np.mean(charging_esr[length - 10 : length])
charging_esr_stdev = sem(charging_esr[length - 10 : length])
print('Charging ESR = ',charging_esr_mean,'+/-',
                                charging_esr_stdev)

discharging_esr_mean = np.mean(discharging_esr[length - 10 :
                                length])
discharging_esr_stdev = sem(discharging_esr[length - 10 : length]
                                )
print('Discharging ESR = ',discharging_esr_mean,'+/-',
                                discharging_esr_stdev)

efficiency_mean = np.mean(efficiency[length - 10 : length])
efficiency_stdev = sem(efficiency[length - 10 : length])
print('Coulombic Efficiency = ',efficiency_mean,'+/-',
                                efficiency_stdev)

charging_e_sample = charging_e[length - 10 : length]
charging_e_mean = np.mean(charging_e_sample)
charging_e_stdev = sem(charging_e_sample)
print('Specific Energy Input = ',charging_e_mean,' +/- ',
                                charging_e_stdev)

discharging_e_sample = discharging_e[length - 10 : length]
discharging_e_mean = np.mean(discharging_e_sample)
discharging_e_stdev = sem(discharging_e_sample)
print('Specific Energy Output = ',discharging_e_mean,' +/- ',
                                discharging_e_stdev)
```

```
    energy_efficiency_sample = energy_efficiency[length - 10 : length
                                        ]
    energy_efficiency_mean = np.mean(energy_efficiency_sample)
    energy_efficiency_stdev = sem(energy_efficiency_sample)
    print('Energy Efficiency = ',energy_efficiency_mean,' +/- ',
                                        energy_efficiency_stdev)

    charging_p_sample = charging_p[length - 10 : length]
    charging_p_mean = np.mean(charging_p_sample)
    charging_p_stdev = sem(charging_p_sample)
    print('Specific Power Input = ',charging_p_mean,' +/- ',
                                        charging_p_stdev)

    discharging_p_sample = discharging_p[length - 10 : length]
    discharging_p_mean = np.mean(discharging_p_sample)
    discharging_p_stdev = sem(discharging_p_sample)
    print('Specific Power Output = ',discharging_p_mean,' +/- ',
                                        discharging_p_stdev)
else:
    charging_csp_mean = np.mean(charging_csp[1:-1])
    charging_csp_stdev = sem(charging_csp[1:-1])
    print('Charging Csp = ',charging_csp_mean,'+/-',
                                        charging_csp_stdev)

    discharging_csp_mean = np.mean(discharging_csp[1:-1])
    discharging_csp_stdev = sem(discharging_csp[1:-1])
    print('Discharging Csp = ',discharging_csp_mean,'+/-',
                                        discharging_csp_stdev)

    charging_esr_mean = np.mean(charging_esr[1:-1])
    charging_esr_stdev = sem(charging_esr[1:-1])
    print('Charging ESR = ',charging_esr_mean,'+/-',
                                        charging_esr_stdev)

    discharging_esr_mean = np.mean(discharging_esr[1:-1])
    discharging_esr_stdev = sem(discharging_esr[1:-1])
```

```
    print('Discharging ESR = ',discharging_esr_mean,'+/-',
                                        discharging_esr_stdev)

    efficiency_mean = np.mean(efficiency[1:-1])
    efficiency_stdev = sem(efficiency[1:-1])
    print('Coulombic efficiency = ',efficiency_mean,' +/- ',
                                        efficiency_stdev)

    charging_e_mean = np.mean(charging_e[1:-1])
    charging_e_stdev = sem(charging_e[1:-1])
    print('Specific Energy Input = ',charging_e_mean,' +/- ',
                                        charging_e_stdev)

    discharging_e_mean = np.mean(discharging_e[1:-1])
    discharging_e_stdev = sem(discharging_e[1:-1])
    print('Specific Energy Output = ',discharging_e_mean,' +/- ',
                                        discharging_e_stdev)

    energy_efficiency_mean = np.mean(energy_efficiency[1:-1])
    energy_efficiency_stdev = sem(energy_efficiency[1:-1])
    print('Energy efficiency = ',energy_efficiency_mean,' +/- ',
                                        energy_efficiency_stdev)

    charging_p_mean = np.mean(charging_p[1:-1])
    charging_p_stdev = sem(charging_p[1:-1])
    print('Specific Power Input = ',charging_p_mean,' +/- ',
                                        charging_p_stdev)

    discharging_p_mean = np.mean(discharging_p[1:-1])
    discharging_p_stdev = sem(discharging_p[1:-1])
    print('Specific Power Output = ',discharging_p_mean,' +/- ',
                                        discharging_p_stdev)

outputs = open((file + '_outputs.txt'), 'w')
outputs.write('Charging Csp = ' + str(charging_csp_mean) + ' +/- ' +
                                    str(charging_csp_stdev) + '\n')
```

```
outputs.write('Discharging Csp = ' + str(discharging_csp_mean) + '
                                    +/- ' + str(discharging_csp_stdev)
                                     + '\n')
outputs.write('Charging ESR = ' + str(charging_esr_mean) + ' +/- ' +
                                    str(charging_esr_stdev) + '\n')
outputs.write('Discharging ESR = ' + str(discharging_esr_mean) + '
                                    +/- ' + str(discharging_esr_stdev)
                                     + '\n')
outputs.write('Coulombic efficiency = ' + str(efficiency_mean) + '
                                    +/- ' + str(efficiency_stdev) + '\
                                    n')
outputs.write('Charging Esp = '+  str(charging_e_mean) + ' +/- ' +
                                    str(charging_e_stdev) + '\n')
outputs.write('Discharging Esp = '+  str(discharging_e_mean) + ' +/-
                                    ' + str(discharging_e_stdev) + '\n
                                    ')
outputs.write('Energy efficiency = ' + str(energy_efficiency_mean) +
                                    ' +/- ' + str(
                                    energy_efficiency_stdev) + '\n')
outputs.write('Charging Psp = '+  str(charging_p_mean) + ' +/- ' +
                                    str(charging_p_stdev) + '\n')
outputs.write('Discharging Psp = '+  str(discharging_p_mean) + ' +/-
                                    ' + str(discharging_p_stdev) + '\n
                                    ')


outputs.close()



charging_csp.clear()
discharging_csp.clear()
charging_esr.clear()
discharging_esr.clear()
charging_q.clear()
discharging_q.clear()
efficiency.clear()
time.clear()
```

```
potential.clear()
current.clear()
```

Colophon

This thesis is based on a template developed by Matthew Townson and Andrew Reeves. It was typeset with LaTeX 2_ε. It was created using the *memoir* package, maintained by Lars Madsen, with the *madsen* chapter style. The font used is Latin Modern, derived from fonts designed by Donald E. Knuth.